

Université du Québec  
Institut National de la Recherche Scientifique  
Centre Énergie, Matériaux et Télécommunication (INRS-EMT)

**Towards the advanced high-energy multidimensional laser  
technology through harnessing the spatiotemporal nonlinear  
enhancement**

Par

Reza Safaei mohammadabadi

Thèse présentée pour l'obtention du grade de  
Philosophiae Doctor (Ph.D.)  
en sciences de l'Énergie et des Matériaux

**Jury d'évaluation**

|   |  |
|---|--|
| Président du jury et<br>examineur interne | François Vidal<br>INRS-EMT                             |
| Examineur externe                         | Frank Wise<br>Cornell University                       |
| Examineur externe                         | David Jones<br>University of British Columbia<br>(UBC) |
| Directeur de recherche                    | François Légaré<br>INRS - EMT                          |

## ABSTRACT

This dissertation can be summarized in three parts. First, we study the principles of the pulse compression in gas filled hollow core fibers (HCF) in single mode regime. Simulations and experiments about the spectra after the fiber filled with Raman inactive gas are studied. In the second part, we demonstrate a new approach for scaling the efficiency of spectral broadening towards the red in HCF filled with Raman active medium. The rotational Raman contribution to the nonlinear index arises from the alignment of molecules interacting with the laser field, modeled by solving the time-dependent Schrödinger equation. We find that alignment induced by laser pulses whose duration is comparable to the characteristic timescale of alignment, enhances the red-shifted spectral broadening compared to noble gases. The applicability of this approach to state-of-the-art ytterbium (Yb) laser technology with longer pulse durations (hundreds of femtoseconds) is discovered, for which efficient broadening based on conventional Kerr nonlinearity is challenging to achieve. This approach paves a new way to upscale the peak power to the multi-TeraWatt (TW) regime while increasing the compactness of nonlinear systems.

Finally, we explore nonlinear pulse propagation in multimode regime through multidimensional numerical simulations and compare with our experimental results. In this regime, nonlinear effects occur between modes, and quantities like energy, phase and frequency are modified on an intermodal basis. We find that by controlling multidimensional intermodal dynamics, it is possible to provide sufficient nonlinearity to counter the potential diffraction while keeping the beam diameter constant in high-energy regime. Furthermore, we demonstrate several key features of the controlled spatiotemporal regime which are counter-intuitive, and they are opposite to the results obtained from spectral broadening based on Kerr nonlinearity.

The ability to generate high-energy and spatiotemporally engineered coherent light fields is expected to lead to breakthroughs in laser science through a wide range of applications such as power scalability, the generation of tunable ultra-broadband long-wavelength sources and scaling of high harmonic generation (HHG) cut-off to generate higher photon energies. Beyond these technology breakthroughs, the formation of high-energy multidimensional solitary states in a molecular gas-filled large core HCF combines the advantages of a many-modes capacity with low modal dispersion and pressure-tunable dispersion and nonlinearity. This provides an influential horizon for the exploration of multidimensionality concepts in other physical systems which are limited by complex experimental conditions.

Key words: multidimensional solitary states, multidimensional intermodal dynamics, Raman nonlinearity, Kerr nonlinearity, multi-TeraWatt (TW) regime, hollow core fiber (HCF), high harmonic generation (HHG) and ytterbium (Yb) lasers.

# RÉSUMÉ

Cette thèse peut être résumée en trois parties. D'abord, nous étudions les principes de la compression d'impulsions ultra-brèves dans des fibres creuses ("Hollow core fiber – HCF") en régime monomode. Des simulations numériques et des expériences étudiant l'élargissement spectral dans les fibres creuses avec un gaz inactif d'un point de vue des transitions Raman sont réalisées. Dans la deuxième partie, nous démontrons une nouvelle approche pour augmenter l'efficacité de l'élargissement spectral vers les grandes longueurs d'onde (vers le rouge) dans des fibres creuses remplies d'un gaz actif en transition Raman. La contribution rotationnelle via des transitions Raman à l'indice de réfraction non linéaire provient de l'alignement des molécules interagissant avec le champ laser, modélisée en solutionnant l'équation de Schrödinger dépendante du temps. Nous constatons que l'alignement induit par des impulsions laser dont la durée est comparable à l'échelle de temps caractéristique de l'alignement améliore l'élargissement spectral décalé vers le rouge par rapport aux gaz nobles (inactif du point de vue Raman). L'applicabilité de cette approche à la technologie laser ytterbium (Yb) ayant des durées d'impulsion plus longues (des centaines de femtosecondes) que les laser Titane-Saphir (Ti-Sa, quelques dizaines de femtosecondes), pour laquelle un élargissement efficace basé sur la non-linéarité par effet Kerr conventionnel est difficile à réaliser, est découverte. Cette approche introduit une nouvelle façon d'augmenter la puissance crête des laser ytterbium et de possiblement atteindre le régime multi-TéraWatt (TW) est discuté. Par ailleurs, cette approche a le potentiel de rendre les systèmes d'élargissement spectral plus compact.

Enfin, nous explorons la propagation d'impulsions non-linéaires en régime multimode à travers des simulations numériques multidimensionnelles et comparons avec nos résultats expérimentaux. Dans ce régime, des effets non-linéaires se produisent entre les modes, et des quantités comme l'énergie, la phase et la fréquence sont modifiées sur une base intermodale. Nous constatons qu'en contrôlant la dynamique intermodale multidimensionnelle, il est possible de fournir une non-linéarité suffisante pour contrer la diffraction potentielle tout en maintenant le diamètre du faisceau constant en régime de haute énergie. De plus, nous démontrons plusieurs caractéristiques clés du régime spatio-temporel contrôlé qui sont contre-intuitives, et elles sont opposées aux résultats obtenus à partir d'un élargissement spectral basé sur la non-linéarité par effet Kerr.

La capacité de générer des champs lumineux cohérents de haute énergie et de contrôler leurs caractéristiques spatio-temporelles pourrait conduire à des percées en optique et photonique grâce à un large éventail d'applications telles que l'augmentation de la puissance, la

génération de sources accordables ultra-large bandes à grande longueur d'onde et l'augmentation de l'énergie de coupure obtenue par génération d'harmoniques d'ordres élevés ("High Harmonic Generation – HHG"). Au-delà de telles percées technologiques, la formation d'états solitoniques multidimensionnels de haute énergie dans une fibre creuse remplie de gaz moléculaire actif du point de vue Raman combine les avantages d'une capacité à plusieurs modes avec une faible dispersion modale et une dispersion et une non-linéarité réglables en pression. Cela fournit une perspective innovante pour l'exploration des concepts de multidimensionnalité dans d'autres systèmes physiques qui sont limités par des conditions expérimentales complexes.

Mots-clés: états solitoniques multidimensionnels, dynamique intermodale multidimensionnelle, non-linéarité par transition Raman stimulée, non-linéarité par effet Kerr, régime multi-TéraWatt (TW), fibre creuse (HCF), génération d'harmoniques d'ordres élevés ("High Harmonic Generation – HHG") et laser ytterbium (Yb).

## SOMMAIRE RÉCAPITULATIF

Le régime multimode de propagation non-linéaire d'impulsions ultra-brèves à travers des fibres creuses remplies de gaz ("Hollow core fiber – HCF") a un grand potentiel pour attirer l'intérêt sur l'étude des dynamiques spatio-temporelles ainsi que dans le contexte des sources laser ultra-rapides. Cet intérêt découle de différences fondamentales par rapport au fonctionnement monomode en raison de la complexité spatio-temporelle et des interactions intermodales complexes en régime multimode. À ce jour, le régime multimode n'a été étudié que dans des cas limites dans des fibres creuses remplies de gaz en raison d'un effet d'autofocalisation à une puissance crête élevée et d'une diffraction inhérente. Dans cette thèse, la propagation non-linéaire dans les HCF remplies de gaz a été étudiée comme une plateforme robuste et pratique pour les interactions non-linéaires. À travers des études expérimentales et des simulations théoriques, nous présentons le contrôle de l'intensification non-linéaire comme un outil polyvalent pour de futures applications.

Dans la première partie, nous étudions les principes de la compression d'impulsions dans des fibres creuses en régime monomode. Des simulations et des expériences sur l'élargissement spectral après le remplissage de la fibre creuse par un gaz inactif d'un point de vue Raman sont étudiées. Pour simuler la propagation des impulsions et l'élargissement spectral, l'équation non linéaire de Schrödinger considérant la dispersion de vitesse de groupe ("Group Velocity Dispersion – GVD"), l'automodulation de phase ("Self-Phase Modulation – SPM"), l'auto-redressement et l'ionisation a été résolue numériquement. Les forces, les faiblesses, et les limites de cette méthode ont été étudiées pour les sources laser à impulsions à haute énergie et à taux de répétition élevé.

Le développement de technologies laser ultrarapides a permis de découvrir des phénomènes physiques suivant l'interaction lumière-matière [186-189]. En atteignant des niveaux de puissance plus élevés ainsi qu'une durée d'impulsion plus courte, il a été possible d'explorer la dynamique jusqu'à la durée de l'attoseconde [190-196] et dans les régimes à forte intensité [152, 156, 158, 197-200]. Dans les dernières décennies du 20<sup>e</sup> siècle, l'avènement du milieu à gain Ti-Sa [201] a disséminé les lasers femtosecondes. Le verrouillage de modes via l'effet Kerr [202] en combinaison avec une amplification des impulsions [203] a accéléré l'accès à une intensité focale élevée comparable ou même supérieure au champ coulombien dans les atomes pour atteindre le régime relativiste [204, 205]. En raison du milieu de gain qui limite la largeur spectrale pouvant être amplifiée, un étage supplémentaire pour l'élargissement spectral et la compression est nécessaire pour raccourcir encore plus la durée des impulsions

des lasers Ti-Sa à quelques cycles optiques. Plus couramment, l'élargissement de la bande spectrale au moyen de l'automodulation de phase dans les gaz nobles dans une HCF et d'une compensation de dispersion ultérieure [169] a démontré une compression jusqu'au régime du cycle unique [206]. De nos jours, le concept de HCF est bien établi et largement utilisé dans la communauté en raison de sa polyvalence et de sa robustesse [81, 84, 135, 207]. La compression d'impulsions de faible énergie utilisant diverses molécules gazeuses dans le HCF a récemment été étudiée [88, 139, 181]. Cela donne la perspective d'appliquer la méthode HCF pour compresser des lasers Yb [19, 208], qui retiennent l'attention de la communauté scientifique en tant que source laser femtoseconde potentielle, par ex. pour la génération d'harmoniques d'ordres élevés (HHG) à haut flux grâce à sa puissance moyenne élevée et son taux de répétition élevé [209-212].

Dans le régime monomode (1D) à énergie faible d'impulsions, 3 travaux principaux ont été réalisés.

- 1) Nous introduisons des molécules d'hydrofluorocarbures comme milieu alternatif aux gaz nobles à faible potentiel d'ionisation comme le krypton ou le xénon pour compresser des impulsions ultra-courtes d'énergie relativement faible dans une fibre creuse conventionnelle avec compensation ultérieure de la dispersion. L'élargissement spectral des impulsions de deux systèmes lasers différents a dépassé ceux obtenus avec l'argon et le krypton. Initialement, des impulsions de 40 fs, 800 nm, 120  $\mu$ J ont été compressées à quelques cycles optiques. Avec la même approche, un facteur de compression supérieur à 10 a été démontré pour un laser Yb (1030 nm, 170 fs, 200  $\mu$ J) conduisant à des durées d'impulsions compressées de 15,6 fs.

Ces travaux indiquent que les gaz moléculaires, plus particulièrement les hydrofluorocarbures, comme le R152a et le R134a, peuvent être une alternative valable aux gaz nobles coûteux pour la compression d'impulsions utilisant une HCF. Les caractéristiques moléculaires conduisant à une réponse non linéaire similaire aux atomes ne sont pas entièrement comprises et doivent plus être étudiées. Cependant, les faibles potentiels d'ionisation qui caractérisent ces molécules sont associés à des indices non linéaires plus élevés  $n_2$ . Par conséquent, un élargissement spectral significatif et économique est possible avec une intensité d'impulsion plus petite, ce qui rend cette méthode idéale pour les applications de puissance moyenne élevée avec une énergie d'impulsion de l'ordre de quelques dizaines à plusieurs centaines de  $\mu$ J.

- 2) La compression d'impulsions laser ultracourtes de faible énergie à l'aide d'un HCF rempli de 1-1 difluoroéthane ( $C_2H_4F_2$ ), également connu sous le nom de R152a, est démontrée.

Une impulsion laser Ti: Sa de 45 fs, 16  $\mu$ J est élargie spectralement dans une HCF remplie de R152a et ensuite compressée à  $\sim$ 9fs avec une énergie d'impulsion de  $\sim$ 6 $\mu$ J, ce qui correspond à une compression d'un facteur 5. Ce gaz abordable et facilement accessible promet de compresser les lasers de puissance moyenne élevée de nouvelle génération en conjonction avec une configuration HCF flexible. De plus, l'influence de la GVD sur l'élargissement spectral et sa dépendance à la pression ont été simulées numériquement. À des pressions supérieures à 2,5 bars, l'élargissement spectral est affecté par une interaction entre deux effets: bien qu'il soit favorisé par un milieu gazeux plus dense conduisant à une non-linéarité plus élevée, il est en même temps limité par la plus faible intensité résultant de l'étirement des impulsions qui provoque une limitation globale à des pressions plus élevées.

Technologiquement, le R152a est un gaz approprié pour la compression d'impulsions utilisant une fibre creuse dans le régime d'impulsions à basse énergie. Ce gaz particulier possède un potentiel d'ionisation relativement faible de  $\sim$  11,9 eV [185] par rapport aux gaz nobles, et simultanément un grand  $n_2$ . Grâce à son prix relativement bas, il peut également être utilisé dans un schéma de pression différentielle, qui est la méthode préférée pour éviter les effets non linéaires perturbant le couplage à l'entrée de la fibre. Nos résultats prometteurs montrent que le gaz R152a peut être un excellent candidat pour compresser des impulsions laser à basse énergie dans une configuration HCF conventionnelle, un substitut au xénon à gaz noble coûteux. À l'avenir, nous allons pousser davantage cette méthode pour compresser les systèmes laser Yb à taux de répétition élevé, tels que les systèmes lasers Yb 100 W sub-300 fs disponibles commercialement et fonctionnant à des centaines de kHz.

- 3) Un schéma conventionnel à HCF est mis en œuvre pour étudier l'élargissement spectral des impulsions lasers femtosecondes Ti-Sa dans les molécules d'hydrocarbures saturés par rapport aux molécules d'hydrocarbures non saturés. Alors que les molécules saturées présentent un élargissement spectral similaire aux gaz nobles, pour celles insaturées avec des liaisons  $\pi$ , l'élargissement vers le bleu est restreint. Les simulations numériques soutiennent qu'il s'agit d'une combinaison de la GVD et de la diffusion Raman qui limite l'élargissement spectral pour les molécules non saturées. La compression d'impulsions de basse énergie de  $\sim$ 40fs à  $\sim$ 8fs en utilisant des hydrocarbures saturés est démontrée, suggérant la faisabilité de ce milieu pour la compression d'impulsions lasers à taux de répétition élevé.

Les progrès récents dans le domaine du contrôle cohérent de l'excitation moléculaire permettent de nouvelles techniques d'élargissement spectral et de manipulation des impulsions lumineuses [107]. Les échelles de temps de l'alignement moléculaire induit par laser peuvent être classées en deux régimes différents: 1) Dans le régime d'excitation adiabatique où la durée de l'impulsion est beaucoup plus longue que la période de rotation moléculaire [105, 213, 214], l'alignement maximal est obtenu au pic de l'enveloppe de l'impulsion laser. Le milieu redevient isotrope une fois l'impulsion terminée. 2) Dans le régime d'excitation impulsive, où la durée de l'impulsion d'entrée est comparable à la période de rotation moléculaire, l'impulsion donnée par le laser persiste après le passage de l'impulsion et est appelée «kicked-rotor» [121, 215]. Dans ce régime, les impulsions de pompage créent des paquets d'ondes correspondant au mouvement de rotation cohérent des molécules, ce qui conduit à des modulations ultra-rapides de l'indice de réfraction [216]. En utilisant cette approche, les spectres et les phases des impulsions lumineuses ultracourtes ont été manipulés selon des schémas pompe-sonde. Une impulsion de pompe déclenche une évolution temporelle de l'alignement moléculaire et de la susceptibilité optique résultante, qui met en œuvre des changements de phase à l'impulsion de sonde qui s'ensuit avec des délais variables [114, 115, 217]. Malgré les grands progrès réalisés jusqu'à présent avec cette approche, l'énergie des impulsions obtenues, la faible efficacité et la complexité de cette méthode la rendent moins pratique que la méthode de pointe basée sur la SPM [19, 81, 218]. Bien que l'approche SPM ait conduit à des applications importantes dans divers domaines de la science laser [219], son efficacité d'élargissement est inversement proportionnelle à la durée de l'impulsion. Cela la rend moins applicable aux impulsions plus longues d'une durée sous-picoseconde (ps). En outre, la puissance crête maximale typique pouvant être obtenue par compression d'impulsions basées sur la SPM dans des fibres creuses est limitée au  $\sim 1$  TW

Dans le chapitre 3, nous démontrons une nouvelle approche pour augmenter l'efficacité de l'élargissement spectral vers le rouge dans les HCF remplies de milieu actif d'un point de vue des transitions Raman. La contribution rotationnelle via les transitions Raman stimulées à l'indice non-linéaire provient de l'alignement des molécules interagissant avec le champ laser. Ceci est modélisé en solutionnant l'équation de Schrödinger dépendante du temps. Nous constatons que l'alignement induit par des impulsions lasers dont la durée est comparable à l'échelle de temps caractéristique de l'alignement améliore l'élargissement spectral décalé vers le rouge par rapport aux gaz nobles. L'applicabilité de cette approche à la technologie laser Yb ayant des durées d'impulsion plus longues (des centaines de femtosecondes), pour laquelle un élargissement efficace basé sur la non-linéarité par effet Kerr conventionnel est difficile à réaliser, est découverte. Cette approche introduit une nouvelle façon d'augmenter la

puissance crête avec le potentiel d'atteindre le régime multi-TéraWatt (TW) tout rendant les systèmes non-linéaires de compression plus compact.

D'un point de vue technologique, l'exploitation de l'alignement moléculaire permet un élargissement spectral très efficace pour des impulsions lasers sous-ps. Cela peut conduire à une augmentation d'énergie jusqu'au niveau multi-TW tout en étant applicable aux sources laser Yb. L'intégration de systèmes moléculaires avec un temps de réponse caractéristique beaucoup plus lent et une technologie avancée de fibre creuse avec un large cœur pourrait ouvrir de nouveaux aspects de la conception de futurs dispositifs non linéaires hautes performances. De plus, l'excitation «impulsive» des molécules se traduit par une forte amélioration du décalage vers le rouge en longueur d'onde, et cet effet est indépendant de la longueur d'onde de l'impulsion stimulant le processus d'alignement. Par conséquent, cette approche conduit à une solution pratique pour la mise en place de sources ultra-larges bandes à haute énergie dans l'infrarouge et le moyen-infrarouge via un décalage vers le rouge, et elle est intéressante pour une variété d'applications de champ fort, qui bénéficient d'une telle augmentation de la longueur d'onde centrale de l'impulsion ultra-brève.

Pour étudier la dépendance de la durée d'impulsion sur l'élargissement spectral avec un milieu actif du point de vue des transitions Raman, la durée des impulsions a été ajustée de 40 fs à 1300 fs, en variant la séparation entre les paires de réseaux d'un amplificateur Ti-Sa (en ajoutant une dispersion de retard de groupe positive). La puissance de crête a été maintenue constante pour les différentes durées d'impulsion. Les résultats expérimentaux de l'élargissement spectral sous une pression de 1000 mbar de N<sub>2</sub> pour des durées d'impulsion d'entrée variables sont illustrés à la Figure 22 (page 58). Lorsque la durée d'impulsion est augmentée de 40 fs à 100 fs, le spectre est décalé vers le rouge de 900 nm à une valeur maximale de 950 nm. En augmentant la durée d'impulsion de 100 fs à 200 fs, l'élargissement maximum vers le rouge se réduit à nouveau à 900 nm. Ceci est parfaitement cohérent avec la théorie de l'alignement moléculaire qui stipule que l'utilisation d'une impulsion laser avec une durée proche de l'échelle caractéristique de la rotation moléculaire permet d'optimiser l'alignement nonadiabatique, tout comme pour pousser une personne sur une balançoire avec le timing parfait pour augmenter l'amplitude du mouvement de balancement. Le spectre simulé pour N<sub>2</sub> en utilisant l'équation de Schrödinger dépendante du temps unidimensionnelle (TDSE) pour différentes durées d'impulsion d'entrée est montré sur la Figure 22(b) (page 58). D'après la simulation, le  $T_{rot}$  pour N<sub>2</sub> est d'environ 100 fs, ce qui correspond au gain Raman maximum. Les simulations présentées ici peuvent reproduire la forme d'asymétrie du spectre en utilisant une impulsion d'entrée d'environ 100 fs. Cependant, ces simulations prédisent une efficacité d'élargissement spectral diminuée avec une durée d'impulsion croissante

accompagnée d'une forme spectrale symétrique. Comme la fonction de réponse en retard des molécules  $h_R(t)$  atteint un pic autour de 100 fs, l'effet retardé de la réponse moléculaire devient de plus en plus faible pour la durée d'impulsion d'entrée plus longue. Il converge vers le même comportement de réponse instantanée que la SPM, donnant lieu à une forme spectrale symétrique et à une baisse d'efficacité d'élargissement spectral. La durée d'impulsion différente peut également être comprise avec le gain Raman dans le domaine fréquentiel. L'étape d'excitation rotationnelle de  $N_2$  est beaucoup plus grande que la largeur de bande instantanée des impulsions 700fs, tandis que le spectre de 100 fs tombe efficacement dans la largeur de bande de rotation. Par conséquent, à 100 fs, le modèle 1D prédit les spectres asymétriques avec un décalage vers le rouge très efficace présentant une contribution dominante du processus Raman, et à plus longue durée d'impulsion, un élargissement plus symétrique du spectre serait attendu, impliquant une contribution très faible de la diffusion Raman stimulée (SRS). Cependant, pour les impulsions jusqu'au domaine picoseconde, les résultats expérimentaux montrent des spectres asymétriques dans  $N_2$  avec un décalage vers le rouge très efficace présentant une contribution dominante du processus Raman qui n'était pas prédite par les simulations 1D. Par conséquent, afin de bien comprendre la physique observée dans la HCF remplie de gaz moléculaire, une étude numérique plus sophistiquée a été nécessaire qui comprennent des effets spatio-temporels très complexes qui ne se produisent pas dans le régime dominé par la SPM. Ceci est démontré dans le chapitre 4.

Les fibres creuses remplies de gaz ont été développées comme un milieu idéal pour l'interaction non linéaire des impulsions de haute énergie. Une grande partie de ce développement s'est concentrée sur la transmission d'impulsions en dessous de la puissance critique à des fins d'élargissement spectral efficace et de compression d'impulsions. Donc, la HCF a été optimisée pour le guidage monomode avec des pertes de propagation minimales uniquement limitées par la perte intrinsèque du guide d'ondes. L'avènement du HCF à large cœur (par exemple 6 mètres 1 mm de diamètre) a ouvert une voie pour une interaction non linéaire efficace des impulsions de haute énergie résultant en une compression d'impulsions de haute énergie à une durée d'impulsion de quelques cycles. Ces développements repoussent les limites de la technologie actuelle pour l'élargissement spectral basé sur la SPM, exigeant des fibres avec des zones de mode plus grandes et d'une plus longueur plus importante. Cependant, comme le montre le chapitre 2, la SPM est un effet non linéaire dominant dans un régime 1D efficace. La non-linéarité SPM est inversement proportionnelle à la durée de l'impulsion, ce qui la rend moins applicable aux impulsions plus longues. Bien que, pour une géométrie donnée d'interaction non linéaire, l'efficacité de l'élargissement spectral puisse être partiellement compensée soit en augmentant la densité moyenne, soit en

utilisant un milieu différent avec une non-linéarité plus élevée, l'autofocalisation et le couplage à des modes d'ordre supérieur ("High Order Modes – HOMs") restent une limitation fondamentale qui entraîne une forte instabilité et une destruction des qualités spatiales à la sortie des HCFs. Dans ce chapitre, nous démontrons une nouvelle avenue pour contrôler les HOMs et le chaos qui en résulte dans les HCFs qui permet d'exploiter des voies multidimensionnelles étendues pour une amélioration non linéaire. Des interactions multidimensionnelles efficaces et la création d'états multimodes stables avec une cohérence spatio-temporelle élevée et une évolutivité de la puissance dans les HCFs à large cœur sont démontrées.

Enfin, nous présentons la principale réalisation de cette thèse au chapitre 4. Nous démontrons la génération d'états solitoniques multidimensionnels (MDSS) dans une fibre creuse à large cœur remplie d'azote ( $N_2$ ). Les résultats expérimentaux et les simulations numériques indiquent que le couplage d'impulsions de haute énergie à des états multimodes à l'entrée du HCF favorise le processus de diffusion Raman stimulée (SRS) dans un milieu actif d'un point de vue des transitions Raman. Par conséquent, la non-linéarité spatio-temporelle améliorée inhibe la diffraction potentielle due à l'autofocalisation, conduisant à une localisation spatiale de haute qualité des états multidimensionnels. Le MDSS généré au début de la fibre subit un processus de cascade par effet Raman stimulé et sur toute la longueur d'interaction du HCF, résultant en des spectres à large bande décalés vers le rouge à la sortie du HCF. De plus, nous constatons que les impulsions MDSS en sortie de fibre possèdent une phase spectrale quadratique négative, ce qui est contre-intuitif, car elle est de signe opposé à la phase spectrale obtenue à partir d'un élargissement spectral basé sur la non-linéarité par effet Kerr. Ainsi, les impulsions MDSS en sortie de fibre peuvent être directement compressées en une durée d'impulsion de quelques cycles par propagation linéaire dans le régime de dispersion normal fourni par une simple lame de verre. Pour confirmer la qualité spatio-temporelle des impulsions compressées, nous employons le processus non-linéaire de génération d'harmoniques d'ordres élevés (HHG) et démontrons l'extension de l'énergie de coupure des photons générés.

Le concept physique de ce travail est illustré et expliqué à la Figure 56(a) (page 124). Comme point de référence de départ, la taille du point focal à l'impulsion d'entrée HCF a été choisie pour obtenir une efficacité de couplage élevée dans le mode fondamental. Sous la condition de guidage faible dans le HCF, les modes se répartissent en groupes de modes polarisés linéairement ( $LP_{mn}$ ) [126]. L'autofocalisation dans la HCF est interprétée comme le transfert d'énergie du mode fondamental ( $LP_{01}$ ) vers d'autres modes  $LP_{0n}$  qui ont une symétrie de rotation avec l'intensité maximale dans la partie centrale [16]. Dans le régime à haute énergie, les effets d'autofocalisation et de diffraction deviennent importants et de multiples modes  $LP_{0n}$

sont créés au début de la fibre. Ces voies multidimensionnelles étendues conduisent à une amélioration du processus Raman, qui fournit une non-linéarité suffisante pour équilibrer la diffraction potentielle. Ce mécanisme d'auto-piégeage non linéaire, associé à la dispersion modale ultra-faible inhérente aux HCF à large cœur, fait que le MDSS généré subit un élargissement spectral efficace décalé vers le rouge via le processus d'effet Raman stimulé. Dans l'expérience, des impulsions de 700 fs de haute énergie (5 mJ / impulsion) avec une longueur d'onde centrale de 780 nm ont été couplées dans une fibre creuse (500  $\mu\text{m}$ ) de 3m de long remplie de  $\text{N}_2$ . Les impulsions de 700 fs sont obtenues en introduisant une dérive de fréquences positive des impulsions de 40 fs à partir d'un amplificateur Ti-Sa. À la sortie de la HCF, les états solitoniques cohérents ont une phase spectrale quadratique négative. Ces états solitoniques sont expérimentalement séparés de la partie pompe en plaçant un filtre passe-haut (supérieur à 830 nm) à la sortie de la HCF (la partie pompe est sélectionnée par un filtre passe-bande (760 nm-790 nm)). Les impulsions MDSS à large bande sont ensuite compressées à l'aide d'un simple morceau de verre.

En conclusion, les sources lasers ultra-brèves ont ouvert de nouveaux horizons pour contrôler et mesurer la dynamique ultra-rapide dans la matière. En plus d'une résolution temporelle élevée, les impulsions ultra-brèves ont la capacité de supporter des puissances crête et des intensités élevées au-delà de toute intuition humaine raisonnable. Leurs impacts remarquables fournissent des outils avancés qui étaient autrefois difficiles, par exemple les sources de rayonnement X ultra-rapides à haut flux et leur utilisation pour sonder la dynamique attoseconde et femtoseconde. Le contrôle de la non-linéarité offre de nombreuses possibilités de trouver de nouvelles générations de lasers ultra-courts qui peuvent répondre à une large gamme de demandes du monde réel d'une manière pratique et commercialement viable. L'observation et la création de faisceaux auto-piégés stables à haute énergie dans un régime hautement multimode avec la capacité de compresser des impulsions à quelques cycles optiques avec une haute qualité spatio-temporelle est une indication claire de la possibilité de contrôler la non-linéarité spatio-temporelle et les interactions multidimensionnelles dans une HCF à large cœur ainsi que les impacts potentiels. L'impact technologique immédiat de ce travail peut être de générer des impulsions à quelques cycles par des lasers Yb avec une approche simple, robuste et efficace fournissant pour la physique des champs forts. La capacité de générer des champs lumineux cohérents à haute énergie devrait conduire à des percées dans la science du laser grâce à un large éventail d'applications telles que l'augmentation de la puissance [226], la génération de sources accordables ultra-larges bandes à grande longueur d'onde [19] et la mise à l'échelle de l'énergie de coupure HHG pour générer des photons de plus courte longueur d'onde. Cela conduirait à une commercialisation réussie qui est toujours une condition préalable à

l'adoption à grande échelle d'outils physiques (ou de presque toutes les technologies), comme ceux que nous pourrions éventuellement créer avec le contrôle de la non-linéarité dans les fibres HCF en régime multimode.

Alors que nous nous tournons vers l'avenir, les lasers et les amplificateurs qui peuvent incorporer élégamment des fibres multimodes peuvent avoir une puissance considérablement plus élevée que les systèmes basés sur la propagation en régime monomode. Cette promesse s'étend au-delà de l'ultra-rapide et de la science des lasers, car la dimensionnalité et les non-linéarités spatio-temporelles représentent des limitations clés pour les lasers hautes puissances de toutes sortes. Cependant, alors que nous considérons les puissances de pointe multi-TW comme une perspective plausible pour les travaux en cours dans les HCF, trois perspectives importantes attendent d'être découvertes dans ce domaine. Premièrement, la découverte de nouveaux concepts physiques potentiels qui peuvent être découverts en utilisant les HCFs remplis de gaz ayant l'avantage d'une capacité à plusieurs modes avec une faible dispersion modale et une dispersion et une non-linéarité réglables en pression. À noter que ces systèmes ont un net avantage sur les fibres solides qui ont une non-linéarité et une dispersion fixes. Deuxièmement, des impulsions multimodes cohérentes à haute énergie multimode peuvent potentiellement être mises en œuvre dans de nouvelles applications qui transcendent fondamentalement les conceptions monomodes traditionnelles. Enfin, des technologies économiques, compactes et fiables sont le résultat que de nombreux scientifiques attendent dans des domaines appliqués. Cependant, le trajet pour faire une source laser spatio-temporellement cohérente nécessite d'apprendre et de comprendre comment contrôler la non-linéarité en régime multidimensionnel. Cela fournit une perspective influente pour l'exploration des concepts de multidimensionnalité dans d'autres systèmes physiques [1] qui sont limités par des conditions expérimentales complexes.

Cette thèse n'est qu'un début et je propose ici une série d'expériences intéressantes à effectuer au laboratoire ALLS. Je suis convaincu du potentiel de celles-ci en termes d'impacts scientifiques et technologiques :

- 1) À ce jour, la principale solution à l'accordabilité en longueur d'onde pour les impulsions énergétiques à large bande repose sur l'amplification paramétrique optique ("Optical Parametric Amplification-OPA"), qui nécessite souvent des étapes multiples et complexes, et peut présenter une qualité de faisceau imparfaite. En tirant parti de l'accordabilité continue et de la haute efficacité de l'élargissement spectral décalé vers le rouge, en particulier pour le régime d'alignement maximal (Figure 30, page X), je propose de sélectionner la partie rouge

des spectres à différentes pressions (différentes longueurs d'onde centrales) et de les compresser en conséquence. Je crois que cette méthode peut être une alternative pratique aux systèmes OPA les plus exigeants pour obtenir un réglage continu dans l'infrarouge et le moyen-infrarouge.

2) L'amélioration spatio-temporelle ne dépend pas de la longueur d'onde du laser, et les gaz moléculaires comme le  $N_2$  offrent une large fenêtre de transparence s'étendant de la fenêtre spectrale de l'ultraviolet au moyen-infrarouge. Par conséquent, le procédé peut être mis en œuvre dans différentes gammes spectrales. Par exemple, au laboratoire ALLS, nous avons accès à des impulsions à haute énergie à  $1,8 \mu\text{m}$ . Nous avons déjà obtenu quelques résultats préliminaires en utilisant cette source dans une HCF remplie de  $N_2$ , et nous avons réussi à obtenir l'élargissement spectral décalé vers le rouge jusqu'à  $2,6 \mu\text{m}$  avec une efficacité élevée.

3) Les impulsions de quelques cycles optiques à haute énergie dans les régions spectrales de l'infrarouge et du moyen-infrarouge sont attrayantes pour un certain nombre d'applications à champ élevé, par exemple, la génération d'harmoniques d'ordres élevés, et nous permettent d'étendre l'énergie de coupure vers des photons avec une énergie de l'ordre du keV en raison de la loi d'échelle en  $\lambda^2$  pour le processus HHG. En utilisant la source développée à la deuxième expérience proposée, une approche simple et efficace de générer des impulsions femtosecondes au voisinage de  $3 \mu\text{m}$  est possible. Il peut conduire à une génération efficace d'harmoniques dans jusqu'au keV pour par exemple sonder la dynamique de magnétisation ultra-rapide aux seuils L des ferromagnétiques.

4) D'un point de vue fondamental, nous pouvons étudier d'autres gaz moléculaires pour vraiment comprendre le rôle des transitions Raman. De plus, nous pouvons utiliser des systèmes moléculaires avec un temps de réponse caractéristique beaucoup plus lent pour l'alignement moléculaire par rapport à  $N_2$  pour étudier le rôle de l'amélioration non linéaire spatio-temporelle pour des impulsions plus longues (quelques picosecondes).

# Tables of Contents

|       |  |    |
|-------|--|----|
| 1     | Introduction .....   | 23 |
| 1.1   | Motivations .....  | 23 |
| 1.1.1 | Demands for ultrafast laser source .....                                   | 24 |
| 1.2   | State of art technology based on 1D nonlinear interaction .....            | 25 |
| 1.2.1 | High energy pulse compression .....  | 25 |
| 1.2.2 | Low energy pulse compression.....  | 28 |
| 1.3   | A new horizon in ultrafast laser technology .....                          | 28 |
| 2     | Hollow-core fiber pulse compression in 1-dimension regime .....            | 31 |
| 2.1   | 1D model .....   | 31 |
| 2.1.1 | Self phase modulation .....  | 33 |
| 2.1.2 | Effect of group velocity dispersion.....                                   | 36 |
| 2.1.3 | Self-steepening.....   | 38 |
| 2.1.4 | The Raman effect .....   | 40 |
| 2.1.5 | Tunneling Ionization, ADK Model .....                                      | 40 |
| 2.1.6 | Plasma contribution .....  | 42 |
| 2.2   | The 1D experimental results and their fundamental limitations .....        | 44 |
| 2.2.1 | Low-energy regime .....  | 45 |
| 2.2.2 | High-energy regime .....   | 46 |
| 3     | Raman effect in molecular gas .....  | 49 |
| 3.1   | Microscopic model of molecular rotation .....                              | 49 |
| 3.2   | Rotational response and Raman gain .....                                   | 52 |
| 3.3   | Spectral broadening in Raman active medium .....                           | 55 |
| 3.4   | Phase construction and pulse compression at maximum alignment regime ..... | 56 |
| 3.5   | Failure of 1D simulations.....   | 58 |
| 4     | Nonlinear enhancement through multidimensional interactions.....           | 61 |
| 4.1   | Theoretical basics .....   | 61 |
| 4.1.1 | Fiber modes.....   | 62 |
| 4.1.2 | The Generalized Multimode NLSE .....                                       | 64 |
| 4.1.3 | The concept of the spatiotemporal nonlinear enhancement .....              | 66 |
| 4.1.4 | Four wave mixing (FWM) .....   | 67 |
| 4.2   | Spatiotemporal dynamics in Raman active medium (N <sub>2</sub> ).....      | 68 |
| 4.2.1 | Comparison with simulations .....  | 70 |
| 4.2.2 | Optimization of HCF input coupling conditions .....                        | 72 |
| 4.2.3 | Phase construction and pulse compression .....                             | 74 |

|       |   |     |
|-------|---|-----|
| 4.2.4 | The efficiency of MD interactions with narrowband sub-picosecond pump pulses .....  | 76  |
| 4.2.5 | Spatiotemporal enhancement at maximum alignment regime .....  | 77  |
| 4.3   | Spatiotemporal dynamics in Raman inactive medium (Ar) .....   | 80  |
| 5     | Articles I-III: pulse compression in 1D regime .....  | 84  |
| 5.1   | Molecular gases for low energy pulse compression in a hollow core fiber .....   | 84  |
| 5.1.1 | Abstract .....  | 84  |
| 5.1.2 | Main manuscript .....   | 84  |
| 5.2   | Low energy pulse compression in hollow core fibers using hydrofluorocarbon molecular gas .....                                | 95  |
| 5.2.1 | Abstract: .....   | 95  |
| 5.2.2 | Main manuscript .....   | 96  |
| 5.3   | Raman effect in the spectral broadening of ultrashort laser pulses in saturated versus unsaturated hydrocarbon molecules..... | 103 |
| 5.3.1 | Abstract .....  | 103 |
| 5.3.2 | Main manuscript .....   | 103 |
| 5.3.3 | Appendix.....   | 111 |
| 6     | Article IV: High energy redshifted and enhanced spectral broadening by molecular alignment .....                              | 113 |
| 6.1   | Abstract .....  | 113 |
| 6.2   | Main manuscript .....   | 114 |
| 7     | Article V: High-energy multidimensional solitary states in hollow core fiber.....   | 123 |
| 7.1   | Abstract .....  | 123 |
| 7.2   | Main manuscript .....   | 124 |
| 8     | Article VI : Coherent Tabletop EUV Ptychography of Nanopatterns .....   | 136 |
| 8.1   | Abstract .....  | 136 |
| 9     | Conclusion and Outlook.....   | 137 |
| 9.1   | Proposed experiments .....  | 138 |
| 10    | References .....  | 140 |

## List of figures

|   |    |
|---|----|
| <b>Figure 1</b> Applications of advanced ultrafast photonics technology, from fundamental research to many important applications in various areas.....   | 25 |
| <b>Figure 2</b> Overview of state-of-art nonlinear pulse compression in the mJ pulse energy level. The compressed pulse energy is plotted versus the input pulse duration. The corresponding peak power is proportional to the size of the symbols. ....  | 27 |
| <b>Figure 3</b> (top) The significant theoretical and experimental breakthroughs of the last 5 years in multimode nonlinear fiber optics (bottom). Sum of times cited per year for source items indexed within Web of Science Core Collection, containing the words: nonlinear multimode optical fiber [74]......   | 29 |
| <b>Figure 4</b> The instantaneous frequency $\Delta\omega$ for SPM based spectral broadening. The blue curve represents instantaneous frequency to the center frequency ( $\omega-\omega_0$ ); the red curve represents the pulse envelope.....   | 35 |
| <b>Figure 5</b> This figure shows the spectrum in different position of 2 meters HCF. The 50 fs input pulses are transform-limited pulse with central wavelength of 800 nm and 144 $\mu$ J energy per pulse.....  | 36 |
| <b>Figure 6</b> The temporal profile and its phase before and after compensation the positive quadric spectral phase induced by SPM. ....   | 36 |
| <b>Figure 7</b> The comparison of the spectrum with and without considering the GVD in the simulations, in the regime where both of the dispersive and the SPM are dominated effects ( $L_d < L$ and $L_n < L$ ).....   | 38 |
| <b>Figure 8</b> Numerical simulations of the temporal and spectral evolution along the propagation in the fiber with considering the effect of self-steepening. ....  | 39 |
| <b>Figure 9</b> Ionization probability for two different laser peak intensity in Ar.....  | 42 |
| <b>Figure 10</b> The influence of the linear refractive index change due to the plasma to the spectrum at the different HCF position. The 50 fs input pulses with 60 TW/cm <sup>2</sup> peak intensity launched to the HCF filled with 1000 mbar of Ar. Note that in order to visualize the blue shift effect, the nonlinear refractive index $n_2$ is set to be zero, and the ionization caused intensity loss is also set to be zero. ....  | 43 |
| <b>Figure 11</b> Photograph of the TW-beamline for further strong field applications at ALLS laboratory of INRS (left). The general schema of pulse compression using HCF (right).....  | 44 |
| <b>Figure 12</b> The transform-limited pulse duration $\tau_{TL}$ (solid symbols, axis below the break) and pulse duration before dispersion compensation $\tau_{chirped}$ (hollow symbols, axis above the break) derived from the experiment (black squares), simulated with dispersion being considered (red circles) and simulations with dispersion being disregarded (blue diamonds) as a function of pressure and (b) numerical simulations of the temporal and spectral evolution along the propagation in the fiber of an input pulse at 4.0 bar. Black thick solid lines depict 1/e <sup>2</sup> of the temporal and spectral profile with respect to the propagation length. .... | 46 |
| <b>Figure 13</b> 70 mJ, 230 fs Yb input pulses at 1030 nm propagate within 3 meters (1 mm core diameter) HCF filled with 2100mbar of Neon in differential pressure scheme. (a) The measured (green), retrieved from SHG-FROG (blue), and simulated (red) output spectra together with the spectral phase of the compressed output pulses. (b) Temporal profiles of the simulated (red) and measured (blue) compressed output pulses. The Fourier transform limited (FT) temporal profile is depicted in green line. ....  | 47 |
| <b>Figure 14</b> Self-focusing and ionization are the intrinsic limitations for high energy pulse compression which lead to energy absorption, distortion of the spectra, and lower temporal compression quality. 70 mJ, 1030 nm Yb input pulses (blue curves) propagate within 3 meters (1 mm core diameter) HCF filled with (a) 2000 mbar and (b) 3000 mbar of Neon. Red curves show the output spectrum. ....  | 48 |
| <b>Figure 15</b> Rotational Raman response ( $hR\tau$ ) of N <sub>2</sub> for 120fs input pulses with the peak intensity of 7 TW/cm <sup>2</sup> . ....   | 53 |
| <b>Figure 16</b> (a) illustrates the instantaneous frequency $\Delta\omega$ and (b) the change of refractive index $\Delta n$ for 100 fs pulses.....  | 53 |
| <b>Figure 17</b> Red: Gaussian spectra supporting 120fs pulses. Blue: Raman gain for N <sub>2</sub> . The 120fs pulses have sufficient bandwidth to provide pump and Stokes frequencies to drive efficiently the Raman process.....   | 54 |

|  |    |
|--|----|
| <b>Figure 18</b> Enhanced redshift spectra at higher gas pressure via maximum alignment with a driver pulse duration of 120 fs at 2000 torr .....  | 55 |
| <b>Figure 19</b> Simulated spectra from the 1D model at the maximum alignment regime for 120 fs pulses. The spectrum has red-shifted asymmetry shape which is consistent with the experimental results....   | 56 |
| <b>Figure 20</b> Time-frequency maps at the HCF output obtained from 1D numerical simulations as a function of pressure for the case of 120fs input pulses. It indicates that the pulses have a negative at the leading edge and a positive chirp at the trailing edge.....  | 57 |
| <b>Figure 21</b> Temporal characterization of output pulses for the case of 120fs input pulses with 1.2 mJ energy per pulse in 2 meter N <sub>2</sub> filled HCF at 1000 mbar pressure. (a). Time-frequency maps (Wigner function) at the HCF output from FROG reconstructed trace (b, c) The corresponding 3D and 1D simulations. (d) Temporal profile from reconstructed FROG trace together with the simulation results after compression with chirped mirror and (e) linear propagation through fused silica. (f) The measured output spectrum together with the reconstructed spectrum for two above mentioned compressed results and simulated spectrum. ....  | 57 |
| <b>Figure 22</b> (a) Experimental results of nonlinear spectral broadening depending on the pulse duration for delayed response medium (N <sub>2</sub> ) at fixed pressure of 760 Torr. (b) The simulation results from the molecular alignment theory predicting low efficiency for the spectral broadening of pulse durations longer than characteristic time ( $T_{rot}$ ) of the molecules which is in strike difference with the experimental results.....  | 59 |
| <b>Figure 23</b> The intensity patterns of the selected LP <sub>m</sub> n modes .....  | 63 |
| <b>Figure 24</b> The measured spectra for the 700 fs input driver after the N <sub>2</sub> -filled HCF (3 bar) indicating the enhanced red-shifted spectra through SRS (red part). The green curve is the pump spectra at the fiber input. (b) These figures illustrate the MDSS spatial profile (obtained by putting an 830 nm long-pass filter after the fiber) for 8 single-shot consecutive pulses demonstrating the self-trapped, highly stable, and clean beam.....  | 70 |
| <b>Figure 25</b> (a) Measured spectral broadening evolution versus gas pressure. The SRS process is dominant and the red-shifted spectra of MDSS reach the longest wavelengths with sharp Raman peaks. Simulation results by solving the generalized multimode nonlinear Schrödinger equations (GMMNLSE) by considering 15 linearly polarized modes called MD simulations (b) and by considering only one mode, called 1D simulation (c). The MD simulations nicely reproduced the experimental results while 1D simulations predicts very narrow spectrum even at highest gas pressure.....   | 71 |
| <b>Figure 26</b> Demonstration of the optimization of MDSS stability and SRS process via the input coupling conditions. Measured spectral broadening evolution versus gas pressure before (a) and after (b) optimization. By suppressing IFWM, the SRS becomes dominant and the red-shifted spectra of MDSS reach the longest wavelengths with sharp Raman peaks. (c)-(g) The spectra for different pressures before (blue line) and after optimization (red line) of the HCF input coupling conditions. For each pressure, 3 consecutive single shot far-field images of the red-shifted beam (selected with a long pass filter at 830 nm) are shown for both conditions (top: after optimization, bottom: before optimization) to emphasize the role of the optimization process in the suppression of intermodal four wave mixing (IFWM). ....  | 73 |
| <b>Figure 27</b> The mode diameter (arbitrary unit) of the red-shifted MDSS beam for 20 shot to shot images per pressure (a) before and (b) after optimization. This figure demonstrates that the suppression of IFWM results in a clean MDSS beam at the HCF output. This is due to self-trapping in modes of the LP <sub>0n</sub> family with confined rotational symmetry. ....   | 74 |
| <b>Figure 28</b> Temporal evolution of the self-trapped MDSS driven by 5 mJ 700 fs pulses at 2500 mbar. (a) and (b) Wigner functions of the output pulse at HCF output predicted by 1D simulations and MD simulations, respectively. The outcome of 1D simulations predicts a positive quadratic phase for the output pulse since nonlinear propagation is dominated by SPM. (c) The Wigner function of the retrieved experimental SHG-FROG trace, directly measured at the output of the HCF. It shows the dominant negative quadratic spectral phase at the leading edge of the pulse, which contains the majority of the energy. This is in very good agreement with the results of MD numerical simulations. (d) The corresponding Frequency and temporal analysis of the compressed pulse with a piece of FS (12 mm). (f) Measured and MD-simulated temporal profile of the compressed pulse. (e) A comparison of the spectra measured with the spectrometer, retrieved from the SHG-FROG reconstruction of the 10.8 fs pulses, and from MD numerical simulations. .... | 75 |

|  |     |
|--|-----|
| <b>Figure 29</b> MD numerical simulations of spectral broadening as a function of pressure for (a) positively chirped input pulse (40 fs stretched to 700 fs with positive chirp) and (b) 700 fs narrowband Fourier transform limited pulses (FT) with the same peak power. ....   | 77  |
| <b>Figure 30</b> Spectral broadening for Fourier transform limited 120fs input pulses (filled spectra in light blue) with energy of 1.5mJ/pulse at 4000 mbar of pressure. Yellow: 1D numerical simulation. Red: MD numerical simulation. Blue: Broadened spectra experimentally measured at the HCF output. The 3D and the 1D simulations reveal red-shifted spectral broadening through maximum Raman gain, but 3D is further enhanced through the contributions of multidimensional solitary states. ....  | 78  |
| <b>Figure 31</b> Modal evolution of the self-trapped SRS beam at maximum Raman gain using 120fs input pulses with 1.5 mJ energy (a) Photon conversion efficiency (CE) from pump to SRS pulse for experimental (dot-blue) and simulation results (solid-red line). (b)-(c) MD simulations results for the energy distributions among 8 modes at SRS beam and pump part. Here mode index (1-8) correspond to LP <sub>01</sub> , LP <sub>11a</sub> , LP <sub>11b</sub> , LP <sub>21a</sub> , LP <sub>21b</sub> , LP <sub>02</sub> , LP <sub>31a</sub> , LP <sub>31b</sub> modes, respectively. .... | 79  |
| <b>Figure 32</b> Spectral broadening through nonlinear propagation in an Ar filled HCF (differentially pumped) with input pulse duration of 700 fs and 5 mJ/pulse at HCF input (3.25 mJ is coupled into the fiber considering 65% transmission). (a) Experimental spectra as a function of pressure. (b) MD simulations and (c) 1D simulations as a function of pressure. ....   | 81  |
| <b>Figure 33</b> Diameter of the beam (arbitrary unit) at the output of the HCF (measured in the far field) for 20 shot to shot images per pressure. Beyond 2000 mbar, we observed a larger output beam with high instability. In this case, due to the absence of SRS, there is no self-trapping effect and instead diffraction and coupling to HOMs. ....  | 82  |
| <b>Figure 34</b> Nine consecutive shot to shot images of the spatial profile at the HCF output for Ar at 4000 mbar of pressure The high instability and the observation of multi-filaments make this regime undesirable for spectral broadening and pulse compression. ....  | 83  |
| <b>Figure 35</b> Schematic experimental setup showing the spectral broadening in the gas-filled HCF followed by the compression stage and the characterization of the output pulses. ....  | 85  |
| <b>Figure 36</b> (a) Comparison of spectra for different gases in the SPM regime: R152a (120 μJ, 475 Torr), R134a (160 μJ, 525 Torr), ethylene (80 μJ, 575Torr), argon (320 μJ, 750 Torr), and krypton (200 μJ, 550 Torr); (b) Comparison of spectra for different gases beyond the SPM regime, all at a pressure of 760 Torr (1 atm): R152a (200 μJ), R134a (200 μJ), ethylene (120 μJ), argon (320 μJ), and krypton (240 μJ). The spectrum of the initial pulse before broadening is shown in shaded grey. ....  | 87  |
| <b>Figure 37</b> (a) Experimental spectral broadening in R134a (120 μJ input pulse energy) as a function of pressure; (b) Quantitative measurement of the total bandwidth as a function of pressure for all investigated gases for an input pulse energy of 120 μJ (except argon, for 240 μJ). ....  | 89  |
| <b>Figure 38</b> (a) Spectral broadening at the ionization threshold (at indicated energies) for different gases at different pressures; (b) Measured spectra at a pressure of 500 Torr. ....  | 90  |
| <b>Figure 39</b> For R152a, E = 120 μJ, p = 650 Torr: (a) Experimental SHG-FROG trace; (b) Retrieved SHG-FROG trace; (c) Retrieved amplitude and phase in the time domain; (d) Retrieved amplitude and phase in the spectral domain. The experimental spectrum is shown in shaded grey. ....   | 91  |
| <b>Figure 40</b> For R134a, E = 200 μJ, p = 2000 Torr: (a) Experimental SHG-FROG trace; (b) Retrieved SHG-FROG trace; (c) Retrieved amplitude and phase in the time domain; (d) Retrieved amplitude and phase in the spectral domain. The experimental spectrum is shown in shaded grey. ....  | 93  |
| <b>Figure 41</b> Experimental setup for the compression of low energy pulse. ....  | 97  |
| <b>Figure 42</b> (a) spectra for different pressures of R152a at 16 μJ input energy. All spectra are normalized to unity and dispersed vertically for discernibility. (b) Transform-limited pulse duration $\tau_{TL}$ (black, left axis) and the spectral bandwidth $\Delta\omega$ (red, right axis) versus pressure obtained from the measured (black squares) and simulated (red squares) spectra for varying pressure. ....  | 99  |
| <b>Figure 43</b> Characterization of dispersion-compensated pulses using SHG-FROG. Input energy is 16 μJ and the HCF is filled with R152a at 3.0 bar. (a) Measured and (b) reconstructed spectrogram; Retrieved intensity and phase in the (c) time and (d) spectral domain. ....  | 100 |
| <b>Figure 44</b> The transform-limited pulse duration $\tau_{TL}$ (solid symbols, axis below the break) and pulse duration before dispersion compensation $\tau_{chirped}$ (hollow symbols, axis above the break) derived from the experiment (black squares), simulated with dispersion being considered (red circles) and simulations with dispersion being disregarded (blue diamonds) as a function of pressure and (b) numerical simulations of the temporal and spectral evolution along the propagation in the fiber of an  |     |

input pulse at 4.0 bar. Black thick solid lines depict  $1/e^2$  of the temporal and spectral profile with respect to the propagation length. .... 101

**Figure 45.** (a) Schematic drawing for the experimental setup (b) exemplary input (gray shaded) and output (black line) spectra with the descriptions for blue and red edges (c) typical transmission drop with respect to increasing input pulse energy, observed in acetylene gas, from which the ionization threshold  $E_{th}$  is derived. The transmission begins to drop around 60% of  $E_{th}$ . .... 105

**Figure 46** spectral broadening after the propagation in a HCF filled with 1 bar of various gases for varying input energy. The shape of symbols denotes the blue edge (triangles) and the red edge (square) of the spectra. The colors represent the species of gas as shown in the legend. Open symbols stand for calculated spectra (ethane and ethylene only). Vertical dashed line stands for the intensity at which the drop of HCF transmission is first perceived, indicating the occurrence of ionization. (b) the spectral width derived from (a). .... 107

**Figure 47** measured (area filled with gray) and simulated (solid black with both GVD and Raman being taken into account, dashed red without GVD and dotted blue without Raman) spectra for ethane (lower panel) and ethylene (upper panel) at a given input energy of 50% of the  $E_{th}$ . The insets are spectral phases conjugated to the simulated spectra with both GVD and Raman components being taken into account. .... 108

**Figure 48** Compressed pulses characterized by means of SHG-FROG. The 40fs, 16 $\mu$ J input pulses are guided through a HCF filled with methane at 6.5bar then compressed using chirped mirrors. (a) measured and (b) reconstructed spectrogram and corresponding (c) temporal and (d) spectral intensity profiles and phases. .... 110

**Figure 49** Measured spectra of hollow core fiber output filled with 1 bar of (a) methane, (b) ethane, (c) ethylene, (d) acetylene and (e) krypton for varying input pulse energy up to  $E_{th}$  of each gas. All spectra are corrected by multiplying the response curve of the spectrometer and the amplitudes are normalized to one. The spectra are vertically fanned out with the spacing of 0.5 unit for clearer visualization. ... 111

**Figure 50** HCF transmission against elapsed time with an exposure to excessive input energy, namely, two to three times higher than  $E_{th}$ . .... 112

**Figure 51** Conceptual illustration of spectral broadening in HCF, (a) comparison of instantaneous response and delayed response. (b). The spectral broadening for longer pulses is more efficient in the molecular gas medium taking advantage of the timescale for nonadiabatic molecular alignment (hundreds of fs to ps). .... 115

**Figure 52** Comparison of nonlinear spectral broadening depending on the pulse duration for a) delayed response medium ( $N_2$ ) and b) Kerr medium (Ar) at fix pressure of 760 Torr. .... 116

**Figure 53** Comparison of a) measured and b) simulated spectral evolution vs. pulse duration at constant laser peak intensity in  $N_2$  at 760 Torr. The maximum spectral broadening was achieved for pulse durations comparable to the characteristic time of nonadiabatic alignment  $T_{RotAlign}$ . c) illustrates the change of refractive index  $\Delta n$  and d) the instantaneous frequency  $\Delta\omega$  with different pulse durations, i.e., 40, 100 and 200 fs, covering the characteristic time of  $T_{RotAlign}$ . Simulated spectra with vibrational (red), rotational (yellow) and both modes (blue) being considered superimposed onto the measured one (purple) for pulses of e) 40 fs and f) 100 fs duration. .... 118

**Figure 54** Compressed pulses characterized by SHG-FROG. The 120 fs input pulses are guided through a HCF filled with Nitrogen at 1 bar, then compressed using chirped mirrors. The (a) measured and (b) reconstructed spectrogram and corresponding (c) spectral and (d) temporal intensity profiles. Sim FT and Sim Chirp represent the numerical results for 120fs transform-limited input pulses and 120fs input pulses positively chirped from 40fs transform-limited pulses. .... 120

**Figure 55** Comparing the measured efficiency of spectral broadening in Ar (a) and  $N_2$  (b) for 230 fs pulse duration at 760 Torr. At 230 fs, we considered the newly generated spectral components (color filled part, blue in Ar, red in  $N_2$ . gray denotes input  $T_i$ : Sapphire spectrum), which corresponded to a Fourier transform limit (FTL) of (c) 25.3 fs from Ar and (d) 17.3 fs from  $N_2$ , respectively. The compressibility of the above spectra is further verified by performing numerical simulation by adding negative chirp to the simulated output pulse. .... 120

**Figure 56** (a) Conceptual illustration of the evolution of the self-trapped solitary states in the  $N_2$  filled HCF. Above the fiber, the creation and propagation of the MDSS are shown. MDSS composed of  $LP_{0n}$  modes are created at the beginning of the fiber on the left. These states are self-trapped in the  $LP_{0n}$  modes family with periodic energy exchange while propagating through the fiber. The evolution of the spectra is depicted below the fiber, starting with the input spectra in blue, up to the broadened redshifted

spectra in dark red. The broad red-shifted spectra originate from the process of enhanced cascaded SRS due to MD interactions over the long interaction length of the HCF. The output broadband MDSS pulses have a negative chirp and are compressed by linear propagation in a window of fused silica (normal dispersion below 1.3 microns). HHG is used to confirm the spatiotemporal quality and peak power of the red-shifted MDSS pulses. (b)-(d) Experimental observation of stable and self-trapped MDSS beam with enhanced red-shifted spectra. (b) The measured spectra for the 700 fs input driver after the N<sub>2</sub>-filled HCF (3 bar) indicating the enhanced red-shifted spectra through SRS (red part). The green curve shows the expected spectrum from a 1D simulation while the blue curve shows the experimental spectra for Ar (at the same pressure). The Ar spectra are much narrower than the N<sub>2</sub> spectra for the same pressure. The gray curve is the pump spectra at the fiber input. (c) These figures illustrate the MDSS spatial profile (obtained by putting an 830 nm long-pass filter after the fiber) for 8 single-shot consecutive pulses demonstrating the self-trapped, highly stable, and clean MDSS beam. (d) These figures report the same measurement for the fundamental beam (obtained using a band-pass filter (760nm-790nm)) indicating strong spatial instability and coupling to HOMs. .... 125

**Figure 57** Demonstration of the creation of MDSS and Raman enhancement via MD interactions. Simulations were performed for 700 fs input pulses with 5 mJ /pulse energy, propagating in an HCF filled with 2500 mbar of N<sub>2</sub> of a total fiber length L of 3 m. (a) This figure shows the coupling of the fundamental mode LP<sub>01</sub> to LP<sub>02</sub> and LP<sub>03</sub> at the very beginning of the fiber (<0.1L), due to the high-energy input pulses. (b) The corresponding spectra of the LP<sub>01</sub> LP<sub>02</sub> and LP<sub>03</sub> modes for four different positions at the beginning of the HCF. Each mode experiences wavelength shifts, primarily via IFWM. Once enough instantaneous bandwidth to support intermodal SRS is provided, the MDSS are created at the red part of the spectrum. The shaded blue spectrum is the 1D simulation result, where the only efficient nonlinear effect is self-phase modulation (SPM). In this case, there are no intermodal terms to enhance the nonlinearity. It should be noted that Fourier transform-limited (FT) input pulses are used in the simulations presented in (a) and (b) to better highlight the physical concept of the creation MDSS at the beginning of the fiber. (c) Experimental spectral broadening in N<sub>2</sub> with 700 fs pulse duration and varying pressure under a constant peak power. (d) The corresponding MD simulations obtained by solving the generalized multimode nonlinear Schrödinger equations (GMMNLSE), considering 15 linearly polarized modes. Here, the input pulses for the simulations are 40fs positively chirped to 700fs. Numerical simulations assuming FT 700fs pulses are presented in the supplementary material. These results cannot be reproduced with 1D simulations (see the white dashed lines in (d)). .... 127

**Figure 58** Modal evolution of the self-trapped MDSS beam using 700 fs driver pulses with 5 mJ input energy. (a) Photon conversion efficiency (CE) from the pump to MDSS for experimental (green solid line) and simulation results (red dotted line) (b) The simulated evolution of energy distribution among different modes for the MDSS and (c) the pump part as a function of pressure. At the very beginning of the HCF, a significant amount of energy transfers from the fundamental to LP<sub>02</sub> and LP<sub>03</sub> modes, resulting in a very efficient SRS process. This leads to an efficient transfer of the pump energy to MDSS, self-trapped in LP<sub>0n</sub> modes. Measured single shot beam profiles of MDSS (d) and pump part (e) for different pressures. Here, the 15 modes used in the simulations are LP<sub>01</sub>, LP<sub>11a</sub>, LP<sub>11b</sub>, LP<sub>21a</sub>, LP<sub>21b</sub>, LP<sub>02</sub>, LP<sub>31a</sub>, LP<sub>31b</sub>, LP<sub>12a</sub>, LP<sub>12b</sub>, LP<sub>41a</sub>, LP<sub>41b</sub>, LP<sub>22a</sub>, LP<sub>22b</sub>, and LP<sub>03</sub>, respectively. LP<sub>mn</sub> modes in the figure indicates nonzero angular momentum modes (m>0). Statistical changes for the full width at half maximum (FWHM) of the spatial profile are shown for the MDSS beam (f) and the pump part (g) for 20 single-shot images per pressure (extracted from experimental measurements). The candlestick chart shows that the FWHM of the MDSS have negligible fluctuations which further confirms the self-trapping effect and the flatness of the waveform of the MDSS beam through its propagation in the HCF. .... 129

**Figure 59** Temporal evolution of the self-trapped MDSS driven by 5 mJ 700 fs pulses at 2500 mbar. (a) and (b) Wigner functions of the output pulse at HCF output predicted by 1D simulations and MD simulations, respectively. The outcome of 1D simulations predicts a positive quadratic phase for the output pulse since nonlinear propagation is dominated by SPM. (c) The Wigner function of the retrieved experimental SHG-FROG trace, directly measured at the output of the HCF. It shows the dominant negative quadratic spectral phase at the leading edge of the pulse, which contains the majority of the energy. This is in very good agreement with the results of MD numerical simulations. (d) The corresponding Frequency and temporal analysis of the compressed pulse with a piece of FS (12 mm). (f) Measured and MD-simulated temporal profile of the compressed pulse. (e) A comparison of the

spectra measured with the spectrometer, retrieved from the SHG-FROG reconstruction of the 10.8 fs pulses, and from MD numerical simulations. .... 130

**Figure 60** High harmonic generation in Ar. (a) The blue curve is the measured HHG spectra with the driver pump (700 fs). Green, orange and red curves are the corresponding spectra driven by the uncompressed, partially and fully compressed MDSS pulses, respectively. The partially and fully compressed pulses are obtained by propagating the output MDSS through 6 mm and 12 mm of FS. The shortening of the pulse duration leads to higher peak intensity and thus to an extension of the HHG cut-off and higher photon flux. (c) Spatial (y-axis) and spectral (x-axis) profiles of the HHG beam driven by 700 fs pulses at the fundamental wavelength with 8 times more energy compared to MDSS and (c) the corresponding HHG profile driven by the compressed red-shifted MDSS. .... 132

## List of Tables

**Table 1** Nonlinear refractive of the noble gases helium, neon, argon, krypton and xenon and their ionization potential index [88-90] ..... 34

**Table 2** Dispersion Coefficients (GD , GVD and TOD) of different Gases[92]. ..... 37

**Table 3** Ionization threshold of gases tested in the present study ..... 106

# 1 Introduction

## 1.1 Motivations

Over the past few years, completely new directions have reemerged in science, bringing a new level of understanding about conditions for the existence, stability, and generation of multidimensional states [1-5]. In physics, multidimensional solitary states, nondiffracting and nondispersing wavepackets or matter waves, draw continuously renewed interest in many fields. They find especially important recognition in nonlinear photonics (optics and plasmonics) [4, 6-14] and Bose Einstein condensates ( BECs ) [15]. The solitary states are classified as fundamental ones, which carry no topological structure, and various topological modes, including 2D and 3D solitons [1]. However, multidimensional solitary states supported by the standard cubic nonlinearity tend to be strongly unstable, a property far less present in one dimensional (1D) systems. Thus, the central challenge is to stabilize multidimensional states, and to that end, numerous approaches have been proposed over the years [3].

Specifically, in this thesis, we consider hollow-core fiber (HCF) having the advantages of a many-modes capacity. Here, fiber modes span the dimension, and they can couple and interact with each other which spans space and time, order and chaos. These extended multidimensional pathways lead to complex multi-frequency mode coupling network's topology. Although intermodal nonlinear interactions provide many pathways to enhance different nonlinear phenomena, so far, the main focus has been on single-mode operation in HCF, and multi-mode regimes have been considered an undesired regime for efficient nonlinear interactions [16]. Indeed, the cubic self attractive nonlinearity, such as self-focusing caused by the optical Kerr effect, play important role in creation of multidimensional solitary states in gas-filled HCF, however, it simultaneously gives rise to the critical and supercritical collapse, i.e., spontaneous formation of a singularity after a finite propagation distance or time (multiple filamentation), and the collapse destabilizes the multimode states. Accordingly, a challenging problem is search for physically relevant settings that admit stabilization of the multidimensional states in gas-filled HCFs.

Gas-filled HCFs have been utilized in 1D regime for nonlinear pulse compression [17-19]. It relies on spectral broadening and subsequent temporal compression. A laser pulse with a certain bandwidth and pulse duration emitted from a laser system is propagated in a nonlinear medium, where it undergoes the process of self-phase modulation (SPM) in the single mode regime. This imposes a temporal chirp on the pulse, which leads to spectral broadening. The

removal of the chirp leads to shorter pulses and, at the same time, to a higher peak power if the losses are sufficiently low. However, efficient multidimensional interactions and the creation of stable multimode states with high spatiotemporal coherence and power scalability in large core HCFs have not been demonstrated. To better understand the multidimensional nonlinear interaction in gas-filled HCF, it is necessary to have thorough knowledge of nonlinear pulse propagation in the single mode regime. Thus, we first perform a comprehensive theoretical and experimental study on the principles of hollow fiber pulse compression in the 1D regime (single mode regime). The strengths, weaknesses and the limitation of this method will be investigated for high energy pulse and high repetition laser sources. Then, we move further to multi-mode areas that exemplify the theme of nonlinear enhancement enabling both new performance levels and new capabilities. The need for a better understanding of nonlinear processes in multimode regime in HCF to have new generation of ultrafast laser sources encouraged us to conduct this research and investigate the nonlinear behavior in the presence of many modes.

### **1.1.1 Demands for ultrafast laser source**

Today, modern ultrafast laser technology has opened up new avenues for many applications related to our daily life (Figure 1). In materials processing [20, 21], employing ultrashort pulses, picosecond and femtosecond, with extremely high peak intensities, are well adapted to the high-quality microfabrication of soft materials [22-24]. Besides, nonlinear absorption (i.e., multiphoton absorption) can induce strong absorption, which permits not only surface processing, but also three-dimensional (3D) [25] internal micro-nano fabrication and volume processing. In biomedical, the applications of ultrafast lasers range from fluorescence microscopy to diffuse optical tomography and photoacoustic [26-29]. Particularly, Raman spectroscopy and microscopy [30-32] are used to identify the chemical compounds of unknown samples, and to enable diverse applications such as tumor detection, drug delivery studies, and biofuel process monitoring. Furthermore, advanced ultrafast laser technology has been utilized in Lasik eye surgery [33, 34] to correct the lens of the eye without damaging the surrounding tissue, and nearly 10 million patients in the United States have had their vision corrected with the procedure. Given the promising developments and applications of the ultrafast laser technology, what can one expect of advanced ultrafast laser technology in the years to come?

In this thesis, we can categorize relevant motivations. The first motivation of this thesis is to investigate the novel spatiotemporal multimodal nonlinear physics in high energy regime to

generate and control extreme short electromagnetic light field for 'basic research', the discovery of how the nature is and how it works, expressly for no particular purpose other than to understand. The second motivation refers to science or technological development that has the capability to improve the human condition with high impact. The findings of this thesis have also the potential to provide some kind of economic benefit.



**Figure 1** Applications of advanced ultrafast photonics technology, from fundamental research to many important applications in various areas.

## 1.2 State of art technology based on 1D nonlinear interaction

### 1.2.1 High energy pulse compression

Today, significant efforts for advanced applications are leading to an increasing demand for the development of novel laser driver sources. Many desired applications require an increase in pulse energy rather than laser repetition rate which is particularly essential for emerging energetic secondary particle and light sources, e.g., laser-plasma electron acceleration [35], THz radiation generation [36], coherent, and incoherent X-ray generation [37, 38]. In particular

isolated attosecond pulses [39] and attosecond pulse trains [37] based on high harmonic generation (HHG), driven by high energy short laser pulses, have opened novel applications such as nonlinear attosecond optics [40], single-shot femtosecond holography [41] and seeding free electron laser [42]. Recently, time-space-resolved experiment on studying nanoscale magnetic dynamics has been demonstrated using intense soft X-ray HHG sources [43]. In contrast to static X-ray nano-imaging applications, such tabletop optical-pump-X-ray-probe studies of condensed matter systems impose high photon X-ray flux requirement. Therefore, high-energy pulses are needed, and they should work at a relatively low repetition rate (sub-few kHz) to avoid damaging the systems with low heat dissipation or materials with slow recovery.

To date, various approaches to pulse compression have been used for pulse energy above the mJ level (see Figure 2). Filamentation was found as a simple, self-guiding technique for pulse compression at a few mJ, where soliton-like self-compression has also been demonstrated [44]. However, the complex spatiotemporal coupling makes the temporal compression non uniform across the beam profile and the up-scaling to the higher pulse energy is complicated. Besides, pulse compression in bulk material has been demonstrated as a very compact and efficient approach [45, 46]. In the mid-infrared, at 3900 nm, pulse compression of 90fs 20 mJ pulses has been demonstrated using bulk material [46]. However, in the NIR spectral range, the critical power of self focusing drops dramatically ( $P_c \sim \lambda^2$ ), and long pulse duration leads to a lower damage threshold and an increase of ionization probability in materials. Using bulk material, pulse compression at mJ level has been recently reported with ~1mJ 170 fs pulses compressed down to 30fs using a >3 meters setup [47]. In addition, the advance of gas-filled multi-pass cells (MPC) has enabled great progress in pulse compression above the mJ level. Using a 1-meter long MPC setup, compression of 200fs, 1.9 mJ pulses has been recently reported, showing its outstanding efficiency and high spatial quality [48]. Furthermore, Kaumanns et al. demonstrated the compression of a ps Yb disk laser amplifier with a pulse energy of ~18.6 mJ, using a setup of a ~300 mm × 130 mm gas-filled MPC chamber [49].

Besides the above approaches, hollow core fiber (HCF) is one of the most successful and used approaches for pulse compression. Because of the absence of the optical elements (MPC approach) and solid material, the hollow core waveguide is an attractive approach for high energy pulse propagation, delivering spatially homogeneous spectra and a high temporal compression ratio. In terms of average power scaling, Nagy et al. have demonstrated 318 W of output power with simultaneous excellent spatial quality and stability [47]. On the other hand, so far, the typical pulse energies of the pulse compression using the HCF approach is

at level below 10 mJ. Although compression of 70mJ pulses in HCF has been reported in a weakly ionized gas regime [50], the output energy is limited to ~13 mJ due to the strong ionization loss (~80%), and the compression factor of this approach is lower than that of the conventional pure self-phase modulation (SPM) regime due to the complex nonlinearity induced by ionization. Besides these approaches, the planar waveguide has been presented as an approach for scaling to higher pulse energy with ~20 mJ compressed pulses [51]. However, small-scale self-focusing causes strong modulations in the spatial beam profile, which may lead to multiple individual filaments, and a lower temporal compression factor.

Despite great progress in scaling the pulse compression to higher average power, scaling pulse compression to higher energy poses a different set of challenges: where the effects of plasma disturbance, optical damage, and the involvement of large-scale setup become intrinsically limiting factors. *In the technology point of view, one important goal of this thesis is to investigate and to develop novel nonlinear techniques to scale energy and peak power of ultrafast pulses towards the target regime (Figure 2).*

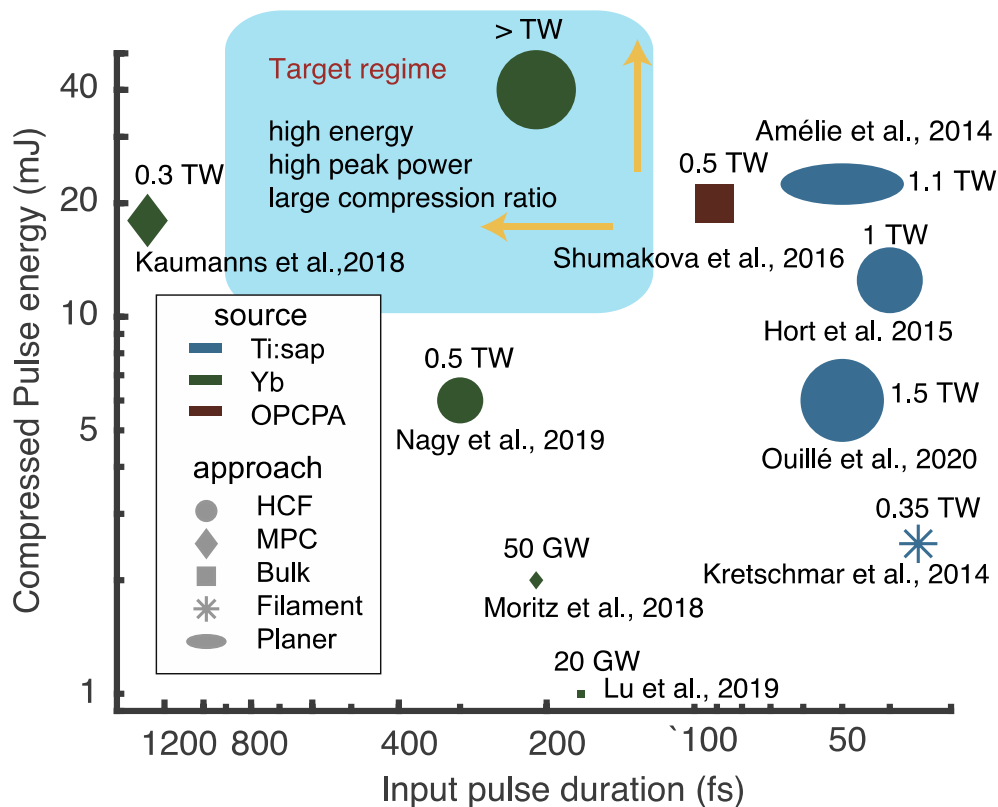


**Figure 2** Overview of state-of-art nonlinear pulse compression in the mJ pulse energy level. The compressed pulse energy is plotted versus the input pulse duration. The corresponding peak power is proportional to the size of the symbols.

### **1.2.2 Low energy pulse compression**

Recently, there has been a rising interest for diode-pumped Ytterbium (Yb)-based laser systems. These lasers can work with very high repetition rates, generating amplified pulses of femtosecond duration [52-54]. Their innovative geometries (thin-disk, slab, or fiber) allow operation at high average power by reducing thermal load, yet the bandwidth remains limited by the Yb based gain media. Therefore, there is a real need for efficient compression techniques suitable for ultrashort pulses with lower energy, in the range of tens to hundreds of microjoules. Such lasers represent an ideal driver for emerging applications of high power light source [55], e.g., coherent diffraction [56], coincidence experiments [57], frequency metrology [58] and photoelectron spectroscopy and microscopy [59].

Kagomé-type hollow core photonic crystal fibers represent one approach to compress very low energy pulses delivered by high average power diode-pumped Yb-based laser systems. These micro-structured fibers enable compression of few microjoule pulses to sub-10 fs duration and can even be designed to support higher energies [60-64]. Despite major progresses, it remains nonetheless challenging to use these fibers due to their complexity [65]. An alternative to these rather complex Kagomé fibers lies in the use of low ionization potential (IP) noble gases, like krypton and xenon, in traditional HCF [66-69]. In this thesis, we propose a distinct category of molecular gases, hydrofluorocarbons, to efficiently compress low-energy pulses using HCFs in the 1D regime. These molecules represent a valuable alternative to rare gases like krypton and xenon.

### **1.3 A new horizon in ultrafast laser technology**

Very recently, various novel phenomena of 3D spatiotemporal nonlinear dynamics based on strongly coupled modes in solid core multimode fibers were observed, which fundamentally differs from 1-D nonlinear dynamic such as control nonlinear multimode interactions [70], spatiotemporal mode-locking [71], accelerated nonlinear interactions [72], and self-organized instability [73]. Despite their complexity, multimode systems are considered highly promising

## spatiotemporal avenue of multimode nonlinear fiber

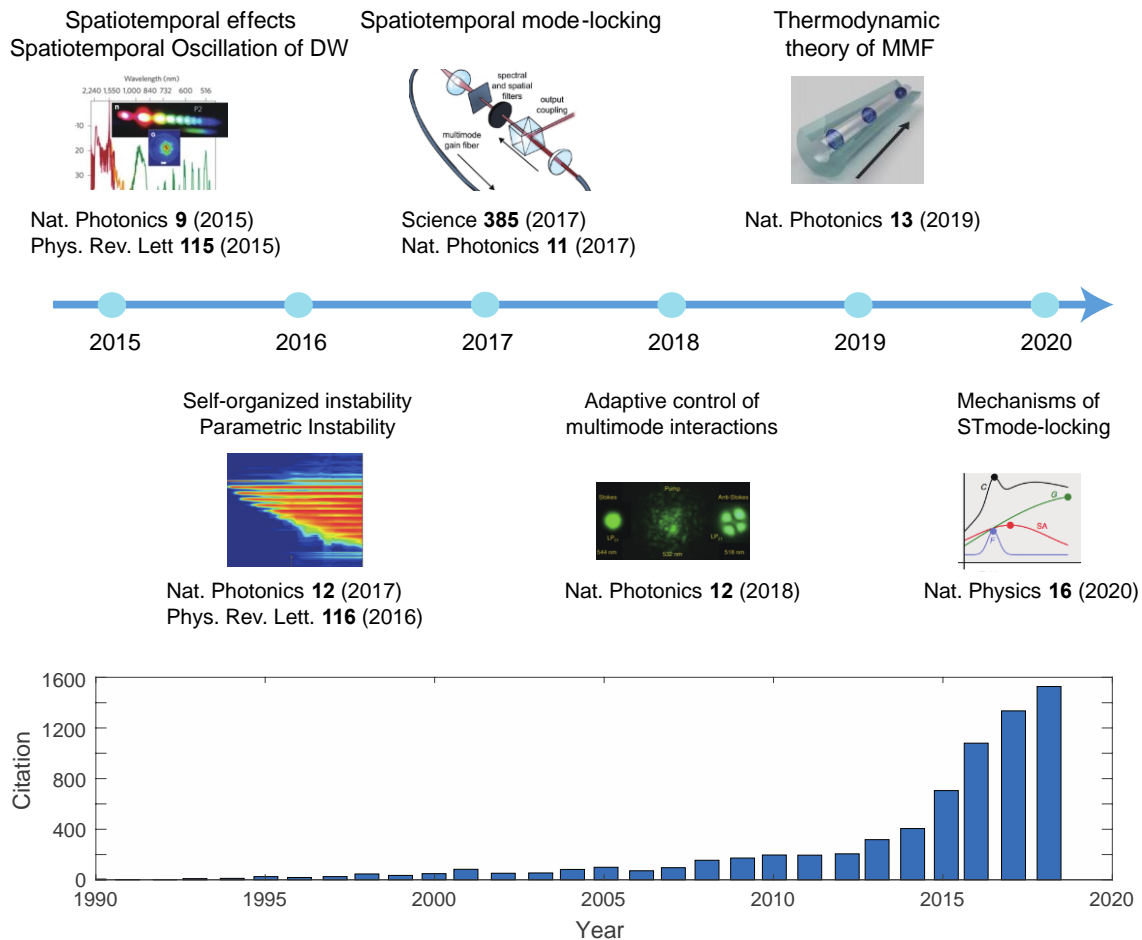


**Figure 3** (top) The significant theoretical and experimental breakthroughs of the last 5 years in multimode nonlinear fiber optics (bottom). Sum of times cited per year for source items indexed within Web of Science Core Collection, containing the words: nonlinear multimode optical fiber [74].

for the creation of fully 3D self-sustained states propagating over considerable distances, provided that the conditions for the stable nonlinear locking of pulses propagating in different spatial modes can be achieved. Their robustness and nonlinear attraction have made them a conceptual framework to understand complex multimode dynamics (see Figure 3). One of the most important recent breakthroughs is the observation of self-organized instability [73] which has now taken a first and bold step towards a theory of spatiotemporal mode-locking [75].

Low modal dispersion together with balancing the diffraction and dispersion through nonlinear propagation in MMFs are the required conditions to generate multidimensional (MD) solitary states (spatial, temporal, modal). In solid core fibers where modal dispersion is the dominant dispersive effect, graded-index MMFs with an engineered parabolic refractive index profile have been designed to overcome this limitation. This has led to the observation of multimode

solitons which are synchronized, non-dispersive pulses in multiple spatial modes [76]. However, solid core fibers restrict the maximum peak power due to their low optical damage threshold. On the other hand, for gas-filled hollow-core fibers (HCF), the modal dispersion and losses scale inversely with the second and third power of the core size, respectively [77]. Consequently, large core size (200~1500  $\mu\text{m}$ ) HCFs provide ultra-low modal dispersion and small losses. Besides, gases provide an extra degree of controllability since their nonlinearity and dispersion can be tuned by varying the pressure and gas mixture [78]. They also offer wide window of transparency extending from the vacuum ultraviolet[79] to the mid-infrared spectra range [19]. Thus, gas-filled HCFs offer a new platform for efficient, tunable and power scalable multidimensional interactions with ability to create stable high-energy multidimensional states. However, the nonlinear interactions in gas filled HCF have been mainly in the effective 1-dimensional (1D) regime, because the coupling to higher-order modes (HOM) of high energy pulses has been considered detrimental due to the strong instability [17]. In this thesis, a successful solution for efficient multidimensional interactions and the creation of stable multimode states with high spatiotemporal coherence in large core HCFs is demonstrated. Our results indicate that large core gas-filled HCF present new opportunities for studying high-energy, multimodal spatiotemporal dynamics with capabilities for considerable applications. The immediate technology impact of this work can be generating few-cycle pulses by ps Yb driver lasers with a simple, robust, and efficient approach providing a new driver technology for strong-field physics. It is especially attractive for scaling of the table-top extreme-ultraviolet (XUV) source at higher photon energies due to the longer central wavelength of the output beam. Above technological breakthrough, the advent of high energy stable multimode state would have a huge potential to observe novel spatiotemporal dynamic in the terawatt (TW) regime. Also, as it is demonstrated in our work, HCF supports a rich and complex mix of spatial and temporal nonlinear phenomena that they may serve as a testbed for the study of complex physical systems.

## 2 Hollow-core fiber pulse compression in 1-dimension regime

This section presents the principles of hollow core fiber (HCF) pulse compression [17]. When optical pulse propagates through the HCF, the intensity variation in transversal direction is small compared to the variation of the electric field in the axial direction, called paraxial approximation. Therefore, below critical power ( $P < .3P_{cr}$ ) [80] for self focusing, the evolution of the individual modes is not influenced by each other. By adjusting the input beam size in a way that the beam size at the HCF input is around 64% of the core diameter of the fiber, 98% of the power can be coupled into fundamental mode due to the fact that the fundamental mode has the largest mode overlap with this Gaussian input beam [81]. Therefore, the fundamental mode is the sole mode propagation through the fiber which can be attributed as a 1 dimensional (1D) system. The group velocity dispersion (GVD), self-phase modulation (SPM), self-steepening, ionization and attenuation are the linear and nonlinear effects in 1D regime. In this chapter, we will investigate the impact of each effect on the pulse propagation in gas-filled HCF.

### 2.1 1D model

The theoretical description of short-pulse propagation in single-mode regime is commonly based on the nonlinear Schrödinger equation (NLSE), modeling the evolution of the electromagnetic pulse envelope [82, 83]. Generalized versions of the NLSE (GNLSE), including higher-order dispersion, and Raman and self-steepening terms, have been successfully employed in the description of octave spanning supercontinua and for pulse duration approaching the single-cycle regime.

$$\begin{aligned} & \frac{\partial A}{\partial z} + \frac{1}{2} \left( \alpha(\omega_0) + \sum_{l=1}^{\infty} i^n \frac{\alpha_l}{l!} \frac{\partial^l}{\partial t^l} \right) A - i \sum_{n=1}^{\infty} i^n \frac{\beta_n}{n!} \frac{\partial^n A}{\partial t^n} \\ & = i \left( \gamma(\omega_0) + \frac{i}{\omega_0} \frac{\partial}{\partial t} \right) \left( A(z, t) \int_0^{\infty} R(t') |A(z, t - t')|^2 dt' \right) \end{aligned} \quad (1)$$

where  $\gamma(\omega_0) = \frac{p_0 n_2 \omega_0}{c A_{ff}}$  is the nonlinear response of the media.  $\omega_0$  is central frequency of the pulse,  $c$  is the speed of light,  $A_{ff}$  is the effective area of the propagation mode,  $p_0$  is gas pressure inside the fiber and  $n_2$  is nonlinear refractive index of the medium at pressure of 1

bar.  $\alpha_l$  is the  $l$ th order of optical loss, and  $\beta_n$  is the  $n$ th order of dispersion. The nonlinear response function  $R(t)$  covers the responses of both electronic and nuclear origin. Assuming that the electronic contribution is nearly instantaneous, the function form of  $R(t)$  can be written as [82]:

$$R(t) = (1 - f_R)\delta(t) + f_R h_R(t) \quad (2)$$

$$h_R(t) = (\tau_1^{-2} + \tau_2^{-2})\tau_1 \exp(-t/\tau_2) \sin(t/\tau_1)$$

$$\int_{-\infty}^{+\infty} R(t) dt = 1.$$

where  $f_R$  represents the fractional contribution of the delayed Raman response to the nonlinear polarization  $P_{NL}$ . The form of the delayed Raman response function  $h_R(t)$  is set by the vibrations of the molecule which can be approximated with a damped-oscillator model.  $\tau_1 = \frac{1}{\Omega_R}$  and  $\tau_2$  is the damping time of vibrations. To include the general case of multiple vibrational or rotational modes (see chapter 3), we consider a linear superposition of  $R(t)$  for the different modes [84, 85].

The GNLSE is solved using a scheme called the fourth-order Runge-Kutta in the interaction picture method (RK4IP), which alternates between the Fourier domain, to evaluate dispersive effects, and the time domain, to evaluate nonlinear effects. Using this method, the GNLSE is expressed by using the following dispersive and nonlinear operators, respectively.

$$\begin{aligned} \hat{D} &= -\frac{1}{2} \left( \sum_{l=1}^{\infty} i^l \frac{\alpha_l}{l!} \frac{\partial^l}{\partial t^l} \right) A - \sum_{n \geq 1} i^{n-1} \frac{\beta_n}{n!} \frac{\partial^n A}{\partial t^n} \\ \hat{N} &= i \left( \gamma(\omega_0) + \frac{i}{\omega_0} \frac{\partial}{\partial t} \right) \left( A(z, t) \int_0^{\infty} R(t') |A(z, t - t')|^2 dt' \right). \end{aligned} \quad (3)$$

Thus, the GNLSE takes on the following form

$$\frac{\partial A}{\partial z} = (\hat{D} + \hat{N})A. \quad (4)$$

By transforming this equation into an interaction picture it can be re-expressed as a first-order ordinary differential equations, which can be solved with arbitrary accuracy by applying methods of perturbation theory, as used in quantum mechanics. However, for computational efficiency the RK4 scheme was used instead. This method then gives an accuracy proportional to the fourth order of the used step-size, as opposed to commonly used split-step Fourier methods which are accurate to the second and third order. A summary of this procedure is detailed in refs [86] and [83].

In order to reduce unwanted nonlinear effects such as self-focusing at HCF input resulting from the intense beam interacting with a dense gaseous medium at the entrance, the gas is injected on the exit side while the entrance side is constantly pumped to build up a pressure gradient along the fiber. The employment of a differential pressure configuration suppresses the ionization, self-focusing and dispersive broadening, which contributes to a higher reliability in fiber coupling. The pressure gradient in the fiber is considered by adopting the following formula in the simulation [87].

$$p(x) = \sqrt{p_l^2 + \frac{x}{L}(p_h^2 - p_l^2)} \quad (5)$$

where  $L$  the length of the fiber,  $x$  the propagation length in the fiber,  $p_l$  and  $p_h$  the pressure at laser entrance and exit, respectively.

### 2.1.1 Self phase modulation

The frequency domain and time domain of a laser pulse are a Fourier transform pair of each other. It means that the broader the bandwidth is, the smaller the pulse duration can be. The idea of hollow fibre compression for generation of the extreme short pulses is to increase the bandwidth as much as possible in frequency to have the capability to generate the corresponding short pulse in time. Self phase modulation (SPM) is an effective way of generating new frequencies to broaden the frequency spectrum. In noble gas where the dispersive effects are negligible at low pressures, and the medium is Raman inactive one, SPM is a dominant nonlinear effect. The gas medium is centre symmetric, thus, all the even orders of susceptibility is zero, and the third order nonlinear susceptibility leads to an intensity and therefore time and space dependent refractive index:

$$n(r, t) = n_0 + n_2 I(r, t) \quad (6)$$

Where  $n_0$  is the refractive index of the medium,  $I(r, t)$  is the intensity profile of the pulse and the nonlinear refractive index  $n_2$  is positive for most transparent materials. The nonlinear refractive index and the ionization potential of a selection of noble gases is shown in Table 1.

| Gas                                      | He   | Ne   | Ar   | Kr   | Xe   |
|--|------|------|------|------|------|
| $n_2(10^{-19} \text{cm}^2/\text{w.bar})$ | 0.34 | 0.75 | 0.97 | 2.78 | 6.83 |
| $I_p(\text{eV})$                         | 24.5 | 21.5 | 15.7 | 14   | 12.1 |

**Table 1** Nonlinear refractive of the noble gases helium, neon, argon, krypton and xenon and their ionization potential index [88-90]

The intensity dependence of  $n(r, t)$  implies a refractive index varying in time and space. The temporal variation leads to a pulse chirp. The (transverse) spatial refractive index dependence leads to lensing effects. These processes are called SPM and self-focusing, respectively. The time dependent refractive index results in a time dependent nonlinear phase. Under the assumption of an instantaneous response, the pulse experiences a nonlinear phase shift

$$\varphi_{nl}(t) = -\frac{2\pi}{\lambda_0} n_2 I(t) L \quad (7)$$

in which  $\lambda_0$  is the central wavelength of the pulse and  $L$  is the HCF length. Through the nonlinear interaction of the pulse with the gas medium, the pulse is modulating its own phase due to the time dependent intensity. The effect of the time dependent nonlinear phase on the spectrum can be understood when looking at the instantaneous frequency

$$\omega(t) = \omega_0 + \frac{d\varphi_{nl}(t)}{dt} = \omega_0 - \frac{2\pi}{\lambda_0} n_2 \frac{dI(t)}{dt} L. \quad (8)$$

$\omega_0$  is the center frequency. From this formula, it is clear that the frequencies at the leading edge of the pulse are decreased while frequencies at the trailing edge are increased (Figure 4). Therefore, the pulse is continuously spectral broadened while it propagates within the fiber. Noted that the positive chirp introduced by SPM is well behaved and almost linear at the center of the pulse.

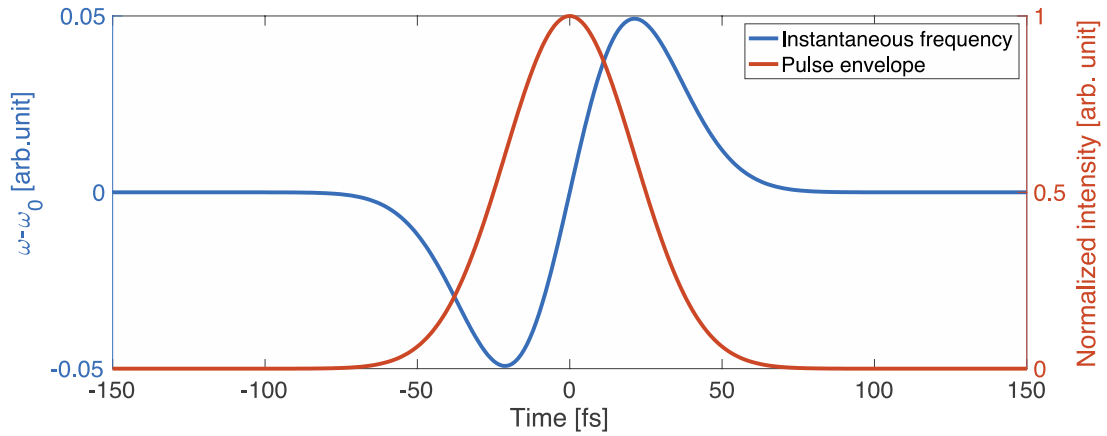


**Figure 4** The instantaneous frequency  $\Delta\omega$  for SPM based spectral broadening. The blue curve represents instantaneous frequency to the center frequency ( $\omega-\omega_0$ ); the red curve represents the pulse envelope.

The simulation's results by considering only SPM effect in NLSE using 1 bar pressure of Ar and differential pressure scheme in 2 meters HCF is presented in Figure 5. The input pulse is 50 fs transform-limited centered at 800 nm pulse with 144  $\mu\text{J}$  energy and a spot size of 160  $\mu\text{m}$ . Noted that the efficient spectral broadening starts at the second half of HCF due to the differential pressure configuration. The intensity spectrum in wavelength are shown at different HCF positions. It is worth to emphasize that although the spectrum is broad at the fiber HCF output, the temporal profile is not influenced at all, since it is only a phase change. The broader spectrum in frequency only gives the possibility of compressing the pulse to shorter pulse duration. The transform limited pulse can be obtained by removing the phase that is caused by SPM in frequency domain provided by chirped mirrors. In the simulations, the output pulse can be compressed to 6.5 fs by adding  $-70 \text{ fs}^2$  spectral phase to the output pulse. The temporal profile and temporal phase before and after compression is illustrated in Figure 6.

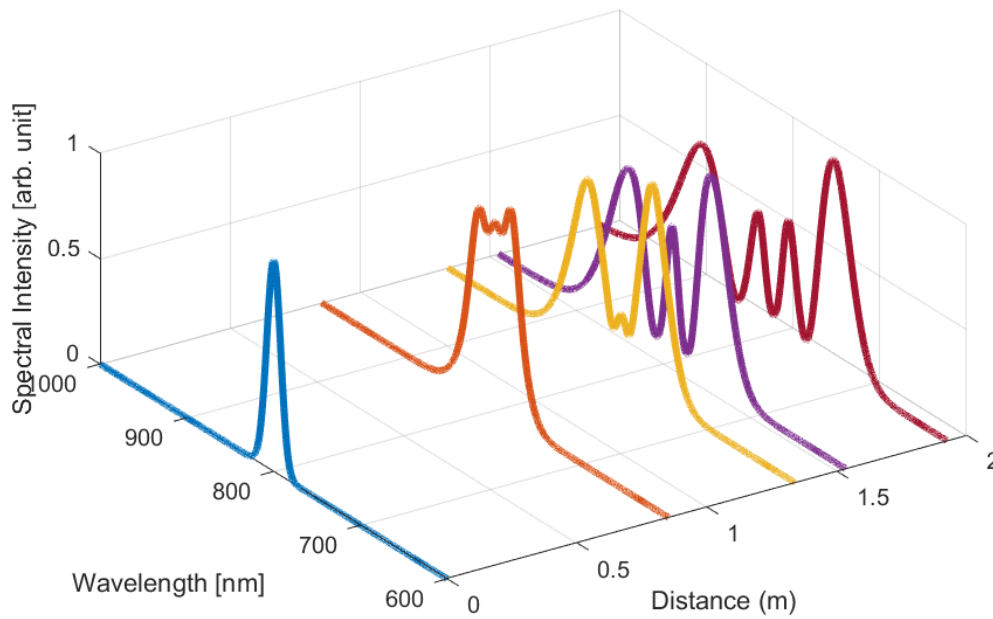


**Figure 5** This figure shows the spectrum in different position of 2 meters HCF. The 50 fs input pulses are transform-limited pulse with central wavelength of 800 nm and 144  $\mu\text{J}$  energy per pulse.

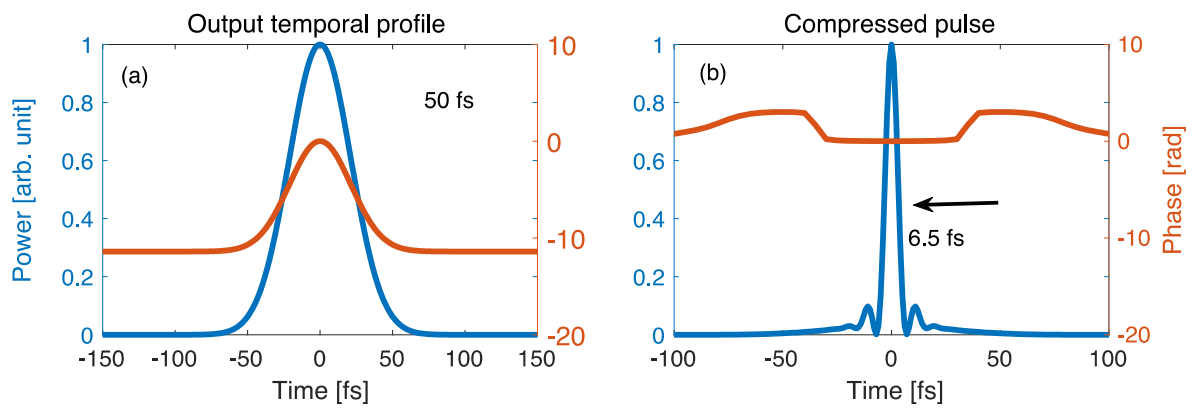


**Figure 6** The temporal profile and its phase before and after compensation the positive quadric spectral phase induced by SPM.

### 2.1.2 Effect of group velocity dispersion

The linear and nonlinear pulse propagation in the HCF depends on gas and pulse parameters. In relatively low pressure (e.g. less than 3 bar), the dispersive effects in gas-filled HCF are negligible. However, it is necessary to consider at least the group velocity dispersion (GVD) effect at higher pressures [91]. Table 2 shows the measured values of group delay (GD), group

velocity dispersion (GVD) and third order dispersion (TOD) for different gases at the pressure of 1000 mbar.

| Gas      | GD (fs/m) | GVD (fs <sup>2</sup> /m) | TOD(fs <sup>3</sup> /m) |
|----------|-----------|--------------------------|-------------------------|
| Air      | 938       | 20                       | 19.4                    |
| Nitrogen | 947       | 18                       | 19.4                    |
| Helium   | 146       | 0.82                     | 19.5                    |
| Neon     | 241       | 2.11                     | 19.7                    |
| Argon    | 895       | 17.98                    | 20.8                    |
| Krypton  | 1366      | 37.32                    | 19.7                    |
| Xenon    | 2225      | 87.42                    | 19.9                    |

**Table 2** Dispersion Coefficients (GD , GVD and TOD) of different Gases[92].

For this purpose, we use two characteristic length scales in order to distinguish get the dominant effect through the pulse propagation within the fiber. The length over which the dispersive effects become important is attributed as dispersion length ( $L_d$ ) and it can be defined as [82]

$$L_d = \frac{T_0^2}{\beta_2} \quad (9)$$

where  $T_0$  is the pulse duration. For a Gaussian pulse  $T_0 = \frac{T_{fwhm}}{2\ln 2}$ .

The nonlinear length  $L_{nl}$  is defined as [82]

$$L_{nl} = \frac{1}{\gamma P_0} \quad (10)$$

Where  $P_0$  is the peak power of the input pulse and  $\gamma$  is the nonlinear response of the media. For given length of fiber  $L$ , if  $L_d \gg L$  and  $L_{nl} \gg L$ , the dispersion and nonlinear effects will not affect the propagating pulse. If  $L_d < L$  and  $L_{nl} \gg L$ , the pulse will be dominated by dispersive effects and nonlinearity will not affect during the propagation and vice-versa. If  $L_d < L$  and  $L_{nl} < L$ , the pulse will be dominantly affected by both dispersive and nonlinear effects. For example, the dispersion length of 50 fs pulse at 5000 mbar Xenon is around ~ 5.6 meters, and the GVD effect, thus, should be considered in the simulations. Figure 7 shows the interplay between SPM and GVD for 50 fs transform limited input pulses with 5  $\mu$ J energy per pulse

and 144  $\mu\text{m}$  beam diameter propagating in 2 meters HCF filled with 5000 mbar of Xenon. With considering only SPM effect, one should attain a broad spectrum to support few-cycle (blue curve). However, consideration of GVD in simulations leads to much narrower spectrum, highlighting the role of dispersion in limiting the spectral broadening in the HCF (red curve). As the pressure is applied, the GVD of the gas interplaying with the broadened spectrum significantly elongates the pulse duration, preventing effective SPM within HCF [66].

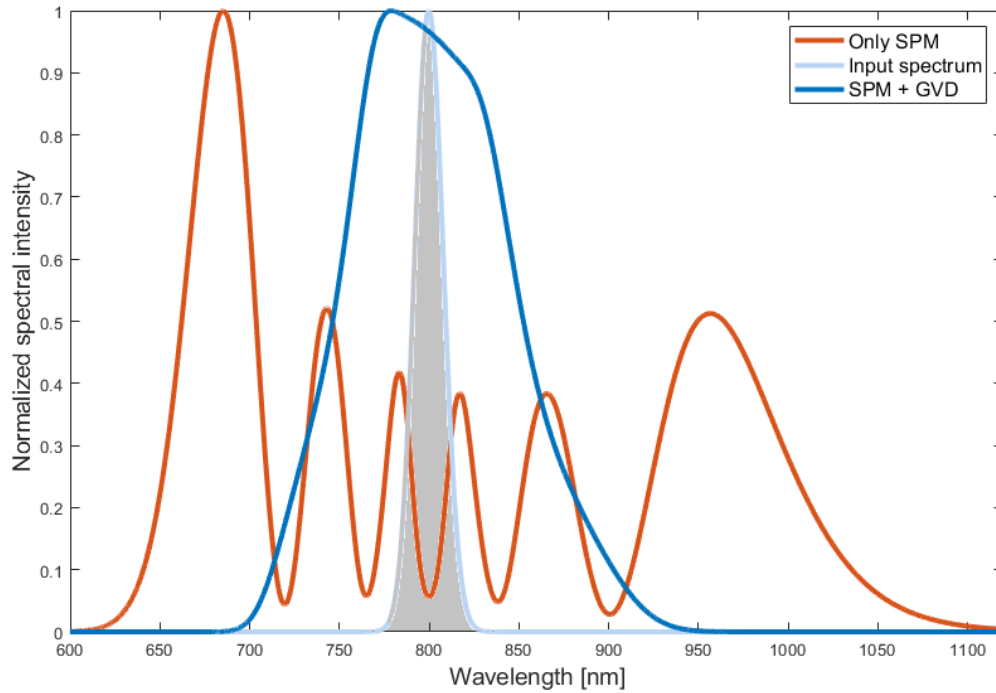


**Figure 7** The comparison of the spectrum with and without considering the GVD in the simulations, in the regime where both of the dispersive and the SPM are dominated effects ( $L_d < L$  and  $L_{nl} < L$ ).

### 2.1.3 Self-steepening

Isolating the term in GNLSE stemming from the power dependence of the refractive index yields

$$\frac{\partial A}{\partial z} = -\frac{\gamma_0}{\omega_0} \frac{\partial}{\partial t} (A|A|^2). \quad (11)$$

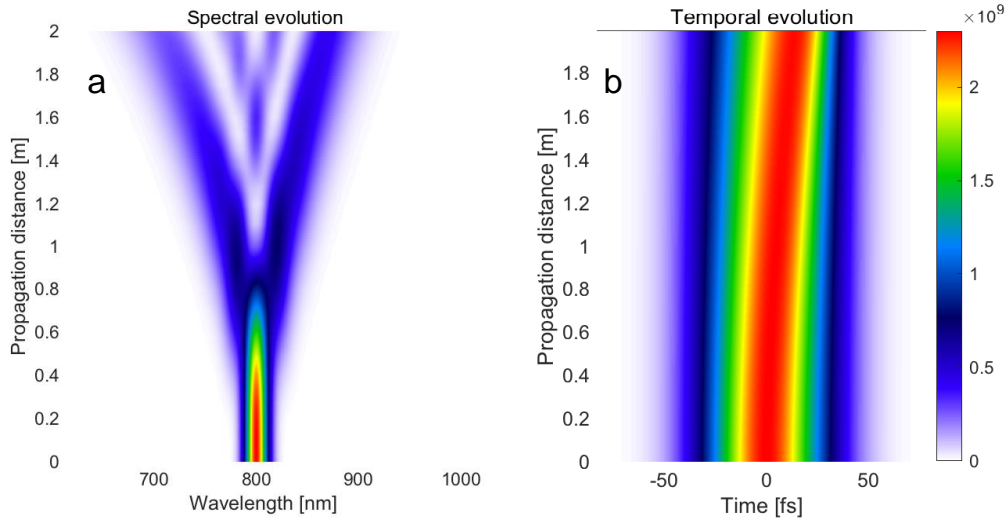


**Figure 8** Numerical simulations of the temporal and spectral evolution along the propagation in the fiber with considering the effect of self-steepening.

Since this equation is nonlinear, it cannot rigorously be solved using Fourier analysis. However, considering a very slowly varying power envelope, with respect to the optical frequency, the basic influence of this term can be analyzed by initially treating the pulse power,  $|A|^2$ , as being constant. The constant pulse power makes it possible to Fourier transform the equation and get

$$A = A \left( t - \frac{\gamma_0}{\omega_0} |A|^2 z \right) \quad (12)$$

which implies that parts of the pulse with higher power will undergo more positive time translation, i.e. experience more lag, than parts with lower power. This suggests that the pulse tails will move faster than the peak. The result is that the trailing pulse edge will get steeper while the front pulse edge gets less steep. This situation is referred to as self-steepening. The influence of the self-steepening is studied by numerically tracing the evolution of pulses in the temporal and the spectral domain for the same condition and HCF geometry presented at Figure 5. The simulation results indicate that the temporal peak of the pulse moves towards the trailing edge as the pulse propagates through the HCF. As it is discussed at Section 2.1.1, the blue components of spectrum are at trailing edge. Therefore, self-steepening leads broader spectrum at the blue part than the red part due to the higher intensity at the trailing edge (Figure 8).

#### 2.1.4 The Raman effect

Introducing the Raman term amounted to an exchange of the pulse power,  $|A|^2$ , for its convolution with the Raman response function,  $R(t)$ . Convolutions give the area of the product between two functions as one is translated relative to the other. Therefore, the Raman convolution can be interpreted as the result of the interaction between the pulse power envelope and the molecular vibrations or rotations. The actual Raman effect consists of a photon being converted into another photon with lower energy, i.e. longer wavelength/lower frequency. This means that the Raman convolution will introduce asymmetry in the spectrum by shifting energy towards lower frequencies. The reversed phenomenon, i.e. when a photon with higher frequency is generated, is referred to the anti-Stokes effect [82]. Since noble gases do not possess Raman cross sections, they are referred to as Raman inactive gases. However, the Raman effect in some molecules is dominant which will be investigated in details in chapter 3.

#### 2.1.5 Tunneling Ionization, ADK Model

An important and unique aspect of pulse propagation in gas filled HCF is that the power damage threshold of the interacting medium in these fibers is much higher than that of solid-core fibers, and hence one can easily reach intensity levels where partial ionization of the gas plays an important role in the pulse dynamics. This extends the boundaries of nonlinear fiber optics into regions where plasma generation must be taken into account. Nearly 50 years ago, Keldysh made the seminal theoretical prediction that atoms, molecules, and solids, under strong electromagnetic fields, are ionized through the process of tunnelling [93] (see [94] for a review). Keldysh theory defines a parameter that can be used to provide a link between multiphoton and tunneling emission. The Keldysh parameter is given by the following equation:

$$\gamma_k = \sqrt{I_p/2U_p} \quad (13)$$

where  $I_p$  is the ionization potential and  $U_p$  is the ponderomotive energy ( $U_p[eV] = 9.34 \times 10^{-20} \times (\lambda[nm])^2 \times I[W/cm^2] = 9.34 \text{ eV} @ \lambda=1 \mu\text{m} \text{ and } 1 \times 10^{14} \text{ W/cm}^2$ ). For atoms and molecules, the physics of tunnelling is observed when the Keldysh parameter is smaller than 1 and when the photon energy is much smaller than the ionization potential. For a laser pulse at 800 nm (1.54 eV of photon energy, most common because of commercial Titanium-Sapphire technology emitting at this wavelength), and an ionization potential of 15 eV (typical range for atoms and molecules), a Keldysh parameter of 1 is obtained at laser intensity in the

range of  $1 \times 10^{14}$  W/cm<sup>2</sup> corresponding to an electric field strength of 270 MV/cm. The Keldysh parameter in our simulations is smaller than 1, and the multiphoton ionization cross sections is very small. Therefore, we consider tunneling as the main ionization effect in the following context.

Ammosov, Delone, and Krainov derived the mathematical model (ADK model) for tunneling ionization rate of complex atoms in ac field [95, 96]. In this model, it is showed that when the optical field is linear polarized, the principal quantum number  $n$  and angular quantum number  $l$  satisfy  $n \gg l$ , the probability  $W_{ADK}$  of ionization per unit time is described in atomic unit by

$$W_{ADK} = C_{n^*l}^2 f(l, m) E_{g,au} \left( \frac{3E_0}{\pi(2E_{g,au})^{\frac{3}{2}}} \right)^{\frac{1}{2}} \left( \frac{2(2E_{g,au})^{\frac{3}{2}}}{E_{0,au}} \right)^{2n^* - |m| - 1} e^{-\frac{2(2E_{g,au})^{\frac{3}{2}}}{3E_{0,au}}} \quad (14)$$

with

$$C_{n^*l} = \left( \frac{2e}{n^*} \right)^{n^*} (2\pi n^*)^{-\frac{1}{2}}, \quad (15)$$

$$f(l, m) = \frac{(2l+1)(l+|m|)!}{2^{|m|} |m|! (l-|m|)!}. \quad (16)$$

This formula introduces the effective principal quantum number  $n^*$ , and the magnetic quantum number  $m$  to the calculation. The effective principal quantum number is given by

$$n^* = \frac{Z}{\sqrt{(2E_g)}} \quad (17)$$

where  $E_g$  in au (atomic unit) is the ground state ionization energy and  $Z$  is the atomic number.  $n^*$  accounts for the quantum defect in Rydberg-atoms by taking into account that the inner electrons do not entirely screen the charge of core. In review [97] it is discussed that the contribution by magnetic quantum numbers except  $m = 0$  is very small and after using the Stirling formula of factorials one arrives at

$$W_{ADK} = \sqrt{\frac{3n^{*3}E_0}{\pi Z^3}} \frac{E_0 D^2}{8\pi Z} \exp\left(-\frac{2Z^3}{3n^{*3}E_0}\right) \quad (18)$$

in which

$$D = \left( \frac{4eZ^3}{n^{*4}E_0} \right)^{n^*} . \quad (19)$$

The probability of ionization is defined as the following

$$P_{ion}(t) = 1 - \exp\left(-\int_0^t W_{ADK}(E_0(t)) dt\right). \quad (20)$$

Here, we solve the above equation for argon. The ionization process is highly nonlinear. Figure 9 shows the probability of the ionization for the laser peak intensity of  $1 \times 10^{14} W/cm^2$  is about 1 %. Therefore, the ionization effect is negligible for the intensities below  $0.5 \times 10^{14} W/cm^2$  . However, laser intensity of  $3 \times 10^{14} W/cm^2$  is able to fully ionize the gas medium.

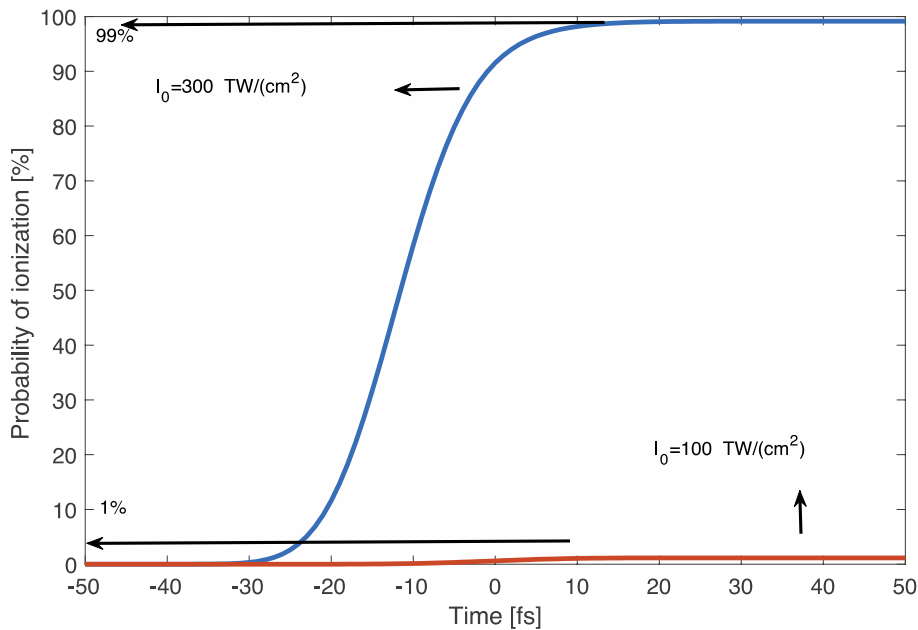


**Figure 9** Ionization probability for two different laser peak intensity in Ar

### 2.1.6 Plasma contribution

The refractive index of the plasma simply follows the Drude free electron model.

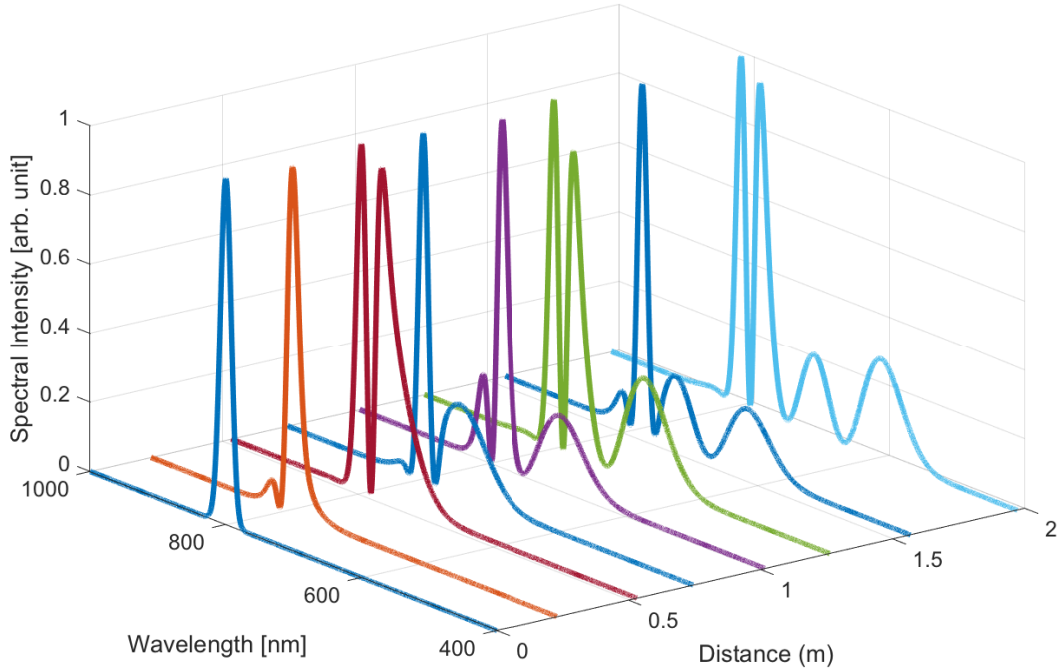


**Figure 10** The influence of the linear refractive index change due to the plasma to the spectrum at the different HCF position. The 50 fs input pulses with  $60 \frac{TW}{cm^2}$  peak intensity launched to the HCF filled with 1000 mbar of Ar. Note that in order to visualize the blue shift effect, the nonlinear refractive index  $n_2$  is set to be zero, and the ionization caused intensity loss is also set to be zero.

$$n_p = \sqrt{1 - \frac{\omega_p^2}{\omega_0^2}} \quad (21)$$

in which  $\omega_p$  is plasma frequency and it is given by

$$\omega_p = \sqrt{\frac{n_0 * P_{ion}(t) e^2}{m_e \epsilon_0}}. \quad (22)$$

Here  $n_0$  is the gas density and  $e$  and  $m_e$  are the electron charge and mass, respectively. The generated plasma modifies the refractive index, and it induces time dependent refractive index change across the pulse. Therefore, NLSE acquires a new nonlinear term

$$N(A)_{plasma} = - \left( 1 - \frac{i}{\omega_0} \frac{\partial}{\partial t} \right) \frac{i}{2} k_0 \frac{\omega_p^2}{\omega_0^2} A \quad (23)$$

which includes a self-steepening correction term.

To visualize the plasma effect, the NLSE is solved by considering only the above term, and it is shown that the free electrons caused by ionization from the plasma lead to the blue shift of the spectrum[98, 99]. Figure 10 illustrate the evolution of pulse spectrum within the fiber in 1000 mbar of Ar. The peak intensity of the input pulses is  $60 \frac{TW}{cm^2}$  and the total ionization rate is only equal 0.0016 percent.

## 2.2 The 1D experimental results and their fundamental limitations

In the previous section, the linear and nonlinear effects for pulse propagation through gas filled HCF in effective 1D regime have been discussed. In this section, we present the experimental results and their intrinsic limitations in 1D regime for high and low energy input pulses. The first experiment is ultra-broadband spectral broadening and pulse compression of low-energy pulses where dispersion is a limitation while the second experiment is the pulse compression of the narrowband high-energy pulses where self focusing and ionization is the limitation factor. A representative layout of the experimental setup for pulse compression in gas filled HCF is illustrated in Figure 11. The input pulses are focused and coupled into a HCF stretched by two holders. At fiber output, the temporal characterization is performed via frequency-resolved optical gating (SHG-FROG), and the spectra are measured with a VIS/NIR spectrometer (Avantes, AvaSpec-ULS2048XL). The beam profiles are captured using a CDD camera (PointGrey, FLEA).

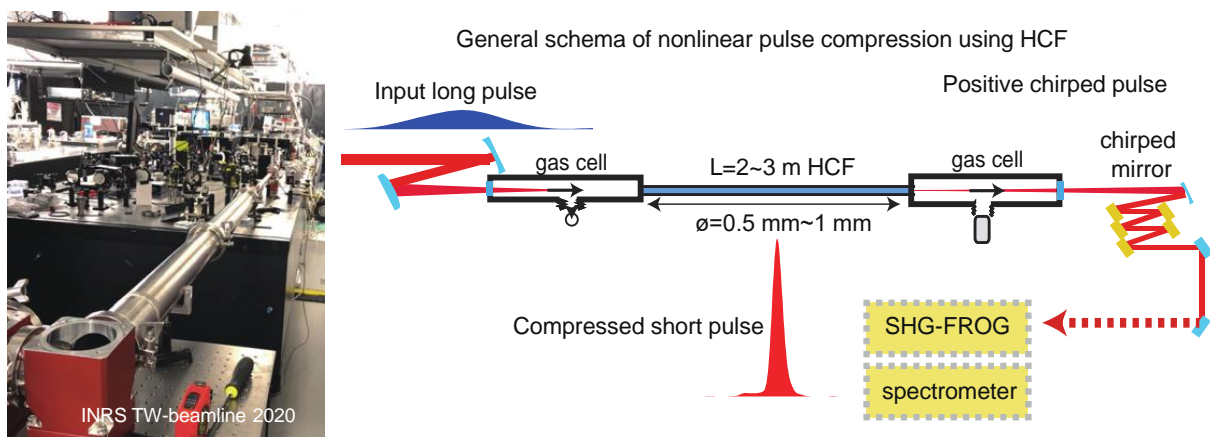


**Figure 11** Photograph of the TW-beamline for further strong field applications at ALLS laboratory of INRS (left). The general schema of pulse compression using HCF (right).

Furthermore, the experimental results are compared with numerical simulations. The numerical modeling assumes only the fundamental mode during pulse propagation, which is justified for the effective 1D regime where the self-focusing effect is insignificant, more specifically, the peak power of the laser pulse during the nonlinear propagation is well below than critical power of self-focusing.

### 2.2.1 Low-energy regime

Compression of low energy ultrashort laser pulses using a HCF filled with 1-1 difluoroethane ( $C_2H_4F_2$ ), also known as R152a, is demonstrated. A 45 fs, 16  $\mu$ J Ti:Sapphire laser pulse is spectrally broadened in an HCF filled with R152a and subsequently compressed to  $\sim$ 9 fs with  $\sim$ 6  $\mu$ J pulse energy, which corresponds to a fivefold compression. This affordable and easily accessible gas is promising to compress new generation high repetition rate lasers in conjunction with a flexible HCF setup.

The simulations confirm the experiments in two independent cases; the transform-limited pulse duration,  $\tau_{TL}$ , and the pulse duration of the direct HCF output without chirped mirrors,  $\tau_{chirped}$ . To identify the contribution of GVD, the calculation is repeated with the second order dispersions being neglected, i.e.,  $\beta_2 = 0$ . The simulations with and without consideration of the GVD are superimposed with the measurements as shown in Figure 12(a). The lower half below the break of the vertical axis corresponds to  $\tau_{TL}$ . Without the effect of GVD, one should have attained a much broader spectrum to support  $<$ 5 fs pulses at higher pressures (filled blue diamonds). However, experimentally, the  $\tau_{TL}$  reaches  $\sim$ 10 fs, as do the simulations including GVD (filled red circles). The consideration of GVD leads to much better agreement with experiment, highlighting the role of dispersion in limiting the spectral broadening in the HCF. The upper half of the axis in Figure 12(a) denotes  $\tau_{chirped}$ , the pulse duration of the direct HCF output without chirped mirrors. It is measured by intensity autocorrelation (black hollow squares). As the pressure is applied, the GVD of the gas interplaying with the broadened spectrum significantly elongates the pulse duration. The corresponding calculation considering GVD (red hollow circles) show a decent fidelity with the experiment, while calculations without GVD (blue hollow diamonds) predict a relatively insignificant increase of the pulse duration. This finding shows that increase of pulse duration during the propagation in the fiber indeed occurs due to GVD and is responsible for the impeded spectral broadening with rising pressure.

With increasing pressure, we anticipate an interplay between two effects: 1) the spectral broadening is promoted by a denser gas medium leading to higher nonlinearity; 2) spectral

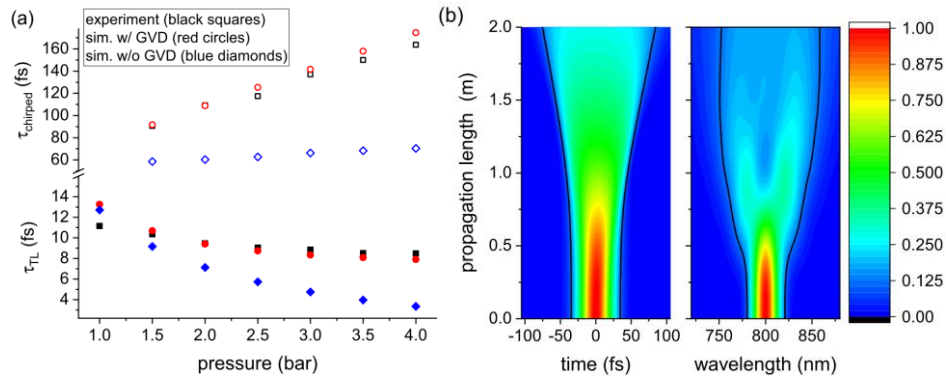


**Figure 12** The transform-limited pulse duration  $\tau_{\text{TL}}$  (solid symbols, axis below the break) and pulse duration before dispersion compensation  $\tau_{\text{chirped}}$  (hollow symbols, axis above the break) derived from the experiment (black squares), simulated with dispersion being considered (red circles) and simulations with dispersion being disregarded (blue diamonds) as a function of pressure and (b) numerical simulations of the temporal and spectral evolution along the propagation in the fiber of an input pulse at 4.0 bar. Black thick solid lines depict 1/e2 of the temporal and spectral profile with respect to the propagation length.

broadening is hampered by the lower intensity resulting from the elongated pulse duration. The competition of these two counteracting effects sets a constraint for the spectral broadening. The influence of an elongated pulse duration is studied by numerically tracing the evolution of pulses in the temporal and the spectral domain (Figure 12(b)). Assuming a high pressure of 4.0 bar, under which temporal broadening owing to GVD seems significantly probable, the suppression of spectral broadening is observed after propagation of  $\sim 1$  m as black lines shown in the right panel of Figure 12(b). This coincides with the point where the temporal broadening begins as shown in the left panel.

### 2.2.2 High-energy regime

In this section, we present the experimental results for pulse compression of the Yb laser system with a pulse energy of  $\sim 70$  mJ. The experiment was preformed through a collaboration with Prof. Andrius Baltuska group in Vienna University of Technology. The aim of this work is to investigate the capability and limitations of high-energy pulse compression in large core stretched HCF for for shortening the pulse duration of the state-of-the-art Yb laser technology. The nonlinear spectral broadening is performed in Neon filled HCF, and the efficient spectral broadening is observed in Neon filled HCF up to  $\sim 2200$  mbar.

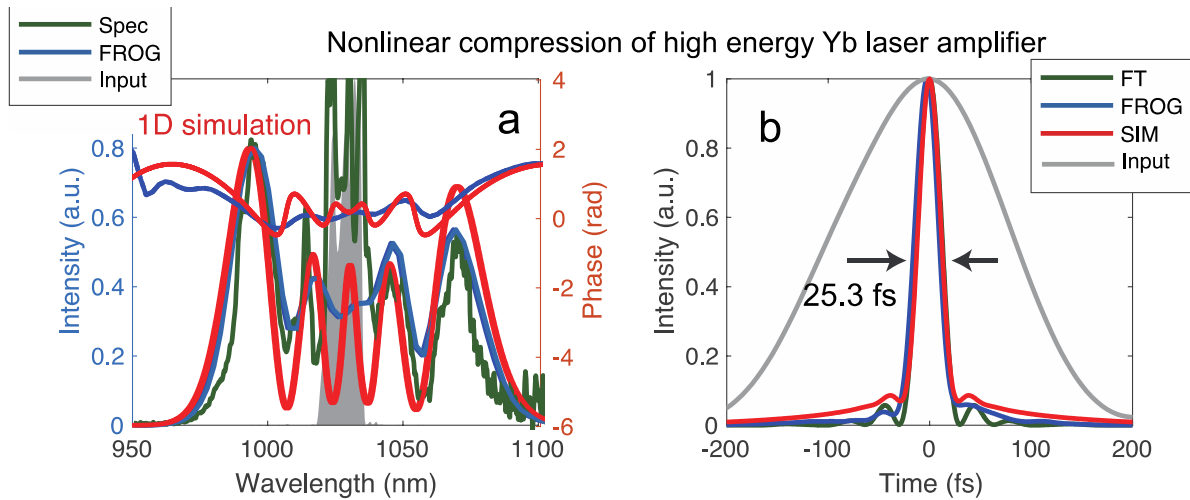


**Figure 13** 70 mJ, 230 fs Yb input pulses at 1030 nm propagate within 3 meters (1 mm core diameter) HCF filled with 2100mbar of Neon in differential pressure scheme. (a) The measured (green), retrieved from SHG-FROG (blue), and simulated (red) output spectra together with the spectral phase of the compressed output pulses. (b) Temporal profiles of the simulated (red) and measured (blue) compressed output pulses. The Fourier transform limited (FT) temporal profile is depicted in green line.

Figure 13 presents the spectral and temporal characterization of the compressed pulse at 2100 mbar. At the output of the HCF, the pulses are compressed using a combination of five chirped mirrors (Ultrafast Innovations GmbH PC1305), which has a total dispersion (GDD) of  $\sim -750 \text{ fs}^2$  and reflection of  $\sim 97\%$  within the whole broad bandwidth of interest. The pulses are characterized using SHG-FROG technique. In Figure 13(a), we present the measured spectra from the spectrometer and compare it to the retrieved spectra from the SHG-FROG. The retrieved temporal profile (Figure 13(b)) shows a good compression quality with a duration of 25.3 fs, which is close to its Fourier limited (FT) pulse duration of 25 fs. The 1D simulations have been performed by solving GNLSE. The results of the simulated spectra and spectral phase of the output pulses are in very good agreement with measured ones. Besides, the simulations predict dispersion amount of  $\sim -738 \text{ fs}^2$  to fully compensate the spectral phase. The agreement between the simulation and measurement indicates the pure SPM process in the pulse propagation through HCF at the pressure of 2100 mbar since the plasma term did not affect the shape of output spectrum at this pressure. However, by further increasing the gas pressure, which is the motivation to obtain broader spectra and shorter output pulses, the spectra will be distorted, and spectral broadening becomes less efficient, which indicates that other nonlinear effects play significant roles. Figure 14 indicates that by increasing the gas pressure from 2000 mbar to 3000 mbar, the red part of the spectra is suppressed due to the plasma induced by ionization [100]. By increasing the gas pressure, the critical power for self focusing is getting lower, thus, the beam is getting focused resulting in higher intensity and ionization. Therefore, the occurrence of self-focusing

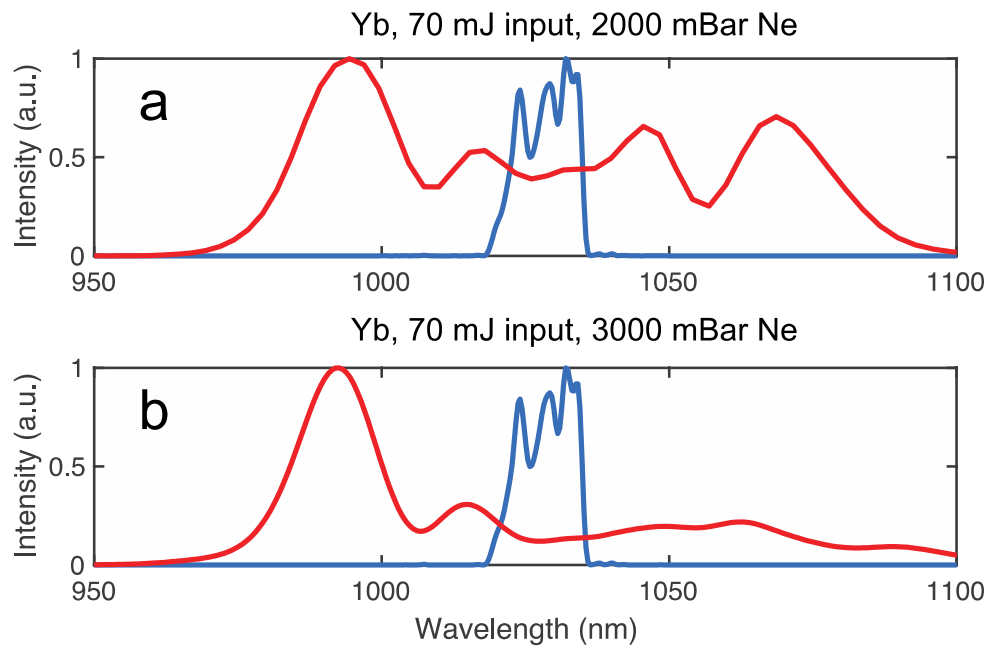


**Figure 14** Self-focusing and ionization are the intrinsic limitations for high energy pulse compression which lead to energy absorption, distortion of the spectra, and lower temporal compression quality. 70 mJ, 1030 nm Yb input pulses (blue curves) propagate within 3 meters (1 mm core diameter) HCF filled with (a) 2000 mbar and (b) 3000 mbar of Neon. Red curves show the output spectrum.

and the consequent ionization impose an intrinsic limitation for high-energy pulse propagation inside gas filled HCFs.

### 3 Raman effect in molecular gas

When laser pulses interact with molecules, wave packets are created and drive vibrational motion [101] and rotational alignment [102], offering a variety of “control knobs” which are at the core of many applications, such as quantum control [103], quantum information [104], molecular orbital tomography [105, 106], attosecond pulse shaping [107], and laser-induced electron diffraction [108]. Recent advances in the field of coherent control of molecular excitation enable new techniques for spectral broadening and light pulse manipulation [109]. The timescales of laser induced molecular alignment can be categorized in two different regimes: (1) In the regime of adiabatic excitation where the pulse duration is much longer than the period of molecular rotation [110-112], maximum alignment is obtained at the peak of the laser pulse envelope and returns to an isotropic medium after the pulses (2) In the regime of impulsive excitation, where the input pulse duration is comparable to the period of molecular rotation, momentum imparted by the laser persists after the passage of the pulse and is referred to as the ‘kicked-rotor’ [113, 114]. In this regime, the pump pulses create wave packets corresponding to coherent rotational motion of the molecules, which leads to ultrafast index transients [115]. Using this approach, the spectra and phase of ultrashort light pulses have been manipulated using pump-probe schemes. A pump pulse triggers a time evolution of the molecular alignment and of the resulting optical susceptibility, which implements phase changes to the ensuing probe pulse with variable time delays [115-120]. However, so far, the scaled energy, the low efficiency and the complexity of this method make it less practical than the state-of-the-art SPM-based method.

#### 3.1 Microscopic model of molecular rotation

We specifically consider molecular gases interacting with linearly polarized infrared laser pulses [121]. Before the laser pulse interacts with the molecular gas, the system is in a thermal ensemble at the temperature of  $T$ . In the quantum picture, this system is described by a statistical mixture of angular momentum states. Each molecule is in a definite state of angular momentum  $|J, M\rangle$  where angular momentum  $J = 0, 1, 2, \dots$ . The  $M$  is the projection of the angular momentum onto the  $z$ -axis of the coordinate system and can take on the values  $M = -J, -(J - 1), \dots, J - 1, J$ . The coordinate wave functions of this basis are the spherical harmonics  $Y_{JM}(\theta, \varphi)$ . The distribution of angular momentum amongst the various molecules in the gas is given by the Boltzmann law:

$$P_J \sim g_J (2J + 1) \exp\left(-\frac{E_J}{kT}\right) \quad (24)$$

where  $E_J$  is the rotational energy of the state  $|J, M\rangle$ . The  $(2J + 1)$  term accounts for the degeneracies within a given  $J$  level because of the different  $M$  sub-levels. An additional factor  $g_J$  arises from the nuclear spin statistics for homonuclear molecules [122].

When the laser pulse interacts with the molecular gas with intrinsic polarizability, rotational wave packets (i.e. superposition of the field-free eigenstates  $|J, M\rangle$ ) are created depending on initial angular momentum state for each molecule. Thus, the induced wave packet starting from all initial states in the equilibrium state must be calculated to have a full response of the medium.

The rotational Raman contribution to the nonlinear index arises from the alignment of molecules interacting with the laser field. To model the time evolution of the molecule, the total wave packet is described by a coherent superposition of field-free rotational states [123, 124]. The creation of this wave packet through the interaction with the laser pulses is modeled by solving the time-dependent Schrödinger equation [117, 123, 124]. In a weak field regime in which neither dissociation nor ionization take place, the Hamiltonian of a molecule subject to an intense laser is considered as an effective Hamiltonian which acts just within the lowest vibronic ground state and is given by

$$H_{eff} = B\mathbf{J}^2 - \frac{E^2(t)}{2}(\Delta\alpha\cos^2\theta + \alpha_{\perp}) \quad (25)$$

where the first term is the field-free rotational Hamiltonian of the molecule in which  $\mathbf{J}^2$  is the squared angular momentum operator and  $B$  is the rotational constant. Rovibrational coupling is included by writing the  $B\mathbf{J}^2$  operator as  $B_0 J(J + 1) - D_0 [J(J + 1)]^2$  in the angular momentum basis. The  $D_0$  term accounts for bond stretching at high angular momentum. Further corrections to the kinetic energy arising from vibrational excitation can be neglected since essentially no thermal vibrational excitation exists for the molecular species considered herein (for example, less than  $10^{-5}N_2$  molecules are vibrationally excited for temperatures smaller than 300 K [122]) [121].  $E(t)$  denotes the electric component of the laser field. The optical properties of the molecule are captured by the polarizability difference  $\Delta\alpha = \alpha_{\parallel} - \alpha_{\perp}$ , where  $\alpha_{\parallel}$  and  $\alpha_{\perp}$  denote the parallel and perpendicular polarizabilities of the molecule. To model the time evolution of the molecule, the total wave function is described by a combination of field-free rotational states  $|\psi(t)\rangle = \sum d_{J,M}(t)|J, M\rangle$ . The wave function satisfies the time-dependent Schrödinger equation

$$i\hbar \frac{\partial |\psi(t)\rangle}{\partial t} = H_{eff} |\psi(t)\rangle. \quad (26)$$

Inserting the total wave packet  $|\psi(t)\rangle$  into the TDSE gives a large system of ordinary differential equations for the time-dependent probability amplitudes  $d_{JM}(t)$ ,

$$i\hbar \frac{d}{dt} d_{J,M}(t) = d_{J,M}(t) \left( B\langle J, M | J^2 | J, M \rangle - \frac{\alpha_{\perp} E(t)^2}{2} \right) - \sum_{J', M'} \frac{d_{J', M'}(t) \Delta \alpha E(t)}{2} \langle J, M | \cos^2 \theta | J', M' \rangle, \quad (27)$$

where the matrix elements  $\langle J, M | \cos^2 \theta | J', M' \rangle$  does not couple even and odd  $J$  due to symmetry of the angular potential. All transitions, thus, occur between  $J \leftrightarrow J + 2$  and  $J \leftrightarrow J - 2$ . Besides,  $M$  states do not couple to each other owing to the cylindrical symmetry of the angular potential. The evolution of the wave functions is obtained by solving the above equation using the fourth-order Runge-Kutta in the interaction picture method (RK4IP) [123].

The standard measure of alignment is defined by the average value of  $\cos^2 \theta$ . This measure would give a value  $\langle \cos^2 \theta \rangle = 1$  for an angular distribution perfectly peaked along the 'poles'  $\theta = 0$  and  $\pi$ ,  $\langle \cos^2 \theta \rangle = 0$  for a distribution peak along the 'equator'  $\theta = \pi/2$ , and  $\langle \cos^2 \theta \rangle = 1/3$  for an isotropic distribution evenly distributed across all  $\theta$ . During the interaction with the laser pulse,  $\langle \cos^2 \theta \rangle$  is calculated by numerical integration over the computed wave function. Molecular alignment is characterized by the expectation value of  $\cos^2 \theta$ , given by

$$\langle \cos^2 \theta \rangle = \sum_{JJ'} d_{J,M}(t) d_{J',M'}(t) (2J+1)^{\frac{1}{2}} (2J'+1)^{\frac{-1}{2}} \times \begin{bmatrix} J & 2 & J' \\ -M & 0 & M \end{bmatrix} \begin{bmatrix} J & 2 & J' \\ 0 & 0 & 0 \end{bmatrix}. \quad (28)$$

The alignment signal is further averaged over an initial Boltzmann distribution of angular momentum states for a given initial temperature  $T$ .

$$\langle \cos^2 \theta \rangle(t) = \frac{\sum_{J,M} g_J (2J+1) \exp\left(-\frac{E_J}{kT}\right) \langle \cos^2 \theta \rangle(t)_{J,M}}{\sum_J P_J} \quad (29)$$

where the rotational energies are  $E_J = B_0 J(J + 1) - D_0 [J(J + 1)]^2$ .

### 3.2 Rotational response and Raman gain

The nonlinear response function  $R(\tau)$  of the gas includes both the electronic and nuclear contributions. The total refractive index change induced by optical pulses with intensity profile of  $I(t)$  can be written as:

$$\Delta n(t) = \int R(\tau) I(t - \tau) d\tau. \quad (30)$$

As the rotational Raman response  $h_R(\tau)$  is modeled as a damped harmonic oscillator (equation 2), the rotational contribution to the nonlinear index is:

$$\begin{aligned} \Delta n_{rot} &= n_2 * f_R \int h_R(\tau) I(t - \tau) d\tau \\ &= f_R (\tau_1^{-2} + \tau_2^{-2}) \tau_1 \int \exp(-t/\tau_2) \sin(t/\tau_1) I(t - \tau) d\tau. \end{aligned} \quad (31)$$

At the same time, the change in the refractive index due to laser induced alignment is calculated by [124]:

$$\Delta n_{rot} = \frac{N \Delta \alpha}{n_0 \epsilon_0} (\langle \cos^2 \theta \rangle(t) - 1/3) \quad (32)$$

where  $N = 2.5 \times 10^{19} \text{ cm}^{-3}$  is the initial molecular density,  $\Delta \alpha$  is the polarizability difference [17], and  $n_0$  is the linear refractive index at the fundamental frequency  $\omega_0$ . By fitting equation (31) with the obtained  $\Delta n_{rot}$  from TDSE calculations (equation (32)), we can extract the coefficients  $\tau_1$ ,  $\tau_2$ , and the ones of  $f_R$ , for different experimental condition. Figure 15 shows the temporal form of rotational Raman response  $h_R(\tau)$  deduced from molecular alignment calculations. Here,  $\langle \cos^2 \theta \rangle$  is calculated for the 120fs input pulses with the peak intensity of  $7 \frac{\text{TW}}{\text{cm}^2}$  in nitrogen ( $\text{N}_2$ ).

For a diatomic molecule like  $\text{N}_2$ , the parallel polarizability is higher than the perpendicular one and under the interaction with a strong laser field, the molecules tend to align with the electric component of the field. This rotational motion induces a change of refractive index  $\Delta n(t)$ .

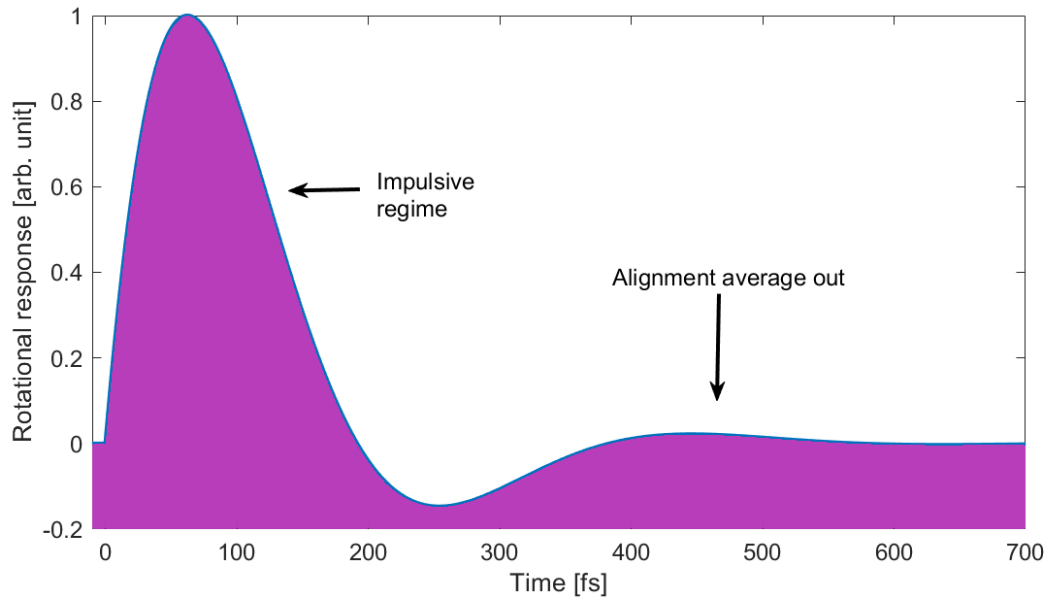


**Figure 15** Rotational Raman response ( $h_R(\tau)$ ) of  $N_2$  for 120fs input pulses with the peak intensity of  $7 \frac{TW}{cm^2}$ .

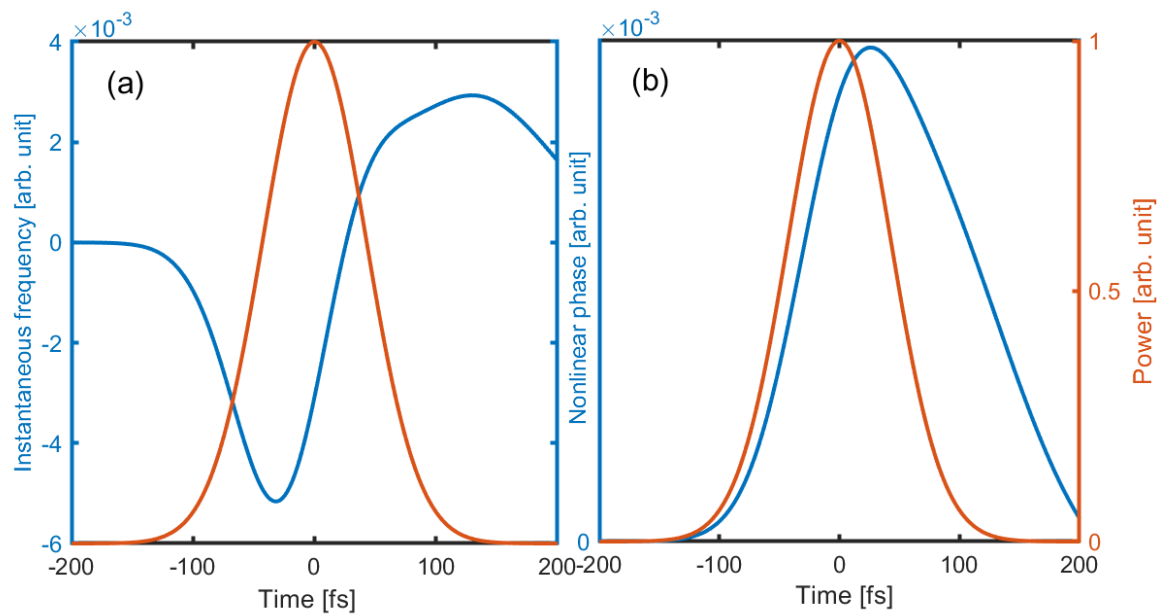


**Figure 16** (a) illustrates the instantaneous frequency  $\Delta\omega$  and (b) the change of refractive index  $\Delta n$  for 100 fs pulses

The rotational contributions to the nonlinear response function is described by the function  $h_R(t)$ . The real part of the Fourier transform of  $h_R(t)$  leads to Raman-induced index changes, while its imaginary part is related to the Raman gain. The change of nonlinear refractive index  $\Delta n(t)$  in instantaneous Kerr response is proportional to the intensity profile of the laser pulse

$I(t)$ ,  $\Delta n(t) = n_2 I(t)$ . Therefore, if  $I(t)$  is symmetric, the 1st order time derivative of  $\Delta n(t)$ , namely, the instantaneous frequency  $\Delta\omega = d\Delta n(t)/dt$ , indicates that the red-shift of the leading edge and the blue-shift of the trailing edge are equal, thus producing symmetrically broadened spectra (Figure 4). In contrast, for Raman active medium, the molecules are not responding instantaneously to the laser intensity, and this response can be described mathematically by the delayed response function  $h_R(\tau)$ . Thus,  $\Delta n(t)$  can be obtained as a convolution of the  $h_R(\tau)$  and  $I(t)$ , i.e.,  $\Delta n(t) = \int h_R(\tau) I(t - \tau) d\tau$ . As  $h_R(\tau)$  is delayed, the convolution presents a sharp rise at the leading edge and a slow fall at the trailing edge. Consequently, minus the time derivative of the phase ( $\Delta\omega$ ) indicates a dominant red-shift. Figure 16 indicates the calculated nonlinear refractive index change  $\Delta n$  and the induced instantaneous frequency  $\Delta\omega$  for pulse duration of 120 fs. The width of the delayed response function is roughly 100 fs. Therefore, for a given  $h_R(\tau)$ , the convolution operation is maximized as the pulse duration of  $I(t)$  is similar to  $h_R(\tau)$ , and since the rotational response follows  $\langle \cos^2\theta \rangle(t)$ , the maximum red-shifted spectral broadening is obtained once the pulse duration is comparable with the timescale where average alignment  $\langle \cos^2\theta \rangle(t)$ , reaches its maximum value ( $T_{rot}$ ). In other words, when the pulse duration is comparable to the characteristic time of the molecular rotation  $T_{rot}$ , the molecules reach maximum alignment within the fastest time scale, resulting in maximum spectral broadening.

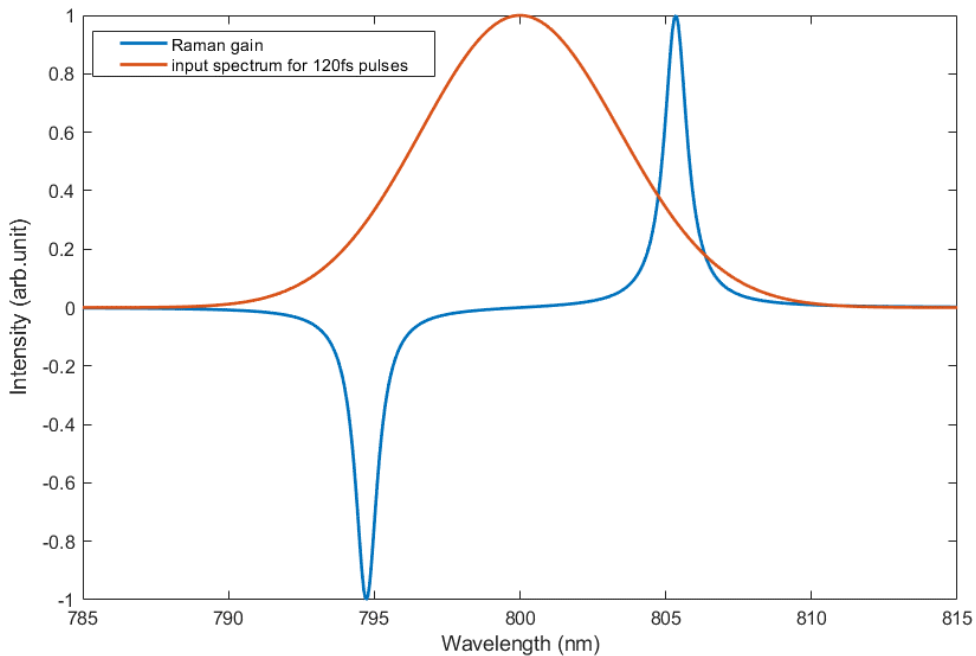


**Figure 17** Red: Gaussian spectra supporting 120fs pulses. Blue: Raman gain for  $N_2$ . The 120fs pulses have sufficient bandwidth to provide pump and Stokes frequencies to drive efficiently the Raman process.

To better understand the criteria for the efficient spectral broadening using molecular alignment, the phenomenon can be described in the frequency domain. The Raman-gain coefficient  $g_R(\Omega)$ , where  $\Omega = \omega_p - \omega_s$  is the frequency difference between the pump and Stokes frequencies, is the most important quantity for describing the Raman process (Figure 17). It is noted that the Raman process is dominated as long as the frequency difference  $\Omega$  lies within the instantaneous bandwidth of the driving laser pulse.

### 3.3 Spectral broadening in Raman active media

Here, we illustrate the high efficiency of spectral broadening in HCF filled with nitrogen ( $N_2$ ) gas at maximum alignment regime. In the experiment, a Ti: Sapphire chirped-pulse amplifier (CPA) which delivered 40 fs transform-limited pulses with a central wavelength of 780 nm at a repetition rate of 100 Hz was used. The output of the CPA was focused and coupled into a 2-meter-long HCF with a core diameter of 500  $\mu\text{m}$  filled  $N_2$  in a static pressure configuration. The peak intensity inside the fiber was kept constant  $\sim 7 \text{ TW}/\text{cm}^2$ . At this peak intensity the characteristic time is around 120 fs for  $N_2$ . Thus, we used spectral filter at the laser output to obtain 120 fs transform limited pulse. Figure 18 shows the experimental results of output redshift spectra at 2500 mbar gas pressure using 120 fs input pulses (maximum alignment regime) with energy of 1.5 mJ centered at 800 nm.

At the maximum alignment regime, the 1D simulations predict very well the asymmetry shape of the spectral broadening in Raman active medium. Simulated spectra for 120 fs input pulses with 1.5 mJ

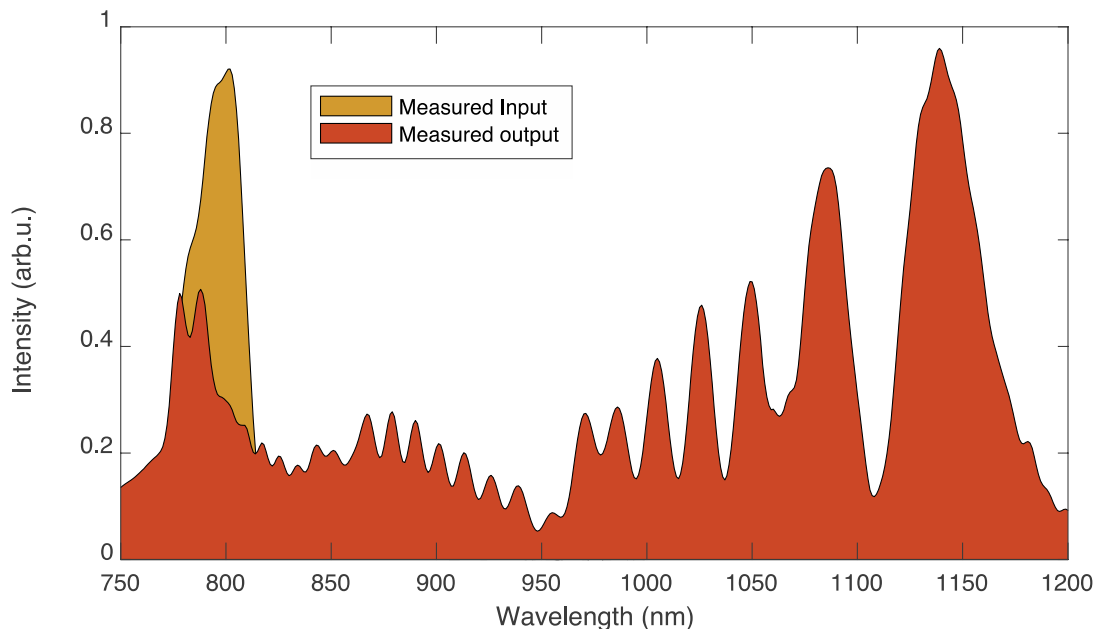


**Figure 18** Enhanced redshift spectra at 2500 mbar gas pressure via maximum alignment with a driver pulse duration of 120 fs.

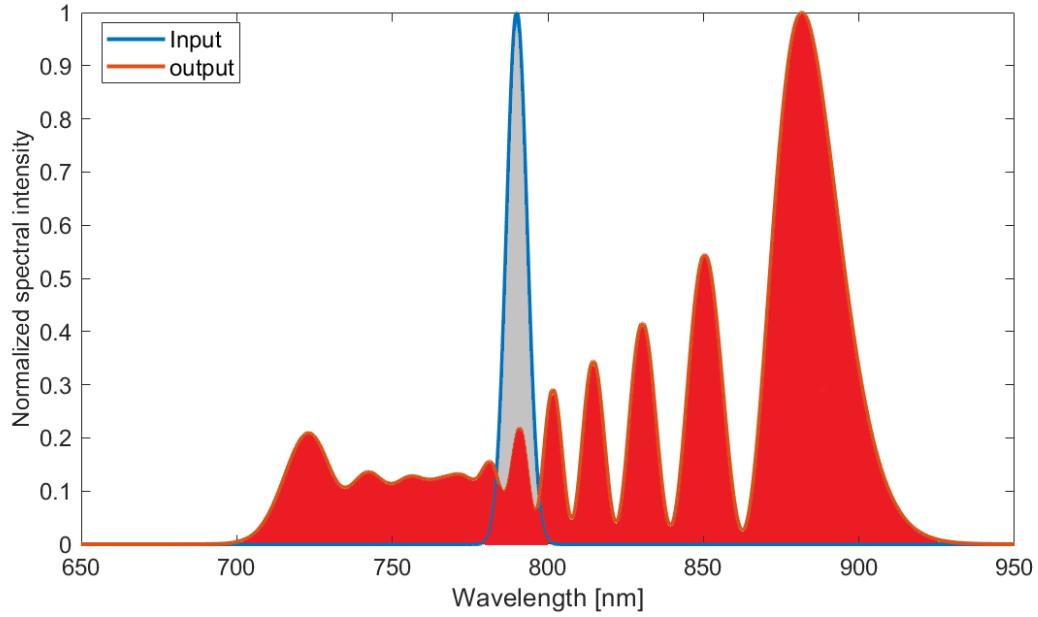


**Figure 19** Simulated spectra from the 1D model at the maximum alignment regime for 120 fs pulses. The spectrum has red-shifted asymmetry shape which is consistent with the experimental results.

energy per pulse in 2 meter HCF (500 $\mu$ m core diameter) filled with 1000 mbar of N<sub>2</sub> in a static configuration are depicted in Figure 19.

### 3.4 Phase construction and pulse compression at maximum alignment regime

As it is indicated in Figure 16(a), the temporal phase at maximum alignment possess negative chirp at the leading edge, and positive chirp at the trailing edge of the pulse. Therefore, one can expect that the output pulses generated at maximum Raman gain can be compressed either by chirp mirrors with negative chirp or with linear propagation through the normal dispersion regime in a piece of glass. To gain more physical insight, the simulation results of the time-frequency maps (Wigner function) as a function of pressure at the HCF output for 120 fs input pulses (maximum Raman gain) obtained from 1D simulations are presented (Figure 20). The obtained output pulse has the clear feature of having a negative chirp at the leading edge and a positive chirp at the trailing edge of the pulse. In addition, the energy ratio between leading and trailing edge is nearly the same.

This feature is further confirmed in the experiment. At the pressure of 1000 mbar of N<sub>2</sub>, the output pulses are directly post compressed by both positive and negative chirp. To compensate the negative, 5 pairs of chirped mirrors (UltraFast Innovations, Garching, Germany) with a group delay dispersion (GDD) of -25 fs<sup>2</sup> per bounce were used, along with few millimeters of fused silica for GDD fine tuning, for a total compensation value of about -180 fs<sup>2</sup>.

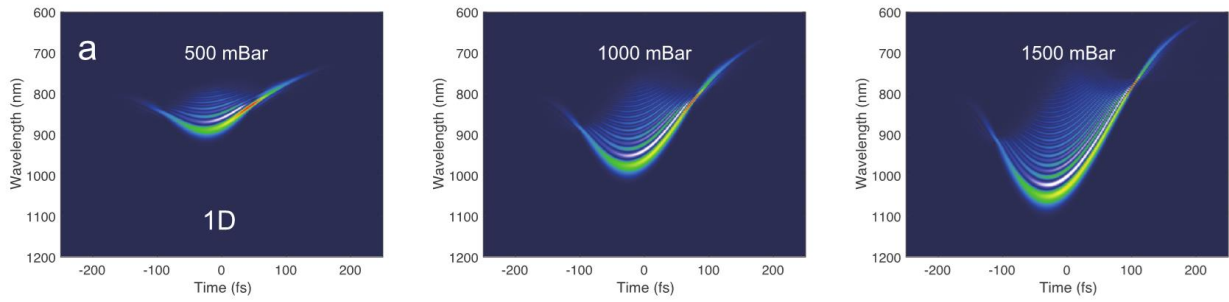


**Figure 20** Time-frequency maps at the HCF output obtained from 1D numerical simulations as a function of pressure for the case of 120fs input pulses. It indicates that the pulses have a negative chirp at the leading edge and a positive chirp at the trailing edge.

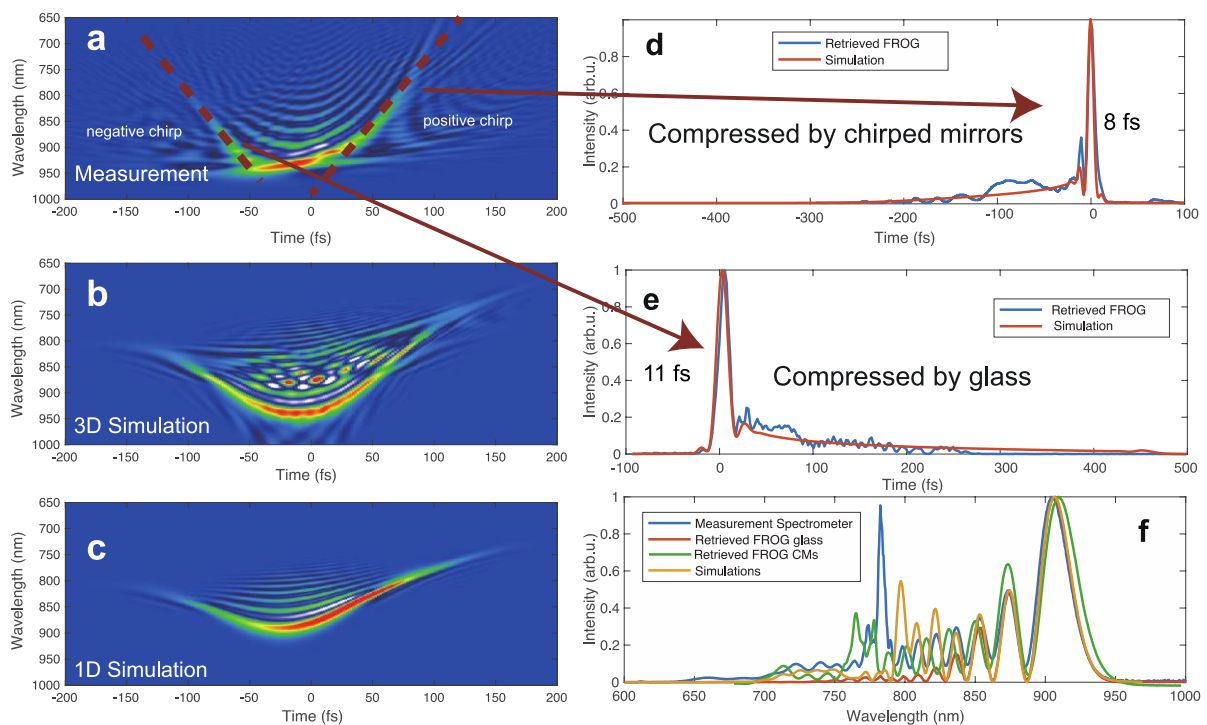


**Figure 21** Temporal characterization of output pulses for the case of 120fs input pulses with 1.2 mJ energy per pulse in 2 meter N<sub>2</sub> filled HCF at 1000 mbar pressure. (a). Time-frequency maps (Wigner function) at the HCF output from FROG reconstructed trace (b, c) The corresponding 3D and 1D simulations. (d) Temporal profile from reconstructed FROG trace together with the simulation results after compression with chirped mirror and (e) linear propagation through fused silica. (f) The measured output spectrum together with the reconstructed spectrum for two above mentioned compressed results and simulated spectrum.

The pulses after compression were temporally characterized by SHG-FROG. On contrary, to compensate the negative chirp at the leading edge of the pulse, the output pulses were simply propagated through 3.5 mm piece of fused silica glass. Figure 21 (a) shows the Wigner function of the output pulses obtained from the reconstructed FROG trace which

experimentally confirms the phase properties of the output pulses. Figure 21 (b, c) are the corresponding 1D and 3D simulation results (3D simulations are explained in detail in the next chapter). Temporal profile from reconstructed FROG trace together with the simulation results after compression with chirped mirror and linear propagation through fused silica are presented in Figure 21(d, e), respectively. The reconstructed spectrum for both compression scheme, presented in Figure 21(f), are in good agreement with the experimental and simulation ones.

### 3.5 Failure of 1D simulations

To investigate the pulse duration dependence of spectral broadening in Raman active medium, the pulse duration was adjusted from 40 fs to 1300 fs, by varying the separation between the grating pairs (adding positive group delay dispersion). The peak power was kept constant for different pulse durations. The experimental results for spectral broadening in 1000 mbar pressure of N<sub>2</sub> for varying input pulse durations is illustrated in Figure 22. When the pulse duration is increased from 40 fs to 100 fs, the spectrum is red-shifted from 900 nm to a maximum value of 950 nm (Figure 22). By increasing the pulse duration from 100 fs to 200 fs, the maximum broadening at red edge reduces again to 900 nm. This is consistent with molecular alignment theory which states that using a pump pulse with a duration close to this characteristic timescale generates the optimal nonadiabatic alignment for the ensemble, just like pushing a person on a swing with the perfect timing to increase the amplitude of the swinging motion. The simulated spectrum for N<sub>2</sub> using the one dimensional time depended Schrödinger equation (TDSE) for different input pulse durations are shown in Figure 22 (b). From the simulation, the  $T_{rot}$  for N<sub>2</sub> is around 100 fs which correspond to maximum Raman gain. The simulations presented here, can reproduce the asymmetry shape of the spectrum using pulses around 100 fs. However, these simulations predict a diminished spectral broadening efficiency with increasing pulse duration accompanied by a symmetric spectral shape. As the delay response function of molecules  $h_R(t)$  peaks around 100 fs, the delayed effect of molecular response becomes weaker and weaker for the longer input pulse duration. It converges to the same behavior of instantaneous response than SPM, giving rise to a symmetric spectral shape and a dropping of spectral broadening efficiency. The different driver pulse durations can also be understood with Raman gain in the frequency domain. The rotational excitation step of N<sub>2</sub> is far larger than the instantaneous bandwidth of the 700 fs pulses, while 100 fs spectrum falls effectively in the rotational bandwidth.

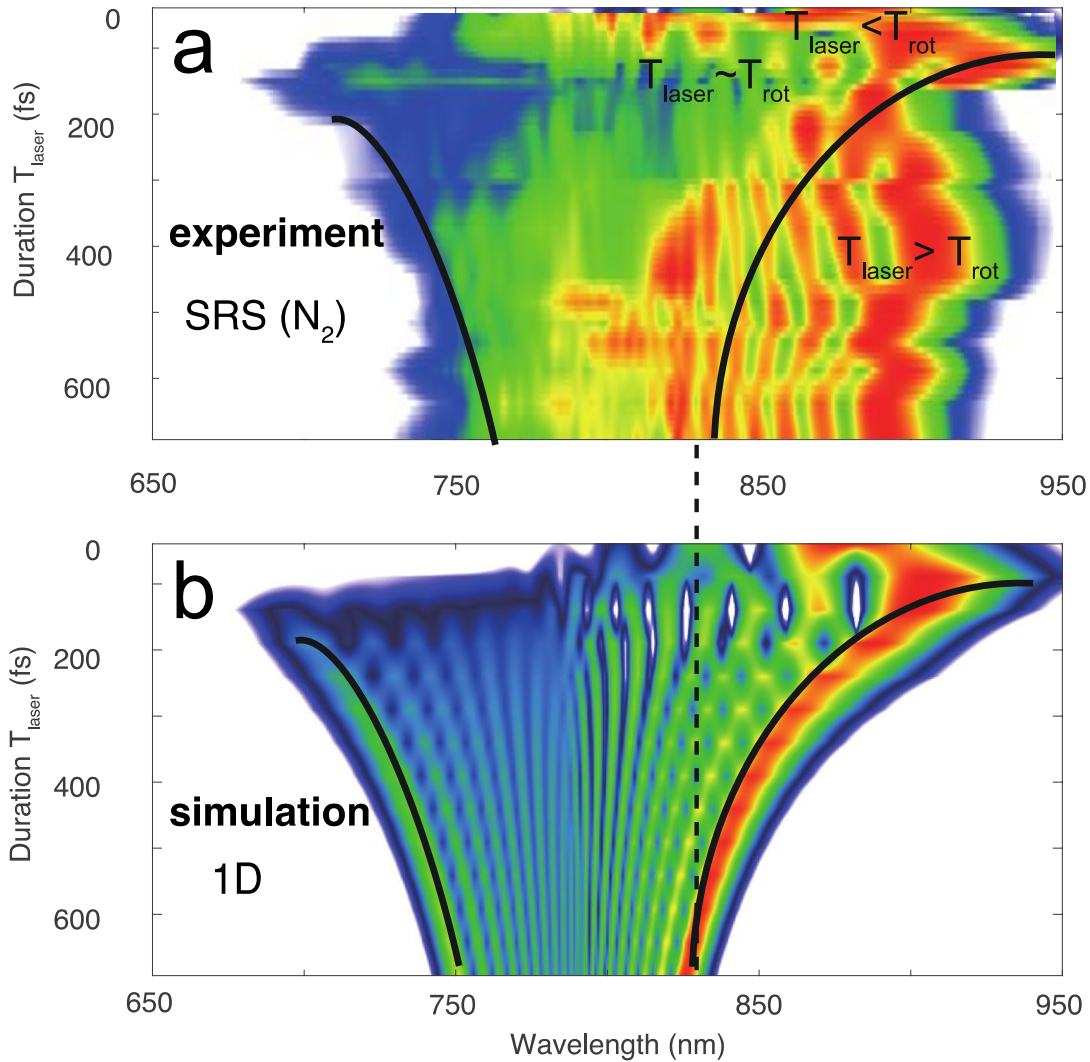


**Figure 22** (a) Experimental results of nonlinear spectral broadening depending on the pulse duration for delayed response medium ( $N_2$ ) at fixed pressure of 760 Torr. (b) The simulation results from the molecular alignment theory predicting low efficiency for the spectral broadening of pulse durations longer than characteristic time ( $T_{rot}$ ) of the molecules which is in strike difference with the experimental results

Therefore, at 100 fs, the 1D model predicts the asymmetric spectra with a highly efficient red-shift exhibiting a dominant contribution of the Raman process, and at longer pulse duration, a more symmetrical broadening of the spectrum would be expected, implying very weak contribution of stimulated Raman scattering (SRS). However, for pulses up to the picosecond domain, the experimental results show asymmetric spectra in  $N_2$  with a highly efficient red-shift exhibiting a dominant contribution of the Raman process which was not predicted by 1D simulations. Therefore, in order to fully understand the observed physics in molecular gas-filled HCF, a more sophisticated numerical study is required that would include highly complex spatiotemporal effects which do not occur in the SPM process. This is demonstrated in the next chapter.



## 4 Nonlinear enhancement through multidimensional interactions

Gas filled hollow core fibers have been developed as an ideal medium for nonlinear interaction of high energy pulses. Much of that development has been focused on the transmission of pulses below critical power of self-focusing for efficient spectral broadening and pulse compression purposes and thus HCF has been optimized for single mode guidance with minimum propagation losses only limited by the intrinsic waveguide loss. The advent of large core stretched HCF (e.g. 6 meters 1 mm core diameter), has opened an avenue for efficient nonlinear interaction of high energy pulses resulting in pulse compression of high energy pulse to few-cycle pulse duration. These developments are pushing the limits of current technology for spectral broadening based on SPM, demanding fibres with larger mode areas and longer length. However, as it is shown in chapter 2, SPM is a dominant nonlinear effect in an effective 1D regime. The SPM nonlinearity is inversely proportional to the pulse duration, making it less applicable for longer pulses. Although, for a given geometry of nonlinear interaction, the efficiency of spectral broadening can be partly compensated by either increasing the medium density or by using a different medium with an higher nonlinearity, self-focusing and coupling to higher order modes (HOMs) remains a fundamental limitation which leads to strong instability and pulse collapse. In this chapter, we demonstrate a new avenue to control HOMs and the consequent instability in HCF which enables exploiting extended multidimensional pathways for nonlinear enhancement. Efficient multidimensional interactions and the creation of stable multimode states with high spatiotemporal coherence and power scalability in large core HCFs is illustrated.

### 4.1 Theoretical basics

In order to design an efficient and compact laser system, to optimize pulse delivery and to control nonlinear applications in the high energy regime, a thorough understanding of pulse propagation and nonlinear interactions in HCF in multimode regime is required. Here, we explain the theoretical model that is used in this thesis to perform multidimensional (MD) simulations.

### 4.1.1 Fiber modes

In general, a given waveguide, defined by the optical potential  $n(x, y)$ , has a number of modes,  $F_p(x, y)$ , which are an orthonormal set, and each of which has a distinct propagation constant  $\beta_p$ , analogous to the different energy or frequency of eigenfunctions in a typical quantum mechanical potential [125]. A hollow core fiber is one of the simplest possible waveguide geometry representing a glass fiber with an air cylinder in its center. Therefore, the boundary conditions that have to be imposed are the ones of a hollow cylinder with a dielectric rim[77]. Due to the symmetry of the problem it is convenient to choose cylindrical coordinates  $\rho$ ,  $\phi$ , and  $z$ . The origin along the radial direction lies then in the center of the inner circle and the  $z$  coordinate lies along the axis of rotational symmetry. In this case, by employing the method of separation of variables, the fiber modes can be obtained by solving the following equation [82]:

$$\frac{d^2 F}{d\rho^2} + \frac{1}{\rho} \frac{dF}{d\rho} + \left( n^2 k_0^2 - \beta^2 - \frac{m^2}{\rho^2} \right) = 0 \quad (33)$$

where  $\beta$  is the propagation constant,  $m$  is an integer,  $k_0$  is wavenumber at central frequency and  $n$  is the refractive index of the core.

Light propagation inside the HCF satisfies the weak guiding condition since the longitudinal component of the electric field is negligible. Therefore, the fields in a practical optical fiber are almost transverse in nature and they can be described as linearly polarized modes ( $LP_{mn}$ ). The first index ( $m$ ) of the LP mode signifies the variation of light intensity in the azimuthal plane i.e. with respect to  $\phi$ . For the lowest order mode, this index turns into 0 because once the direction of the field has been ascertained, the field intensity is constant at all  $\phi$  for a given value of  $\rho$ . The second index of the LP modes indicates the number of zero crossings in the light intensity pattern. The number of zero crossings is one less than the index. Hence  $LP_{01}$  mode has  $(1-1=0)$  no zero crossings in the intensity pattern, though the intensity decreases radially outwards. In  $LP_{1n}$  modes there would be one cycle variation in the light intensity in the azimuthal plane and the number of zero crossings would be  $m-1$ . Thus, under the weakly guiding approximation, the dominant mode of propagation is the  $LP_{01}$  mode. The next mode that propagates is the  $LP_{11}$  mode and in such a way all the consequent modes propagate. Furthermore, there is intrinsic degeneracy for each mode due to the two orthogonal

polarization. Figure 23 shows the intensity pattern of different  $LP_{mn}$  modes. As it is shown, there are several possible field patterns for each mode. For example, when we speak of  $LP_{11}$

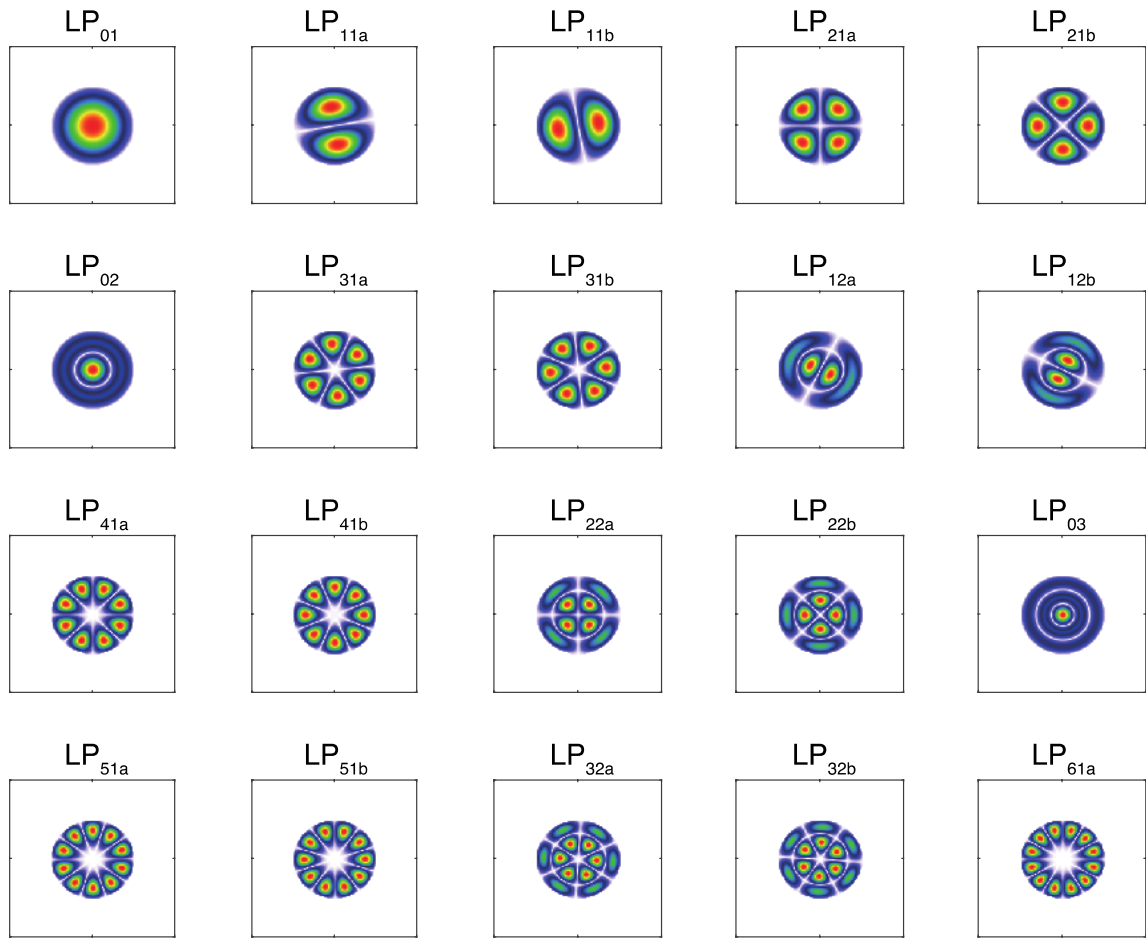


**Figure 23** The intensity patterns of the selected  $LP_{mn}$  modes

mode, we inherently mean four possible field patterns having polarizations (two orthogonal states) and intensity patterns ( $LP_{11a}$  and  $LP_{11b}$ ). Thus, if input pulse of arbitrary polarization has an excitation mode of  $LP_{11}$  when it is launched to the fiber, the light propagating inside the fiber is in fact a combination of the four possible patterns of the  $LP_{11}$  mode propagating simultaneously inside the optical fiber. Similar possibilities also exist for the  $LP_{01}$  mode. The only difference comes due to the circularly symmetric nature of the intensity pattern due to which any angular rotation of the pattern about the axis makes no difference in the intensity pattern but only has a change in the orientation of the polarization.

In the case of linearly polarized pump pulse, nonlinear coupling between orthogonal polarization modes is in principle allowed, leading to, for example, birefringent phase matching

and vector modulation instability. However, since modes can be described as  $LP_{mn}$  modes, if linearly polarized light is launched into the fiber, nonlinear coupling to orthogonal polarization states is effectively so small that most of the pulse energy remains in its original polarization throughout the entire pulse propagation. This allows halving the number of modes to be considered in the model with significant computational advantage, and a simpler definition of the modes overlap factors, presented in the next section.

#### 4.1.2 The Generalized Multimode NLSE

Pulse propagation in single mode fibres is frequently modelled by a generalized nonlinear Schrödinger equation (GNLSE), fully described in chapter 2. This framework has been extremely successful in incorporating all linear and nonlinear effects usually encountered in fibers, such as second and higher order dispersion, Kerr and Raman nonlinearities and self-steepening. Its predictions have been corroborated by numerous experiments using conventional fibers, photonic crystal fibers, hollow core fibers and fiber tapers of different materials, as well as laser sources from the continuous wave regime down to few cycle pulses. Perhaps the most prominent application of the NLSE is in the description of supercontinuum generation where all the linear and nonlinear dispersion effects come together to induce spectacular spectral broadening of light, often over very short propagation distances [126]. For very high power applications, as motivated above, a further extension of the NLSE is required to deal with the multimode aspects of HCF. A very general multimode framework has been presented by Poletti and Horak allowing for arbitrary mode numbers [127]. Here we consider a slightly simplified version, mainly for the sake of reducing the complexity of this description, that is more easily tractable and still is applicable to many realistic situations [128].

Starting from pulse propagating in a multimode regime, the pulse is considered as the product of a carrier wave  $\exp[i(\beta_0^{(0)} z - \omega_0 t)]$ , where  $\omega_0$  is the carrier angular frequency and  $\beta_0^{(0)}$  is its propagation constant in the fundamental fibre mode, and an envelope function  $\mathbf{E}(r, t)$  in space and time. The bold face of quantities in the formula is due to their vector nature and  $r = x, y, z$ .  $\mathbf{E}(r, t)$  is complex-valued consisting of the envelope phase and the amplitude ( $A(r, t)$ ). Here, we consider the pulse evolution in a reference frame moving with the group velocity of the fundamental mode. Note that all units are set in a way that  $|\mathbf{E}(r, t)|^2$  is the field intensity in  $\frac{W}{m^2}$ . The envelope function can then be expanded into a superposition of individual modes  $p = 0, 1, 2, \dots$ , each represented by a discrete transverse fibre mode profile  $F_p(x, y)$  and a modal envelope  $A_p(z, t)$ , as

$$\mathbf{E}(r, t) = \frac{\sum_p \mathbf{F}_p(x, y)}{\left[ \int dx dy |\mathbf{F}_p|^2 \right]^{\frac{1}{2}}} A_p(z, t) \quad (34)$$

where  $|A_p(z, t)|^2$  is the instantaneous power propagating in mode  $p$  in units of Watt.

The generalized multimode nonlinear Schrödinger equations (GMMNLSE) are, then, a system of coupled NLSE-type equations for the electric field temporal envelope for spatial mode  $p$ ,  $A_p(z, t)$ :

$$\begin{aligned} \frac{\partial A_p(z, t)}{\partial z} = & \quad (35) \\ & i(\beta_0^p - \Re[\beta_0^0])A_p - i(\beta_1^p - \Re[\beta_1^0])\frac{\partial A_p(z, t)}{\partial t} + i \sum_{n=2}^{\infty} i^n \frac{\beta_n^p}{n!} \frac{\partial^n A_p}{\partial t^n} + \\ & i \frac{n_2 \omega_0}{c} \left( + \frac{i}{\omega_0} \frac{\partial}{\partial t} \right) \sum_{l, m, n} [(1 - f_R) S_{plmn}^k A_l A_m A_n^* + \\ & f_R A_l S_{plmn}^R \int_0^{\infty} h_R(t) A_m(z, t - t') A_n(z, t - t') dt']. \end{aligned}$$

Briefly, terms 1 through 3 on the right-hand side are the result of approximating the dispersion operator in the mode  $p$  by a Taylor series expansion about  $\omega_0$ , then transforming the terms into the time domain. In general, the modal propagation constants  $\beta^p$  can have complex values where the imaginary part describes mode and wavelength dependent losses;  $\Re [..]$  denotes the real part. The first two terms are expressed relative to the lowest-order longitudinal phase evolution and group velocity of the fundamental mode. The third term represents higher-order dispersion effects (group velocity dispersion, third-order dispersion, etc.). The fourth represents the effects of optical nonlinearity with a nonlinear refractive index  $n_2$ . The term  $\frac{i}{\omega_0} \frac{\partial}{\partial t}$  describes self-steepening and the two terms within the sum describe Kerr and Raman nonlinearities.  $h_R$  is the Raman response of the fiber medium and  $f_R$  is the Raman contribution to the Kerr effect which are calculated through the molecular alignment theory presented in the previous chapter.  $S_{plmn}^k$  and  $S_{plmn}^R$  are the nonlinear coupling coefficients for the Raman and Kerr effect respectively [128]. For many practical situations, we can significantly simplify the tensors by assuming that the modes excited are in a single linear polarization and neglecting spontaneous processes which may cause coupling into these modes. In this case, we have:

$$S_{plmn}^k = S_{plmn}^R = \frac{\int dx dy F_p F_l F_m F_n}{[\int F_p^2 dx dy \int F_l^2 dx dy \int F_m^2 \int F_n^2]^{1/2}} \quad (36)$$

where given the fact that we use a linearly polarized light into the HCF, it is sufficient to express each mode in terms of a real scalar function  $F_p(x, y)$ .

#### 4.1.3 The concept of the spatiotemporal nonlinear enhancement

The GMMNLSE is based on the fact that the modes are orthogonal, and we are working in mode space. In real space (x and y), the 3+1-D Schrödinger equation, can be used [129]:

$$\begin{aligned} \frac{\partial A(x, y, t; z)}{\partial z} = & \frac{i}{2\beta(\omega_0)} \nabla_T^2 A - \frac{i\beta_2}{2} \frac{\partial^2 A}{\partial t^2} + \frac{i\beta(\omega_0)}{2} \left[ \left( \frac{n(x, y; z)}{n_0} \right)^2 - 1 \right] A \\ & + \frac{in_2\omega_0}{c} |A|^2 A \end{aligned} \quad (37)$$

where  $\nabla_T^2 = \frac{\partial}{\partial^2 x} + \frac{\partial}{\partial^2 y}$  is the Laplacian for the transverse coordinates (x and y, being orthogonal or transverse to the 'long', or 'evolution', coordinate z), and the Raman contribution is neglected.

The last term represents the optical Kerr nonlinearity. The nonlinear term modifies the phase of the field in space and time, and the amount it modifies the phase is larger where  $|A|^2$  is larger. Recalling that  $|A|^2$  is the intensity (in  $W/m^2$ ), this can be interpreted as an 'intensity-dependent refractive index':

$$n(x, y, t; z) = n_0(x, y; z) + n_2 |A(x, y, t; z)|^2 = n_0(x, y; z) + n_2 I(x, y, t; z). \quad (38)$$

In practical situations, as a starting reference point, the focal spot size at the HCF input pulse is chosen for obtaining high coupling efficiency into the fundamental mode ( $LP_{01}$ ). Noted that all  $LP_{0n}$  are peaked functions. Therefore, the nonlinear term acts a like a lens. In general, a lens shape introduces an inhomogeneous phase front to an incident field which is largest at

the center of the lens, and decreasing towards the edges. Besides, the nonlinear index is self-generated, which means that, through the medium, light affects itself, which effects its propagation, which affects its effect on itself, etc. A nonlinear self-lens, for example, does not have a fixed focal length. Instead, as the field focuses and becomes more and more intense, the focal length of the nonlinear self-lens becomes shorter and shorter.

This is the essence of nonlinearity. Especially in long fibers and/or with high intensity pulses, the cumulative effects of nonlinearity on the behavior and propagation of light are positively enormous, even when their effect at any given instant is rather small. This should be interesting enough. However, one additional difference between the nonlinear perturbation to the refractive index should be considered. While it is easy to imagine an optical component for which  $n(x, y)$  varies in space, it is much more special to have such a variation in space-time. Something like this may be called spatiotemporal.

The beauty of GMMNLSE equations is the fact that mode space allows us to gain more physical insight about spatiotemporal interactions. In mode space, self-focusing in the HCF is interpreted as the transfer of energy from the fundamental mode ( $LP_{01}$ ) to other  $LP_{0n}$  modes which have rotational symmetry with the maximum intensity in the central part [16]. In the high-energy regime, the effects of self-focusing and diffraction become significant and multiple  $LP_{0n}$  modes can be created at the beginning of the fiber. These extended multidimensional pathways lead to nonlinear enhancement. The simulations based on GMMNLSE are performed by employing a set of  $N$  (numbers of modes) coupled nonlinear equations[128]. These equations are coupled to each other by four-dimensional nonlinear coupling tensors for Raman ( $S_{plmn}^R$ ) and Kerr nonlinearities ( $S_{plmn}^K$ ) since a cubic nonlinearity couples up to four distinct waves. Although with multiple coupled modes, the physics can be conceptually complex, the extended intermodal nonlinear interactions (expanded nonlinear terms in each equation via  $S_{plmn}^R$  and  $S_{plmn}^K$ ) provide many pathways to enhance different nonlinear phenomena. For example, if we assume only the first three modes of  $LP_{0n}$  are excited,  $3^4$  terms are contributing in the Kerr nonlinearity term. Thus, we can expect enhanced nonlinearity compared to 1D regime where only one term contributes to Kerr nonlinearity.

#### 4.1.4 Four wave mixing (FWM)

Fundamentally, nonlinearity introduces coupling between the different modes, and is incorporated in the last term(s) of the GMMNLSE. The origin of FWM lies in the instantaneous nonlinear Kerr response of bound electrons of a material to an electromagnetic field.  $S_{plmn}^K$

describes the nonlinear mode coupling due to Kerr nonlinearity in GMMNLSE. Self-phase modulation (SPM) corresponds to  $S_{pppp}^K$  and terms of the form  $i|A_p|^2 A_p$  with effective areas of  $A_{eff} = 1/S_{pppp}^K$  for each mode. Terms with  $S_{pnpn}^K$  or  $S_{ppnn}^K$ , where  $n \neq p$ , are of the form  $i|A_n|^2 A_p$ . These are cross-phase modulations (XPM).

All other nonlinear coupling terms can be described as “four-wave mixing” (FWM), which are the terms that can cause transfer of energy. It should be noted that XPM and SPM are degenerate forms of FWM. We can understand FWM as the scattering between four waves due to the nonlinear index modulations created by their interference. Here the medium plays a catalytic role and optical momentum conservation is required for nonlinearities to build up. In multimode regime, the presence of multiple propagating modes with different dispersive properties and momenta results in expanded phase-matching combinations for the generation of FWM signals [130]. The conditions for FWM processes are that (conservation laws: energy and momentum):

$$\omega_1 + \omega_2 - \omega_3 - \omega_4 = 0 \quad (39)$$

$$\Delta\beta = \beta_4(\omega_4) + \beta_3(\omega_3) - \beta_2(\omega_2) - \beta_1(\omega_1) = 0.$$

Practically, the phase-matching requirements show that there are many degrees of freedom for controlling a FWM process in a highly-multimode fiber. We may be interested in controlling the generated frequency, the generated mode, the bandwidth of the four-wave mixing process, or some features of the generated photon’s correlations/entanglement. Therefore, by adjusting the input coupling conditions at the HCF input, controlling the dispersion and nonlinearity of the medium by changing the gas pressure, one has a significant degree of control over the modes or frequencies of the contributing waves. One can also control the rate of change of  $\Delta\beta$  near 0, so as to affect the bandwidth, or range of frequencies, generated by the FWM process.

## 4.2 Spatiotemporal dynamics in Raman active medium (N<sub>2</sub>)

So far, nonlinear propagation in atomic gas-filled HCF is fundamentally limited due to the self-focusing effect at high peak power (comparable with the critical power) and inherent diffraction [16]. This causes the beam to couple to higher-order modes (HOMs) and induces instability

as it propagates through the HCF. We find that by controlling the spatiotemporal interactions in HCF, it is possible to balance the diffraction by the spatiotemporal nonlinearity which can lead to the generation of multidimensional solitary states. In gas-filled hollow-core fibers (HCF), the modal dispersion and losses scale inversely with the second and third power of the core size, respectively[77]. Consequently, large core size (200~1500  $\mu\text{m}$ ) HCFs provide ultra-low modal dispersion and small losses. Besides, gases provide an extra degree of controllability since their nonlinearity and dispersion can be tuned by varying the pressure and gas mixture[78]. They also offer wide window of transparency extending from the vacuum ultraviolet[79] to the mid-infrared spectra range[19]. Thus, gas-filled HCFs offer a new platform for efficient, tunable and power scalable multidimensional interactions with ability to create stable high-energy multidimensional states. Although a considerable body of work exists on nonlinear process through conventional 1D interactions in hollow core waveguides[17-19], efficient multidimensional interactions and creation of stable multimode states with high spatiotemporal coherence and power scalability in large core HCFs have not been demonstrated.

In this section, we demonstrate the generation of multidimensional solitary states (MDSS) in a large core HCF filled with nitrogen ( $\text{N}_2$ ). The experimental results and the numerical simulations indicate that the coupling to multimode states by high-energy driver pulses at HCF input favors the stimulated Raman scattering (SRS) process in a Raman active medium. Consequently, the enhanced spatiotemporal nonlinearity inhibits the potential diffraction due to self-focusing, leading to a high quality spatial localization of multidimensional states. The generated self-trapped MDSS at the beginning of the fiber undergo an enhanced Raman cascading process over the long interaction length of the HCF, resulting in broadband, red-shifted spectra at the HCF output.

In the experiment, 700 fs, high-energy pulses (5 mJ /pulse) with a central wavelength of 780 nm were launched into a 3 m long hollow-core (500  $\mu\text{m}$ ) fiber filled with  $\text{N}_2$ . The 700 fs pulses are obtained by positively chirping 40 fs pulses from a Titanium-Sapphire amplifier. The solitary states are experimentally separated from the pump part by placing a long pass filter (above 830 nm) at the HCF output (the pump part is selected by a band-pass filter (760nm-790nm)). The spectra at the output of the HCF were measured with a VIS/NIR spectrometer (Avantes, AvaSpec-ULS2048XL). The spatial profile of the beams (pump and MDSS) was captured using a CCD camera (PointGrey, FLEA).

We now observe enhanced red-shifted spectra in  $\text{N}_2$  with stable spatial properties at peak powers comparable to the critical power for self-focusing (red curve in Figure 24(a)). The spectra extend towards much longer wavelengths than the prediction from 1D simulations

(green curve). The stability of the self-trapped MDSS is demonstrated in Figure 24(b) with 8 consecutive single-shot far-field images. This is in strong contrast to the high instability observed for the pump part and caused by the nonlinear interactions and competition between HOMs (see Figure 24(c)). To illustrate the

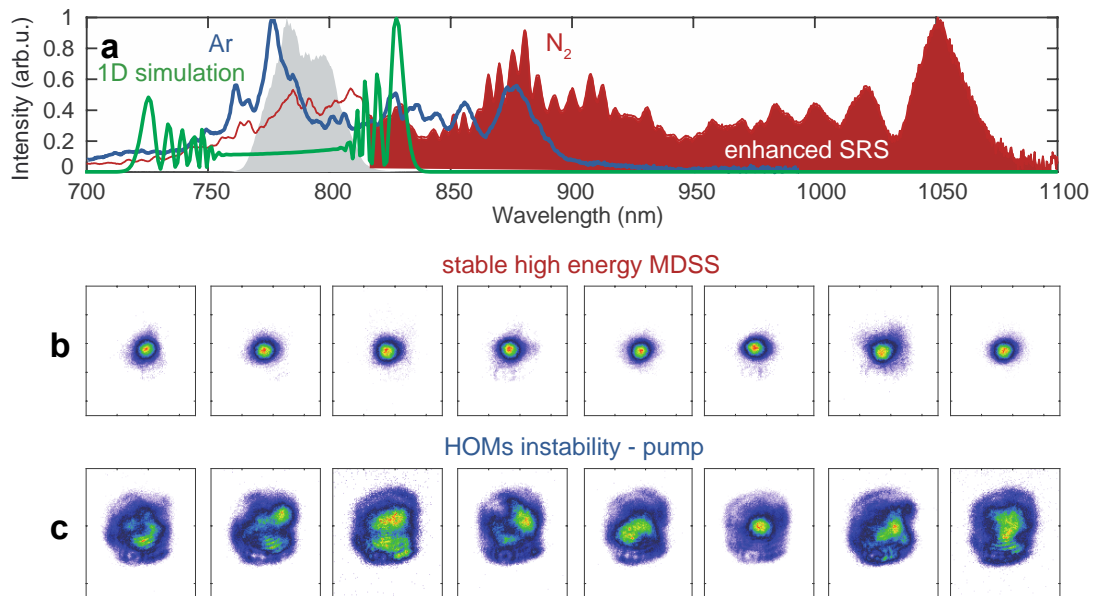


**Figure 24** The measured spectra for the 700 fs input pulses after the N<sub>2</sub>-filled HCF (3 bar) indicating the enhanced red-shifted spectra through SRS (red part). The green curve is the pump spectra at the fiber input. (b) These figures illustrate the MDSS spatial profile (obtained by putting an 830 nm long-pass filter after the fiber) for 8 single-shot consecutive pulses demonstrating the self-trapped, highly stable, and clean beam. (d) These figures report the same measurement for the fundamental beam (obtained using a band-pass filter (760nm-790nm)) indicating strong spatial instability and coupling to HOMs.

importance of the SRS process for the observed self-trapping effect, the measured spectra for argon (Ar) (Raman inactive medium) at the same conditions is shown as the blue curve in Figure 24(a). The output spectra are much narrower compared with N<sub>2</sub> which indicates no enhancement effect. In addition, self-focusing and multiple filamentation make this regime undesirable in the absence of the SRS process. Therefore, the coupling to multidimensional states together with the SRS process provides a unique regime in which the self-trapped solitary states can be created at peak powers comparable with the critical power for self-focusing.

#### 4.2.1 Comparison with simulations

As it is indicating in the previous chapter, the 1D simulations fail to reproduce the asymmetric

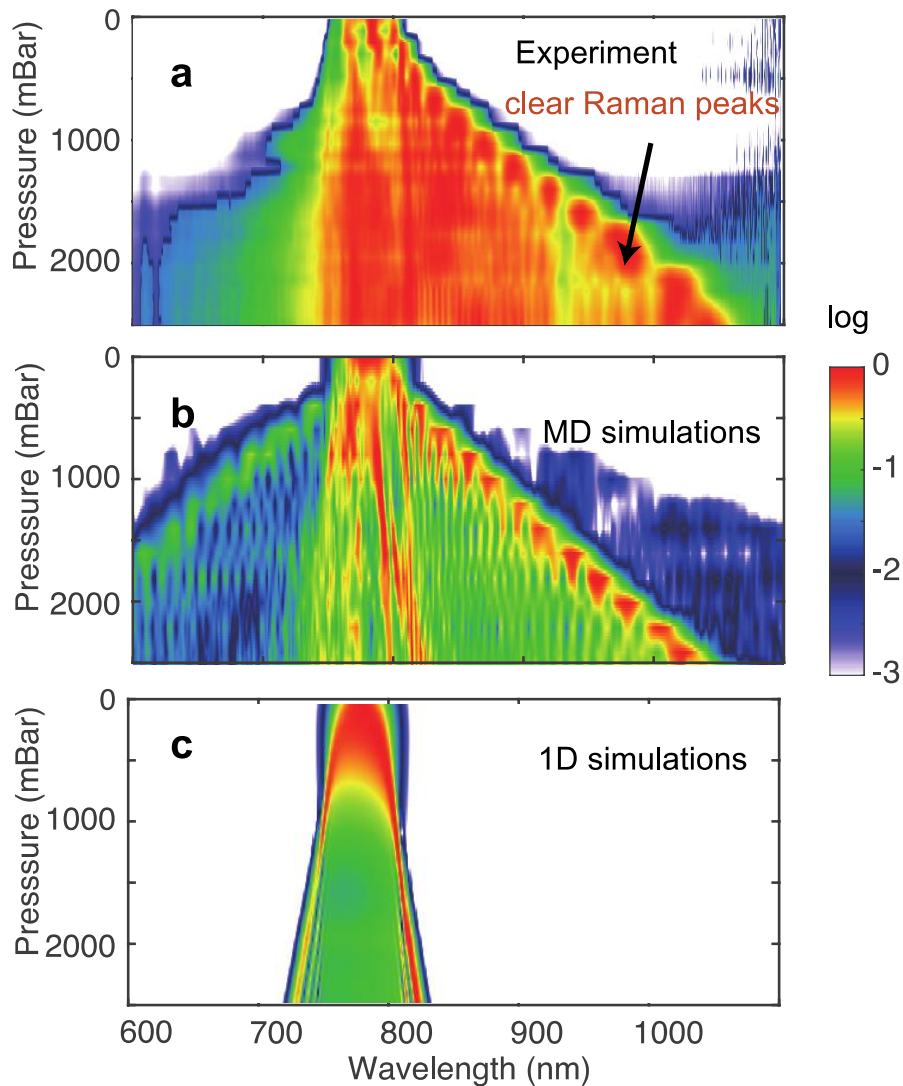


**Figure 25** (a) Measured spectral broadening evolution versus gas pressure. The SRS process is dominant and the red-shifted spectra of MDSS reach the longest wavelengths with sharp Raman peaks. Simulation results by solving the generalized multimode nonlinear Schrödinger equations (GMMNLSE) by considering 15 linearly polarized modes called MD simulations (b) and by considering only one mode, called 1D simulation (c). The MD simulations nicely reproduced the experimental results while 1D simulations predicts very narrow spectrum even at highest gas pressure.

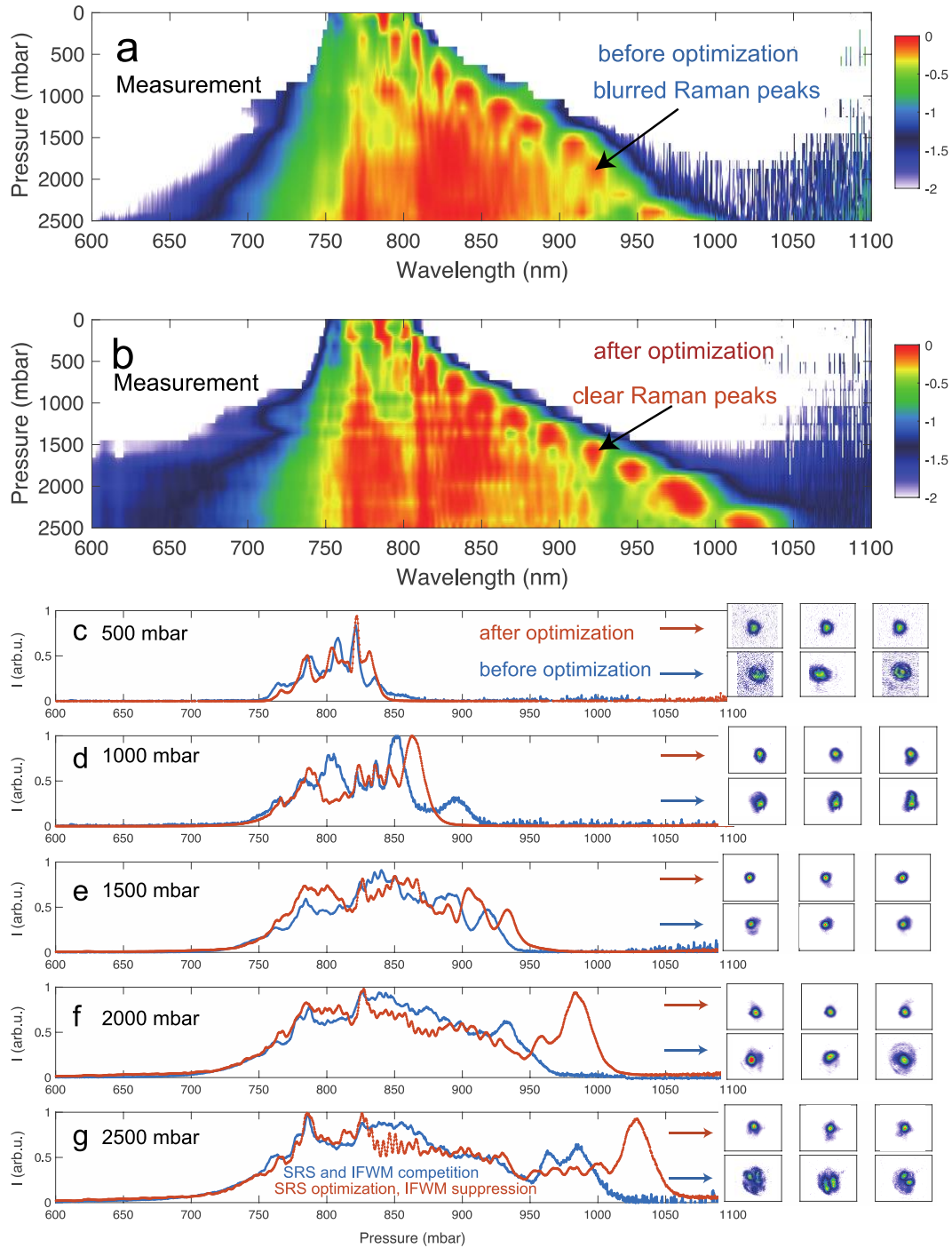
spectra arising from a highly efficient red-shift exhibiting an effective contribution of the Raman process for input pulse duration far from the timescale for maximum nonadiabatic molecular alignment. This is due to the fact that the instantaneous bandwidth of 700 fs pulses is too narrow to cover the rotational excitation step of  $N_2$ . Thus, in 1D regime, the broadening is dominated by the Kerr nonlinearity resulting in a symmetric spectrum (see Figure 17). Therefore, to fully understand the physics of our experimental observation, a more sophisticated numerical study is required that includes highly complex spatiotemporal effects arising from the mode coupling. The measured spectra for different pressures are presented

in Figure 25(a). These results are well reproduced by MD simulations (Figure 25(b)) and demonstrate the clear signature of the rich dynamics originating from extended multidimensional intermodal pathways. In contrast, the 1D simulations cannot reproduce the enhanced red-shifted spectra since the instantaneous frequency bandwidth of the fundamental mode (the only mode in the simulation) is too narrow to cover the Raman gain bandwidth. Thus, nonlinear propagation in 1D regime is dominated by self-phase modulation. The spectral bandwidth obtained from the 1D simulations are presented in Figure 25(c).

#### 4.2.2 Optimization of HCF input coupling conditions

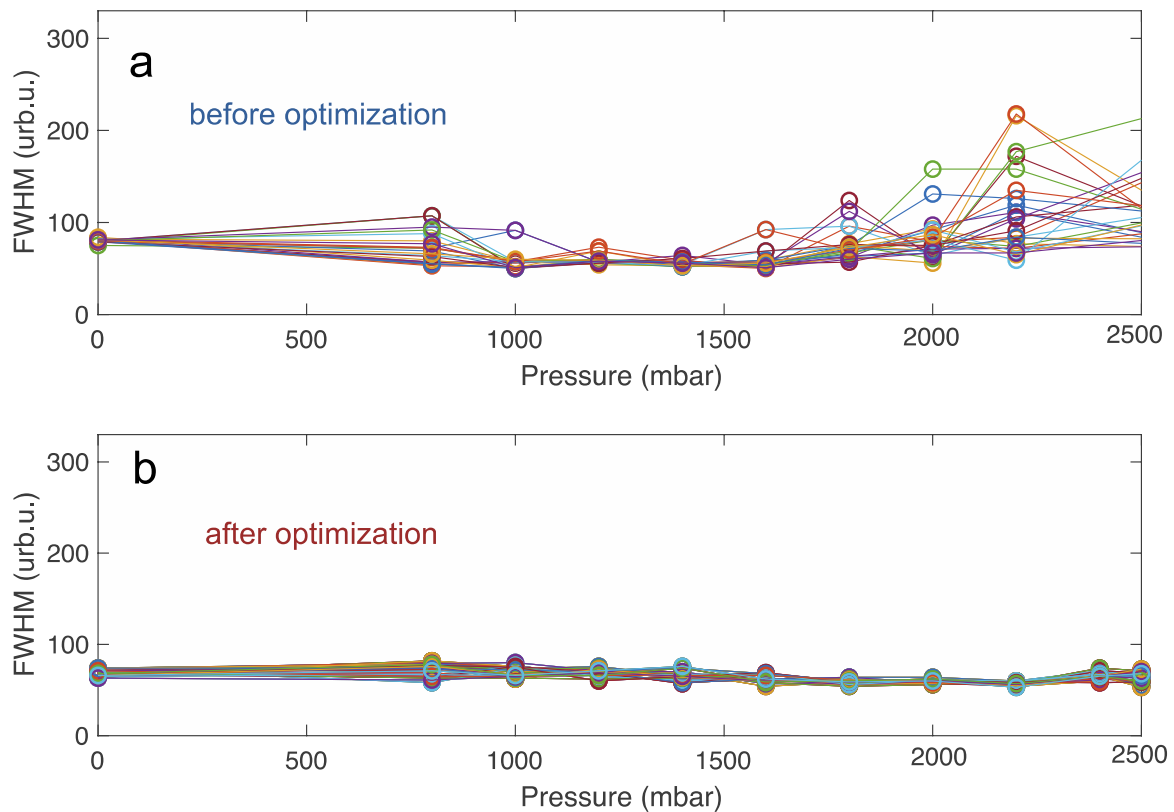
The coupling of the pump part to HOMs provides many new pathways to phase-match other nonlinear phenomena such as intermodal four wave mixing (IFWM), modulation instability (MI) and dispersive waves (DW) [131] which can suppress the SRS process as well as create instabilities in the spatial beam profile of the red-shifted beam [130]. Most importantly, the competition between SRS (active gain process) and IFWM may occur when sufficient phase-matching pathways are established in favor of the latter, and the SRS gain may increase or decrease from its value, depending on the amplitude of phase-matching ( $\Delta k$ ).

Figure 26 illustrates the generation of on-demand self-trapped states by adjusting the HCF input coupling conditions. In practice, it was controlled by adjusting the angle and position of the HCF entrance relative to the launched beam, while monitoring simultaneously the broadened spectra and the beam stability. To show experimentally the (negative) effect of IFWM across MDSS, we recorded the spectral evolution as a function of gas pressure (Figure 26(a)) before optimization. Up to 1 bar, the SRS beam with distinguishable red peaks and a clean spatial profile is generated in the  $LP_{0n}$  family. By further increasing the pressure, thus reducing the critical power, the pump is coupled more and more to HOMs (other than  $LP_{0n}$  family) creating new pathways to phase-match IFWM. Thus, through the IFWM process, new frequencies, generated in the red part of the spectra, can propagate in different modes based on satisfying  $\Delta k$ , and they start to build up across the MDSS spectral range resulting in blurred SRS peaks. Thus, to drive very efficiently the cascade of the Raman process and to get a clean spatial MDSS, IFWM that leads to generation of HOMs (other than  $LP_{0n}$  family) across MDSS has to be suppressed by inducing a phase-mismatch. This is experimentally realized by adjusting the input coupling conditions to optimize the extension of the spectra towards the red and the spatial properties of the MDSS. For argon (Ar) on the other hand, we did not observe any enhancement in stability and spectral broadening by tuning the HCF input conditions (see section 4.3). This comes as no surprise since the observed effect in  $N_2$  results from the interplay of IFWM and SRS, and for Ar there is no Raman effect. The output spectra



**Figure 26** Demonstration of the optimization of MDSS stability and SRS process via the input coupling conditions. Measured spectral broadening evolution versus gas pressure before (a) and after (b) optimization. By suppressing IFWM, the SRS becomes dominant and the red-shifted spectra of MDSS reach the longest wavelengths with sharp Raman peaks. (c)-(g) The spectra for different pressures before (blue line) and after optimization (red line) of the HCF input coupling conditions. For each pressure, 3 consecutive single shot far-field images of the red-shifted beam (selected with a long pass filter at 830 nm) are shown for both conditions (top: after optimization, bottom: before optimization) to emphasize the role of the optimization process in the suppression of intermodal four wave mixing (IFWM).

and stability of the beam profile depending on the gas pressure is illustrated in Figure 26(c)-(g) before and after the optimization by showing 3 single-shot far-field images. The retrieved beam diameter (in arbitrary unit) of the red-shifted MDSS beam before and after optimization as a function of pressure is shown in Figure 27. As is illustrated, the suppression of IFWM not only brings stability to the SRS beam but also enhances the SRS process via spatiotemporal intermodal interactions. This leads to sharp SRS peaks with spectra extending to the longest wavelength. Note that the SRS spectra at optimized conditions have clean modulations that originate from the cascaded SRS process.



**Figure 27** The mode diameter (arbitrary unit) of the red-shifted MDSS beam for 20 shot to shot images per pressure (a) before and (b) after optimization. This figure demonstrates that the suppression of IFWM results in a clean MDSS beam at the HCF output. This is due to self-trapping in modes of the  $LP_{0n}$  family with confined rotational symmetry.

#### 4.2.3 Phase construction and pulse compression

Now, we investigate the temporal properties of the output MDSS. For this purpose, we used time-frequency analysis (Wigner function) which provides a conceptual guide to interpret the complex spatiotemporal interactions. Figure 28(a) indicates the expected Wigner function of

the output pulses from a 1D simulation. The 1D simulations always predict a positive chirp as the pulses propagate nonlinearly in the HCF indicating dominant Kerr nonlinearity (no Raman enhancement). On the other hand, the Wigner distribution of the output pulse from MD simulations illustrates a different time-frequency structure, building up a dominant negative chirp for the MDSS pulses at the HCF output (Figure 28(b)). This is mainly because the

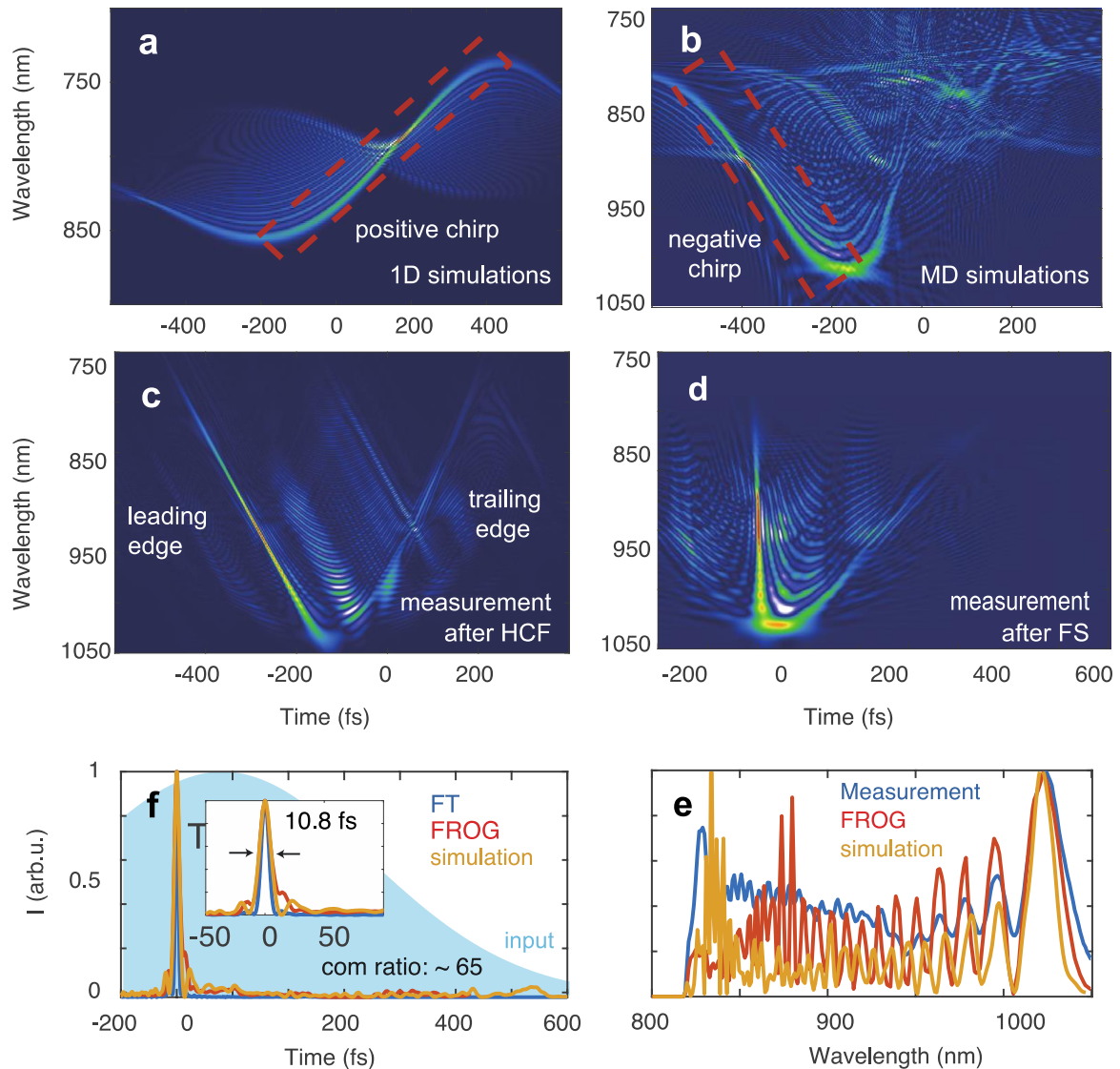


**Figure 28** Temporal evolution of the self-trapped MDSS driven by 5 mJ 700 fs pulses at 2500 mbar. (a) and (b) Wigner functions of the output pulse at HCF output predicted by 1D simulations and MD simulations, respectively. The outcome of 1D simulations predicts a positive quadratic phase for the output pulse since nonlinear propagation is dominated by SPM. (c) The Wigner function of the retrieved experimental SHG-FROG trace, directly measured at the output of the HCF. It shows the dominant negative quadratic spectral phase at the leading edge of the pulse, which contains the majority of the energy. This is in very good agreement with the results of MD numerical simulations. (d) The corresponding Frequency and temporal analysis of the compressed pulse with a piece of FS (12 mm). (f) Measured and MD-simulated temporal profile of the compressed pulse. (e) A comparison of the spectra measured with the spectrometer, retrieved from the SHG-FROG reconstruction of the 10.8 fs pulses, and from MD numerical simulations.

coherent rotational response of the molecular gas develops very slowly. This leads to an effective negative “chirp” for MDSS which experiences an enhanced Raman nonlinearity. Figure 28(c) shows the Wigner function of the output pulses from the reconstructed SHG-FROG trace. These results are in good agreement with MD simulations, indicating the localization of MDSS at the leading edge of the driver pulse with a negative chirp. Consequently, MDSS are post-compressed experimentally down to 10.8 fs by propagating through a piece of fused silica (FS) glass (positive GVD below 1.3 microns) (Figure 28(d)). Figure 28(e) shows the temporal characterization of the compressed pulses, which agrees well with the results from MD numerical simulations. The corresponding spectra are presented in Figure 28(f). It is noted that the ratio between the pump pulse duration and the compressed red-shifted MDSS pulse duration,  $\sim 65$ , is much higher than what is achieved with pulse compression schemes based on Kerr nonlinearities under the same HCF geometry [69].

#### **4.2.4 The efficiency of MD interactions with narrowband sub-picosecond pump pulses**

To confirm the fact that driving the SRS process through multidimensional solitary states in HCF is only related to the temporal profile of the input pulses, we have performed MD simulations (spectral broadening as a function of pressure) for both narrowband sub-ps pulses and positively chirped broadband pulses (40fs stretched to 700fs). Since the change of the refractive index only depends on the convolution of the pulse intensity profile with the Raman response time, the results show that the spectral broadening is almost independent of the spectral phase of the input pulses (see Figure 29(a, b)). This confirms that this technique is promising to compress sub-picosecond Ytterbium laser systems[53, 69, 132].

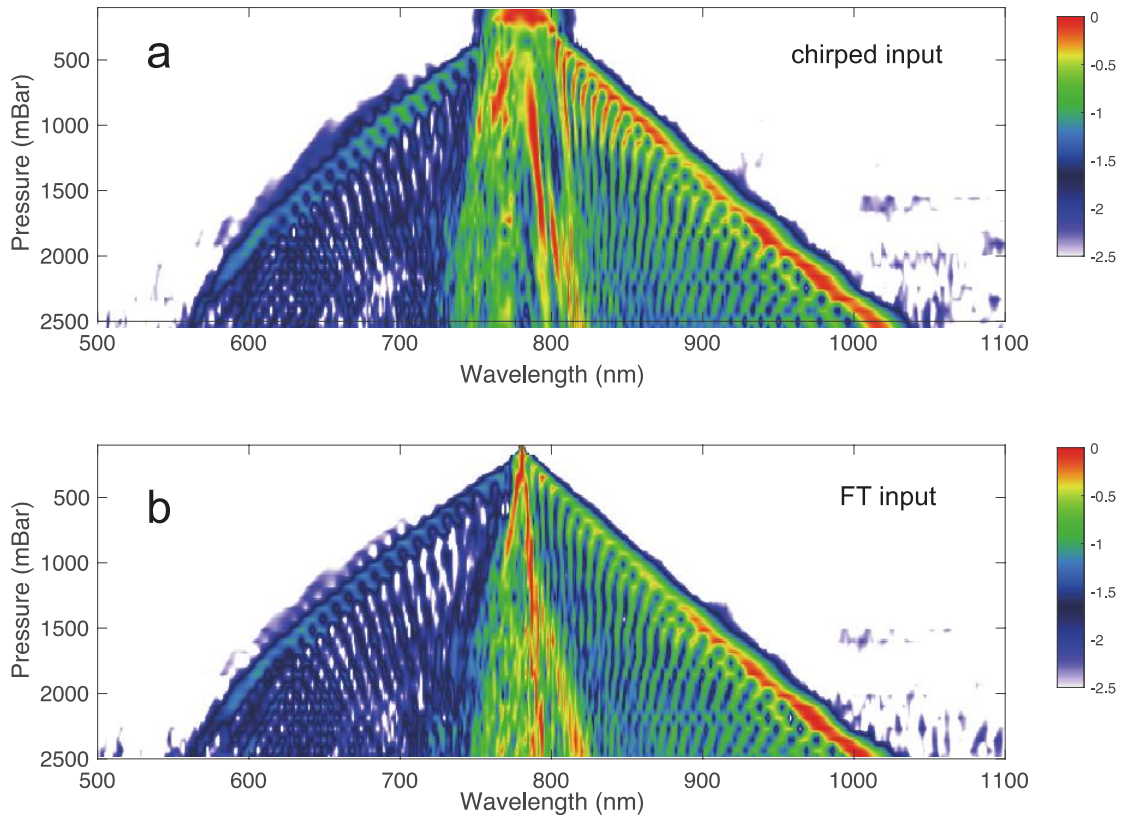


**Figure 29** MD numerical simulations of spectral broadening as a function of pressure for (a) positively chirped input pulse (40 fs stretched to 700 fs with positive chirp) and (b) 700 fs narrowband Fourier transform limited pulses (FT) with the same peak power.

#### 4.2.5 Spatiotemporal enhancement at maximum alignment regime

In previous section, we have performed the experiments with 700fs driving pulses to highlight the role of spatiotemporal dynamics for red-shifted spectral broadening via SRS. Since we are in a regime of nonlinear interaction close to critical power, we were also expecting the contributions of spatiotemporal dynamics for the red-shifted spectral broadening of ~120fs input pulses.

In Figure 30, we present MD and 1D simulations together with experimental results using narrowband 120fs pulses (obtained by spectral filtering of the 40fs Ti-Sa pulses) coupled to the HCF. As it is discussed in the previous chapter, 1D simulation can nicely reproduce the asymmetry shape of the spectral broadening at the maximum alignment regime. However, the efficiency of the broadening is not predicted by 1D simulation. The simulation results clearly illustrate the very efficient spectral broadening when driving the SRS at maximum Raman gain and the role of multidimensional solitary states to drive even more efficiently the nonlinear

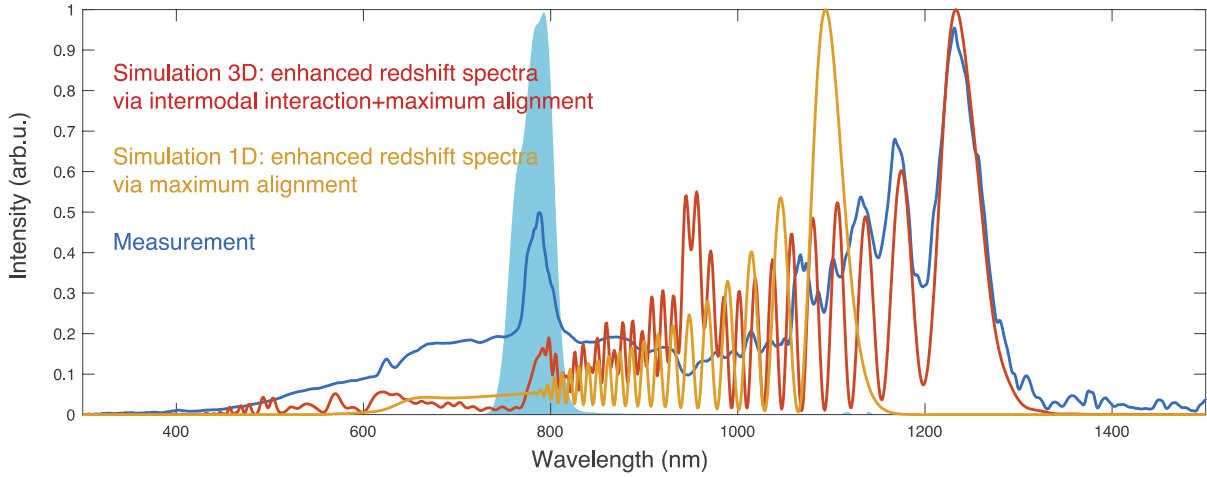


**Figure 30** Spectral broadening for Fourier transform limited 120fs input pulses (filled spectra in light blue) with energy of 1.5mJ/pulse at 4000 mbar of pressure. Yellow: 1D numerical simulation. Red: MD numerical simulation. Blue: Broadened spectra experimentally measured at the HCF output. The 3D and the 1D simulations reveal red-shifted spectral broadening through maximum Raman gain, but 3D is further enhanced through the contributions of multidimensional solitary states.

propagation. Since we have two types of the enhancement in this regime, very broadband red-shifted spectra, spanning from 600 nm to above 1300 nm, are obtained in this regime.

In maximum alignment regime, the measured and simulated self-trapping evolution and energy distribution of different modes of the pump and MDSS for different pressures are illustrated in Figure 31. Through the nonlinear propagation and multimodal coupling in the HCF, a transfer of energy from the pump pulses centered at the fundamental wavelength to the red-shifted MDSS occurs. Figure 31(a) displays the experimental and MD numerical results of the photon conversion efficiency (CE) from pump to MDSS versus pressure. Up to 1 bar, the pump depletes rapidly while the MDSS energy grows exponentially. By further increasing the pressure, this process becomes slower owing to the spatiotemporal walk-off between the MDSS and the pump. Figure 31(b) and (c) illustrate the simulation results of the energy exchange among 8 individual modes in the MDSS and the pump part, respectively. This indicates that the MDSS beam is self-trapped into  $LP_{01}$ ,  $LP_{02}$  modes (creating multidimensional solitary states) with periodic energy exchange between them due to the extended intermodal dynamics[16, 133].

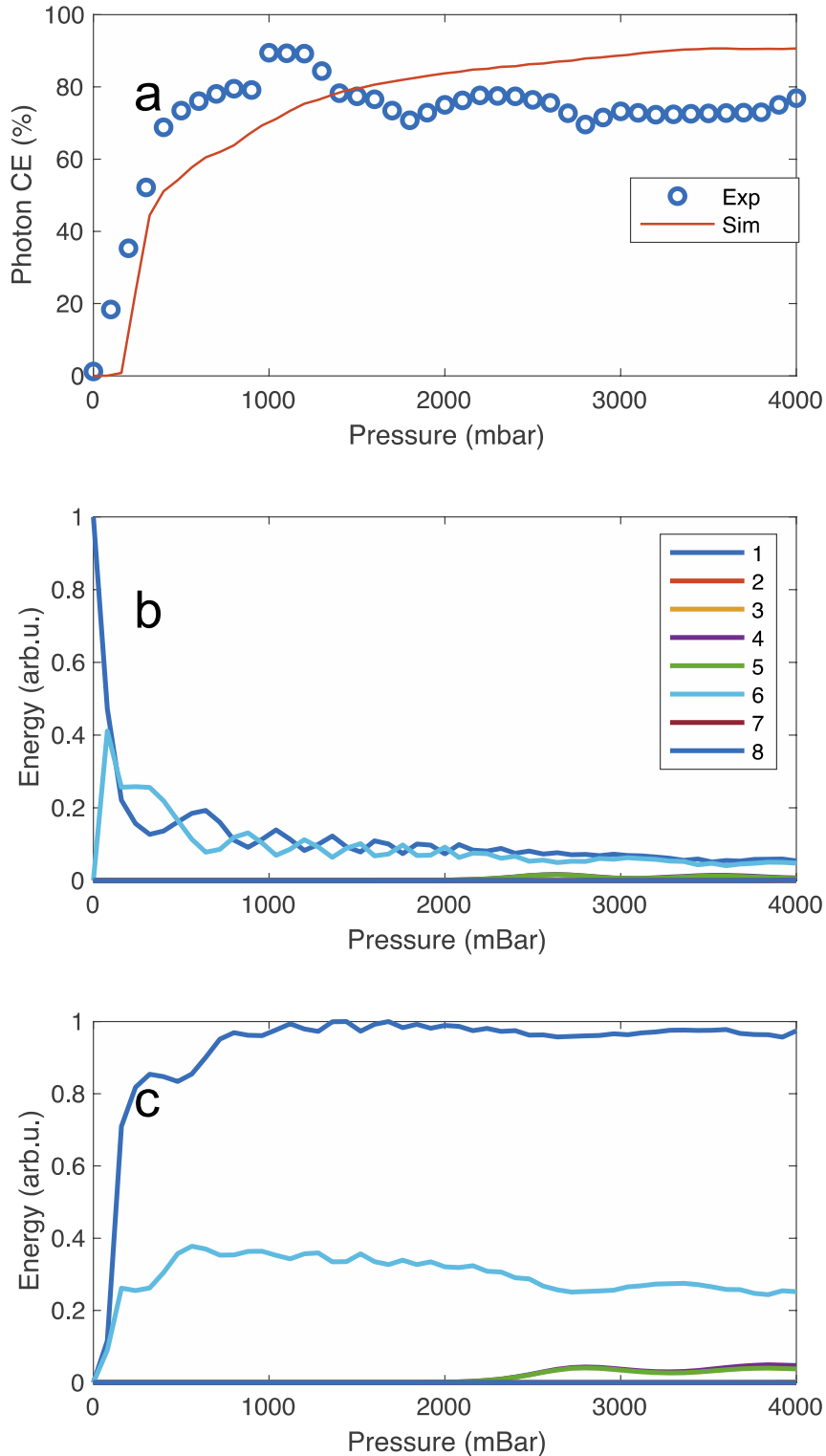


**Figure 31** Modal evolution of the self-trapped SRS beam at maximum Raman gain using 120fs input pulses with 1.5 mJ energy (a) Photon conversion efficiency (CE) from pump to SRS pulse for experimental (dot-blue) and simulation results (solid-red line). (b)-(c) MD simulation results for the energy distributions among 8 modes at SRS beam and pump part. Here mode index (1-8) correspond to LP<sub>01</sub>, LP<sub>11a</sub>, LP<sub>11b</sub>, LP<sub>21a</sub>, LP<sub>21b</sub>, LP<sub>02</sub>, LP<sub>31a</sub>, LP<sub>31b</sub> modes, respectively.

### 4.3 Spatiotemporal dynamics in Raman inactive medium (Ar)

In this section, we show results (both numerical and experimental) where Ar is used as the filling gas in the HCF. These results demonstrate that for the multidimensional (MD) regime, there is a significant difference of spectral broadening efficiency and spatial properties at the HCF output for a Raman inactive medium (Ar) compared to N<sub>2</sub> (presented in the previous section).

The measured and simulated spectra as a function of pressure for an input pulse duration of 700 fs (Ti-Sa positively chirped pulses) in Ar is shown in Figure 32(a-c). Compared to N<sub>2</sub> (Figure 24), we do not observe enhanced red-shifted spectral broadening since the medium is Raman inactive. For Ar, the dominant nonlinear phenomenon is four wave mixing (FWM). The origin of FWM lies in the instantaneous nonlinear Kerr response of bound electrons of a material to an electromagnetic field. In the single mode regime (1D system), the nonlinear propagation is dominated mainly by the FWM process of self-phase modulation (SPM). In the multimode regime (MD system), the presence of multiple propagating modes with different dispersive properties results in expanded phase-matching combinations for the generation of FWM signals which is called intermodal FWM (IFWM). For the 1D regime, the broadening efficiency through SPM is inversely proportional to the input pulse duration, making it less applicable for longer pulses. This is consistent with 1D simulations for Ar presented in Figure 32(c). For a given geometry of nonlinear interaction, the efficiency of spectral broadening can be partly compensated by either increasing the medium density or by using a different medium with a higher nonlinearity. By increasing the pressure, this increases the probability for the fundamental mode to couple to higher order modes (HOMs) as the peak power approaches the critical power. Figure 32(b) presents the MD simulations for Ar where the dominant spatiotemporal nonlinear effect is IFWM. While comparing the 1D and MD simulations for Ar, we observe difference in the spectral features but not in the level of spectral broadening, indicating the key role of SRS together with MD dynamics to explain the spectral broadening in N<sub>2</sub>. For Ar, the multidimensional regime results in no additional significant spectral broadening compared to N<sub>2</sub>. In addition, in this regime, self-focusing is detrimental as it couples energy to HOMs resulting in the degradation of the spatial properties and high instability at HCF output. Self-focusing is interpreted as the transfer of energy from the fundamental mode to the LP<sub>0n</sub> with smaller beam diameter compared to the fundamental mode[134]. In the absence of active nonlinear process such as stimulated Raman scattering (SRS), intense LP<sub>0n</sub> beams couple to other HOMs, and the beam spread out among many modes. Experimentally, this has been verified by monitoring the beam diameter in the far field at the HCF output. The single-shot beam diameter is presented in Figure 33. While below

2000 mbar the beam profile is stable, above this pressure, we observed highly unstable conditions.

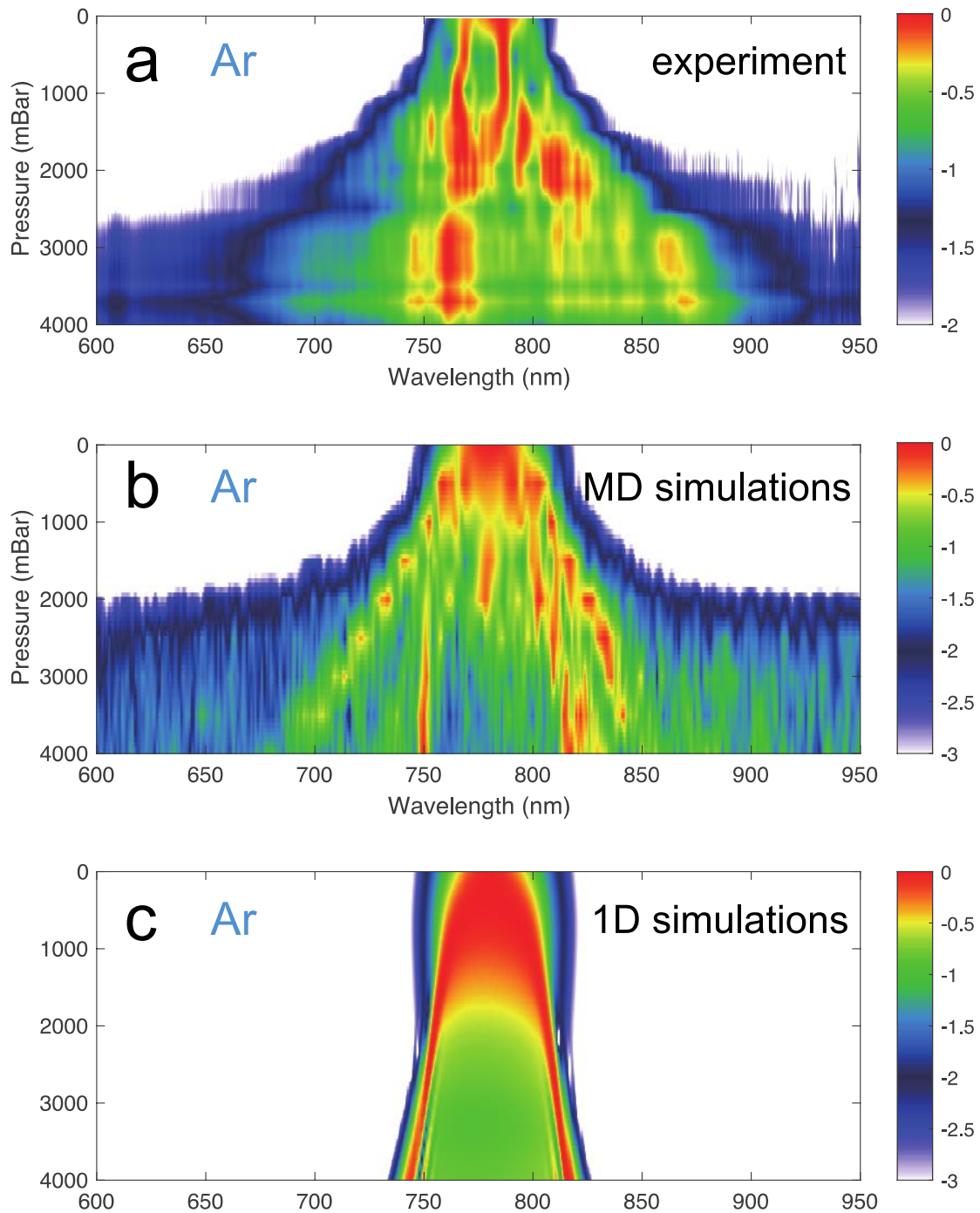


**Figure 32** Spectral broadening through nonlinear propagation in an Ar filled HCF (differentially pumped) with input pulse duration of 700 fs and 5 mJ/pulse at HCF input (3.25 mJ is coupled into the fiber considering 65% transmission). (a) Experimental spectra as a function of pressure. (b) MD simulations and (c) 1D simulations as a function of pressure.

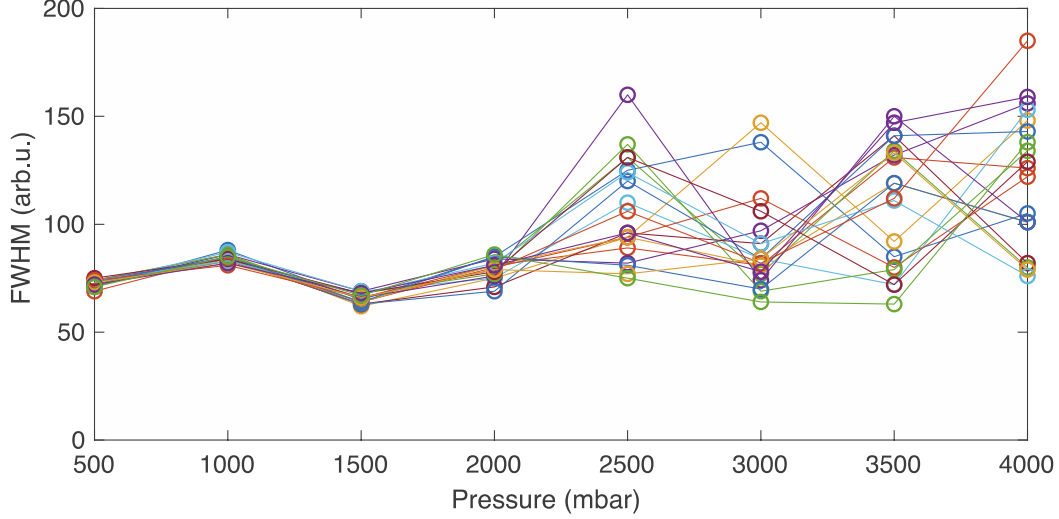


**Figure 33** Diameter of the beam (arbitrary unit) at the output of the HCF (measured in the far field) for 20 shot to shot images per pressure. Beyond 2000 mbar, we observed a larger output beam with high instability. In this case, due to the absence of SRS, there is no self-trapping effect and instead diffraction and coupling to HOMs.

This can be explained as followed. For Ar, we have observed 65% of transmission through the HCF such that we assume 3.3mJ propagating into the fundamental mode (65% of 5mJ/pulse). For 700fs pulse duration, this corresponds to a peak power of ~ 5 GW. Self-focusing occurs if the peak power is comparable to the critical power [16]

$$p_{cr} = \alpha \frac{\lambda^2}{4\pi n_0 n_2 p}. \quad (40)$$

In the equation of critical power,  $n_0$  is the refractive index of the medium and  $n_2$  is the nonlinear refractive index at 1 bar pressure and  $p$  is the gas pressure. For Gaussian beam,  $\alpha \approx 1.86$ . For Ar,  $n_0 \approx 1$ ,  $n_2 \approx 0.97 \times 10^{-23} \text{ m}^2/\text{W}$  at  $\lambda = 800 \text{ nm}$  [135]. At 2000 mbar of pressure, the critical power is  $P_{cr} \approx 4.9 \text{ GW}$ . This is very close to the estimation of peak power propagating through the fundamental mode (5 GW). Furthermore, for Ar, the competition between HOMs leads to high instability and multiple filamentations. This is shown in Figure 34 by showing nine consecutive shot to shot images of the spatial profile at the HCF output at 4000 mbar.

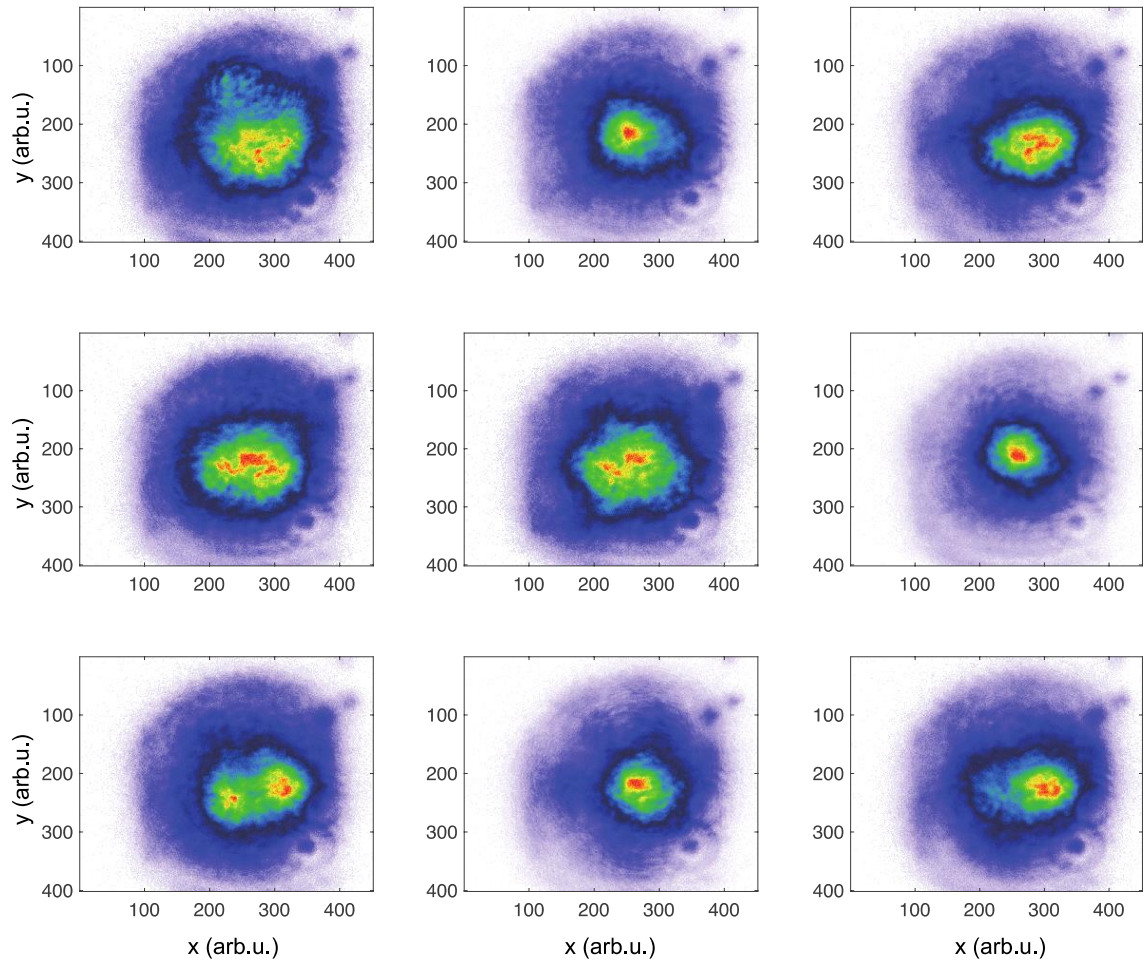


**Figure 34** Nine consecutive shot to shot images of the spatial profile at the HCF output for Ar at 4000 mbar of pressure. The high instability and the observation of multi-filaments make this regime undesirable for spectral broadening and pulse compression.

## 5 Articles I-III: pulse compression in 1D regime

### 5.1 Molecular gases for low energy pulse compression in a hollow core fiber

ELISSA HADDAD,<sup>1</sup> **REZA SAFAEI**,<sup>1</sup> ADRIEN LEBLANC,<sup>1</sup> RICCARDO PICCOLI,<sup>1</sup> YOUNG-GYUN JEONG,<sup>1</sup> HEIDE IBRAHIM,<sup>1</sup> BRUNO E. SCHMIDT,<sup>2</sup> LUCA RAZZARI,<sup>1</sup> FRANÇOIS LÉGARÉ,<sup>1,\*</sup> AND PHILIPPE LASSONDE<sup>1</sup>

<sup>1</sup>Institut National de la Recherche Scientifique, Centre Énergie Matériaux et Télécommunications, 1650 Boulevard Lionel-Boulet, Varennes, Quebec, J3X 1S2, Canada

<sup>2</sup>Few-cycle Inc., 2890 Rue de Beaurivage, Montreal, Quebec, H1L 5W5, Canada

\*legare@emt.inrs.ca

E. Haddad, **R. Safaei**, A. Leblanc, R. Piccoli, Y.-G. Jeong, H. Ibrahim, B. E. Schmidt, R. Morandotti, L. Razzari, and F. Légaré, "Molecular gases for pulse compression in hollow core fibers," *Optics express* 26, 25426-25436 (2018).

**Personal contribution:** I have participated in all experiments and analysis of the results. Furthermore, I have worked with E. Haddad to prepare the first version of the manuscript and to incorporate the comments of all co-authors.

#### 5.1.1 Abstract

We introduce hydrofluorocarbon molecules as an alternative medium to noble gases with low ionization potential like krypton or xenon to compress ultrashort pulses of relatively low energy in a conventional hollow core fiber with subsequent dispersion compensation. Spectral broadening of pulses from two different laser systems exceeded those achieved with argon and krypton. Initially 40 fs, 800 nm, 120  $\mu$ J pulses were compressed to few optical cycles duration. With the same approach a compression factor of more than 10 was demonstrated for an ytterbium-based laser (1030 nm, 170 fs, 200  $\mu$ J) leading to 15.6 fs.

#### 5.1.2 Main manuscript

Over the last decades, the quest to study light-matter interaction at increasingly short time scales and high intensities promoted the development of ultrashort laser sources and few-

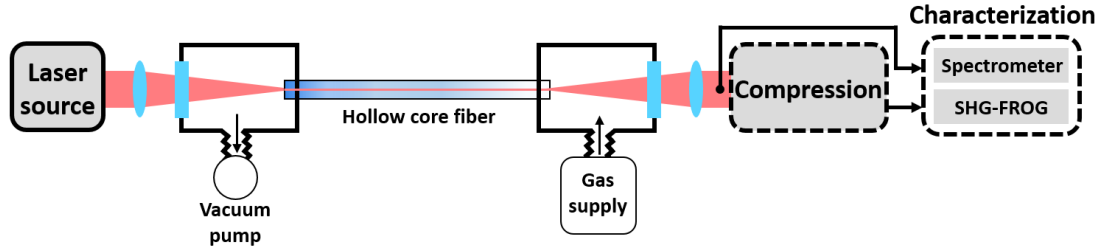


**Figure 35** Schematic experimental setup showing the spectral broadening in the gas-filled HCF followed by the compression stage and the characterization of the output pulses.

cycle pulses are now routinely generated. The generation of few-cycle pulses typically requires an external pulse compression stage due to the limited gain bandwidth of optical amplifiers, which restricts the shortest durations achievable directly from the laser system. One of the most common techniques consists in increasing the bandwidth through self-phase modulation (SPM) in a noble gas-filled hollow core fiber (HCF) followed by dispersion compensation, via e.g. chirped mirrors [136]. First introduced in 1996 by Nisoli et al. [17], this technique is now well-established and enables to compress pulses with a wide variety of parameters [19, 87, 137]. More recently, there has been a rising interest for diode-pumped Ytterbium (Yb)-based laser systems. These lasers can work with very high repetition rates, generating amplified pulses of femtosecond duration [52] [53, 54, 138, 139]. Their innovative geometries (thin-disk, slab, or fiber) allow operation at high average power by reducing thermal load, yet the bandwidth remains limited by the gain medium. Therefore, there is a real need for efficient compression techniques suitable for ultrashort pulses with lower energy, in the range of tens to hundreds of microjoules. Such lasers represent an ideal driver for generating coherent XUV with high flux through high-harmonic generation [55, 138, 140] [9, 12, 13]. Kagomé-type hollow core photonic crystal fibers represent one approach to compress very low energy pulses delivered by high average power diode-pumped Yb-based laser systems. These microstructured fibers enable compression of few microjoule pulses to sub-10 fs duration and can even be designed to support higher energies [14–18]. Despite major progresses, it remains nonetheless challenging to use these fibers [65]. An alternative to these rather complex Kagomé fibers lies in the use of low ionization potential (IP) noble gases, like krypton and xenon, in traditional hollow core fibers [66, 67, 69]. Simple HCFs can support both lower and higher energy pulses as well as being very versatile and robust. So far, the proposed technique has focused on noble gases, neglecting molecular gases because they are subjected to a delayed nonlinear response from the excitation of rotational or vibrational modes such as reported for SF<sub>6</sub> [141] or N<sub>2</sub> and O<sub>2</sub> [142].

In this article, we propose a distinct category of molecular gases, hydrofluorocarbons, to efficiently compress low-energy pulses using HCFs. These molecules represent a valuable

alternative to rare gases like krypton and xenon. First, we demonstrate that nonlinear propagation of ultrashort pulses using hydrofluorocarbons results in similar spectra as for noble gases, despite the fact that they have a complex molecular structure in comparison with atoms. Then, with such a molecular gas, we achieve sub-20 fs post-compression starting from 200  $\mu$ J, 170 fs initial pulses of an ytterbium-doped potassium-gadolinium tungstate (Yb:KGW) amplified laser system.

First of all, we have investigated the spectral broadening evolution of ultrashort pulses under the nonlinear response of the targeted molecular gases using 40-fs-long pulses centered at 800 nm, at a repetition rate of 2.5 kHz delivered by a Ti:Sa laser system. As depicted in Figure 35, the pulses are focused in a 1 m long gas-filled rigid HCF of 250  $\mu$ m core diameter to be spectrally broadened. To avoid perturbation of the beam coupling at the fiber input, vacuum is maintained in the entrance cell, as the setup is employed in a differential pressure configuration. The gas flows from the output (right) to the input of the HCF (left), where the vacuum pump is connected, thus creating a gradient of pressure. The pressure was measured using two digital pressure gauges (910 DualTrans, MKS) connected on both cells. The pressures reported in this paper correspond to the output cell pressure, while the entrance cell was maintained close to vacuum between 0.5 – 5 Torr, depending on the gas flow and pressure gradient. Throughout the measurements, the fiber transmission was around 60%.

The spectral broadening upon propagation in the HCF was studied for three molecular gases: 1,1-difluoroethane (C<sub>2</sub>H<sub>4</sub>F<sub>2</sub>, also known as R152a), 1,1,1,2-tetrafluoroethane (C<sub>2</sub>H<sub>2</sub>F<sub>4</sub>, also known as R134a), and ethylene (C<sub>2</sub>H<sub>4</sub>), a small hydrocarbon molecule. These gases have relatively low IPs, and are therefore expected to exhibit high polarizabilities and suitable nonlinear responses for pulse compression at low input pulse energies. In parallel, reference measurements were taken for two atomic gases, argon and krypton. The spectral broadening at different input pulse energies as a function of gas pressure was characterized before the compression stage using a spectrometer (HR4000, Ocean Optics). Figure 36(a) and Figure 36(b) present typical spectra measured after the nonlinear propagation through the gas-filled HCF. The initial spectrum is shown in shaded grey. The angular frequency axis is provided for visualization purposes only, as the spectra were measured with respect to the wavelength.

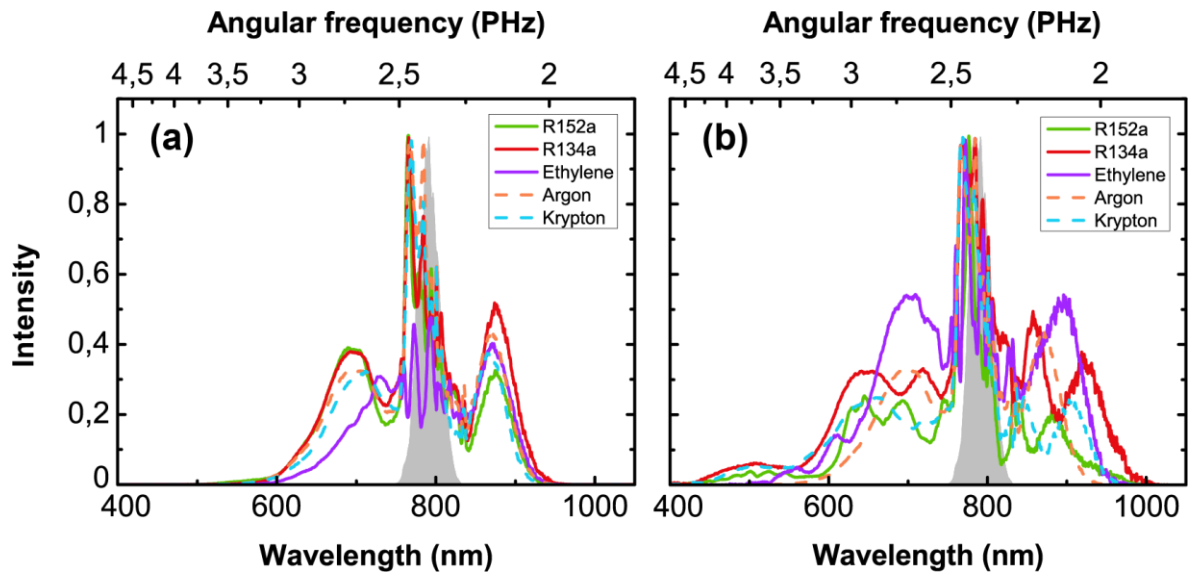


**Figure 36** (a) Comparison of spectra for different gases in the SPM regime: R152a (120  $\mu\text{J}$ , 475 Torr), R134a (160  $\mu\text{J}$ , 525 Torr), ethylene (80  $\mu\text{J}$ , 575 Torr), argon (320  $\mu\text{J}$ , 750 Torr), and krypton (200  $\mu\text{J}$ , 550 Torr); (b) Comparison of spectra for different gases beyond the SPM regime, all at a pressure of 760 Torr (1 atm): R152a (200  $\mu\text{J}$ ), R134a (200  $\mu\text{J}$ ), ethylene (120  $\mu\text{J}$ ), argon (320  $\mu\text{J}$ ), and krypton (240  $\mu\text{J}$ ). The spectrum of the initial pulse before broadening is shown in shaded grey.

In Figure 36(a), energy and pressure parameters were chosen to obtain broadened spectra with equal bandwidth for each gas. As observed in Figure 36(a), the broadened spectra extend from the visible to the near infrared (550 nm to 950 nm) over approximately 400 nm, corresponding to a broadening factor of 5. In comparison, the initial spectrum has a spectral width of 80 nm, extending from 750 nm to 830 nm and centered around 790 nm. Also, the spectra obtained for all gases, except for ethylene, exhibit highly similar shapes with smooth SPM lobes at the same wavelength positions. For ethylene, in contrast to all the other gases, the spectral extension appears strongly diminished at shorter wavelengths. Considering that shorter wavelengths are generated at the pulse trailing edge, through self-phase modulation, we infer that this part of the pulse undergoes a different nonlinear response. On the other hand, we observe for the red side that the spectrum is nearly identical to that of all the other gases. This finding suggests that ethylene may be somehow modified at the peak of the pulse, thus resulting in a different electronic response seen by the pulse trailing edge. For this reason, we would not consider this molecule for laser pulse compression. This feature is not observed for hydrofluorocarbon molecules and atomic gases, in which the broadened spectra are smooth and regular, such as expected from the instantaneous Kerr nonlinear response.

In Figure 36(b), parameters were set to study spectral broadening at higher levels of nonlinearity. For this, we increased gas pressures and pulse energies. In those conditions, we observe new features as the spectra become asymmetric around the central wavelength and

present more complex structures with new peaks arising. This is the case for both atoms and molecules. In particular, we note the extension of the blue side of the spectra. Such a blue-shift has already been associated experimentally to self-steepening [143, 144] and can also be an indicator of ionization [98, 145]. It was also shown in previous work that the excitation of molecular vibrational states may lead to periodic modulations such as those observed in the spectrum of R152a in Figure 36(b) [141]. On the other hand, such modulations are not necessarily observed for R134a or ethylene, for which the effect of a delayed response or vibrational modes would have been expected as well. Therefore, it is not trivial to identify the exact combination of mechanisms leading to this particular spectrum, given that the behavior is observed for a high level of nonlinearity where several effects may be coupled. Quantitatively, the spectra broadened in R152a and R134a at a pressure of 760 Torr (1 atm) and input energy of 200  $\mu\text{J}$  extend over 600 nm (from 400 nm to 1000 nm). As a comparison, higher input energy (240  $\mu\text{J}$ ) is required to broaden krypton from 400 nm to 950 nm. In the case of ethylene, the spectrum in Figure 36(b) shows the maximal broadening achieved in our conditions. Here, the broadening saturates at low energy (120  $\mu\text{J}$  at 760 Torr), and the spectrum gets more irregular without broadening anymore when the energy is increased. At the same time, transmission in the fiber starts dropping significantly, thus further underlining that ionization plays a role at higher intensity.

In order to further compare the nonlinear propagation, we quantified the total bandwidth  $\Delta\omega$  as a function of pressure for all gases under investigation. For fixed laser parameters, 800 nm, 40 fs pulses, the output spectra were measured while varying the pressure by small increments, up to 760 Torr. Throughout this paper, the total bandwidth  $\Delta\omega$  is a parameter defined by applying the following numerical method. The frequencies at levels of 1%, 50% and 99% of the integrated intensity with respect to frequency were determined for each pressure. They correspond respectively to the bottom, middle, and top dotted lines on Figure 37(a). For this study, we have defined the parameter  $\Delta\omega$  as the difference between frequencies corresponding to 1% and 99% of the total integrated energy (bottom and top dotted lines). We observe that the center of mass remains constant for all pressures in R134a. It is also the case for the other gases studied in this paper, including ethylene. Presenting the results on an angular frequency  $\omega$  axis allows us to observe the evolution of broadening. For self-phase modulation, the broadening is expected to be linear and symmetric in frequency. As observed on Figure 37(a), the spectrum expands with pressure more rapidly for higher frequencies, as opposed to the case of lower frequencies. This is assumed to be related to self-steepening. In Figure 37(b), the total bandwidth  $\Delta\omega$  for each pressure is obtained by applying the numerical method described above, that is from the difference between the angular frequencies corresponding to 1% and 99% of the integrated energy. It shows the total bandwidth  $\Delta\omega$

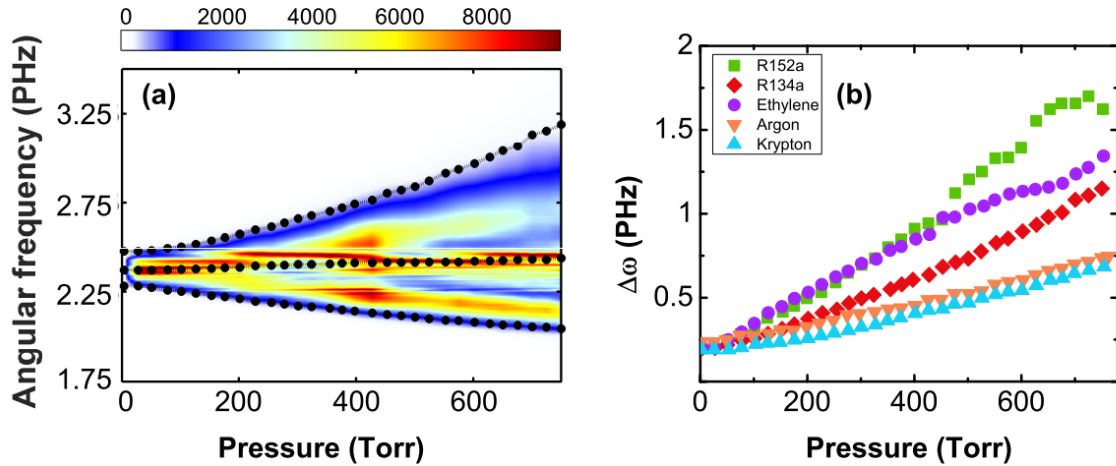


**Figure 37** (a) Experimental spectral broadening in R134a (120  $\mu\text{J}$  input pulse energy) as a function of pressure; (b) Quantitative measurement of the total bandwidth as a function of pressure for all investigated gases for an input pulse energy of 120  $\mu\text{J}$  (except argon, for 240  $\mu\text{J}$ ).

obtained with 800 nm, 120  $\mu\text{J}$ , 40 fs pulses in R152a (green squares), R134a (red diamonds), ethylene (purple circles), and krypton (blue upward triangles) and for 240  $\mu\text{J}$  for argon (orange downward triangles). Compared to the initial pulse bandwidth, we observe a broadening factor of approximately 3 for argon and krypton at 760 Torr. The broadening is significantly stronger for molecular gases, as we achieved factors of approximately 6, 7, and 8 respectively for R134a, ethylene, and R152a.

As expected from the linear dependence of  $n_2$  on pressure [90], the measured spectral broadening  $\Delta\omega$  scales almost linearly as a function of pressure, as shown in Figure 37(b). In general, for atoms, lower ionization potentials can be associated to higher nonlinear indices. In fact, there is no direct equation linking the IP to the nonlinear index  $n_2$ , and therefore to  $\Delta\omega$ . Theoretical models have been developed to calculate the nonlinear index based on the particle density and the ionization potential, but are only valid for noble gases [146]. More complex models would be required for molecular gases and calculations should take into account the electronic polarizability in different spatial orientations. This is not trivial and goes beyond the scope of the work presented here. However, Figure 37(b) confirms the same tendency for these molecules as for the atomic gases. The two noble gases with the highest IPs lead to the smallest slopes for  $\Delta\omega$  as a function of pressure, while R152a and ethylene, which have the lowest IPs, feature the highest slopes. From these slopes, we can conclude that the  $n_2$  of R152a is approximately 3 times higher than that of krypton, which is similar to the  $n_2$  ratio of xenon to krypton. Noticeably, ethylene has the lowest IP but is not broadening more than R152a. This is attributed to the feature observed in Figure 36(a) in which the broadening from the blue side appears to be suppressed in ethylene.

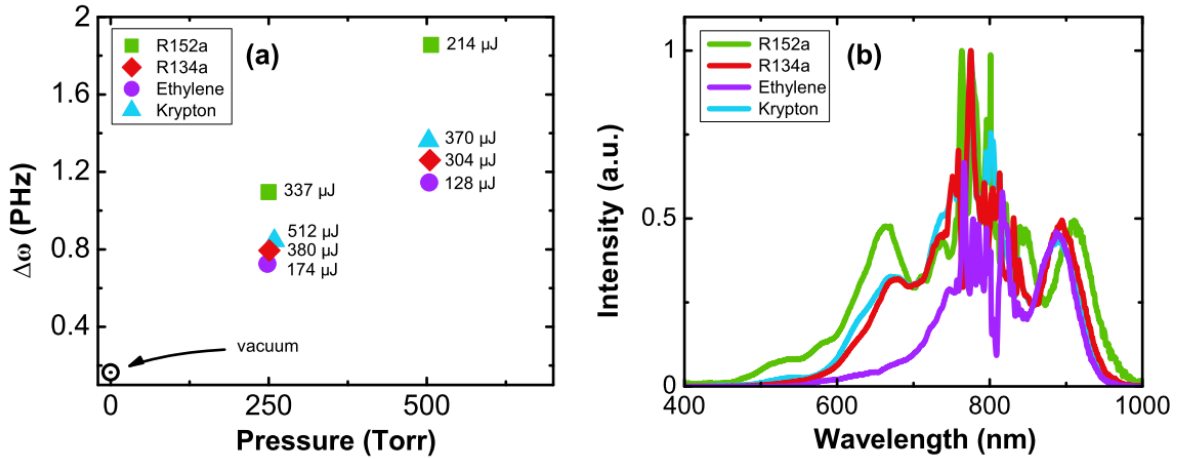


**Figure 38** (a) Spectral broadening at the ionization threshold (at indicated energies) for different gases at different pressures; (b) Measured spectra at a pressure of 500 Torr.

Although these measurements allow to sort the nonlinear response in different gases, there is no information concerning the effect of ionization, which may also contribute to the total broadening. Therefore, we have performed another set of measurements where we defined the onset of ionization and compared the total broadening obtained in each gas at this threshold. For each gas, the pressure was kept constant and the pulse energy was increased until we observed a 5% drop in transmission through the HCF due to ionization. We attribute the decrease in transmission to the ionization process. The photons are absorbed by atoms or molecules, generating charged species and free electrons, and this process results in a reduced transmission through the HCF. Given that the input of the fiber is kept under vacuum, the transmission drop cannot be attributed to fiber coupling issues such as self-focusing of the laser beam.

These measurements were performed with a fiber whose core diameter was 350  $\mu\text{m}$ . The total broadening obtained at the critical ionization threshold for each gas is presented in Figure 38(a), with the corresponding pulse energies. Two molecular gases, ethylene and R152a, show opposite behaviors compared to krypton. On the one hand, ethylene ionizes quickly before reaching appreciable spectral broadening. R152a, on the other hand, can undergo significant spectral broadening before ionizing when compared to the other gases. As for R134a and krypton, they have comparable bandwidth at this critical point. From this measurement, we conclude that R152a actually represents a valuable option to ensure maximal spectral broadening together with high overall throughput.

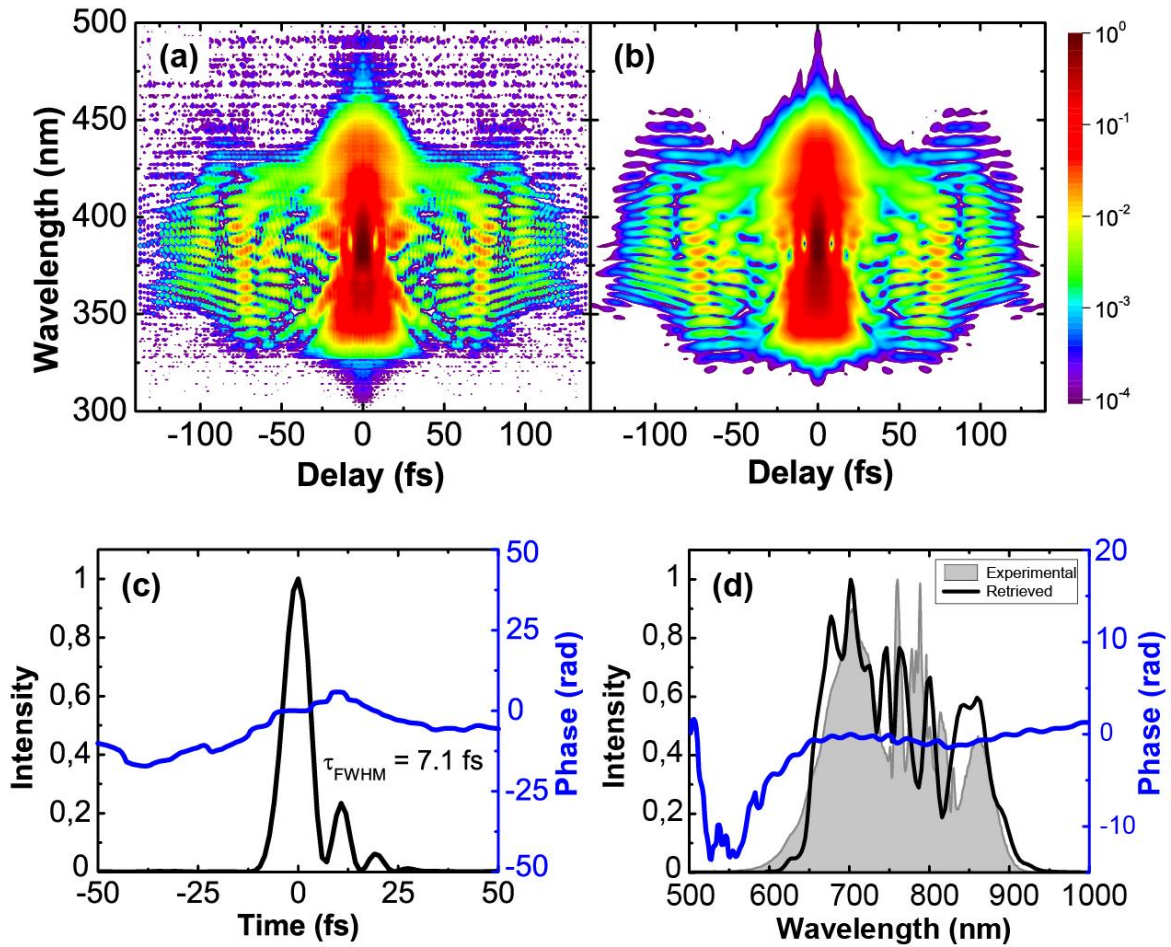


**Figure 39** For R152a,  $E = 120 \mu\text{J}$ ,  $p = 650 \text{ Torr}$ : (a) Experimental SHG-FROG trace; (b) Retrieved SHG-FROG trace; (c) Retrieved amplitude and phase in the time domain; (d) Retrieved amplitude and phase in the spectral domain. The experimental spectrum is shown in shaded grey.

Interestingly, in agreement with this result, it was previously reported that organic molecules can be more difficult to ionize than atoms for equivalent ionization potentials[147, 148]. In Figure 38(b), spectra measured at the critical ionization energy are shown. We observe that even under these conditions, the spectral shape for the refrigerant molecules remains highly similar to that of krypton, with the one of R134a actually being identical to the krypton one. The spectra for R152a are broader from both the blue and the red side. For ethylene, the broadening on the blue side is once again strongly suppressed. It should be noted that fine dust deposition was observed when using ethylene for conditions of high nonlinearity. This is attributed to the polymerisation of hydrocarbon chains that leads to carbon deposition and permanent degradation of the fiber such as reported in the conclusion of the paper by Mansour et al. [66]. This detrimental effect was not observed when using hydrofluorocarbon gases under our present conditions and we assume that HFC fragments do not polymerise like

hydrocarbon fragments. However, we do not exclude that hydrocarbon chains could be formed also for these gases in conditions of high excitation and/or ionization and therefore may represent in some cases a limiting factor for applications.

Since broadened spectra from R152a and R134a are highly similar to the reference spectra of argon and krypton, positively chirped pulses generated in these molecular gases are expected to be compressible in the same way as it is routinely achieved for atomic gases. Indeed, we were able to compress the 800 nm Ti:Sa pulses in both gases, using chirped mirrors for dispersion compensation. To compensate the chirp induced by SPM, 5 pairs of chirped mirrors (UltraFast Innovations, Garching, Germany) with a group delay dispersion (GDD) of  $-25 \text{ fs}^2$  per bounce were used, along with few millimeters of fused silica for GDD fine tuning, for a total compensation value of about  $-180 \text{ fs}^2$ . The pulses after compression were temporally characterized by second-harmonic generation frequency-resolved optical gating (SHG-FROG). As an example, the experimental SHG-FROG spectrogram measured for a  $120 \mu\text{J}$  input pulse in R152a at a pressure of 650 Torr is shown in Figure 39(a). Figure 39(b) illustrates the numerically retrieved spectrogram. The corresponding intensity and phase of the reconstructed pulse and spectrum are depicted in Figure 39(c) and 5(d) respectively. In this case, we were able to shorten the pulse duration from 40 fs down to 7.1 fs (FWHM). The retrieved spectrum is not strictly identical to the measured experimental one in Figure 39(d) but essential features are however reproduced. The residual oscillations observable in the temporal trace in Figure 39(c) are related to third order dispersion, which is not exactly compensated here. Based on the experimental spectrum in shaded grey, the transform limited pulse duration is 5.6 fs.

### **Spectral broadening and pulse compression of the Yb-based laser pulses**

Pulse compression was achieved also with a Yb:KGW laser source. The experiment is carried out with an R134a-filled HCF in order to demonstrate the potential of hydrofluorocarbons for relatively low pulse energy and high repetition rate applications, for which ytterbium-based lasers are typically used. It should be noted that a shorter fiber with a smaller diameter could have been chosen but for convenience we used this readily available setup. The ytterbium laser delivers 170-fs pulses centered at 1030 nm at a repetition rate of 1 kHz. The flexible hollow fiber has a length of 6 m and a core diameter of 500  $\mu\text{m}$ .

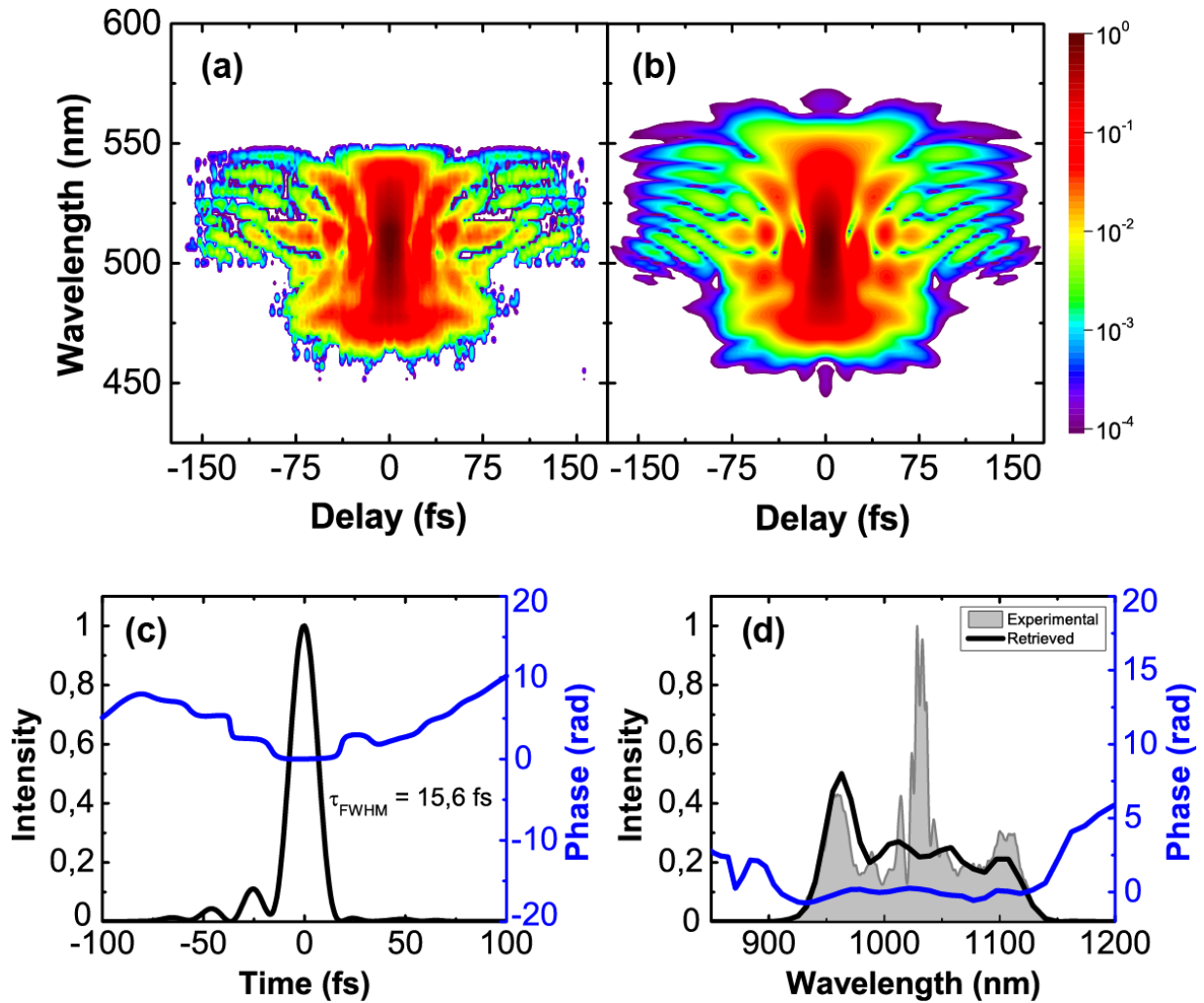


**Figure 40** For R134a,  $E = 200 \mu\text{J}$ ,  $p = 2000$  Torr: (a) Experimental SHG-FROG trace; (b) Retrieved SHG-FROG trace; (c) Retrieved amplitude and phase in the time domain; (d) Retrieved amplitude and phase in the spectral domain. The experimental spectrum is shown in shaded grey.

In this experiment, the fiber was filled with gas at a static pressure because a higher nonlinearity was required to broaden the narrow spectrum in comparison with the Ti:Sa system. This way, the higher pressure combined with the increased length of the fiber yields stronger SPM. The positive chirp induced by SPM is then compensated using one of the two following compression setups. (i) For  $E = 150 \mu\text{J}$ , dispersion compensation is achieved by successive reflections on pairs of chirped mirrors, with a group velocity dispersion of  $-50 \text{ fs}^2$  per reflection. The optimal compensation was obtained with 12 bounces, for a total GDD value of  $-600 \text{ fs}^2$ . (ii) For all the other energies ( $50 \mu\text{J}$  and  $200 \mu\text{J}$ ), a folded 4f stretcher/compressor was used to arbitrarily tune and optimize the amount of GDD. The 4f setup consists of a concave aluminium mirror ( $f = 200 \text{ mm}$ ), a 600 lines/mm grating, and a plane mirror reflecting back the spectral components through the same path, slightly offset, resulting in a total

transmission of  $\sim 50\%$ . While grating compressors enable continuous control of the GDD, chirped mirrors offer optimal reflectivity. Overall, the throughput of the HCF itself remained above 65% for the experimental measurements. Input pulses with 3 different energies, 50  $\mu\text{J}$ , 150  $\mu\text{J}$ , and 200  $\mu\text{J}$ , were compressed with our setup. The experimental SHG-FROG trace obtained after compression of the 200  $\mu\text{J}$  pulse in R134a at 2000 Torr is depicted in Figure 40(a). The reconstructed spectrogram, presented in Figure 40(b), is in good agreement with the experimental one in Figure 40(a). The shortest pulse, a sub-five-cycle pulse at 1030 nm, was obtained after compression of the 200- $\mu\text{J}$ , 170-fs pulse to 15.6 fs (compression factor of about 11), as shown by the reconstructed pulse intensity and phase in the time domain in Figure 40(c). The retrieved spectrum is also in very good agreement with the experimental one, as shown in Figure 40(d), except for the peak at the fundamental frequency of 1030 nm. We believe that this peak in the experimental spectrum corresponds to a temporal background from the laser. The spectrometer is unable to distinguish a background signal with low intensity on a ps or ns timescale from the main pulse. Therefore, we assume that the poor temporal contrast of the laser system is accountable for the mismatch between both spectra at 1030 nm. This also implies that the pulse energies presented are overestimated, as they include the energy contained in the temporal background signal.

In conclusion, we have demonstrated that molecular gases, more specifically hydrofluorocarbons like R152a (1,1-difluoroethane) and R134a (1,1,1,2-tetrafluoroethane), can be a valuable alternative to expensive noble gases for pulse compression using hollow core fibers. Molecular characteristics leading to a nonlinear response similar to atoms is not fully understood and has to be further investigated. However, the low ionization potentials which characterize these molecules are associated with higher nonlinear indices  $n_2$ . Therefore, significant and cost efficient spectral broadening is possible with smaller pulse intensity, making this method ideal for high average power applications with pulse energy on the order of tens to hundreds of  $\mu\text{J}$ . In R134a, we were able to broaden the spectra of 170-fs, 200- $\mu\text{J}$  Yb:KGW input pulse by a factor of 20 to achieve pulse compression down to 15.6 fs at a pressure of 2000 Torr. The pulse durations obtained are already sufficiently short for interesting applications, such as high harmonics generation in the range of hundreds of eV. For example, if we refer to the work of Bouillet et al. [140], they were able to generate harmonics up to order 31 (approximately 40 eV) in argon with 100  $\mu\text{J}$ , 270 fs pulses at 100 kHz. In our experiment, we compressed pulses of similar energies to sub-20 fs duration. From this result, we expect the output pulses to constitute an efficient driver for a coherent XUV source with cut-off photon energies in the range of 200 to 250 eV [149].

## 5.2 Low energy pulse compression in hollow core fibers using hydrofluorocarbon molecular gas

REZA SAFAEI<sup>1</sup>, OJOON KWON<sup>1</sup>, PHILIPPE LASSONDE<sup>1</sup>, VINCENT CARDIN<sup>1</sup>, ELISSA HADDAD<sup>1</sup>, ADRIEN LEBLANC<sup>1</sup>, BRUNO E. SCHMIDT<sup>2</sup>, HEIDE IBRAHIM<sup>1</sup> AND FRANÇOIS LÉGARÉ<sup>1\*</sup>

<sup>1</sup> Institut National de la Recherche Scientifique, Centre Énergie Matériaux et Télécommunications, 1650 Boulevard Lionel-Boulet, Varennes, Quebec, J3X 1S2, Canada

<sup>2</sup> Few-cycle Inc., 2890 Rue de Beauvillage, Montreal, Quebec, H1L 5W5, Canada

\*legare@emt.inrs.ca

R. Safaei, O. Kwon, P. Lassonde, V. Cardin, E. Haddad, A. Leblanc, B. E. Schmidt, H. Ibrahim, and F. Légaré, "Low energy pulse compression in hollow core fibers using hydrofluorocarbon molecular gas," OSA Continuum 2, 1488-1495 (2019).

**Personal contribution:** I designed the high pressure HCF setup. I and O. Kwon conducted the experiments. I also analysed the experimental results. Besides, I have developed a code to perform numerical simulations to explain the results. I wrote the first draft of the manuscript and include the comments of all co-authors.

### 5.2.1 Abstract:

Compression of low energy ultrashort laser pulses using a hollow core fiber (HCF) filled with 1-1 difluoroethane ( $C_2H_4F_2$ ), also known as R152a, is demonstrated. A 45 fs, 16  $\mu$ J Ti:Sapphire laser pulse is spectrally broadened in an HCF filled with R152a and subsequently compressed to ~9 fs with ~6  $\mu$ J pulse energy, which corresponds to a fivefold compression. This affordable and easily accessible gas is promising to compress new generation high average power lasers in conjunction with a flexible HCF setup. Additionally, the influence of the group velocity to the spectral broadening dispersion and its pressure dependence was numerically simulated. At pressures higher than 2.5 bar, the spectral broadening is affected by an interplay between two effects: while it is promoted by a denser gas medium leading to higher nonlinearity it is hampered at the same time by the lower intensity resulting from the pulse stretching which causes an overall limitation at higher pressures.

### 5.2.2 Main manuscript

Rapid development in ultrashort pulse laser techniques has facilitated numerous applications in innovative research in science and industry [150-152]. There is, however, still a vast demand to improve laser sources to enhance the performance of applications that require high peak power to enable the exploration of recently discovered phenomena; particularly, strong field interaction in solids [153], high harmonics generation [154-159], the modification of physical properties using light [160-165], and the generation and manipulation of electric currents [166-170]. In this regard, in order to boost intensities, a well-known approach is to shorten the pulse duration. Because of limited gain bandwidth of optical amplifiers, which imposes the limitation in shortest pulse duration from the laser, an external pulse compression is often employed to increase the spectral bandwidth, consequently shortening the pulse duration [171, 172]. The most common technique to broaden a spectrum is the implementation of a gas-filled hollow core fiber (HCF) in which the pulses undergo self-phase modulation (SPM) inducing a positive chirp that is compensated by chirped mirrors. Other possible compression methods include thin bulk plates [173, 174], conventional step-index solid glass fibers [175], and multi-pass cells [176, 177]. While these methods can be successfully applied to low energy pulses, they are individually designed for a specified energy range whose ceiling is set by the damage threshold of the material and the lower bound by insufficient nonlinearity to achieve spectral broadening [176, 177]. This is in contrast to the gas-filled HCF, which offers the essential advantage that one experimental setup is capable of handling a wide range of input pulse energies.

Although gas-filled HCF have been successful for the generation of few-cycle pulses at the millijoule (mJ) energy level [137, 178], downscaling the energy to the microjoule ( $\mu\text{J}$ ) level with sufficient spectral broadening has been challenging. For noble gases with rather high ionization potential (IP), such as argon, it is impossible to induce a sufficient nonlinear effect with energies below the hundred  $\mu\text{J}$  level. In the  $\mu\text{J}$  energy level, inducing enough nonlinear phase to an optical pulse requires either to increase the nonlinear parameter  $n_2$  or a tighter focal diameter. In the search for an optimal nonlinear medium, low IP noble gases, like xenon, have been tested at high pressure in a regular HCF in order to compress high repetition rate laser pulses with only a few  $\mu\text{J}$  of energy [54, 66, 67, 179]. To address the addition of the geometry parameter, Kagomé hollow-core photonic crystal fibers were recently used with low IP noble gases, like krypton and xenon, in order to compress low energy pulses, which enabled high repetition rate laser pulses to be compressed to below 10 fs pulses [61, 180,

181]. However, these fibers are complicated to fabricate, which limits their accessibility, and there are also physical difficulties which accompany their use [65, 182].

Recently, we have demonstrated pulse compression of Titanium:Sapphire (Ti:Sa) pulses to few-cycles duration, at the hundred  $\mu\text{J}$  level, using hydrofluorocarbon molecular gases near 1 bar pressure with a conventional 1 m long HCF [183]. In this paper we further downscale this approach to the few  $\mu\text{J}$  level and study the mechanisms underlying the spectral broadening in an HCF setup filled with 1-1 difluoroethane ( $\text{C}_2\text{H}_4\text{F}_2$ ), also known as R152a. Unlike other molecular gases which exhibit a delayed nonlinear response, such as the excitation of rotational or vibrational modes [141, 142], R152a behaves as a low-cost alternative to expensive noble gases like krypton and xenon. Here, we attain sufficient spectral broadening to generate  $<10$  fs pulses, starting from 16  $\mu\text{J}$ , 45 fs pulses at 800nm using only 3 bar of R152a. This result indeed indicates the capability of this gas to compress low energy laser pulses at the 10  $\mu\text{J}$  level. In addition, substantial impact of the group velocity dispersion (GVD) of the gas on the spectral broadening is observed at higher pressure, which has not been reported in previous literature. To highlight this effect, numerical simulations have been performed to estimate the pressure dependency of second order dispersion,  $\beta_2$ , and nonlinear refractive index,  $n_2$ .

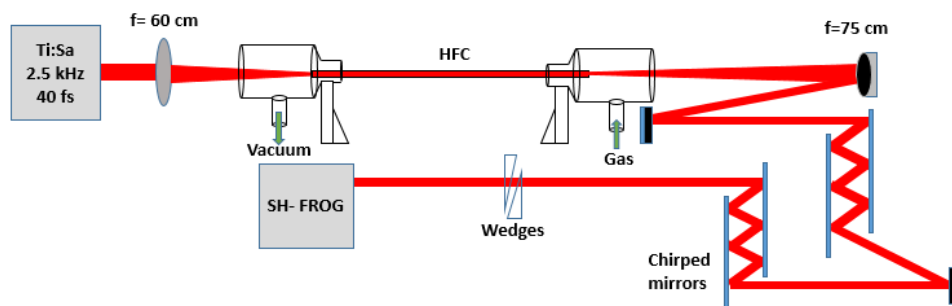


**Figure 41** Experimental setup for the compression of low energy pulse.

The experimental setup is shown in Figure 41, including the HCF. In this experiment, the output from a Ti:Sa amplifier, which delivers 45 fs-FWHM pulses at a rate of 2.5 kHz with 800 nm central wavelength, is attenuated to 16  $\mu\text{J}$ . With an  $f = +60$  cm convex lens, the beam is focused and coupled into the HCF, which is 2 meters long with an inner diameter of 250 microns. The two vacuum tubes attached to the fiber holders are enclosed by 3 mm thick UV fused silica windows. In order to reduce unwanted nonlinear effects resulting from the intense beam interacting with a dense gaseous medium at the entrance, the gas is injected on the exit side while the entrance side is constantly pumped to build up a pressure gradient along the fiber. The employment of a differential pressure configuration suppresses the ionization, self-

focusing and dispersive broadening, which contributes to a higher reliability in fiber coupling. An aperture is positioned after the lens to control the focal size. Here, the opening of the aperture is adjusted to optimize the focal diameter for transmission. The highest transmission of 53% is achieved when the  $1/e^2$  focal diameter is 150 microns, about 60% of the fiber diameter, which is close to the theoretical value of 64% for optimal mode coupling to the fundamental mode [81]. An  $f = +75$  cm silver-coated spherical concave mirror is placed after the exit to collimate the diverging output beam. Afterwards, the pulses are reflected between chirped mirrors (Ultrafast Innovations GmbH, PC70). As each pair of bounces, at the 5 and 19-degree incidence angle, induces  $-50 \text{ fs}^2$  group delay dispersion (GDD), we employ seven pairs according to the required resultant GDD. A pair of wedges is used to provide continuous and precise tunability of the GDD. A series of reflections on pairs of chirped mirrors and uncoated wedge surfaces lead to an energy loss of  $\sim 25\%$ . Eventually, the temporal profile of the compressed pulses is measured by second harmonic generation frequency resolved optical gating (SHG-FROG).

First, the spectral broadening under propagation in the HCF is investigated. Figure 42(a) describes the spectra for varying gas pressure for an input pulse energy of  $16 \mu\text{J}$ . The pressure is spanned from vacuum till 4 bar, being kept well below the vapor pressure of R152a,  $\sim 5.1$  bar at  $20^\circ\text{C}$  [184], to avoid condensation. The fiber transmission remains almost constant for this pressure interval with the given pulse energy, indicating no sign of ionization. Increasing the pressure results in extension of the spectral edge towards both the blue and the red side, dominated by SPM. The degree of spectral broadening is quantified by defining  $\Delta\omega$  as the width of the spectrum in angular frequency within which 50% of the spectral intensity is encompassed.  $\Delta\omega$  with respect to the pressure is plotted as red symbols in Figure 42(b). The transform-limited pulse duration,  $\tau_{\text{TL}}$ , corresponding to each spectrum are calculated and overlaid in Figure 42(b) as black squares, exhibiting a strong inverse correlation with  $\Delta\omega$ . By increasing pressure,  $\tau_{\text{TL}}$  decreases noticeably till 2.5 bar, then the pace of the decrease is slowed down at higher pressure. We conjecture that this is due to the hindrance of spectral broadening attributed to the temporal broadening of laser pulses in the dispersive gas. The influence of the GVD of R152a is discussed in the context of Figure 12. The estimation of  $\tau_{\text{TL}}$  suggests the feasibility of compressing a  $\sim 45$  fs pulse to  $<10$  fs with well-controlled dispersion.

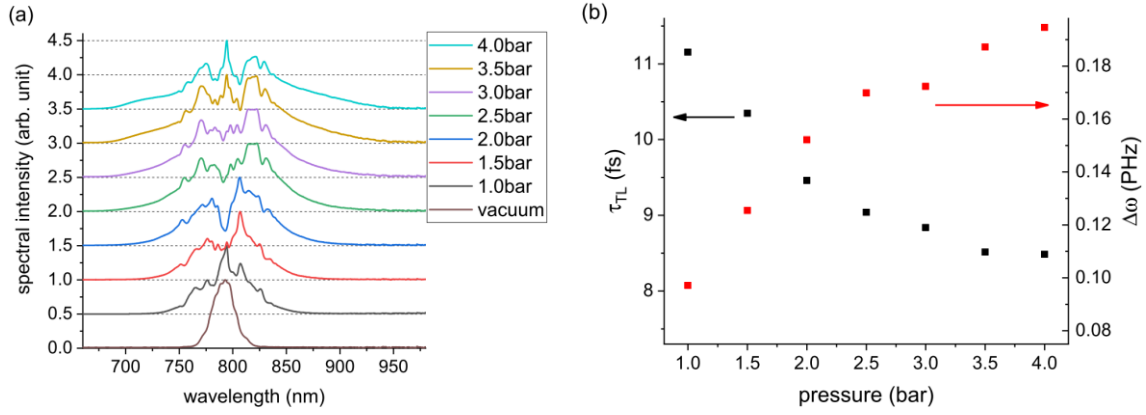


**Figure 42** (a) spectra for different pressures of R152a at 16  $\mu\text{J}$  input energy. All spectra are normalized to unity and dispersed vertically for discernibility. (b) Transform-limited pulse duration  $\tau_{\text{TL}}$  (black, left axis) and the spectral bandwidth  $\Delta\omega$  (red, right axis) versus pressure obtained from the measured (black squares) and simulated (red squares) spectra for varying pressure.

To verify the compressibility, the broadened pulses are compressed with chirped mirrors. Since the spectral broadening encounters the obstruction at 2.5 bar as depicted in Figure 42(b), increasing the pressure beyond this does not result in noticeably shorter pulses. Hence, the pressure of 3.0 bar is chosen, compromising between spectral width and consequent GDD which needs to be compensated. Equipped with chirped mirrors and a wedge pair, we have characterized the compressed pulses using SHG-FROG. The measured spectrogram (Figure 43 (a)) and the iteratively retrieved one (Figure 43 (b)) bear fair semblance to each other, confirming the validity of the characterization. The reconstructed temporal profile reveals that the pulse is as short as  $\sim 9$  fs FWHM (Figure 43(c)), in line with the calculated  $\tau_{\text{TL}}$ . In the spectral domain, the agreement of measured versus retrieved spectra is also confirmed (Figure 43(d)). This leads to the compression of low energy laser pulses by a factor of  $\sim 5$  using R152a molecular gas with HCF. The energy of the compressed pulse is about 6  $\mu\text{J}$ .

To address the effect of GVD through the propagation, the spectral evolution during the guided propagation in the fiber is simulated by solving the generalized nonlinear Schrödinger equation using the fourth-order Runge-Kutta in the interaction picture method (RK4IP) and considering the effect of GVD [86]. We use 40 fs input pulse duration and 8  $\mu\text{J}$  input pulse energy, which is equal to the actual pulse energy of the HCF, since we assume a differential pressure scheme in which most of interaction takes place at the end of the fiber. The pressure distribution in the fiber is modeled by the formula  $P = P_0\sqrt{z/L}$ , where  $P_0$  is the applied pressure at the fiber output and  $L$  the propagation length in the fiber [185]. At each propagation step, the contribution of second order dispersion is calculated in the frequency

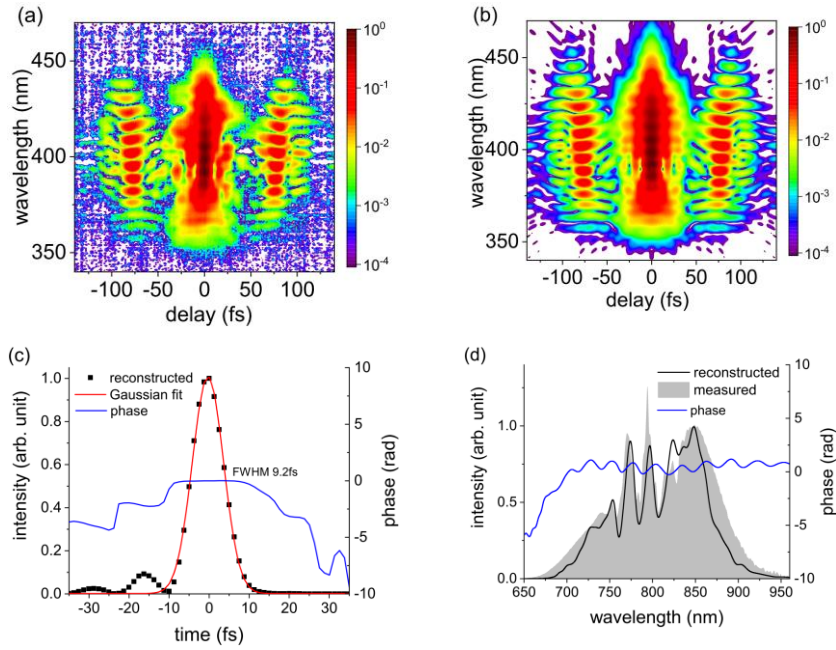


**Figure 43** Characterization of dispersion-compensated pulses using SHG-FROG. Input energy is 16  $\mu\text{J}$  and the HCF is filled with R152a at 3.0 bar. (a) Measured and (b) reconstructed spectrogram; Retrieved intensity and phase in the (c) time and (d) spectral domain.

domain, while both the nonlinear term and the self-steepening are computed in the time domain. As it was revealed in our latest publication, R152a possesses an  $n_2$  comparable to that of xenon [183], therefore the  $n_2$  of xenon is adopted as that of R152a in our simulations. Since the  $n_2$  of xenon widely varies in the literature, we choose to rely on the mean value of the  $n_2$ 's presented in [146]. The second order dispersion  $\beta_2$  is adjusted to show the best agreement with experiment.

By taking the parameters  $n_2 = 6.0 \times 10^{-23} \text{ m}^2/\text{W}$  and  $\beta_2 = 6 \text{ fs}^2/\text{m}$  at the pressure of 1 bar, the simulations confirm the experiments in two independent cases; the transform-limited pulse duration,  $\tau_{\text{TL}}$ , and the pulse duration of the direct HCF output without chirped mirrors,  $\tau_{\text{chirped}}$ . To identify the contribution of GVD, the calculation is repeated with the second order dispersions being neglected, i.e.,  $\beta_2 = 0$ . The simulations with and without consideration of the GVD are superimposed with the measurements as shown in Figure 44(a). The lower half below the break of the vertical axis corresponds to  $\tau_{\text{TL}}$ . Without the effect of GVD, one should have attained a much broader spectrum to support  $<5 \text{ fs}$  pulses at higher pressures (filled blue diamonds). However, experimentally (filled black squares, the same as in Figure 42(b)), the  $\tau_{\text{TL}}$  reaches  $\sim 10 \text{ fs}$ , as do the simulations including GVD (filled red circles). The consideration of GVD leads to much better agreement with experiment, highlighting the role of dispersion in limiting the spectral broadening in the HCF. The upper half of the axis in

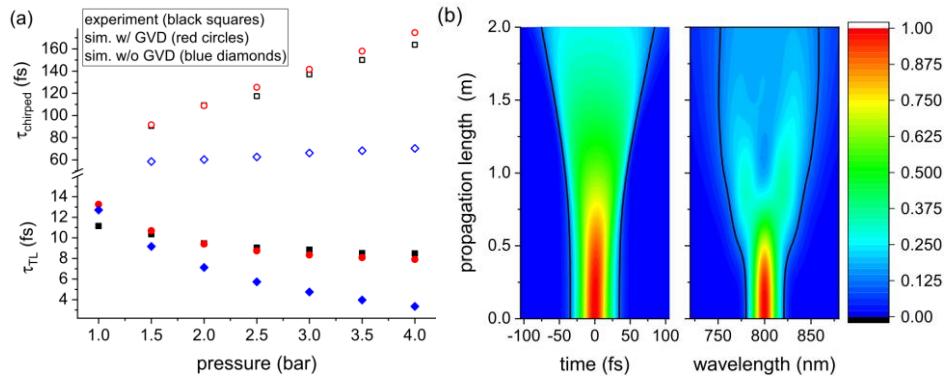


**Figure 44** The transform-limited pulse duration  $\tau_{TL}$  (solid symbols, axis below the break) and pulse duration before dispersion compensation  $\tau_{chirped}$  (hollow symbols, axis above the break) derived from the experiment (black squares), simulated with dispersion being considered (red circles) and simulations with dispersion being disregarded (blue diamonds) as a function of pressure and (b) numerical simulations of the temporal and spectral evolution along the propagation in the fiber of an input pulse at 4.0 bar. Black thick solid lines depict 1/e2 of the temporal and spectral profile with respect to the propagation length.

Figure 44(a). denotes  $\tau_{chirped}$ , the pulse duration of the direct HCF output without chirped mirrors. It is measured by intensity autocorrelation (black hollow squares). As the pressure is applied, the GVD of the gas interplaying with the broadened spectrum significantly elongates the pulse duration. The corresponding calculation considering GVD (red hollow circles) show a decent fidelity with the experiment, while calculations without GVD (blue hollow diamonds) predict a relatively insignificant increase of the pulse duration. This finding shows that pulse broadening during the propagation in the fiber indeed occurs due to GVD and is responsible for the impeded spectral broadening with rising pressure.

With increasing pressure, we anticipate an interplay between two effects: 1) the spectral broadening is promoted by a denser gas medium leading to higher nonlinearity; 2) spectral broadening is hampered by the lower intensity resulting from the elongated pulse duration. The competition of these two counteracting effects sets a constraint for the spectral broadening. The influence of an elongated pulse duration is studied by numerically tracing the evolution of pulses in the temporal and the spectral domain (Figure 44(b)). Assuming a high pressure of 4.0 bar, under which temporal broadening owing to GVD seems significantly probable, the suppression of spectral broadening is observed after propagation of  $\sim 1$  m as black lines shown in the right panel of Figure 44(b). This coincides with the point where the temporal broadening begins as shown in the left panel. Thus, the GVD of the molecular gas restricts the spectral broadening.

In conclusion, we have illustrated that R152a is a suitable gas for pulse compression using hollow core fibers in the low energy pulse regime. This particular gas possesses a relatively low IP of  $\sim 11.9$  eV [186] compared to noble gases, and simultaneously a large  $n_2$ . Thanks to its relatively low price, it can also be used in a differential pressure scheme, which is the preferred method to avoid disruptive nonlinear effects at the fiber entrance. In this paper, 45 fs, 16  $\mu$ J pulses are compressed to 9.2 fs with an energy of  $\sim 6$   $\mu$ J; the pulse duration is reduced by a factor of 5. The overall energy efficiency amounts to  $\sim 40\%$ , including the fiber transmission of  $\sim 53\%$  and reflectance of chirped mirrors of  $\sim 75\%$ . Such promising results show that R152a gas can be an excellent candidate to compress low energy laser pulses in a conventional HCF setup, a substitute for the expensive noble gas xenon. In the future, we will further push this method to compress high repetition rate Ytterbium (Yb) laser systems, such as commercially available 100 W sub-300 fs Yb laser systems operating at hundreds of kHz.

### 5.3 Raman effect in the spectral broadening of ultrashort laser pulses in saturated versus unsaturated hydrocarbon molecules

OJOON KWON<sup>1</sup>, REZA SAFAEI<sup>1</sup>, PHILIPPE LASSONDE<sup>1</sup>, GUANGYU FAN<sup>1</sup>, ANDRIUS BALTUŠKA<sup>2</sup>, BRUNO E. SCHMIDT<sup>3</sup>, HEIDE IBRAHIM<sup>1</sup> AND FRANÇOIS LÉGARÉ<sup>1</sup>

<sup>1</sup>Institut National de la Recherche Scientifique, Centre Énergie Matériaux et Télécommunications, 1650 Boulevard Lionel-Boulet, Varennes, Québec, J3X 1S2, Canada

<sup>2</sup>Photonics Institute, Vienna University of Technology, Gusshausstrasse 27/387, Vienna, Austria

<sup>3</sup>Few-cycle Inc., 2890 Rue de Beauvillage, Montréal, Québec, H1L 5W5, Canada

\*legare@emt.inrs.ca

O. Kwon, R. Safaei, P. Lassonde, G. Fan, A. Baltuška, B. E. Schmidt, H. Ibrahim, and F. Légaré, "Raman effect in the spectral broadening of ultrashort laser pulses in saturated versus unsaturated hydrocarbon molecules," *Optics Express* 28, 980-990 (2020).

**Personal contribution:** O. Kwon and I designed and conducted the experiments. O. Kwon and I also analyzed the experimental results. Besides, I performed the numerical simulation to explain the role of Raman active molecules on spectral broadening.

#### 5.3.1 Abstract

A conventional hollow core fiber (HCF) scheme is implemented to investigate spectral broadening of Titanium:Sapphire (Ti-Sa) femtosecond laser pulses in saturated hydrocarbon molecules compared to unsaturated ones. While the saturated molecules exhibit a spectral broadening similar to noble gases, for the unsaturated ones with  $\pi$  bonds, broadening towards blue is restrained. Numerical simulations underpin that it is a combination of group velocity dispersion (GVD) and Raman scattering which limits the spectral broadening for the unsaturated molecules. Compression of low energy  $\sim 40$ fs pulses to  $\sim 8$ fs using saturated hydrocarbons is demonstrated, suggesting the feasibility of this media for high repetition rate laser pulse compression.

#### 5.3.2 Main manuscript

The development of ultrafast laser technologies has allowed to discover unprecedented physical phenomena in light-matter interaction [187-190]. By reaching higher power levels as well as shorter pulse duration, it has been possible to explore dynamics down to the attosecond duration [191-197] and in strong intensity regimes [154, 158, 160, 198-201]. In the last decades of the 20<sup>th</sup> century, the advent of Ti-Sa gain medium [202] has disseminated femtosecond lasers. Kerr lens mode-locking [203] in combination with chirped pulse amplification [204] has expedited access to high focal intensity comparable or even higher to the Coulomb field in atoms to reach the relativistic regime [205, 206]. As the gain narrowing of the amplification medium limits the spectral width, an additional stage for spectral broadening and compression is necessary to further shorten the pulse duration of Ti-Sa lasers to few optical cycles. Most popularly, expanding the spectral bandwidth by means of self-phase modulation in noble gases in a HCF and subsequent dispersion compensation [171] have demonstrated compression down to the single-cycle regime [207]. Nowadays, the concept of HCF is well established and widely used in the community due to its versatility and robustness [81, 87, 137, 208]. Compression of low energy pulses using various gaseous molecules (apart from noble gases) in HCF has recently been investigated [91, 141, 183]. This provides the perspective of applying the HCF method to compress Ytterbium-based lasers [19, 209], which lately receives attention as a prospective femtosecond laser source, e.g. to drive high flux high harmonics generation (HHG) thanks to its high average power and high repetition rate [210-213].

In the present study, several hydrocarbons are tested as nonlinear medium for pulse compression using HCF. It is observed that methane (CH<sub>4</sub>) and ethane (C<sub>2</sub>H<sub>6</sub>), referred to as saturated hydrocarbons, function like well-known noble gases for spectral broadening and compression; pulse compression down to sub-10fs with CH<sub>4</sub> is demonstrated. On the other hand, for the unsaturated molecules ethylene (C<sub>2</sub>H<sub>4</sub>) and acetylene (C<sub>2</sub>H<sub>2</sub>), a lack of blue shift at the output of the HCF is observed. This behavior results in a narrower spectral bandwidth, making them less suitable for pulse compression. Through numerical simulations, we highlight that an interplay between GVD and Raman response is responsible for this distinct spectral aspect between saturated and unsaturated molecules.

The experiments have been performed at the Advanced Laser Light Source infrastructure located at INRS-EMT. The experimental setup is described in Figure 45(a). A Ti-Sa multipass amplifier is used which generates 40fs pulses with an adjustable pulse energy up to a few mJ at a repetition rate of 2.5kHz. The output is focused and coupled to a 2-meter-long HCF with an inner diameter of 250 microns (*few-cycle* Inc.). The  $1/e^2$  focal spot size amounts to 150 microns, which approximately coincides with an optimal ratio against the core diameter, ensuring a decent transmission efficiency of 55%. The HCF assembly is equipped with a

vacuum pump connected to the laser input side and a gas supply tube attached to the laser output side. This configuration enables one to build a pressure gradient in the HCF; low at the laser entrance and high at the exit. It is intended to avoid undesired interaction between the focusing laser beam and the gas media before being coupled into the fiber [87].

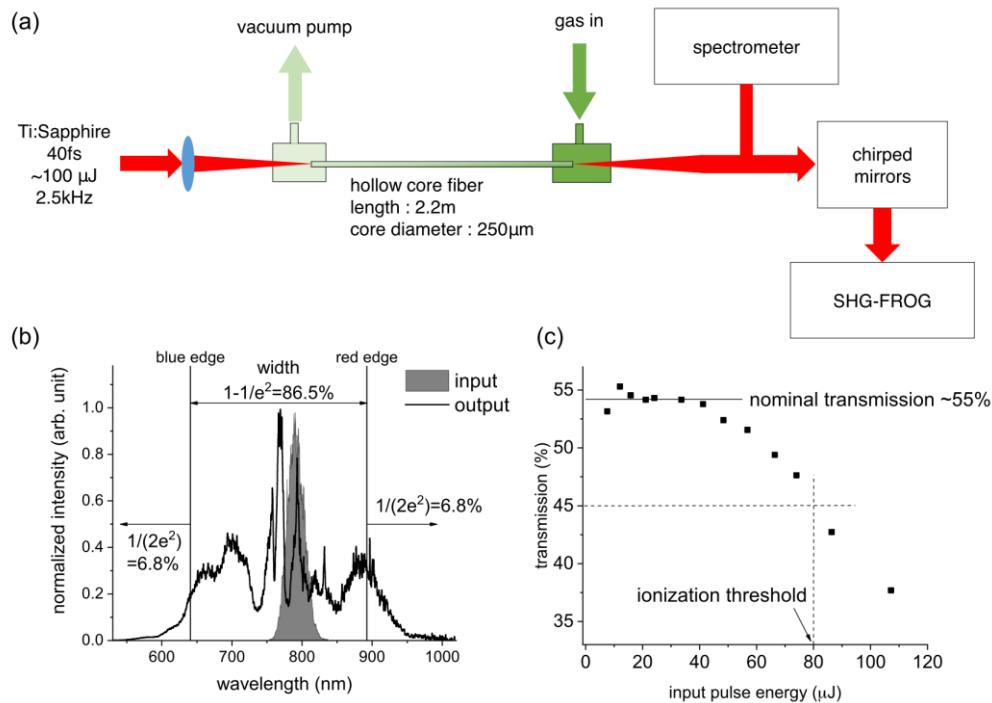


**Figure 45.** (a) Schematic drawing for the experimental setup (b) exemplary input (gray shaded) and output (black line) spectra with the descriptions for blue and red edges (c) typical transmission drop with respect to increasing input pulse energy, observed in acetylene gas, from which the ionization threshold  $E_{th}$  is derived. The transmission begins to drop around 60% of  $E_{th}$ .

The output spectra from the HCF filled with different hydrocarbon molecules are recorded for varying input energies. In addition, the same measurements are repeated with krypton as a reference. The pressure of each gas is controlled to 1 bar in order to keep the number of molecules participating in the interaction constant. It also complies with the regulation imposed by material safety data sheets (MSDS), staying below the limit pressure of 1.5 bar for acetylene.

Example spectra for an input pulse and a broadened output pulse are presented in Figure 45(b). For analysis, the red (or blue) edge of a spectrum is defined as the wavelength above (or below) which 6.77% ( $= 1/2e^2$ ) of spectral intensity is encompassed. Therefore, 86.5% ( $= 1 - 1/e^2$ ) of spectral intensity is contained between the blue and the red edge, namely, within

the spectral width. With growing input energy, all gases undergo a drop of transmission which is an indication of ionization of the molecules. We define the threshold of ionization  $E_{th}$  as the input pulse energy at which the HCF transmission reduces to 45% (see Figure 45(c)). The input energies in the following context are normalized with respect to the  $E_{th}$  of each gas, which are displayed in Table 3.

| Gas                 | CH <sub>4</sub> | C <sub>2</sub> H <sub>6</sub> | C <sub>2</sub> H <sub>4</sub> | C <sub>2</sub> H <sub>2</sub> | Kr  |
|---------------------|-----------------|-------------------------------|-------------------------------|-------------------------------|-----|
| $E_{th}$ ( $\mu$ J) | 160             | 100                           | 64                            | 80                            | 300 |

**Table 3** Ionization threshold of gases tested in the present study

The evolution of blue and red edges with increasing energy is depicted as filled symbols in Figure 46(a). The complete set of raw spectra is presented in Figure 49 in the appendix. All gases exhibit a similar spectral extension towards the red, i.e., the deviation among different media is insignificant as presented in Figure 46(a). On the contrary, for the blue shift, ethylene and acetylene behave in a well-distinguishable manner compared to the rest. Ethylene and acetylene broaden with the magnitude of the descending slope of the blue edge being comparable to that of the ascending slope of the red edge. For the other gases, the slope for the blue shift is greater than the red one by about  $\sim 2.5$  times due to the combination of self-phase modulation and self-steepening. This leads to approximately half the spectral width for unsaturated hydrocarbons compared to the saturated ones (Figure 46(b)).

At a half of  $E_{th}$  input energy, simulated spectra for both gases are overlapped on the measured ones (gray shaded area) as shown in Figure 47. The red and blue edges and positions of some peaks and valleys are well reproduced in the simulation considering GVD and Raman effect (solid black line). In order to identify the contribution of each effect, we repeated simulation with either GVD or Raman effect being ignored (dashed red and dotted blue lines in Figure 47, respectively). 1) The neglect of GVD, assumes a constant pulse duration during the propagation, which is not the case in reality; GVD of gases elongates the pulse duration to effectively reduce the intensity. Therefore, consideration of GVD tends to correct the overestimated spectral broadening. 2) The Raman can be neglected by putting  $f_R = 0$  thus  $R(t) = \delta(t)$  which signifies domination of instantaneous responses. The consideration of Raman tends to induce spectral shift toward red. Lower energy photons generated by inelastic

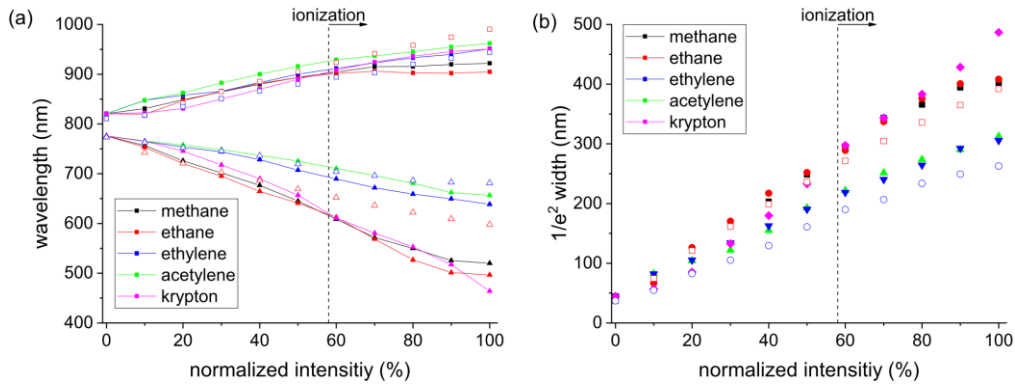


**Figure 46** spectral broadening after the propagation in a HCF filled with 1 bar of various gases for varying input energy. The shape of symbols denotes the blue edge (triangles) and the red edge (square) of the spectra. The colors represent the species of gas as shown in the legend. Open symbols stand for calculated spectra (ethane and ethylene only). Vertical dashed line stands for the intensity at which the drop of HCF transmission is first perceived, indicating the occurrence of ionization. (b) the spectral width derived from (a).

scattering are amplified by Raman gain, being pumped by the blue part of the same pulse. The process continues along the fiber, continuously transferring energy from blue components to red. Such an energy transfer appears as a red shift of the spectrum, with shift increasing with propagation length.

At a half of  $E_{th}$  input energy, simulated spectra for both gases are overlapped on the measured ones (gray shaded area) as shown in Figure 47. The red and blue edges and positions of some peaks and valleys are well reproduced in the simulation considering GVD and Raman effect (solid black line). In order to identify the contribution of each effect, we repeated simulation with either GVD or Raman effect being ignored (dashed red and dotted blue lines in Figure 47, respectively). 1) The neglect of GVD, assumes a constant pulse duration during the propagation, which is not the case in reality; GVD of gases elongates the pulse duration to effectively reduce the intensity. Therefore, consideration of GVD tends to correct the overestimated spectral broadening. 2) The Raman can be neglected by putting  $f_R = 0$  thus  $R(t) = \delta(t)$  which signifies domination of instantaneous responses. The consideration of Raman tends to induce spectral shift toward red. Lower energy photons generated by inelastic scattering are amplified by Raman gain, being pumped by the blue part of the same pulse. The process continues along the fiber, continuously transferring energy from blue components to red. Such an energy transfer appears as a red shift of the spectrum, with shift increasing with propagation length.

In the case of ethylene, a neglect of either GVD or Raman worsens the agreement with the measured spectrum. It denotes that both GVD and Raman contribute substantially to the

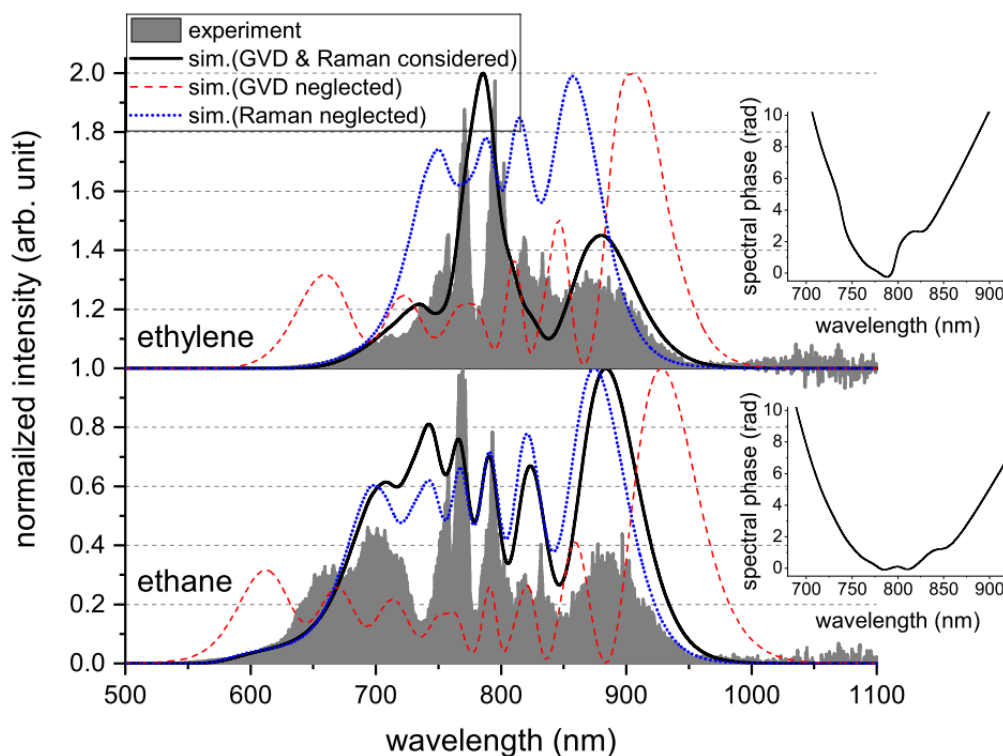


**Figure 47** measured (area filled with gray) and simulated (solid black with both GVD and Raman being taken into account, dashed red without GVD and dotted blue without Raman) spectra for ethane (lower panel) and ethylene (upper panel) at a given input energy of 50% of the  $E_{th}$ . The insets are spectral phases conjugated to the simulated spectra with both GVD and Raman components being taken into account.

spectral shape in ethylene. On the other hand, for ethane, disregard of GVD induced noticeable divorce from the measured spectrum whereas that of Raman exerts little influence; decent agreement with the experiment is revealed by considering solely GVD. Relatively weak Raman contribution in ethane is accounted for the smaller  $f_R$  for the C-C stretch mode compared to ethylene. It implies that the  $\pi$ -bond between two carbon atoms in ethylene (C=C) is responsible for larger Raman cross section than ethane (C-C). It makes the Raman contribution of ethylene nonnegligible while the electronic contribution dominates in ethane. Eventually it results in a dissimilar spectral shape in ethane and ethylene. In ethane, noble gas-like spectral broadening takes place via SPM whereas ethylene renders the spectrum redshifted by Raman, leading to relative frustration of blue.

In the calculations on spectral broadening with respect to increasing input pulse energy, which are superimposed onto Figure 46(a) and (b) (hollow symbols), a comparable red shift and a stronger blue shift for the saturated molecules is predicted, in agreement with our experimental

observations. The agreement is noticeably better for lower energies. This is because the ionization, recognized by a decrease in transmission, onsets around ~60% of  $E_{th}$  (Figure 45(c)) and the numerical simulations do not take the contribution of an ionized medium into account. Especially for the saturated hydrocarbons, as well as for krypton, the ionization is also manifested by an intensified blue shift (see spectral modulation in the blue Figure 46(a), (b) and (e)); the measured blue edges for higher input energies tend to be overestimated. It elucidates the discrepancy between measurement and simulation at the blue edge for higher energy regimes near  $E_{th}$ .

As the saturated hydrocarbons exhibit spectra about two times broader than the unsaturated ones as shown in Figure 46(b), they are deemed proper nonlinear media for pulse compression. An input pulse energy well below  $E_{th}$  (~16  $\mu$ J) in conjunction with a higher pressure (~6.5 bar in absolute pressure) facilitates a sufficient spectral width to support sub-10fs pulses. The employment of pressure gradient minimizes unwanted nonlinear effects like self-focusing and filamentation at the input of the hollow core fiber [87]. The spectrally broadened pulses are compressed by chirped mirrors installed downstream, and characterized by second harmonic generation frequency resolved optical gating (SHG-FROG), demonstrating ~8fs pulse as displayed in Figure 48. Unsaturated hydrocarbons, in contrast, cannot compress below 15fs. This is also consistent with the simulations. The calculated spectral phase of ethane is nearly parabolic, thus compressible to the transform-limit by compensating the group delay dispersion (GDD). On the other hand, ethylene is subjected to a stronger high order spectral phase, which allows considerable residual phase in spite of the cancellation of GDD (insets of Figure 47).

Moreover, the unsaturated hydrocarbons gradually degrade in transmission over time, which makes them unsuitable for practical use, while the saturated ones maintain the performance over time. This is tested with input pulses with an excessive energy of about two to three times the  $E_{th}$ , in order to expedite the response. For the unsaturated molecules, an exposure to such high energy pulses leads to a steady drop of the HCF transmission (see Figure 50 in the appendix). A visible deterioration of the HCF is recognized after a prolonged irradiation, as its inner wall near the laser entrance gets coated with black dust. This is because  $C_2H_4$  and  $C_2H_2$  are highly reactive when ionized as the carbons are not saturated and new chemical bonds can be created resulting in the formation of larger molecules, namely, polymerization.

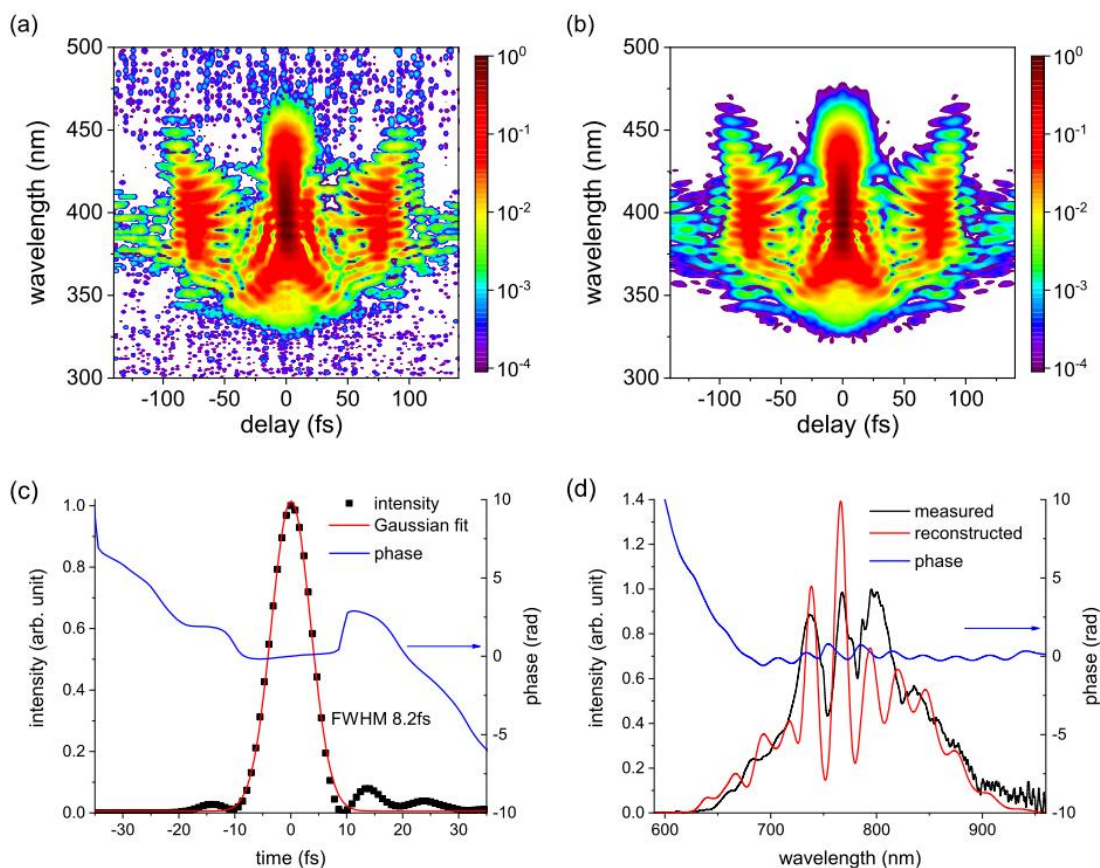


**Figure 48** Compressed pulses characterized by means of SHG-FROG. The 40fs, 16 $\mu$ J input pulses are guided through a HCF filled with methane at 6.5bar then compressed using chirped mirrors. (a) measured and (b) reconstructed spectrogram and corresponding (c) temporal and (d) spectral intensity profiles and phases.

To summarize, spectral broadening of femtosecond laser pulses using HCF is compared for single- and multiple-bonded hydrocarbons under controlled conditions. The spectral widths from saturated hydrocarbons are roughly twice broader than those from the unsaturated ones, and similar to the reference noble gas, krypton. This is mainly because of the suppressed blue shift for the unsaturated carbon bonds due to a larger Raman cross section originating from their  $\pi$ -bonds. The compressibility of wider spectra from the saturated molecules is confirmed by characterizing  $\sim$ 8fs pulses after optimizing the GDD. This work suggests the feasibility of saturated hydrocarbons as an inexpensive compression media for low energy, high repetition rate laser sources.

### 5.3.3 Appendix

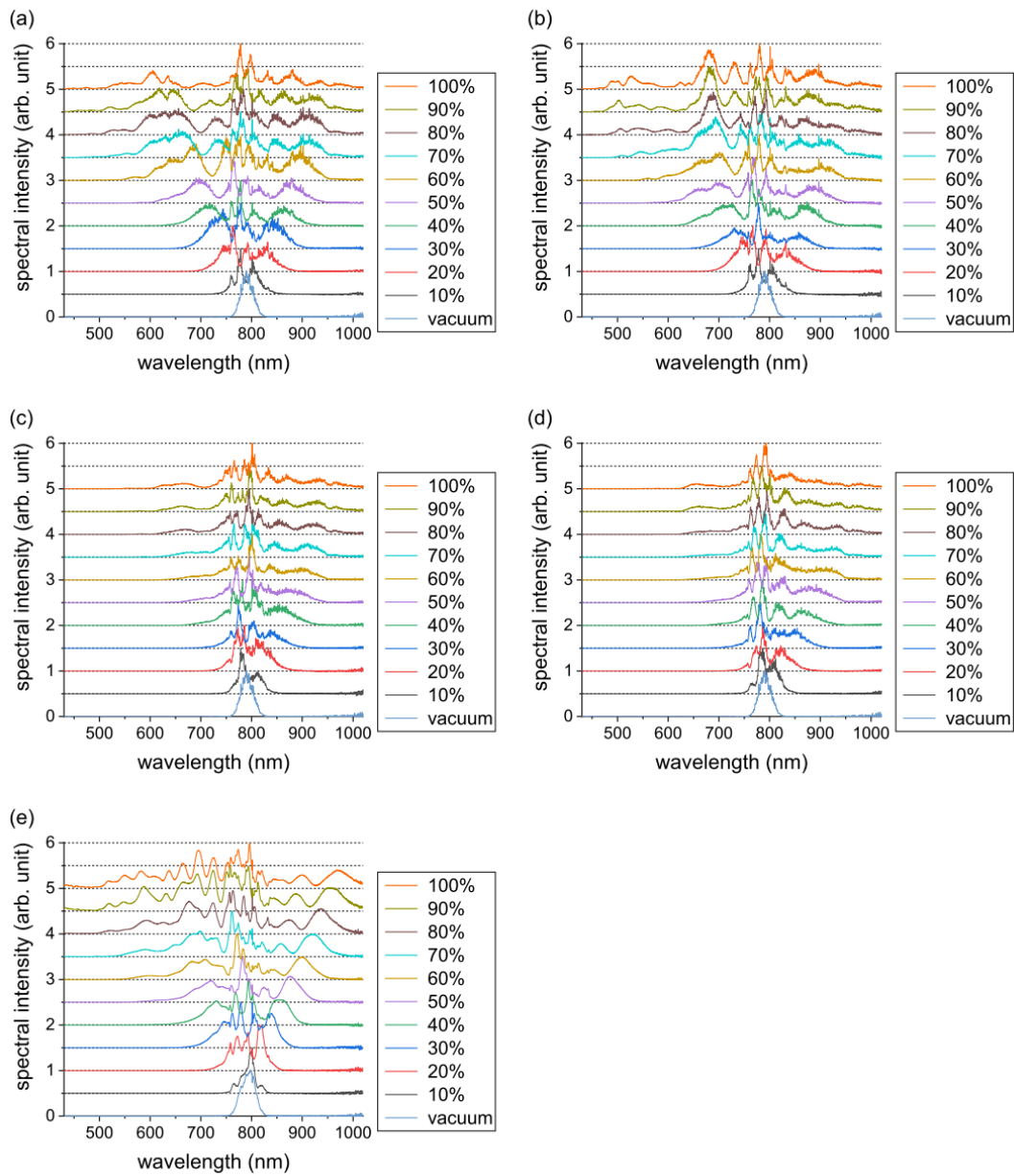


**Figure 49** Measured spectra of hollow core fiber output filled with 1 bar of (a) methane, (b) ethane, (c) ethylene, (d) acetylene and (e) krypton for varying input pulse energy up to  $E_{th}$  of each gas. All spectra are corrected by multiplying the response curve of the spectrometer and the amplitudes are normalized to one. The spectra are vertically fanned out with the spacing of 0.5 unit for clearer visualization.

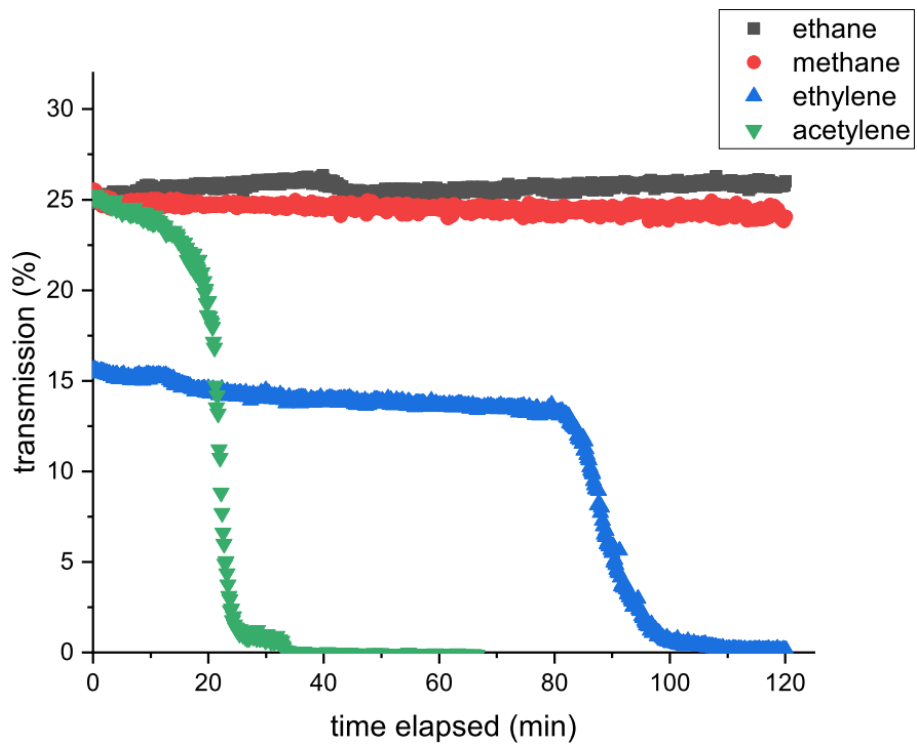


**Figure 50** HCF transmission against elapsed time with an exposure to excessive input energy, namely, two to three times higher than  $E_{th}$ .

## 6 Article IV: High energy redshifted and enhanced spectral broadening by molecular alignment

G. FAN,<sup>1\*</sup> R. SAFAEI<sup>1\*</sup>, O. KWON<sup>1</sup>, V. SCHUSTER<sup>2</sup>, K. LÉGARÉ<sup>1</sup>, P. LASSONDE<sup>1</sup>, A. EHTESHAMI<sup>1</sup>, L. ARIAS<sup>3</sup>, A. LARAMÉE<sup>1</sup>, J. BEAUDOIN-BERTRAND<sup>3</sup>, J. LIMPERT<sup>2</sup>, Z. TAO<sup>4</sup>, M. SPANNER<sup>5</sup>, B. E. SCHMIDT<sup>6</sup>, H. IBRAHIM<sup>1</sup>, A. BALTUŠKA<sup>7</sup> AND F. LÉGARÉ<sup>1†</sup>

<sup>1</sup>Institut National de la Recherche Scientifique, Centre Énergie Matériaux et Télécommunications, 1650 Boulevard Lionel-Boulet, Varennes, Québec, J3X 1S2, Canada

<sup>2</sup>Institute of Applied Physics, Abbe Center of Photonics, Friedrich Schiller University Jena, Jena, Germany

<sup>3</sup>Centre d'optique, photonique et laser (COPL), D'épartement de physique, génie physique et optique, Université Laval, Québec, G1V 0A6, Canada

<sup>4</sup>State Key Laboratory of Surface Physics, Department of Physics, Fudan University, Shanghai 200433, China

<sup>5</sup>National Research Council Canada, 100 Sussex Dr., Ottawa, Ontario K1A 0R6, Canada

<sup>6</sup>Few-cycle Inc., 2890 Rue de Beaurivage, Montreal, Quebec, H1L 5W5, Canada

<sup>7</sup>Institute of Photonics, TU Wien, Gusshausstrasse 27/387, Vienna, Austria

\*These authors have contributed equally.

†Corresponding author: [legare@emt.inrs.ca](mailto:legare@emt.inrs.ca)

G. Fan, R. Safaei, O. Kwon, V. Schuster, K. Légaré, P. Lassonde, A. Ehteshami, L. Arias, A. Laramée, and J. Beaudoin-Bertrand, "High energy redshifted and enhanced spectral broadening by molecular alignment," *Opt. Lett.* 45, 3013-3016 (2020).

**Personal contribution:** G. Fan and I designed and conducted the experiments. Besides, I I have improved the code for numerical simulations to take into account the effect of nonadiabatic molecular alignment. The numerical simulations were used to explain the experimental results. G.Fan and I also analyzed the experimental results and we wrote the first draft of the manuscript together, and include the comments of all co-authors. The failure of the 1D numerical simulations for sub-picosecond pulse duration has been the indication of spatiotemporal dynamics in the HCF (see next chapter).

### 6.1 Abstract

The spectral broadening of long laser pulses and for efficient frequency red-shifting by exploiting the intrinsic temporal properties of molecular alignment inside a gas filled hollow-core fiber

(HCF). We find that laser induced alignment with durations comparable to the characteristic rotational timescale  $T_{Rot}^{Align}$ , enhances the efficiency of red-shifted spectral broadening compared to noble gases. The applicability of this approach to Yb lasers with (few hundred fs) long pulse duration is illustrated, for which efficient broadening based on conventional Kerr nonlinearity is challenging to achieve. Furthermore, this approach proposes a practical solution for high energy broadband long-wavelength light sources, and it is attractive for many strong field applications.

## 6.2 Main manuscript

Recent advances in the field of coherent control of molecular excitation enable new techniques for spectral broadening and light pulse manipulation [109]. The timescales of laser induced molecular alignment can be categorized in two different regimes: 1) In the regime of adiabatic excitation where the pulse duration is much longer than the period of molecular rotation [107, 214, 215], maximum alignment is obtained at the peak of the laser pulse envelope. The medium returns to isotropic once the pulse is over. 2) In the regime of impulsive excitation, where the input pulse duration is comparable to the period of molecular rotation, momentum imparted by the laser persists after the passage of the pulse and is referred to as the ‘kicked-rotor’ [123, 216]. In this regime, the pump pulses create wave packets corresponding to coherent rotational motion of the molecules, which leads to ultrafast index transients [217]. Using this approach, the spectra and phases of ultrashort light pulses have been manipulated following pump-probe schemes. A pump pulse triggers a time evolution of the molecular alignment and of the resulting optical susceptibility, which implements phase changes to the ensuing probe pulse with variable time delays [116, 117, 218]. Despite the great progresses, so far, the scaled energy, the low efficiency and the complexity of this method make it less practical than the state-of-the-art SPM-based method [19, 81, 219]. Although, the SPM approach has led to significant applications in diverse fields of laser science [220], its broadening efficiency is inversely proportional to the pulse duration. This makes it less applicable for longer pulses of (sub-)picosecond duration. Furthermore, the typical maximum peak power achievable through SPM-based pulse compression is limited to  $\sim 1$  TW.

In this work, we investigate a simple single pulse approach to broaden the spectrum of long laser pulses (sub-ps) that relies on nonadiabatic molecular alignment. We experimentally and numerically clarify that the efficiency of spectral broadening reaches its maximum when the duration of the pulse is comparable to the time at which the nonadiabatic alignment of the molecules is maximized ( $T_{Rot}^{Align}$ ) (Figure 51). We illustrate the high efficiency of spectral broadening in HCF filled with N<sub>2</sub> gas by

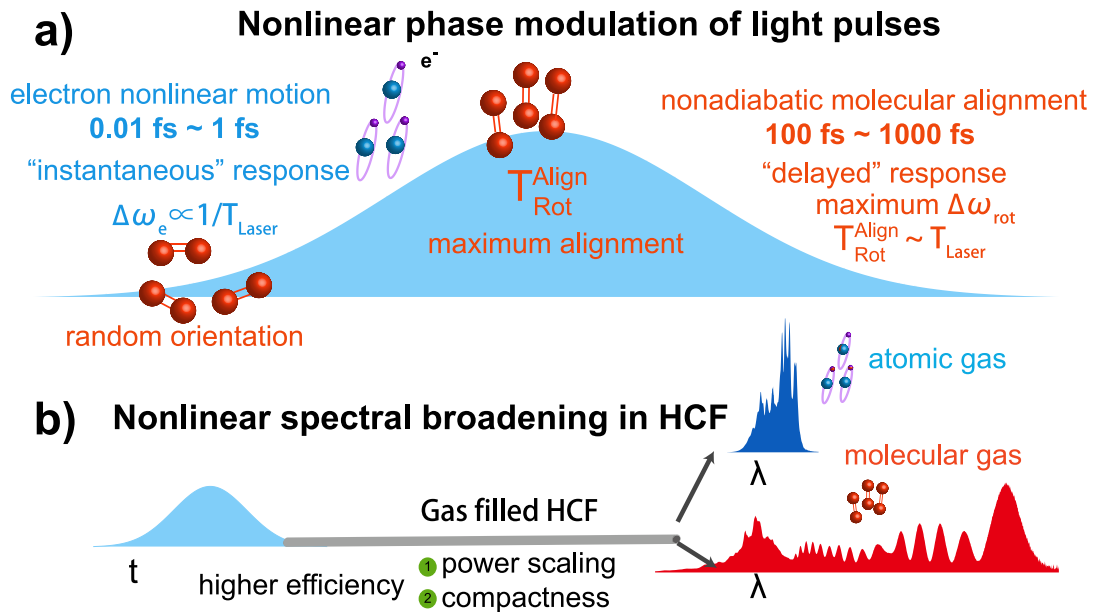


**Figure 51** Conceptual illustration of spectral broadening in HCF, (a) comparison of instantaneous response and delayed response. (b). The spectral broadening for longer pulses is more efficient in the molecular gas medium taking advantage of the timescale for nonadiabatic molecular alignment (hundreds of fs to ps).

scanning the pulse duration from 40 femtosecond (fs) to the sub-ps regime. The resulting spectra support not only few-cycle pulse duration but are also red-shifted, making this feature suitable for particular applications such as extending the cutoff in high harmonic generation [221] and efficient terahertz generation [222].

To conduct a comparative study,  $\text{N}_2$  and Ar were chosen as representative specimens of molecular and atomic gases since they possess a comparable ionization potential [88]. The experiment was carried out at the Advanced Laser Light Source (ALLS) laboratory. A Ti:Sa chirped pulse amplifier (CPA) which delivered 40 fs transform-limited pulses with a central wavelength of 780 nm and maximum energy of 13 mJ at a repetition rate of 100 Hz was used. The output of the CPA was focused on a spot size of  $\sim 330 \mu\text{m}$  and coupled into a 2-meter-long HCF (few-cycle Inc.). The measured transmission was about 50%. The HCF has a core diameter of 500  $\mu\text{m}$ , and was filled with either Ar or  $\text{N}_2$  at a pressure of 760 torr. The peak intensity inside the fiber was kept constant ( $\sim 7 \text{ TW}/\text{cm}^2$ ) when pre-chirping the Ti:Sa pulses from 40 fs to 1300 fs by increasing the energy from 0.4 mJ to 13 mJ. The pulse duration was varied by changing the separation between the grating pairs (adding positive group delay dispersion (GDD)). The spectra at the output of the HCF were measured with a VIS/NIR spectrometer (Avantes, AvaSpec-ULS2048XL).

The spectral broadening in atomic and molecular gases for varying input pulse durations is illustrated in Figure 52. We note two striking aspects. (1) The spectral shapes from Ar and N<sub>2</sub> clearly differ. In Ar, the generated spectra were broadened more symmetrically, still conserving the central wavelength near 780 nm. Noted that the slight asymmetry in Ar spectra towards the blue side comes from self-steepening effect. The dynamic can be mainly attributed to the instantaneous nature of the electronic Kerr response; the change of nonlinear refractive index  $\Delta n(t)$  is proportional to the intensity profile of the laser pulse  $I(t)$ ,  $\Delta n(t) = n_2 I(t)$ . Therefore, if  $I(t)$  is symmetric, the 1st order time derivative of  $\Delta n(t)$ , namely, the instantaneous frequency  $\Delta\omega \sim \frac{d}{dt} \Delta n(t)$ , indicates that the red-shift of the leading edge and the blue-shift of the trailing edge are equal, thus producing broadened symmetric spectra. In contrast, for N<sub>2</sub>, the center of gravity of the pulse spectra is clearly red-shifted. In this case, the molecules are not responding instantaneously to the temporal profile of the pulses. Such response can be described mathematically by

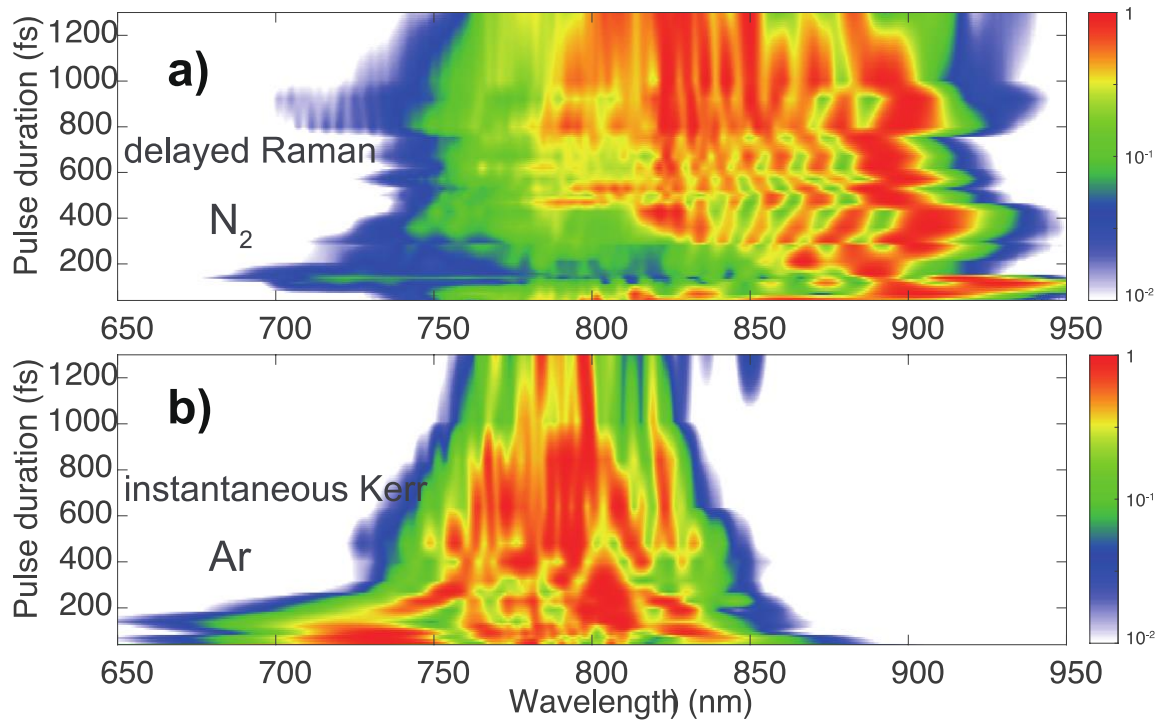


**Figure 52** Comparison of nonlinear spectral broadening depending on the pulse duration for a) delayed response medium (N<sub>2</sub>) and b) Kerr medium (Ar) at fix pressure of 760 Torr.

the delayed molecular response function  $R(\tau)$ . Thus,  $\Delta n(t)$  can be obtained as a convolution of the  $R(t)$  and  $I(t)$ , i.e.,  $\Delta n(t) = \int R(\tau)I(t - \tau)d\tau$  which is delayed with respect to the input pulse. Consequently, the pulse overlaps temporally mainly with the leading edge of  $\Delta n(t)$ , which generates new frequencies at longer wavelengths, resulting in asymmetric spectra. It is noted that the degree of

the spectral asymmetry depends on the ratio between the overlap of the pulse envelope with the leading and the trailing edges of  $\Delta n(t)$ . (2) Another apparent difference was revealed in the spectral width for increasing pulse durations. In Ar, the spectral bandwidth decreased when the pulses were stretched to several hundred fs. Longer pulse durations imply a gentle slope of  $I(t)$  and thus a smaller spectral broadening ( $\Delta\omega$ ). On the other hand, the behavior of N<sub>2</sub> showed a clear difference with a maximum spectral width appearing for 100 fs pulses, which remained up to the ps regime.

To gain physical insight into this delayed response nonlinearity and its link to the vibrational and rotational motion of the molecules, numerical simulations were conducted. They provide a qualitative explanation of the observed results. For the rotational response, the molecular alignment  $\langle \cos^2\theta \rangle$  is calculated by solving the time-dependent Schrodinger equations (TDSE) using a basis of pendular (field-free rotational) states.  $T_{Rot}^{Align}$  is attributed to the input pulse duration that drives the strongest alignment for a fixed peak power. In other words,  $T_{Rot}^{Align}$  is the pulse duration for which the average alignment  $\langle \cos^2\theta \rangle$  reaches its maximum value [223]. Furthermore, the rotational contribution to the response function  $R(\tau)$  is modeled as a damped harmonic oscillator [82]  $R_0 \exp(-\frac{t}{\tau_2}) \sin \frac{t}{\tau_1}$ , and the values of the parameters  $R_0$ ,  $\tau_1$ , and  $\tau_2$  are determined from fits of  $\Delta n(t) = \int R(\tau) I(t - \tau) d\tau$  to the refractive index change calculated from TDSE simulations. Finally, the pulse evolution in the gas filled HCF is simulated through solving the nonlinear Maxwell-Schrodinger equation by adopting the calculated  $R(\tau)$  for N<sub>2</sub>.

The simulated spectra for N<sub>2</sub> are in good agreement with the measured ones, as shown in Figure 53(a) and Figure 53(b). When the pulse duration is increased from 40 fs to 100 fs, the spectrum is red-shifted from 900 nm to a maximum value of 950 nm. To corroborate the optimal broadening at a particular pulse duration, we calculated the nonlinear refractive index change  $\Delta n$  and the induced instantaneous frequency  $\Delta\omega$  for three pulse durations, characterized as shorter (40fs), similar (100fs), and longer (200 fs) than the time scale for maximum nonadiabatic alignment of N<sub>2</sub> (Figure 53(c) and Figure 53(d). In Figure 53(d), the calculated  $R(t)$  is also illustrated (gray line). We observed that for a given  $R(t)$ , the convolution ( $\Delta n(t) = \int R(\tau) I(t - \tau) d\tau$ ) results in the most steepest slope for the change of refractive index ( $\Delta n(t)/dt$ ) when the pulse duration is similar to  $R(t)$ . In other words, when the pulse duration is comparable to the characteristic time of the molecular rotation, the molecules reach maximum alignment within the fastest time scale, resulting in maximum spectral broadening.

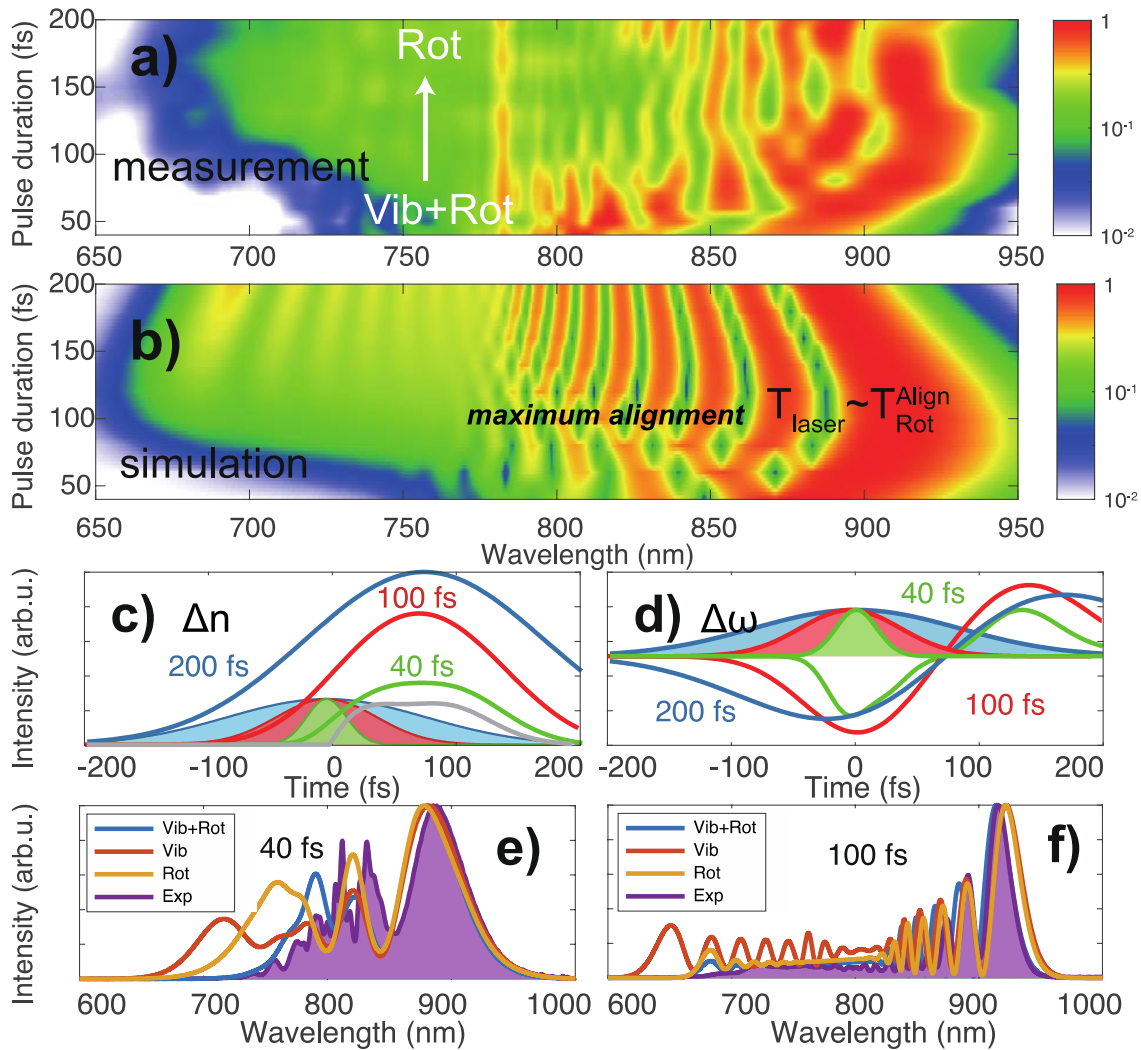


**Figure 53** Comparison of a) measured and b) simulated spectral evolution vs. pulse duration at constant laser peak intensity in  $N_2$  at 760 Torr. The maximum spectral broadening was achieved for pulse durations comparable to the characteristic time of nonadiabatic alignment  $T_{Rot}^{Align}$ . c) illustrates the change of refractive index  $\Delta n$  and d) the instantaneous frequency  $\Delta\omega$  with different pulse durations, i.e., 40, 100 and 200 fs, covering the characteristic time of  $T_{Rot}^{Align}$ . Simulated spectra with vibrational (red), rotational (yellow) and both modes (blue) being considered superimposed onto the measured one (purple) for pulses of e) 40 fs and f) 100 fs duration.

To identify whether vibrations and/or rotations play the major role in the observed broadening, we have studied their individual contributions to  $R(t)$ . Simulated spectra for 100 fs pulses are depicted in Figure 53(f). It is demonstrated that the vibrational contribution is negligible for 100 fs pulses by showing the simulated spectra with (blue) and without (yellow) the vibrational terms. We observed almost the same spectral shape, which indicates that the effect of rotational motion dominates for  $>100$ fs pulses. This comes at no surprise since the input pulses are not short enough to impulsively excite vibrational states. For 40 fs pulses studied in e) on the other side, considering only vibrations or only rotations

result in simulated spectra that deviate from the measured one (red and yellow lines). Only the simulation taking into account both vibrational and rotational modes agrees very well with the measurement (blue line). This can be understood from the fact that in the case of  $N_2$ , the characteristic vibrational time is around 14.9 fs [124] and denotes that 40 fs pulses activate both vibrational and rotational modes with substantial weights. We thus were able to confirm that rotational effects play the major role in the few hundreds fs regime while both vibrational and rotational effects are significant for sub-100 fs pulse.

In order to demonstrate the compressibility of the broadened spectra, we post-compress them with chirped mirrors and compare the compressed results with numerical simulations. Figure 54 presents the case where 120 fs transform-limited pulses are broadened in the hollow core fiber at constant pressure. The pulses were obtained by filtering the spectra of 40 fs pulses with a band pass filter. Temporal pulse characterization was performed with second harmonic generation frequency resolved optical gating (SHG-FROG). Figure 54(a) is the SHG-FROG trace for the input 120 fs pulses. At the output of the hollow core fiber, the pulses are compressed using a combination of chirped mirrors (Ultrafast Innovations GmbH PC70) with fused silica for fine tuning the GDD at the HCF output, for a total compensation value of about  $-176 \text{ fs}^2$ .

The SHG-FROG traces for the compressed pulses are presented in Figure 54(a) with the reconstruction in Figure 54(b). In Figure 54(c), we present the spectra of the broadened pulses and we compare the experimental spectra to the retrieved spectra from the SHG-FROG. The observed periodic structure in the spectra has an increasing spacing towards the long wavelength side. This feature can be understood as spectral interference, where the same instantaneous frequencies are generated at two distinct temporal positions (Figure 53(d)). From the SHG-FROG reconstruction, the retrieved temporal profile (Figure 54 (d)) shows the main pulse contains around 50% of the energy with a duration of 7.8fs, close to its Fourier limited pulse duration of 6.2 fs. The pre-pedestal originates from an intrinsic feature of the Raman process which induces a negative chirp at the leading edge of the pulse at the maximum alignment regime, as indicated at Figure 53(d). Finally, when comparing the experimental results with the numerical simulations, we find that the positive chirp of the HCF input pulses has no impact on the broadening. Furthermore, we have achieved pulse compression similarly as for Fourier limited input pulses by using  $-155 \text{ fs}^2$  in the simulations (see Figure 54(d), Simulation FT vs Simulation Chirp).

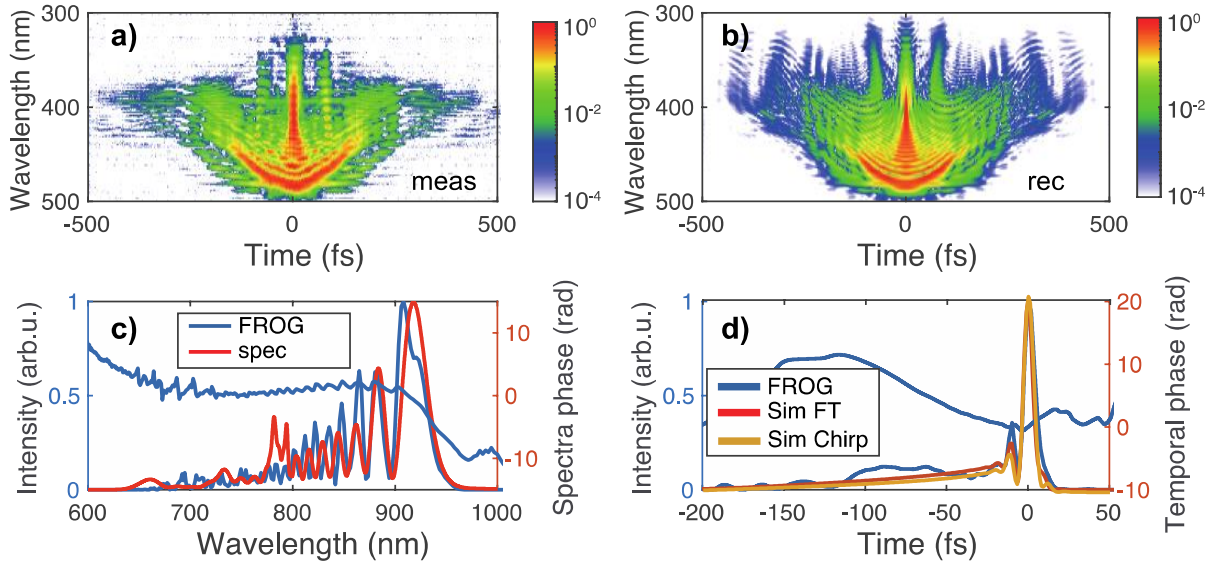


**Figure 54** Compressed pulses characterized by SHG-FROG. The 120 fs input pulses are guided through a HCF filled with nitrogen at 1 bar, then compressed using chirped mirrors. The (a) measured and (b) reconstructed spectrogram and corresponding (c) spectral and (d) temporal intensity profiles. Sim FT and Sim Chirp represent the numerical results for 120fs transform-limited input pulses and 120fs input pulses positively chirped from 40fs transform-limited pulses.

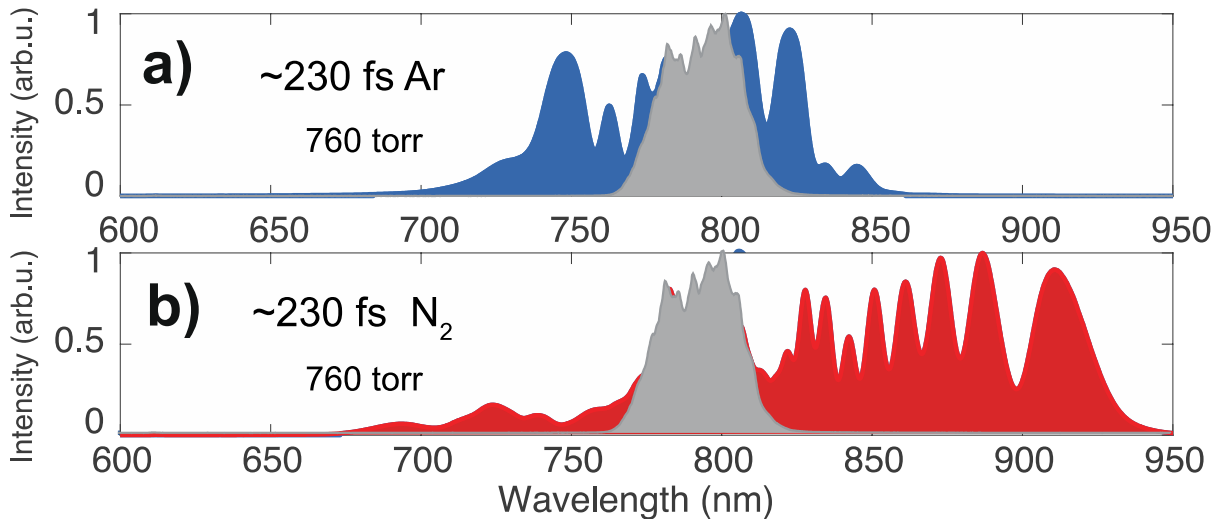


**Figure 55** Comparing the measured efficiency of spectral broadening in Ar (a) and N<sub>2</sub> (b) for 230 fs pulse duration at 760 Torr. At 230 fs, we considered the newly generated spectral components (color filled part, blue in Ar, red in N<sub>2</sub>. gray denotes input Ti: Sapphire spectrum), which corresponded to a Fourier transform limit (FTL) of (c) 25.3 fs from Ar and (d) 17.3 fs from N<sub>2</sub>, respectively. The compressibility of the above spectra is further verified by performing numerical simulation by adding negative chirp to the simulated output pulse.

At a few hundred fs timescale, where the characteristic times of nonadiabatic alignment ( $T_{Rot}^{Align}$ ) of most molecules lay ( $N_2 \sim 100$  fs,  $O_2 \sim 150$  fs), these molecules are more suitable than noble gases for spectral broadening. In Figure 55, we compare the spectral broadening in Ar and  $N_2$  for a commonly available laser pulse duration for Yb lasers (230 fs). For a fixed laser peak power and pressure, the  $N_2$  yields over 50% more spectral broadening than Ar. Thus, the broadening from molecular alignment is a promising approach to compress, with a simpler setup, longer laser pulses as compared to SPM in noble gases. This is consistent with recently reported pulse compression of  $>200$  fs Yb laser systems using HCF filled with molecular gases [224]. We note the present approach for pulse compression via rotational Raman process may not be ideal to generate few-cycle pulses with the cleanest temporal profile as resulting from SPM. Despite, given its simplicity the present approach has the potential to be very attractive for the pulse compression of laser systems with hundreds of fs pulse duration.

Here, we demonstrate the applicability of our approach to the spectral broadening of laser sources delivering pulses with a few hundred fs to ps durations. On this time scale, the molecular alignment induced nonlinear phase is the convolution of the pulse envelope with the response function of the molecules. As a result, most features of the spectral broadening induced by molecular alignment are not sensitive to the initial phase but only to the envelope. As shown in both our experiments and our numerical simulations, for a fixed pulse duration, the spectral broadening is slightly more efficient for pulses with a positive chirp compared to Fourier transform limited pulses of the same duration (using spectral filtering). For a negative chirp, we have performed numerical simulations and we observe a slightly smaller bandwidth than for a Fourier transform limited pulse. Therefore, our approach could be used for the efficient spectral broadening of sub-ps pulses from Ytterbium laser systems such as fiber[53] based, InnoSlab[132] and thin-disk ones[69]. Furthermore, the demonstrated results predict a clear potential for further power scaling. Previous studies of optical response near the ionization threshold reported that the threshold intensity of  $N_2$ , around  $50\text{-}70$  TW/cm<sup>2</sup>, is slightly lower than that of Ar [225]. In this work, the laser pulse intensity was kept well below the threshold where ionization becomes important. This suggests the feasibility of compressing tens of mJ pulses to the few-cycle regime, if combined with a reasonable upscaling of capillary systems (For example:  $d=1$  mm,  $L=6$  meters).

In conclusion, we demonstrated a single pulse approach to scale the efficiency of spectral broadening in molecular gas-filled HCF by matching the intrinsic timescales of laser pulses and nonadiabatic molecular alignment. From a technological aspect, the exploitation of molecular alignment provides highly efficient spectral broadening of sub-ps laser pulses. This can lead to an energy upscaling up to the multi-TW level while also being applicable to Yb laser sources. The integration of molecular systems with a much slower characteristic response time and advanced hollow-core waveguide

technology could open new aspects of designing future high-performance nonlinear devices. Furthermore, the “impulsive” excitation of the molecules results in a strong wavelength red-shift enhancement, and this effect is independent on the driver wavelength. Therefore, this approach leads to a practical solution for red-shifting high energy ultra-broadband long-wavelength IR/mid-IR driver sources, and it is attractive for a variety of strong field applications, which benefit from such wavelength scaling.

## 7 Article V: High-energy multidimensional solitary states in hollow core fiber

REZA SAFAEI<sup>1\*</sup>, GUANGYU FAN<sup>1</sup>, OJOON KWON<sup>1</sup>, KATHERINE LÉGARÉ<sup>1</sup>, PHILIPPE LASSONDE<sup>1</sup>, BRUNO E SCHMIDT<sup>2</sup>, HEIDE IBRAHIM<sup>1</sup> AND FRANÇOIS LÉGARÉ<sup>1†</sup>

<sup>1</sup>Institut National de la Recherche Scientifique, Centre Énergie Matériaux et Télécommunications, 1650 Boulevard Lionel-Boulet, Varennes, Québec, J3X 1S2, Canada.

<sup>2</sup>Few-cycle Inc., 2890 Rue de Beaurivage, Montreal, Quebec, H1L 5W5, Canada.

†Corresponding authors: reza.safaei@emt.inrs.ca, legare@emt.inrs.ca

**Personal Contribution:** I designed and convinced the experiments with the help of G. F. Besides, I have improved the 1D code developed for the previous article (chapter 6) to take into account 3D effects. I. and G.F. performed the experiment with the support of O.K. and K.L. I and G. F analyzed the experimental data. Furthermore, I wrote the manuscript with the input from all co-authors.

### 7.1 Abstract

Multidimensional solitary states (MDSS), self-sustained wave packets, have attracted renewed interest in many different fields of physics[1-5]. MDSS find particularly important recognition in nonlinear optics, especially for the nonlinear propagation of ultrashort pulses in multimode fibers (MMF), which contain rich spatiotemporal intermodal interactions and dynamics[70, 71, 73], however often in an unstable manner. Here, we report the first time observation of the formation of highly MDSS in a molecular gas-filled large core hollow fiber (HCF). We experimentally and numerically demonstrate the creation of MDSS by multi-mJ sub-picosecond (ps) near-infrared pulses and its underlying physics. We find that the MDSS have a broadband red-shifted spectra with an uncommon negative quadratic spectral phase at HCF output, originating from Raman enhancement due to the strong intermodal nonlinear interactions. The spatial and temporal localization of MDSS enables the compression of the broadened pulses at the output to 10.8 fs by simple linear propagation in a piece of fused-silica. The high spatiotemporal quality of MDSS is further verified by high harmonic generation. Our results indicate that large core gas-filled HCF present new opportunities for studying high-energy, multimodal spatiotemporal dynamics with capabilities for considerable applications.

## 7.2 Main manuscript

In this letter, we demonstrate the generation of multidimensional solitary states (MDSS) in a large core HCF filled with nitrogen ( $N_2$ ). The experimental results and the numerical simulations indicate that the coupling to multimode states by high-energy driver pulses at HCF input favors the stimulate Raman scattering (SRS) process in a Raman active medium. Consequently, the enhanced spatiotemporal nonlinearity inhibits the potential diffraction due to self-focusing, leading to a high quality spatial localization of multidimensional states. The generated self-trapped MDSS at the beginning of the fiber undergo an enhanced Raman cascading process over the long interaction length of the HCF, resulting in broadband, red-shifted spectra at the HCF output. Furthermore, we find that the output MDSS pulses possess a negative quadratic spectral phase, which is counter-intuitive, as it is opposite to the spectral phase obtained from spectral broadening based on Kerr nonlinearity<sup>21</sup>. Thus, the output MDSS pulses can be directly compressed to few-cycle pulse duration through linear propagation in the normal dispersion regime provided by a simple piece of glass. To confirm the spatiotemporal quality of the compressed pulses, we drive the nonlinear process of high harmonic generation (HHG) and show the extension of the cut-off photon energy.

The physical concept of this work is illustrated and explained in Figure 56(a). As a starting reference point, the focal spot size at the HCF input pulse was chosen for obtaining high coupling efficiency into the fundamental mode. Under the weak guiding condition in the HCF, modes fall into groups of linearly polarized modes ( $LP_{mn}$ ) [128]. Self-focusing in the HCF is interpreted as the transfer of energy from the fundamental mode ( $LP_{01}$ ) to other  $LP_{0n}$  modes which have rotational symmetry with the maximum intensity in the central part[16]. In the high-energy regime, the effects of self-focusing and diffraction become significant and multiple  $LP_{0n}$  modes are created at the beginning of the fiber. These extended multidimensional pathways lead to an enhancement of the Raman process, which provides sufficient nonlinearity to balance the potential diffraction. This nonlinear self-trapping mechanism, together with the ultra-low modal dispersion inherent to large core HCFs, make the generated MDSS undergo efficient red-shifted spectral broadening through cascaded SRS. In the experiment, 700 fs, high-energy pulses (5 mJ /pulse) with a central wavelength of 780 nm were launched into a 3 m long hollow-core (500  $\mu\text{m}$ ) fiber filled with  $N_2$ . The 700 fs pulses are obtained by positively chirping 40 fs pulses from a Titanium-Sapphire amplifier (see methods). At the HCF output, the coherent solitary states are located at the leading edge of the initial driver pulse with a negative quadratic spectral phase. These solitary states are experimentally separated from the pump part by placing a long pass filter (above 830 nm) at the HCF output (the pump part

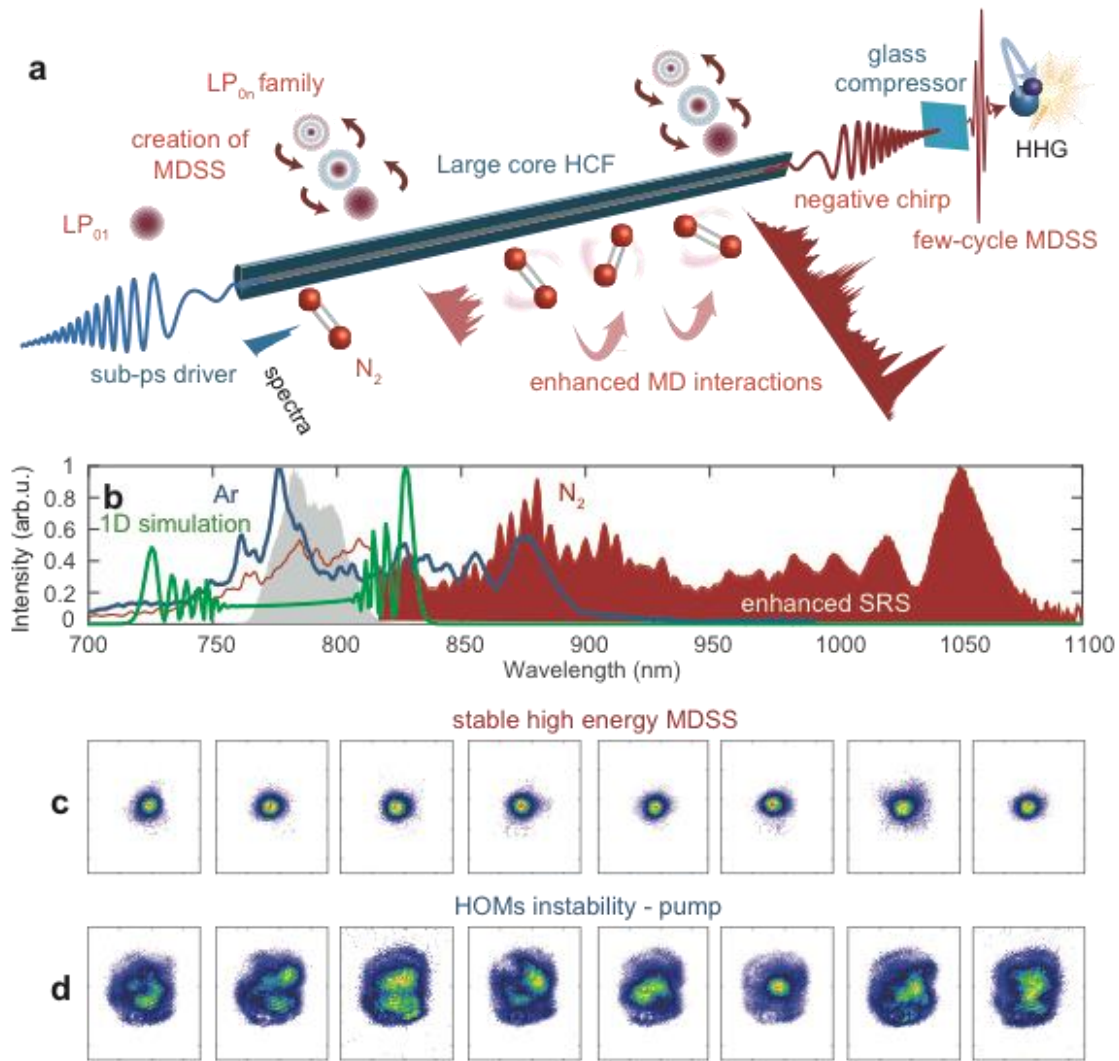


**Figure 56** (a) Conceptual illustration of the evolution of the self-trapped solitary states in the N<sub>2</sub> filled HCF. Above the fiber, the creation and propagation of the MDSS are shown. MDSS composed of LP<sub>0n</sub> modes are created at the beginning of the fiber on the left. These states are self-trapped in the LP<sub>0n</sub> modes family with periodic energy exchange while propagating through the fiber. The evolution of the spectra is depicted below the fiber, starting with the input spectra in blue, up to the broadened redshifted spectra in dark red. The broad red-shifted spectra originate from the process of enhanced cascaded SRS due to MD interactions over the long interaction length of the HCF. The output broadband MDSS pulses have a negative chirp and are compressed by linear propagation in a window of fused silica (normal dispersion below 1.3 microns). HHG is used to confirm the spatiotemporal quality and peak power of the red-shifted MDSS pulses. (b)-(d) Experimental observation of stable and self-trapped MDSS beam with enhanced red-shifted spectra. (b) The measured spectra for the 700 fs input driver after the N<sub>2</sub>-filled HCF (3 bar) indicating the enhanced red-shifted spectra through SRS (red part). The green curve shows the expected spectrum from a 1D simulation while the blue curve shows the experimental spectra for Ar (at the same pressure). The Ar spectra are much narrower than the N<sub>2</sub> spectra for the same pressure. The gray curve is the pump spectra at the fiber input. (c) These figures illustrate the MDSS spatial profile (obtained by putting an 830 nm long-pass filter after the fiber) for 8 single-shot consecutive pulses demonstrating the self-trapped, highly stable, and clean MDSS beam. (d) These figures report the same measurement for the fundamental beam (obtained using a band-pass filter (760nm-790nm)) indicating strong spatial instability and coupling to HOMs.

is selected by a band-pass filter (760nm-790nm)). The broadband MDSS pulses are subsequently compressed using a simple piece of fused-silica (FS). Details about beam characterization (temporal and spatial) are provided in the method section.

So far, nonlinear propagation in atomic gas-filled HCF is fundamentally limited due to the self-focusing effect at high peak power (comparable with the critical power) and inherent diffraction[16]. This causes the beam to couple to higher-order modes (HOMs) and induces instability as it propagates through the HCF. This imposes a threshold for the maximum pulse energy and gas pressure[78]. Surprisingly, we now observe enhanced red-shifted spectra in N<sub>2</sub> with stable spatial properties at peak powers comparable to the critical power for self-focusing (red curve in Figure 56(b)). The spectra extend towards much longer wavelengths than the prediction from 1D simulations (green curve). The stability of the self-trapped MDSS is demonstrated in Figure 56(c) with 8 consecutive single-shot far-field images. This is in strong contrast to the high instability observed for the pump part and caused by the nonlinear interactions and competition between HOMs (see Figure 56(d)). To illustrate the importance of the SRS process for the observed self-trapping effect, the measured spectra for argon (Ar) (Raman inactive medium) at the same conditions is shown as the blue curve in Figure 56(b). The output spectra are much narrower compared with N<sub>2</sub> which indicates no enhancement effect. In addition, self-focusing and multiple filamentation make this regime undesirable in the absence of the SRS process. Therefore, the coupling to multidimensional states together with the SRS process provides a unique regime in which the self-trapped solitary states can be created at peak powers comparable with the critical power for self-focusing.

The 1D simulations fail to reproduce the asymmetric spectra arising from a highly efficient red-shift exhibiting an effective contribution of the Raman process. This is due to the fact that the bandwidth of 700 fs pulses is too narrow to cover the rotational excitation step of N<sub>2</sub>. Thus, in 1D regime, the broadening is dominated by the Kerr nonlinearity resulting in a symmetric spectrum. Therefore, to fully understand the physics of our experimental observation, a more sophisticated numerical study is required that includes highly complex spatiotemporal effects arising from the mode coupling. Such MD simulations are performed by employing a set of N (numbers of modes) coupled nonlinear equations[128]. These equations are coupled to each other by four-dimensional nonlinear coupling tensors for Raman ( $S_{plmn}^R$ ) and Kerr nonlinearities ( $S_{plmn}^K$ ) since a cubic nonlinearity couples up to four distinct waves. Although with multiple coupled modes, the physics can be conceptually complex, the extended intermodal nonlinear interactions (expanded nonlinear terms in each equation via  $S_{plmn}^R$  and

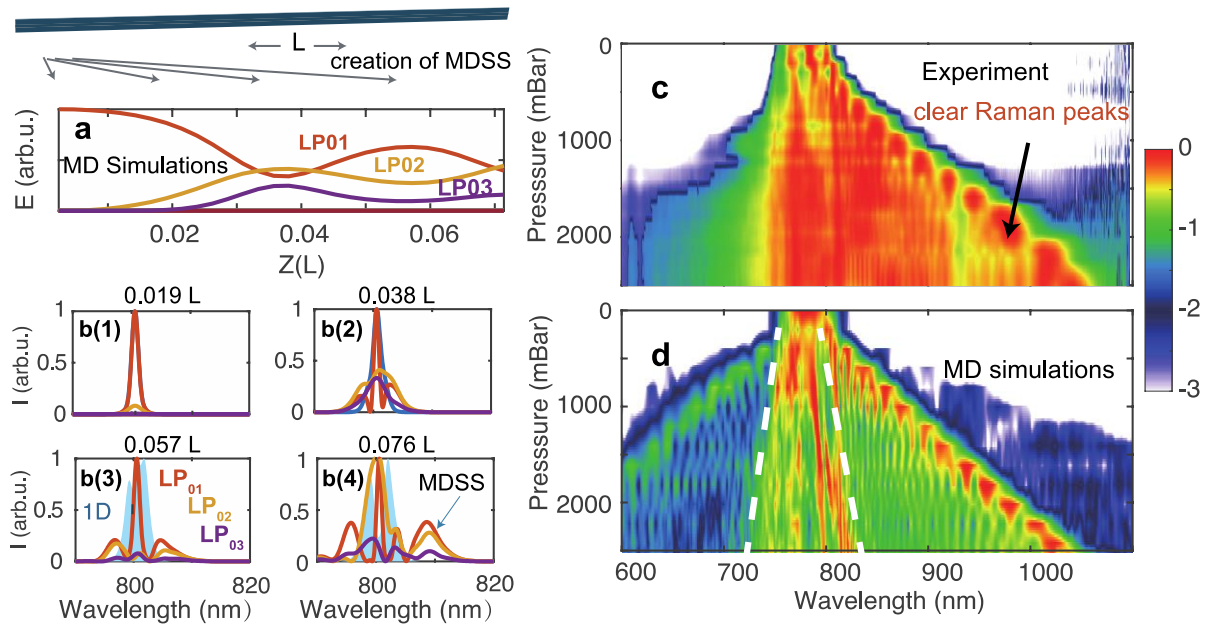


**Figure 57** Demonstration of the creation of MDSS and Raman enhancement via MD interactions. Simulations were performed for 700 fs input pulses with 5 mJ /pulse energy, propagating in an HCF filled with 2500 mbar of  $N_2$  of a total fiber length  $L$  of 3 m. (a) This figure shows the coupling of the fundamental mode  $LP_{01}$  to  $LP_{02}$  and  $LP_{03}$  at the very beginning of the fiber ( $<0.1L$ ), due to the high-energy input pulses. (b) The corresponding spectra of the  $LP_{01}$ ,  $LP_{02}$  and  $LP_{03}$  modes for four different positions at the beginning of the HCF. Each mode experiences wavelength shifts, primarily via IFWM. Once enough instantaneous bandwidth to support intermodal SRS is provided, the MDSS are created at the red part of the spectrum. The shaded blue spectrum is the 1D simulation result, where the only efficient nonlinear effect is self-phase modulation (SPM). In this case, there are no intermodal terms to enhance the nonlinearity. It should be noted that Fourier transform-limited (FT) input pulses are used in the simulations presented in (a) and (b) to better highlight the physical concept of the creation MDSS at the beginning of the fiber. (c) Experimental spectral broadening in  $N_2$  with 700 fs pulse duration and varying pressure under a constant peak power. (d) The corresponding MD simulations obtained by solving the generalized multimode nonlinear Schrödinger equations (GMMNLSE), considering 15 linearly polarized modes. Here, the input pulses for the simulations are 40fs positively chirped to 700fs. Numerical simulations assuming FT 700fs pulses are presented in the supplementary material. These results cannot be reproduced with 1D simulations (see the white dashed lines in (d)).

$S_{plmn}^K$ ) provide many pathways to enhance different nonlinear phenomena. To understand how the 700 fs pulses can drive efficiently the cascaded SRS, we present in Figure 57(a) and (b) the results of MD simulations corresponding to the nonlinear propagation at the very beginning of the HCF for a pressure of 2500 mbar. At the HCF input, the rotational excitation step of  $N_2$  is far larger than the bandwidth of 700 fs input pulse, thus, primarily intermodal four-wave mixing (IFWM) is the dominant nonlinear process for exchanging the energy between modes. This leads to the energy transfer from the fundamental mode ( $LP_{01}$ ) to higher  $LP_{0n}$  modes due to their high spatial overlap and high-energy input pulses. In this case, the most efficient

energy coupling takes place between the first three  $LP_{0n}$  modes (Figure 57(a)). In frequency domain, the pulses in each mode start to generate new frequencies through nonlinear interactions. This enables synchronized frequency components from different modes with a frequency difference that lies efficiently within the Raman gain bandwidth, which provides sufficient Raman gain for intermodal SRS (see method). Such interplay between the intermodal SRS and IFWM at the beginning of the fiber results in the creation of MDSS at the red part of the spectrum (4<sup>th</sup> figure in Figure 57(b)). It is noted that the created MDSS have sufficient instantaneous bandwidth to support the Raman gain, and their spectrum shifts towards the red due to a process resembling the well-known soliton self-frequency shift over the long interaction length of the HCF[76, 226]. However, through the propagation of MDSS through the fiber, the competition between SRS (active gain process) and IFWM may raise when more phase-matching pathways are established in favor of IFWM (coupling to HOMs other than  $LP_{0n}$  modes), and the SRS gain may increase or decrease from its value depending on the amplitude of phase-matching ( $\Delta k$ ). Thus, to drive very efficiently the cascade of the Raman process and to obtain a clean and stable output, IFWM for higher order modes other than  $LP_{0n}$  modes has to be suppressed by inducing a phase-mismatch. This is experimentally realized by adjusting the input coupling conditions to optimize the extension of the spectra towards the red and the spatial properties of the MDSS beam. The measured spectra for different pressures are presented in Figure 57(c). These results are well reproduced by MD simulations (Figure 57(d)) and demonstrate the clear signature of the rich dynamics originating from extended multidimensional intermodal pathways. In contrast, the 1D simulations cannot reproduce the enhanced red-shifted spectra since the instantaneous frequency bandwidth of the fundamental mode (the only mode in the simulation) is too narrow to cover the Raman gain bandwidth. Thus, nonlinear propagation in 1D regime is dominated by self-phase modulation. The spectral bandwidth obtained from the 1D simulations are presented as white dashed line in Figure 57(d).

The measured and simulated self-trapping evolution and energy distribution of different modes of the pump and MDSS for different pressures are illustrated in Figure 58. Through the nonlinear propagation and multimodal coupling in the HCF, a transfer of energy from the pump pulses centered at the fundamental wavelength to the red-shifted MDSS occurs. Figure 58(a) displays the experimental and MD numerical results of the photon conversion efficiency (CE) from pump to MDSS versus pressure, which leads to an enhanced red-shifted spectra. Up to 1 bar, the pump depletes rapidly while the MDSS energy grows exponentially. By further increasing the pressure, this process becomes slower owing to the spatiotemporal walk-off between the MDSS and

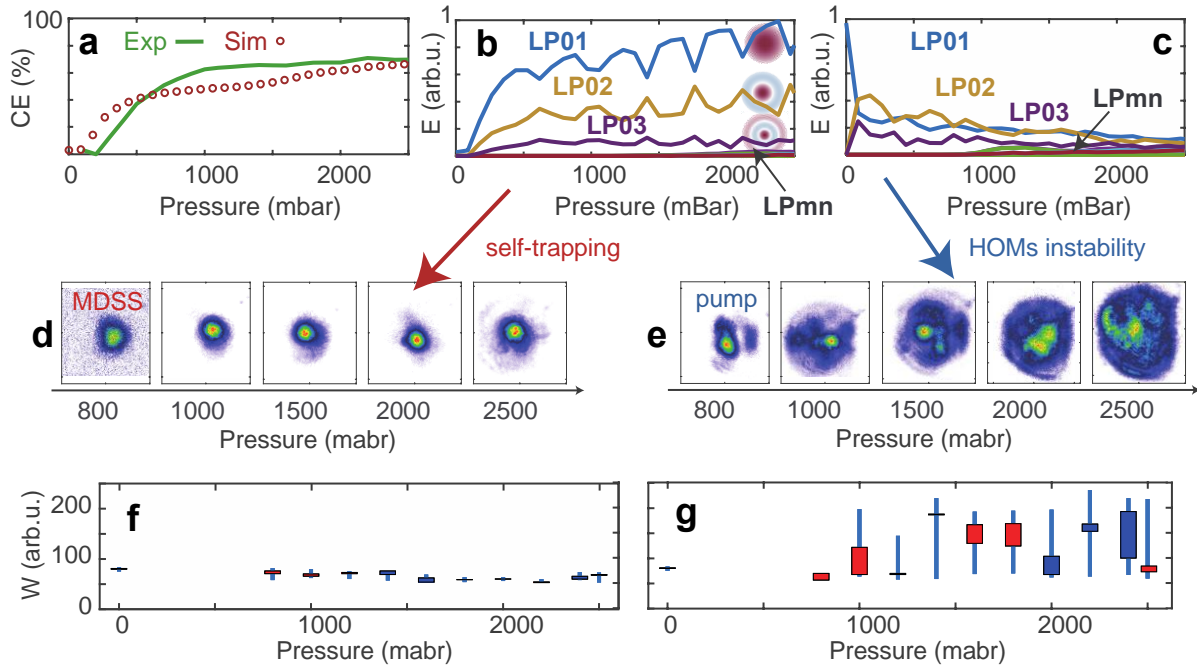


**Figure 58** Modal evolution of the self-trapped MDSS beam using 700 fs driver pulses with 5 mJ input energy. (a) Photon conversion efficiency (CE) from the pump to MDSS for experimental (green solid line) and simulation results (red dotted line) (b) The simulated evolution of energy distribution among different modes for the MDSS and (c) the pump part as a function of pressure. At the very beginning of the HCF, a significant amount of energy transfers from the fundamental to LP<sub>02</sub> and LP<sub>03</sub> modes, resulting in a very efficient SRS process. This leads to an efficient transfer of the pump energy to MDSS, self-trapped in LP<sub>0n</sub> modes. Measured single shot beam profiles of MDSS (d) and pump part (e) for different pressures. Here, the 15 modes used in the simulations are LP<sub>01</sub>, LP<sub>11a</sub>, LP<sub>11b</sub>, LP<sub>21a</sub>, LP<sub>21b</sub>, LP<sub>02</sub>, LP<sub>31a</sub>, LP<sub>31b</sub>, LP<sub>12a</sub>, LP<sub>12b</sub>, LP<sub>41a</sub>, LP<sub>41b</sub>, LP<sub>22a</sub>, LP<sub>22b</sub>, and LP<sub>03</sub>, respectively. LP<sub>mn</sub> modes in the figure indicates nonzero angular momentum modes ( $m > 0$ ). Statistical changes for the full width at half maximum (FWHM) of the spatial profile are shown for the MDSS beam (f) and the pump part (g) for 20 single-shot images per pressure (extracted from experimental measurements). The candlestick chart shows that the FWHM of the MDSS have negligible fluctuations which further confirms the self-trapping effect and the flatness of the waveform of the MDSS beam through its propagation in the HCF.

the pump. Figure 58(b) and Figure 58(c) illustrate the simulation results of the energy exchange among 15 individual modes in the MDSS and the pump part, respectively. This indicates that the MDSS beam is self-trapped into LP<sub>01</sub>, LP<sub>02</sub> and LP<sub>03</sub> modes (creating multidimensional solitary states) with periodic energy exchange between them due to the extended intermodal dynamics[16, 133]. The experimental evolution of the observed spatial solitary states with high spatial beam quality is displayed in Figure 58(d) and Figure 58(f). Furthermore, in the experiments, we did not observe any significant change in the input/output power-transmission

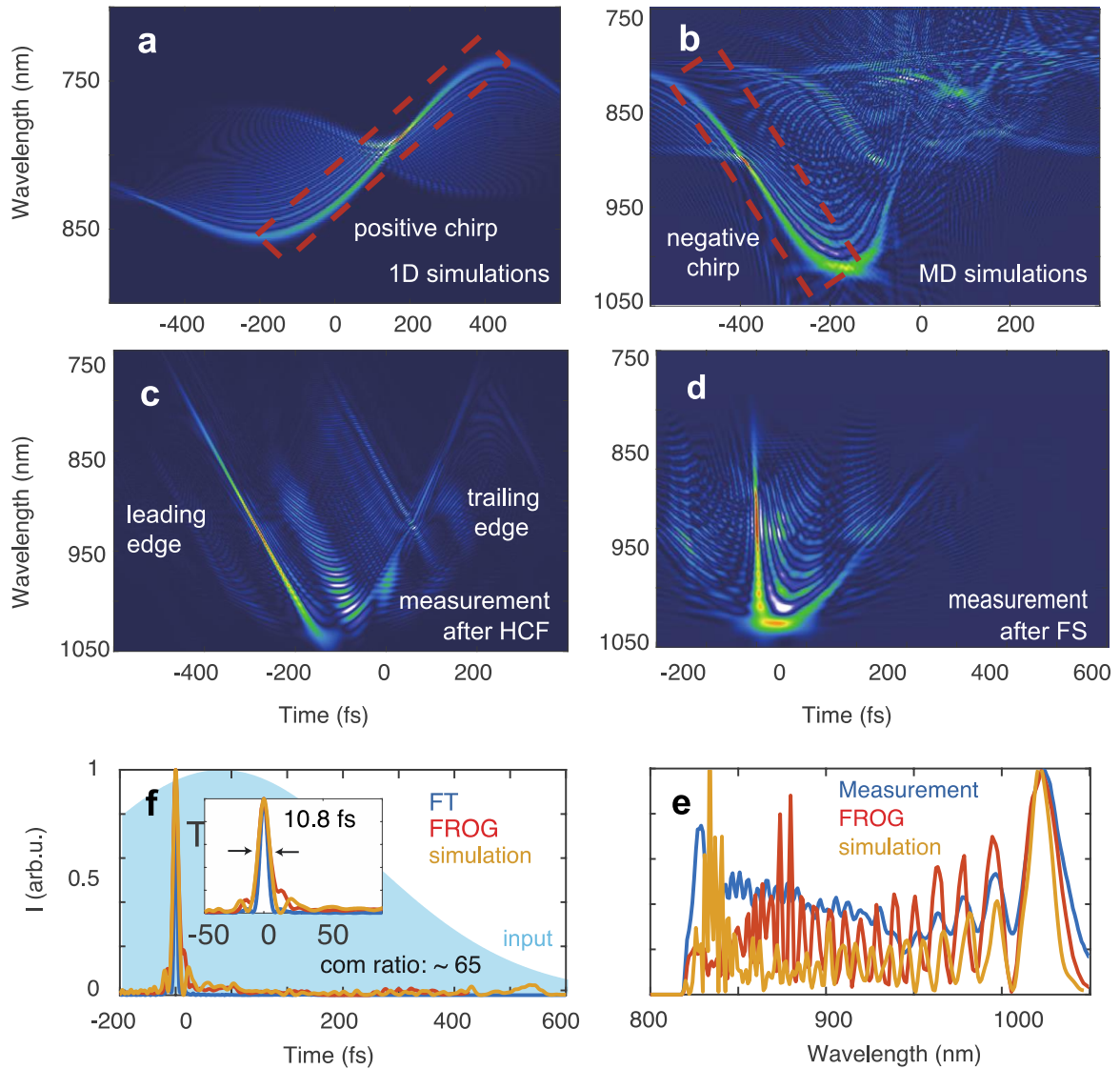


**Figure 59** Temporal evolution of the self-trapped MDSS driven by 5 mJ 700 fs pulses at 2500 mbar. (a) and (b) Wigner functions of the output pulse at HCF output predicted by 1D simulations and MD simulations, respectively. The outcome of 1D simulations predicts a positive quadratic phase for the output pulse since nonlinear propagation is dominated by SPM. (c) The Wigner function of the retrieved experimental SHG-FROG trace, directly measured at the output of the HCF. It shows the dominant negative quadratic spectral phase at the leading edge of the pulse, which contains the majority of the energy. This is in very good agreement with the results of MD numerical simulations. (d) The corresponding Frequency and temporal analysis of the compressed pulse with a piece of FS (12 mm). (f) Measured and MD-simulated temporal profile of the compressed pulse. (e) A comparison of the spectra measured with the spectrometer, retrieved from the SHG-FROG reconstruction of the 10.8 fs pulses, and from MD numerical simulations.

ratio from low to high pressure. This observation rules out the possibility of a simple linear self-cleaning effect due to linear spatial filtering in the HCF, which would originate from higher losses for the HOMs compared to the fundamental mode. In contrast, for the pump part, the

random linear mode coupling leads to a spreading of the pump among a large number of guided transverse modes (Figure 58(e)) resulting into a high spatial instability at the HCF output (Figure 58(g)).

So far, we have illustrated the creation, self-trapping, and amplification of MDSS within the fiber. Now, we investigate the temporal properties of the output MDSS. For this purpose, we used time-frequency analysis (Wigner function) which provides a conceptual guide to interpret the complex spatiotemporal interactions. Figure 59(a) indicates the expected Wigner function of the output pulses from a 1D simulation. The 1D simulations always predict a positive chirp as the pulses propagate nonlinearly in the HCF indicating dominant Kerr nonlinearity (no Raman enhancement). On the other hand, the Wigner distribution of the output pulse from MD simulations illustrates a different time-frequency structure, building up a dominant negative chirp for the MDSS pulses at the HCF output (Figure 59(b)). This is mainly because the coherent rotational response of the molecular gas develops very slowly. This leads to an effective negative “chirp” for MDSS which experience an enhanced Raman nonlinearity. Figure 59(c) shows the Wigner function of the output pulses from the reconstructed SHG-FROG trace (see method section for details). These results are in good agreement with MD simulations, indicating the localization of MDSS at the leading edge of the driver pulse with negative chirp. Consequently, MDSS are post-compressed experimentally down to 10.8 fs by propagating through a piece of fused silica (FS) glass (positive GVD below 1.3 microns) (Figure 59(d)). Figure 59(e) shows the temporal characterization of the compressed pulses, which agrees well with the results from MD numerical simulations. The corresponding spectra are presented in Figure 59(f). It is noted that the ratio between the pump pulse duration and the compressed red-shifted MDSS pulse duration,  $\sim 65$ , is much higher than what is achieved with pulse compression schemes based on Kerr nonlinearities under the same HCF geometry[69].

Finally, to further confirm this intrinsic negative quadratic phase and the spatiotemporal quality of the MDSS beam, we performed high harmonic generation (HHG) experiments (see method). For this purpose, we generate harmonics with uncompressed, partially compressed, and fully compressed output pulses. The extension of the cut-off photon energy and increasing flux of the XUV radiation unequivocally proves the sign of the chirp and the high spatiotemporal quality of the compressed MDSS (Figure 60, a-c). Besides, we find that around 75% of the energy is in the main peak of the compressed pulses (10.8 fs) by comparing with the HHG spectra driven by known reference pulses.

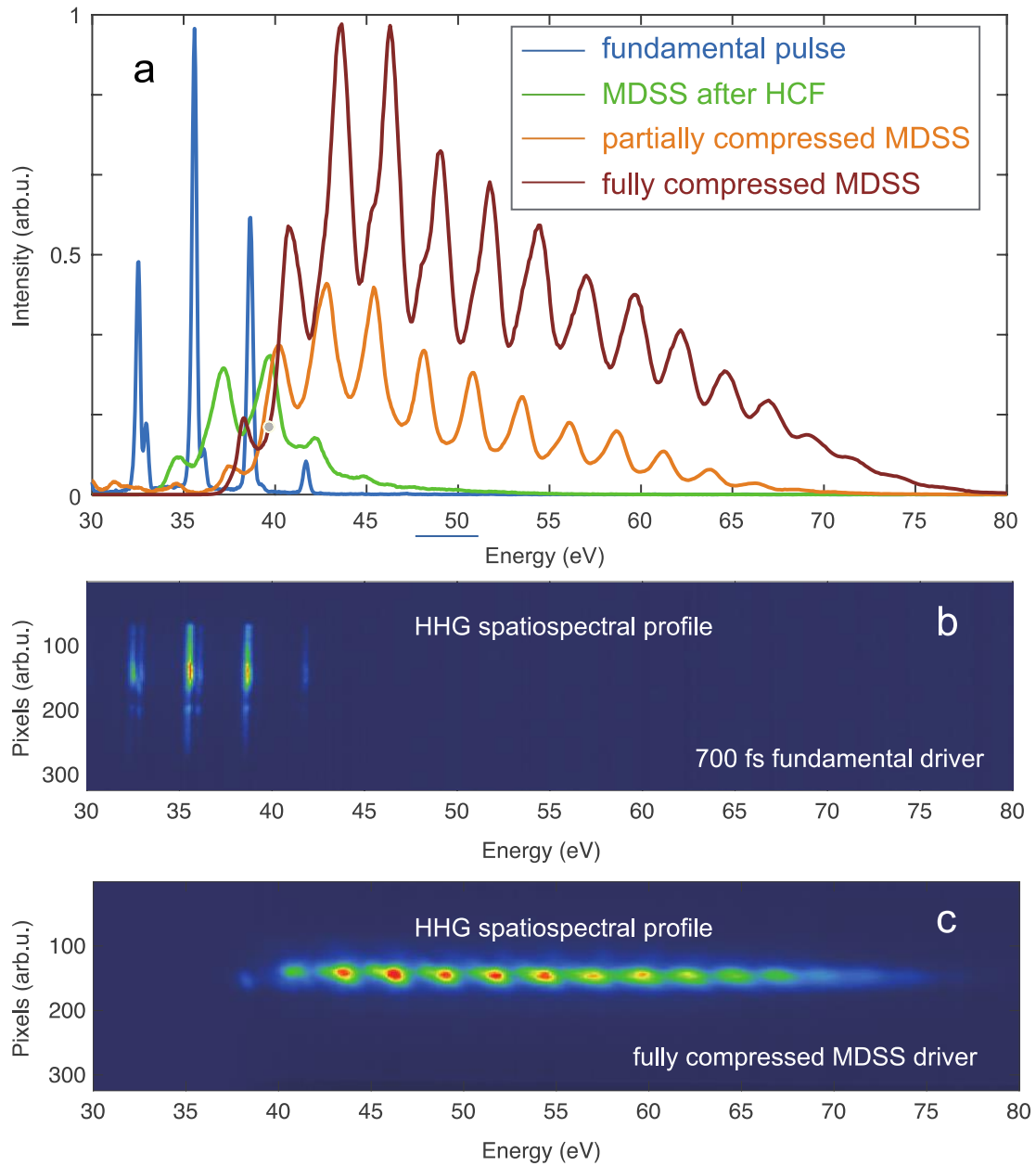


**Figure 60** High harmonic generation in Ar. (a) The blue curve is the measured HHG spectra with the driver pump (700 fs). Green, orange and red curves are the corresponding spectra driven by the uncompressed, partially and fully compressed MDSS pulses, respectively. The partially and fully compressed pulses are obtained by propagating the output MDSS through 6 mm and 12 mm of FS. The shortening of the pulse duration leads to higher peak intensity and thus to an extension of the HHG cut-off and higher photon flux. (c) Spatial (y-axis) and spectral (x-axis) profiles of the HHG beam driven by 700 fs pulses at the fundamental wavelength with 8 times more energy compared to MDSS and (c) the corresponding HHG profile driven by the compressed red-shifted MDSS.

In conclusion, we have observed the creation of high-energy stable self-trapped beams with broadband red-shifted spectra, and the capability for compression down to few-cycle pulse duration in a large core HCF filled with nitrogen, driven by sub-ps laser pulses. Through MD numerical simulations and the comparison with our experimental results, we attribute these experimental observations to multidimensional intermodal dynamics. In this regime, nonlinear effects occur between modes, and quantities like energy, phase and frequency are modified on an intermodal basis. This provides sufficient nonlinearity to counter the potential diffraction while keeping the beam diameter constant. The high efficiency of intermodal multidimensional interactions in large core diameter HCF is mainly due to the ultra-low modal dispersion and strong nonlinear coupling. The ability to generate high-energy and spatiotemporally engineered coherent light fields is expected to lead to breakthroughs in laser science through a wide range of applications such as power scalability[227], the generation of tunable ultra-broadband long-wavelength sources[19] and scaling of the HHG cut-off to generate higher photon energies[228]. Beyond such a technology breakthrough, the formation of high-energy multidimensional solitary states in a molecular gas-filled large core HCF combines the advantages of a many-modes capacity with low modal dispersion and pressure-tunable dispersion and nonlinearity. This provides an influential horizon for the exploration of multidimensionality concepts in other physical systems[3] which are limited by complex experimental conditions.

## **Method**

The experiments were conducted at the Advanced Laser Light Source (ALLS) laboratory based at INRS-EMT. A Ti:Sa chirped-pulse amplifier (CPA) delivering 40 fs transform-limited pulses with a central wavelength at 780 nm and energy of 5 mJ at a repetition rate of 100 Hz was used. 700 fs pulses were achieved by chirping positively the input pulses by changing the separation between the grating pairs of the Ti:Sa compressor. The output of the CPA was focused on a spot size of  $\sim 330 \mu\text{m}$  and coupled into a 3-meter-long HCF stretched between two holders (from few-cycle Inc.). The holder at the fiber entrance includes four fine screws that translate and tilt the fiber tip to ensure the alignment at both ends as well as to optimize the mode quality at output. The optimization of the coupling conditions is achieved by feedback adjustment of the fine screws while monitoring the output spectrum. The measured transmission was about 65%. The HCF has a core diameter of 500  $\mu\text{m}$ , and was filled with either Ar or N<sub>2</sub> with a differential pump scheme (injection of gas from the HCF output). The use of a differential pressure configuration suppresses ionization and self-focusing at the fiber input, which contributes to higher reliability of fiber coupling. The spectra at the output of the HCF were measured with a VIS/NIR spectrometer (Avantes, AvaSpec-ULS2048XL). The

spatial profile of the beams (pump and MDSS) was captured using a CDD camera (PointGrey, FLEA). The MDSS pulses were compressed by linear propagation in fused silica windows, and temporal characterization was performed with a home built SHG-FROG.

High harmonic generation (HHG) provides an elegant in situ intensity measurement method to calibrate the spatiotemporal compression quality of the compressed MDSS pulses. The maximum X-ray photon energy produced by HHG is given by  $E_{\text{cut-off}} = I_p + 3.17 U_p$ , where  $U_p$  is the ponderomotive energy which is proportional to the peak laser intensity  $I$  and the laser wavelength, defined as  $U_p \propto I \lambda^2$ . The saturation laser intensity can be defined as the minimum value at which the HHG cut-off does not extend anymore, which is limited by ionization of the atomic gas. Therefore, the laser intensity can be determined by HHG cut-off before reaching the saturation intensity. Experimentally, the harmonics were generated by focusing (with a 50 cm plano-convex lens) the compressed output pulses from the HCF in an Ar-filled gas cell with a length of 8 mm. The pulse energy before the HHG chamber was 600  $\mu\text{J}$ . The backing pressure of the gas cell was adjusted to phase match the HHG process and was optimized to 130 Torr. The XUV spectrometer includes a curved-groove laminar replica grating with 1200gr/mm. The detector in the image plane of the grating is a typical micro-channel plate/P20 phosphor screen/low-noise CMOS camera. Spectral calibration was done using both the harmonic comb and absorption edges from metallic thin foils (Al and Ti).

For a diatomic molecule, the parallel polarizability is higher than the perpendicular one and under the interaction with a strong laser field, the molecules tend to align with the electric component of the field. This rotational motion induces a change of refractive index  $\Delta n(t)$ . The rotational contributions to the nonlinear response function can be described by the function  $h_R(t)$ . The real part of the Fourier transform of  $h_R(t)$  leads to Raman-induced index changes, while its imaginary part is related to the Raman gain. The Raman-gain coefficient  $g_R(\Omega)$ , where  $\Omega \equiv \omega_p - \omega_s$  is the frequency difference between the pump and Stokes frequencies, which is the most important quantity for describing SRS. In our simulations, the Raman gain is calculated by solving the time-dependent Schrodinger equations (TDSE). In these simulations, to model the time evolution of the molecular rotation, the total wave packet is described by a coherent superposition of field-free rotational states. The temporal evolution of the system as it interacts with the laser field is obtained by solving TDSE equation using the fourth-order Runge-Kutta in the interaction picture method (RK4IP).

The SRS pulse is amplified due to the Raman gain as long as the frequency difference  $\Omega$  lies within the instantaneous bandwidth of the driving laser pulse. For 700 fs input pulses, the calculated rotational excitation step of N<sub>2</sub> is far larger than the bandwidth of 700fs pulses (Fig. S8), and the Raman gain is negligible in 1D regime. Therefore, 1D simulations which were performed using the standard molecule alignment theory by considering one mode, predict a diminished spectral broadening efficiency with increasing pulse duration accompanied by symmetric spectral shape. Therefore, we adopt the SRS gain obtained from TDSE calculations to generalized multimode nonlinear Schrödinger equations (GMMNLSE). In MD simulations, 15 linearly polarized LP<sub>mn</sub> modes are taken into account, including 3 first modes from LP<sub>0n</sub> family. We have verified, through extensive convergence tests, that including higher modes have a negligible effect on the final results, and that a negligible amount of energy is transferred to any higher-order LP<sub>0n</sub> modes.

## 8 Article VI : Coherent Tabletop EUV Ptychography of Nanopatterns

NGUYEN XUAN TRUONG<sup>1,2,\*</sup>, **REZA SAFAEI**<sup>3</sup>, VINCENT CARDIN<sup>3</sup>, SCOTT M. LEWIS<sup>1</sup>, FRANÇOIS LÉGARÉ<sup>3</sup>, MELISSA A. DENECKE<sup>1,2</sup>

<sup>1</sup>School of Chemistry, The University of Manchester, M13 9PL Manchester, UK

<sup>2</sup>Dalton Nuclear Institute, The University of Manchester, M13 9PL Manchester, UK

<sup>3</sup>INRS, Energie, Matériaux et Télécommunications, 1650 Blvd. Lionel Boulet, Varennes, Québec, Canada, J3X 1S2

<http://dx.doi.org/10.10631/1.4914344>

N. X. Truong, R. Safaei, V. Cardin, S. M. Lewis, X. L. Zhong, F. Légaré, and M. A. Denecke, "Coherent Tabletop EUV Ptychography of Nanopatterns," Scientific reports 8, 1-9 (2018).

**Personal contribution:** Nguyen Xuan Truong and I conducted all experiments and measurements in ALLS. I also optimized and operated the laser beam and HHG in ALLS.

### 8.1 Abstract

Coherent diffraction imaging (CDI) or lensless X-ray microscopy has become of great interest for high spatial resolution imaging of, e.g., nanostructures and biological specimens. There is no optics required in between an object and a detector, because the object can be fully recovered from its far-field diffraction pattern with an iterative phase retrieval algorithm. Hence, in principle, a sub-wavelength spatial resolution could be achieved in a high-numerical aperture configuration. With the advances of ultrafast laser technology, high photon flux tabletop Extreme Ultraviolet (EUV) sources based on the high-order harmonic generation (HHG) have become available to small-scale laboratories. In this study, we report on a newly established high photon flux and highly monochromatic 30 nm HHG beamline. Furthermore, we applied ptychography, a scanning CDI version, to probe a nearly periodic nanopattern with the tabletop EUV source. A wide-field view of about  $15 \times 15 \mu\text{m}$  was probed with a  $2.5 \mu\text{m}$ -diameter illumination beam at 30 nm. From a set of hundreds of far-field diffraction patterns recorded for different adjacent positions of the object, both the object and the illumination beams were successfully reconstructed with the extended ptychographical iterative engine. By investigating the phase retrieval transfer function, a diffraction-limited resolution of reconstruction of about 32 nm is obtained.

## 9 Conclusion and Outlook

Ultrafast lasers have opened new horizons for controlling and measuring ultrafast dynamics in matter. In addition to high temporal resolution, ultrafast pulses have the capability to support peak powers and intensities beyond any reasonable human intuition. Their remarkable impacts provide advanced tools that were once rare (e.g., high-brightness XUV sources) into more routine laboratory use. Controlling nonlinearity brings rich possibilities to find new generations of ultrashort lasers that can meet diverse range of real –world demands in a practical and commercially-viable manner. The observation and the creation of high-energy stable self-trapped beams in highly multimode regime with ability to compress to few-cycle pulses with high spatiotemporal quality is a clear indication of the possibility to control spatiotemporal nonlinearity and multidimensional interactions in large core diameter HCF as well as the potential impacts. The immediate technology impact of this work can be generating few-cycle pulses by ps Yb driver lasers with a simple, robust, and efficient approach providing a new driver technology for strong-field physics. The ability to generate high-energy and spatiotemporally engineered coherent light fields is expected to lead to breakthroughs in laser science through a wide range of applications such as power scalability [227], the generation of tunable ultra-broadband long-wavelength sources [19] and scaling of the HHG cut-off to generate higher photon energies. This would lead to successful commercialization which is always a prerequisite for the wide adoption of physical tools (or almost any technology), like those we might eventually create with controlling nonlinear enhancement in high-energy regime.

As we look to the future, lasers and amplifiers that can elegantly incorporate multimode fibers may have significantly higher power than devices based on single-mode. This promise extends beyond ultrafast and across laser science, since dimensionality and spatial/spatiotemporal nonlinearities represent key limitations for high-power lasers of all kinds. However, while we see multi-TW peak powers as a plausible prospect for the current work in HCF, three important outlooks are waited to be discovered in this field. First, the discovery of new potential physical concepts which can be discovered utilizing HCF gas filled with advantages of a many–modes capacity with low modal dispersion and pressure-tunable dispersion and nonlinearity. Noted that these systems have a clear advantage over solid core fibers which have fixed nonlinearity and dispersion. Second, coherent multimode high-energy few-cycle pulses can potentially have implemented in new applications that fundamentally transcends traditional single-mode designs. Finally, cost efficient, compact and reliable technologies are the outcome that many scientists expect from the applied fields. However,

the journey to make spatiotemporally coherent laser source requires to learn and understand how to control the nonlinearity. This provides an influential horizon for the exploration of multidimensionality concepts in other physical systems [3] which are limited by complex experimental conditions.

## 9.1 Proposed experiments

Here are some experiments that I found interesting to perform in ALLS:

- 1) To date, the main answer to the wavelength tunability for energetic, broadband pulses still relies on optical parametric amplification (OPA), which often requires multiple and complex stages, and may feature imperfect beam quality. By taking advantage of continuous tunability and high efficiency of the red-shifted spectra especially for maximum alignment regime (Figure 30), I propose to select the red-part of the spectra at different pressures (different central wavelength) and compressed them accordingly. I believe that this method can be a convenient alternative to the more demanding OPA systems to achieve a gap-free tuning in the near-IR.
- 2) The spatiotemporal enhancement does not depend on the driving laser wavelength, and molecular gases like N<sub>2</sub> offer wide window of transparency extending from the vacuum ultraviolet to the mid-infrared spectra range. Therefore, the method can be implemented in different spectral range. In ALLS, we have access to high energy 1.8 μm pulses. We have already obtained some preliminary results utilizing this source as a pump, and we succeeded to obtain the red shifted spectra up to 2.6 μm with high efficiency.
- 3) High-energy few-cycle pulses in the mid-wave IR (mid-IR) spectral range are attractive for a number of high field applications, e.g., high-order harmonic generation, and allow us to extend the cut-off to the keV spectral range due to  $\lambda^2$  scaling. Using the developed source at the second proposed experiment, a scalable and efficient way to generate femtosecond mid-IR pulses in the 3 μm spectral range is possible. It can lead to efficient generation of harmonics in the water window allowing absorption spectroscopy in a single laser shot at the carbon K edge (284 eV).
- 4) From fundamental point of view, we can investigate other molecular gases to really understand the role of Raman transitions. In addition, we can utilize molecular systems with a much slower characteristic response time for molecular alignment compared to N<sub>2</sub>

to study the role of spatiotemporal nonlinear enhancement for longer driver pulses (few picoseconds).

## 10 References

1. Malomed, B., et al., *On multidimensional solitons and their legacy in contemporary atomic, molecular and optical physics*. Journal of Physics B: Atomic, Molecular and Optical Physics, 2016. **49**(17): p. 170502.
2. Grellu, P. and N. Akhmediev, *Dissipative solitons for mode-locked lasers*. Nature photonics, 2012. **6**(2): p. 84.
3. Kartashov, Y.V., et al., *Frontiers in multidimensional self-trapping of nonlinear fields and matter*. Nature Reviews Physics, 2019. **1**(3): p. 185-197.
4. Chen, Z., M. Segev, and D.N. Christodoulides, *Optical spatial solitons: historical overview and recent advances*. Reports on Progress in Physics, 2012. **75**(8): p. 086401.
5. Kivshar, Y.S. and G. Agrawal, *Optical solitons: from fibers to photonic crystals*. 2003: Academic press.
6. Efremidis, N.K., et al., *Discrete solitons in photorefractive optically induced photonic lattices*. Physical Review E, 2002. **66**(4): p. 046602.
7. Neshev, D.N., et al., *Observation of discrete vortex solitons in optically induced photonic lattices*. Physical review letters, 2004. **92**(12): p. 123903.
8. Mihalache, D., et al., *Stable three-dimensional spatiotemporal solitons in a two-dimensional photonic lattice*. Physical Review E, 2004. **70**(5): p. 055603.
9. Martin, H., et al., *Discrete solitons and soliton-induced dislocations in partially coherent photonic lattices*. Physical review letters, 2004. **92**(12): p. 123902.
10. Terhalle, B., et al., *Observation of multivortex solitons in photonic lattices*. Physical review letters, 2008. **101**(1): p. 013903.
11. Chong, A., et al., *Airy–Bessel wave packets as versatile linear light bullets*. Nature photonics, 2010. **4**(2): p. 103.
12. Malomed, B.A., et al., *Spatiotemporal solitons in multidimensional optical media with a quadratic nonlinearity*. Physical Review E, 1997. **56**(4): p. 4725.
13. Liu, X., L. Qian, and F. Wise, *Generation of optical spatiotemporal solitons*. Physical review letters, 1999. **82**(23): p. 4631.
14. Liu, X., K. Beckwitt, and F. Wise, *Two-dimensional optical spatiotemporal solitons in quadratic media*. Physical Review E, 2000. **62**(1): p. 1328.
15. Ruostekoski, J., *Stable particlelike solitons with multiply quantized vortex lines in Bose-Einstein condensates*. Physical Review A, 2004. **70**(4): p. 041601.
16. Fibich, G. and A.L. Gaeta, *Critical power for self-focusing in bulk media and in hollow waveguides*. Optics letters, 2000. **25**(5): p. 335-337.
17. Nisoli, M., S. De Silvestri, and O. Svelto, *Generation of high energy 10 fs pulses by a new pulse compression technique*. Applied Physics Letters, 1996. **68**(20): p. 2793-2795.
18. Goulielmakis, E., et al., *Single-cycle nonlinear optics*. Science, 2008. **320**(5883): p. 1614-1617.
19. Fan, G., et al., *Hollow-core-waveguide compression of multi-millijoule CEP-stable 3.2  $\mu\text{m}$  pulses*. Optica, 2016. **3**(12): p. 1308-1311.
20. Gattass, R.R. and E. Mazur, *Femtosecond laser micromachining in transparent materials*. Nature photonics, 2008. **2**(4): p. 219-225.
21. Sundaram, S. and E. Mazur, *Inducing and probing non-thermal transitions in semiconductors using femtosecond laser pulses*. Nature materials, 2002. **1**(4): p. 217-224.
22. Sugioka, K. and Y. Cheng, *Femtosecond laser processing for optofluidic fabrication*. Lab on a Chip, 2012. **12**(19): p. 3576-3589.
23. Yanik, M.F., et al., *Functional regeneration after laser axotomy*. Nature, 2004. **432**(7019): p. 822-822.

24. Bärsch, N., et al., *Ablation and cutting of planar silicon devices using femtosecond laser pulses*. Applied Physics A, 2003. **77**(2): p. 237-242.
25. Deubel, M., et al., *Direct laser writing of three-dimensional photonic-crystal templates for telecommunications*. Nature materials, 2004. **3**(7): p. 444-447.
26. Lichtman, J.W. and J.-A. Conchello, *Fluorescence microscopy*. Nature methods, 2005. **2**(12): p. 910-919.
27. Robles, F.E., et al., *Molecular imaging true-colour spectroscopic optical coherence tomography*. Nature photonics, 2011. **5**(12): p. 744-747.
28. Theer, P., M.T. Hasan, and W. Denk, *Two-photon imaging to a depth of 1000  $\mu\text{m}$  in living brains by use of a Ti: Al<sub>2</sub>O<sub>3</sub> regenerative amplifier*. Optics letters, 2003. **28**(12): p. 1022-1024.
29. Helmchen, F. and W. Denk, *Deep tissue two-photon microscopy*. Nature methods, 2005. **2**(12): p. 932-940.
30. Horton, N.G., et al., *In vivo three-photon microscopy of subcortical structures within an intact mouse brain*. Nature photonics, 2013. **7**(3): p. 205-209.
31. Dudovich, N., D. Oron, and Y. Silberberg, *Single-pulse coherently controlled nonlinear Raman spectroscopy and microscopy*. Nature, 2002. **418**(6897): p. 512-514.
32. Karpf, S., et al., *A Time-Encoded Technique for fibre-based hyperspectral broadband stimulated Raman microscopy*. Nature Communications, 2015. **6**(1): p. 1-6.
33. Patel, S.V., et al., *Femtosecond laser versus mechanical microkeratome for LASIK: a randomized controlled study*. Ophthalmology, 2007. **114**(8): p. 1482-1490.
34. Yun, S.H. and S.J. Kwok, *Light in diagnosis, therapy and surgery*. Nature biomedical engineering, 2017. **1**(1): p. 1-16.
35. Ouillé, M., et al., *Relativistic-intensity near-single-cycle light waveforms at kHz repetition rate*. Light: Science & Applications, 2020. **9**(1): p. 1-9.
36. Zhang, D., et al., *Segmented terahertz electron accelerator and manipulator (STEAM)*. Nature photonics, 2018. **12**(6): p. 336-342.
37. Popmintchev, T., et al., *The attosecond nonlinear optics of bright coherent X-ray generation*. Nature Photonics, 2010. **4**(12): p. 822.
38. Weisshaupt, J., et al., *High-brightness table-top hard X-ray source driven by sub-100-femtosecond mid-infrared pulses*. Nature Photonics, 2014. **8**(12): p. 927.
39. Sansone, G., L. Poletto, and M. Nisoli, *High-energy attosecond light sources*. Nature Photonics, 2011. **5**(11): p. 655.
40. Tzallas, P., et al., *Direct observation of attosecond light bunching*. Nature, 2003. **426**(6964): p. 267-271.
41. Gauthier, D., et al., *Single-shot femtosecond X-ray holography using extended references*. Physical review letters, 2010. **105**(9): p. 093901.
42. Lambert, G., et al., *Injection of harmonics generated in gas in a free-electron laser providing intense and coherent extreme-ultraviolet light*. Nature physics, 2008. **4**(4): p. 296-300.
43. Fan, G., et al., *Time-resolving magnetic scattering on rare-earth ferrimagnets with a bright soft-X-ray high-harmonic source*. arXiv preprint arXiv:1910.14263, 2019.
44. Kretschmar, M., et al., *Direct observation of pulse dynamics and self-compression along a femtosecond filament*. Optics express, 2014. **22**(19): p. 22905-22916.
45. Baumgarten, C., et al., *1 J, 0.5 kHz repetition rate picosecond laser*. Optics Letters, 2016. **41**(14): p. 3339-3342.
46. Shumakova, V., et al., *Multi-millijoule few-cycle mid-infrared pulses through nonlinear self-compression in bulk*. Nature communications, 2016. **7**(1): p. 1-6.
47. Lu, C.-H., et al., *Greater than 50 times compression of 1030 nm Yb: KGW laser pulses to single-cycle duration*. Optics express, 2019. **27**(11): p. 15638-15648.
48. Ueffing, M., et al., *Nonlinear pulse compression in a gas-filled multipass cell*. Optics letters, 2018. **43**(9): p. 2070-2073.
49. Kaumanns, M., et al., *Multipass spectral broadening of 18 mJ pulses compressible from 1.3 ps to 41 fs*. Optics letters, 2018. **43**(23): p. 5877-5880.

50. Hort, O., et al., *Postcompression of high-energy terawatt-level femtosecond pulses and application to high-order harmonic generation*. JOSA B, 2015. **32**(6): p. 1055-1062.
51. Jarnac, A., et al., *Compression of TW class laser pulses in a planar hollow waveguide for applications in strong-field physics*. The European Physical Journal D, 2014. **68**(12): p. 373.
52. Baer, C.R.E., et al., *Femtosecond thin-disk laser with 141 W of average power*. Optics Letters, 2010. **35**(13): p. 2302-2304.
53. Hädrich, S., et al., *Energetic sub-2-cycle laser with 216 W average power*. Optics letters, 2016. **41**(18): p. 4332-4335.
54. Lavenu, L., et al., *High-energy few-cycle Yb-doped fiber amplifier source based on a single nonlinear compression stage*. Optics express, 2017. **25**(7): p. 7530-7537.
55. Hädrich, S., et al., *High photon flux table-top coherent extreme-ultraviolet source*. Nature Photonics, 2014. **8**(10): p. 779-783.
56. Gardner, D.F., et al., *Subwavelength coherent imaging of periodic samples using a 13.5 nm tabletop high-harmonic light source*. Nature Photonics, 2017. **11**(4): p. 259.
57. Zhou, X., et al., *Probing and controlling non-Born–Oppenheimer dynamics in highly excited molecular ions*. Nature Physics, 2012. **8**(3): p. 232-237.
58. Porat, G., et al., *Phase-matched extreme-ultraviolet frequency-comb generation*. Nature Photonics, 2018. **12**(7): p. 387-391.
59. Saule, T., et al., *High-flux ultrafast extreme-ultraviolet photoemission spectroscopy at 18.4 MHz pulse repetition rate*. Nature communications, 2019. **10**(1): p. 1-10.
60. Heckl, O., et al., *Temporal pulse compression in a xenon-filled Kagome-type hollow-core photonic crystal fiber at high average power*. Optics express, 2011. **19**(20): p. 19142-19149.
61. Emaury, F., et al., *Beam delivery and pulse compression to sub-50 fs of a modelocked thin-disk laser in a gas-filled Kagome-type HC-PCF fiber*. Optics Express, 2013. **21**(4): p. 4986-4994.
62. Mak, K., et al., *Two techniques for temporal pulse compression in gas-filled hollow-core kagomé photonic crystal fiber*. Optics letters, 2013. **38**(18): p. 3592-3595.
63. Balciunas, T., et al., *A strong-field driver in the single-cycle regime based on self-compression in a kagome fibre*. Nature communications, 2015. **6**(1): p. 1-7.
64. Elu, U., et al., *High average power and single-cycle pulses from a mid-IR optical parametric chirped pulse amplifier*. Optica, 2017. **4**(9): p. 1024-1029.
65. Seidel, M., et al., *All solid-state spectral broadening: an average and peak power scalable method for compression of ultrashort pulses*. Optics express, 2016. **24**(9): p. 9412-9428.
66. Mansour, B., et al., *Generation of 11 fs pulses by using hollow-core gas-filled fibers at a 100 kHz repetition rate*. Optics letters, 2006. **31**(21): p. 3185-3187.
67. Hädrich, S., et al., *High energy ultrashort pulses via hollow fiber compression of a fiber chirped pulse amplification system*. Optics express, 2009. **17**(5): p. 3913-3922.
68. Rothhardt, J., et al., *1 MHz repetition rate hollow fiber pulse compression to sub-100-fs duration at 100 W average power*. Optics letters, 2011. **36**(23): p. 4605-4607.
69. Chen, B.-H., et al., *Compression of picosecond pulses from a thin-disk laser to 30fs at 4W average power*. Optics express, 2018. **26**(4): p. 3861-3869.
70. Wright, L.G., D.N. Christodoulides, and F.W. Wise, *Controllable spatiotemporal nonlinear effects in multimode fibres*. Nature Photonics, 2015. **9**(5): p. 306-310.
71. Wright, L.G., D.N. Christodoulides, and F.W. Wise, *Spatiotemporal mode-locking in multimode fiber lasers*. Science, 2017. **358**(6359): p. 94-97.
72. Eftekhari, M., et al., *Accelerated nonlinear interactions in graded-index multimode fibers*. Nature communications, 2019. **10**(1): p. 1-10.
73. Wright, L.G., et al., *Self-organized instability in graded-index multimode fibres*. Nature Photonics, 2016. **10**(12): p. 771-776.
74. Krupa, K., et al., *Multimode nonlinear fiber optics, a spatiotemporal avenue*. APL Photonics, 2019. **4**(11): p. 110901.

75. Wright, L.G., et al., *Mechanisms of spatiotemporal mode-locking*. Nature Physics, 2020: p. 1-6.
76. Wright, L.G., et al., *Spatiotemporal dynamics of multimode optical solitons*. Optics express, 2015. **23**(3): p. 3492-3506.
77. Marcatili, E.A. and R. Schmeltzer, *Hollow metallic and dielectric waveguides for long distance optical transmission and lasers*. Bell System Technical Journal, 1964. **43**(4): p. 1783-1809.
78. Russell, P.S.J., et al., *Hollow-core photonic crystal fibres for gas-based nonlinear optics*. Nature Photonics, 2014. **8**(4): p. 278.
79. Travers, J.C., et al., *High-energy pulse self-compression and ultraviolet generation through soliton dynamics in hollow capillary fibres*. Nature Photonics, 2019. **13**(8): p. 547-554.
80. Vozzi, C., et al., *Optimal spectral broadening in hollow-fiber compressor systems*. Applied Physics B, 2005. **80**(3): p. 285-289.
81. Cardin, V., et al., *0.42 TW 2-cycle pulses at 1.8  $\mu$  m via hollow-core fiber compression*. Applied Physics Letters, 2015. **107**(18): p. 181101.
82. Agrawal, G.P., *Nonlinear fiber optics*, in *Nonlinear Science at the Dawn of the 21st Century*. 2000, Springer. p. 195-211.
83. Lindberg, R., *Experimental and numerical study of a high-repetition rate Yb-fiber amplifier source*. 2014.
84. Zheltikov, A.M., *Raman response function of atmospheric air*. Optics Letters, 2007. **32**(14): p. 2052-2054.
85. Stolen, R.H., et al., *Raman response function of silica-core fibers*. Journal of the Optical Society of America B, 1989. **6**(6): p. 1159-1166.
86. Lindberg, R., et al., *Accurate modeling of high-repetition rate ultrashort pulse amplification in optical fibers*. Scientific reports, 2016. **6**: p. 34742.
87. Suda, A., et al., *Generation of sub-10-fs, 5-mJ-optical pulses using a hollow fiber with a pressure gradient*. Applied Physics Letters, 2005. **86**(11): p. 111116.
88. Wahlstrand, J., Y.-H. Cheng, and H. Milchberg, *Absolute measurement of the transient optical nonlinearity in N<sub>2</sub>, O<sub>2</sub>, N<sub>2</sub>O, and Ar*. Physical Review A, 2012. **85**(4): p. 043820.
89. Wang, D., Y. Leng, and Z. Xu, *Measurement of nonlinear refractive index coefficient of inert gases with hollow-core fiber*. Applied Physics B, 2013. **111**(3): p. 447-452.
90. Börzsönyi, Á., et al., *Measurement of pressure dependent nonlinear refractive index of inert gases*. Optics Express, 2010. **18**(25): p. 25847-25854.
91. Safaei, R., et al., *Low energy pulse compression in hollow core fibers using hydrofluorocarbon molecular gas*. OSA Continuum, 2019. **2**(4): p. 1488-1495.
92. Börzsönyi, A., et al., *Dispersion measurement of inert gases and gas mixtures at 800 nm*. Applied optics, 2008. **47**(27): p. 4856-4863.
93. Keldysh, L., *Ionization in the field of a strong electromagnetic wave*. Sov. Phys. JETP, 1965. **20**(5): p. 1307-1314.
94. Popruzhenko, S., *Keldysh theory of strong field ionization: history, applications, difficulties and perspectives*. Journal of Physics B: Atomic, Molecular and Optical Physics, 2014. **47**(20): p. 204001.
95. Ammosov, M.V., *Tunnel ionization of complex atoms and of atomic ions in an alternating electromagnetic field*. Sov. Phys. JETP, 1987. **64**: p. 1191.
96. Bauer, D. and P. Mulser, *Exact field ionization rates in the barrier-suppression regime from numerical time-dependent Schrödinger-equation calculations*. Physical Review A, 1999. **59**(1): p. 569.
97. Delone, N.B. and V.P. Krainov, *Tunneling and barrier-suppression ionization of atoms and ions in a laser radiation field*. Physics-Uspexhi, 1998. **41**(5): p. 469.
98. Rae, S. and K. Burnett, *Detailed simulations of plasma-induced spectral blueshifting*. Physical Review A, 1992. **46**(2): p. 1084.
99. Chang, W., et al., *Influence of ionization on ultrafast gas-based nonlinear fiber optics*. Optics express, 2011. **19**(21): p. 21018-21027.

100. Nurhuda, M., et al., *Control of self-phase modulation and plasma-induced blueshifting of high-energy, ultrashort laser pulses in an argon-filled hollow fiber using conjugate pressure-gradient method*. JOSA B, 2005. **22**(8): p. 1757-1762.
101. Li, W., et al., *Time-resolved dynamics in N<sub>2</sub>O<sub>4</sub> probed using high harmonic generation*. Science, 2008. **322**(5905): p. 1207-1211.
102. Koch, C.P., M. Lemeshko, and D. Sugny, *Quantum control of molecular rotation*. Reviews of Modern Physics, 2019. **91**(3): p. 035005.
103. Lee, K.F., et al., *Phase control of rotational wave packets and quantum information*. Physical review letters, 2004. **93**(23): p. 233601.
104. Ospelkaus, S., et al., *Quantum-state controlled chemical reactions of ultracold potassium-rubidium molecules*. Science, 2010. **327**(5967): p. 853-857.
105. Itatani, J., et al., *Tomographic imaging of molecular orbitals*. Nature, 2004. **432**(7019): p. 867-871.
106. Boutu, W., et al., *Coherent control of attosecond emission from aligned molecules*. Nature Physics, 2008. **4**(7): p. 545-549.
107. Chan, H.-S., et al., *Synthesis and measurement of ultrafast waveforms from five discrete optical harmonics*. Science, 2011. **331**(6021): p. 1165-1168.
108. Blaga, C.I., et al., *Imaging ultrafast molecular dynamics with laser-induced electron diffraction*. Nature, 2012. **483**(7388): p. 194-197.
109. Baker, S., et al., *Femtosecond to attosecond light pulses from a molecular modulator*. Nature Photonics, 2011. **5**(11): p. 664.
110. Chan, H.-S., et al., *Synthesis and Measurement of Ultrafast Waveforms from Five Discrete Optical Harmonics*. Science, 2011. **331**(6021): p. 1165.
111. Harris, S.E. and A.V. Sokolov, *Subfemtosecond Pulse Generation by Molecular Modulation*. Physical Review Letters, 1998. **81**(14): p. 2894-2897.
112. Stapelfeldt, H. and T. Seideman, *Colloquium: Aligning molecules with strong laser pulses*. Reviews of Modern Physics, 2003. **75**(2): p. 543-557.
113. Ortigoso, J., et al., *Time evolution of pendular states created by the interaction of molecular polarizability with a pulsed nonresonant laser field*. The Journal of Chemical Physics, 1999. **110**(8): p. 3870-3875.
114. Seideman, T., *Revival Structure of Aligned Rotational Wave Packets*. Physical Review Letters, 1999. **83**(24): p. 4971-4974.
115. Bartels, R.A., et al., *Phase Modulation of Ultrashort Light Pulses using Molecular Rotational Wave Packets*. Physical Review Letters, 2001. **88**(1): p. 013903.
116. Zhavoronkov, N. and G. Korn, *Generation of Single Intense Short Optical Pulses by Ultrafast Molecular Phase Modulation*. Physical Review Letters, 2002. **88**(20): p. 203901.
117. Kalosha, V., et al., *Generation of single dispersion precompensated 1-fs pulses by shaped-pulse optimized high-order stimulated Raman scattering*. Physical review letters, 2002. **88**(10): p. 103901.
118. Kida, Y., S.-i. Zaitsev, and T. Imasaka, *Coherent molecular rotations induced by a femtosecond pulse consisting of two orthogonally polarized pulses*. Physical Review A, 2009. **80**(2): p. 021805.
119. Bartels, R.A., et al., *Nonresonant Control of Multimode Molecular Wave Packets at Room Temperature*. Physical Review Letters, 2002. **88**(3): p. 033001.
120. Bernhardt, B., et al., *Cavity-enhanced dual-comb spectroscopy*. Nature Photonics, 2010. **4**(1): p. 55-57.
121. Spanner, M., *Field-free alignment and strong field control of molecular rotors*. 2004.
122. Huberg, K. and G. Herzberg, *Molecular Spectra and Molecular Structure-IV*. Constants of Diatomic Molecules (Reinhold, New York, 1979), 1989.
123. Ortigoso, J., et al., *Time evolution of pendular states created by the interaction of molecular polarizability with a pulsed nonresonant laser field*. The Journal of chemical physics, 1999. **110**(8): p. 3870-3875.

124. Langevin, D., et al., *Determination of molecular contributions to the nonlinear refractive index of air for mid-infrared femtosecond laser-pulse excitation*. Physical Review A, 2019. **99**(6): p. 063418.
125. Buck, J.A., *Fundamentals of optical fibers*. Vol. 50. 2004: John Wiley & Sons.
126. Dudley, J.M., G. Genty, and S. Coen, *Supercontinuum generation in photonic crystal fiber*. Reviews of modern physics, 2006. **78**(4): p. 1135.
127. Poletti, F. and P. Horak, *Description of ultrashort pulse propagation in multimode optical fibers*. JOSA B, 2008. **25**(10): p. 1645-1654.
128. Horak, P. and F. Poletti, *Multimode nonlinear fibre optics: theory and applications*. Recent Progress in Optical Fiber Research, 2012: p. 3-25.
129. Wright, L.G., *SPATIOTEMPORAL NONLINEAR OPTICS IN MULTIMODE FIBERS*. 2018.
130. Tzang, O., et al., *Adaptive wavefront shaping for controlling nonlinear multimode interactions in optical fibres*. Nature Photonics, 2018. **12**(6): p. 368-374.
131. Wright, L.G., et al., *Ultrabroadband dispersive radiation by spatiotemporal oscillation of multimode waves*. Physical review letters, 2015. **115**(22): p. 223902.
132. Schmidt, B.E., et al., *Highly stable, 54mJ Yb-InnoSlab laser platform at 0.5 kW average power*. Optics Express, 2017. **25**(15): p. 17549-17555.
133. Stegeman, G.I. and M. Segev, *Optical spatial solitons and their interactions: universality and diversity*. Science, 1999. **286**(5444): p. 1518-1523.
134. Tempea, G. and T. Brabec, *Theory of self-focusing in a hollow waveguide*. Optics letters, 1998. **23**(10): p. 762-764.
135. Nibbering, E., et al., *Determination of the inertial contribution to the nonlinear refractive index of air, N<sub>2</sub>, and O<sub>2</sub> by use of unfocused high-intensity femtosecond laser pulses*. JOSA B, 1997. **14**(3): p. 650-660.
136. Cerullo, G., et al., *Mirror-dispersion-controlled sub-10-fs optical parametric amplifier in the visible*. Optics letters, 1999. **24**(21): p. 1529-1531.
137. Schmidt, B.E., et al., *CEP stable 1.6 cycle laser pulses at 1.8 μm*. Optics express, 2011. **19**(7): p. 6858-6864.
138. Feehan, J.S., et al., *Efficient high-harmonic generation from a stable and compact ultrafast Yb-fiber laser producing 100 μJ, 350 fs pulses based on bendable photonic crystal fiber*. Applied Physics B, 2017. **123**(1): p. 43.
139. Beetar, J.E., S. Gholam-Mirzaei, and M. Chini, *Spectral broadening and pulse compression of a 400 μJ, 20 W Yb: KGW laser using a multi-plate medium*. Applied Physics Letters, 2018. **112**(5): p. 051102.
140. Bouillet, J., et al., *High-order harmonic generation at a megahertz-level repetition rate directly driven by an ytterbium-doped-fiber chirped-pulse amplification system*. Optics letters, 2009. **34**(9): p. 1489-1491.
141. Hoffmann, A., et al., *Spectral broadening and compression of sub-millijoule laser pulses in hollow-core fibers filled with sulfur hexafluoride*. Optics Express, 2014. **22**(10): p. 12038-12045.
142. Li, C., et al., *Spectral broadening and temporal compression of ~ 100 fs pulses in air-filled hollow core capillary fibers*. Optics express, 2014. **22**(1): p. 1143-1151.
143. Yang, G. and Y. Shen, *Spectral broadening of ultrashort pulses in a nonlinear medium*. Optics letters, 1984. **9**(11): p. 510-512.
144. Béjot, P., et al., *Mechanism of hollow-core-fiber infrared-supercontinuum compression with bulk material*. Physical Review A, 2010. **81**(6): p. 063828.
145. Dutin, C.F., et al., *Post-compression of high-energy femtosecond pulses using gas ionization*. Optics letters, 2010. **35**(2): p. 253-255.
146. Bree, C., A. Demircan, and G. Steinmeyer, *Method for computing the nonlinear refractive index via Keldysh theory*. IEEE Journal of Quantum Electronics, 2010. **46**(4): p. 433-437.
147. Hankin, S.M., et al., *Nonlinear ionization of organic molecules in high intensity laser fields*. Physical review letters, 2000. **84**(22): p. 5082.

148. Hankin, S., et al., *Intense-field laser ionization rates in atoms and molecules*. Physical Review A, 2001. **64**(1): p. 013405.
149. Hädrich, S., et al., *Single-pass high harmonic generation at high repetition rate and photon flux*. Journal of Physics B: Atomic, Molecular and Optical Physics, 2016. **49**(17): p. 172002.
150. Sugioka, K. and Y. Cheng, *Ultrafast lasers—reliable tools for advanced materials processing*. Light: Science & Applications, 2014. **3**(4): p. e149.
151. Südmeyer, T., et al., *Femtosecond laser oscillators for high-field science*. Nature Photonics, 2008. **2**(10): p. 599-604.
152. Bolton, P., K. Parodi, and J. Schreiber, *Applications of Laser-driven Particle Acceleration*. 2018: CRC Press.
153. Shambhu, G., et al., *Strong-field and attosecond physics in solids*. Journal of Physics B: Atomic, Molecular and Optical Physics, 2014. **47**(20): p. 204030.
154. Ghimire, S., et al., *Observation of high-order harmonic generation in a bulk crystal*. Nature Physics, 2010. **7**: p. 138.
155. Hohenleutner, M., et al., *Real-time observation of interfering crystal electrons in high-harmonic generation*. Nature, 2015. **523**: p. 572.
156. Luu, T.T., et al., *Extreme ultraviolet high-harmonic spectroscopy of solids*. Nature, 2015. **521**: p. 498.
157. Ndabashimiye, G., et al., *Solid-state harmonics beyond the atomic limit*. Nature, 2016. **534**: p. 520.
158. Schubert, O., et al., *Sub-cycle control of terahertz high-harmonic generation by dynamical Bloch oscillations*. Nature Photonics, 2014. **8**: p. 119.
159. Zaks, B., R.B. Liu, and M.S. Sherwin, *Experimental observation of electron–hole recollisions*. Nature, 2012. **483**: p. 580.
160. Ghimire, S., et al., *Redshift in the Optical Absorption of ZnO Single Crystals in the Presence of an Intense Midinfrared Laser Field*. Physical Review Letters, 2011. **107**(16): p. 167407.
161. Lucchini, M., et al., *Attosecond dynamical Franz-Keldysh effect in polycrystalline diamond*. Science, 2016. **353**(6302): p. 916.
162. Mashiko, H., et al., *Petahertz optical drive with wide-bandgap semiconductor*. Nature Physics, 2016. **12**: p. 741.
163. Schlaepfer, F., et al., *Attosecond optical-field-enhanced carrier injection into the GaAs conduction band*. Nature Physics, 2018. **14**(6): p. 560-564.
164. Schultze, M., et al., *Controlling dielectrics with the electric field of light*. Nature, 2012. **493**: p. 75.
165. Schultze, M., et al., *Attosecond band-gap dynamics in silicon*. Science, 2014. **346**(6215): p. 1348.
166. Kwon, O. and D. Kim, *PHz current switching in calcium fluoride single crystal*. Applied Physics Letters, 2016. **108**(19): p. 191112.
167. Kwon, O., et al., *Semimetallization of dielectrics in strong optical fields*. Scientific Reports, 2016. **6**: p. 21272.
168. Paasch-Colberg, T., et al., *Sub-cycle optical control of current in a semiconductor: from the multiphoton to the tunneling regime*. Optica, 2016. **3**(12): p. 1358-1361.
169. Paasch-Colberg, T., et al., *Solid-state light-phase detector*. Nature Photonics, 2014. **8**: p. 214.
170. Schiffrin, A., et al., *Optical-field-induced current in dielectrics*. Nature, 2012. **493**: p. 70.
171. Nisoli, M., S.D. Silvestri, and O. Svelto, *Generation of high energy 10 fs pulses by a new pulse compression technique*. Applied Physics Letters, 1996. **68**(20): p. 2793-2795.
172. Nisoli, M., et al., *Compression of high-energy laser pulses below 5 fs*. Optics Letters, 1997. **22**(8): p. 522-524.
173. Schmidt, B.E., et al., *Compression of 1.8  $\mu$  m laser pulses to sub two optical cycles with bulk material*. Applied Physics Letters, 2010. **96**(12): p. 121109.

174. Rolland, C. and P.B. Corkum, *Compression of high-power optical pulses*. JOSA B, 1988. **5**(3): p. 641-647.
175. Tomlinson, W., R. Stolen, and C. Shank, *Compression of optical pulses chirped by self-phase modulation in fibers*. JOSA B, 1984. **1**(2): p. 139-149.
176. Schulte, J., et al., *Nonlinear pulse compression in a multi-pass cell*. Optics Letters, 2016. **41**(19): p. 4511-4514.
177. Weitenberg, J., et al., *Multi-pass-cell-based nonlinear pulse compression to 115 fs at 7.5  $\mu$ J pulse energy and 300 W average power*. Optics Express, 2017. **25**(17): p. 20502-20510.
178. Giguère, M., et al., *Pulse compression of submillijoule few-optical-cycle infrared laser pulses using chirped mirrors*. Optics letters, 2009. **34**(12): p. 1894-1896.
179. Chen, B.-H., et al., *Compression of picosecond pulses from a thin-disk laser to 30fs at 4W average power*. Optics express, 2018. **26**(4): p. 3861-3869.
180. Heckl, O., et al., *Temporal pulse compression in a xenon-filled Kagome-type hollow-core photonic crystal fiber at high average power*. Optics express, 2011. **19**(20): p. 19142-19149.
181. Mak, K., et al., *Compressing  $\mu$ J-level pulses from 250 fs to sub-10 fs at 38-MHz repetition rate using two gas-filled hollow-core photonic crystal fiber stages*. Optics letters, 2015. **40**(7): p. 1238-1241.
182. Matsubara, E., et al., *Generation of 2.6 fs optical pulses using induced-phase modulation in a gas-filled hollow fiber*. JOSA B, 2007. **24**(4): p. 985-989.
183. Haddad, E., et al., *Molecular gases for pulse compression in hollow core fibers*. Optics Express, 2018. **26**(19): p. 25426-25436.
184. Kang, J.W., A.R. Kim, and J.S. Lim, *High pressure isothermal vapor-liquid equilibria of carbon dioxide+1,1-difluoroethane*. Korean Journal of Chemical Engineering, 2010. **27**(1): p. 261-266.
185. Froemel, P., *Generation of few-cycle laser pulses by hollow-core fiber compression for high harmonic generation*. 2014, Master's thesis, Department of Physics, Humboldt University of Berlin.
186. Heinis, T., et al., *Photoionization mass spectrometry of 1,1-difluoroethane*. Chemical Physics, 1985. **94**(1): p. 235-245.
187. Beaupaire, E., et al., *Ultrafast Spin Dynamics in Ferromagnetic Nickel*. Physical Review Letters, 1996. **76**(22): p. 4250-4253.
188. Klimov, V.I., *Optical Nonlinearities and Ultrafast Carrier Dynamics in Semiconductor Nanocrystals*. The Journal of Physical Chemistry B, 2000. **104**(26): p. 6112-6123.
189. Cavalleri, A., et al., *Femtosecond Structural Dynamics in VO<sub>2</sub> during an Ultrafast Solid-Solid Phase Transition*. Physical Review Letters, 2001. **87**(23): p. 237401.
190. Jimenez, R., et al., *Femtosecond solvation dynamics of water*. Nature, 1994. **369**(6480): p. 471-473.
191. Sansone, G., et al., *Isolated single-cycle attosecond pulses*. Science, 2006. **314**(5798): p. 443-446.
192. Hammond, T., et al., *Attosecond pulses measured from the attosecond lighthouse*. Nature Photonics, 2016. **10**(3): p. 171.
193. Li, J., et al., *53-attosecond X-ray pulses reach the carbon K-edge*. Nature communications, 2017. **8**(1): p. 186.
194. Hassan, M.T., et al., *Optical attosecond pulses and tracking the nonlinear response of bound electrons*. Nature, 2016. **530**(7588): p. 66-70.
195. Gaumnitz, T., et al., *Streaking of 43-attosecond soft-X-ray pulses generated by a passively CEP-stable mid-infrared driver*. Optics Express, 2017. **25**(22): p. 27506-27518.
196. Goulielmakis, E., et al., *Single-Cycle Nonlinear Optics*. Science, 2008. **320**(5883): p. 1614-1617.
197. Zhao, K., et al., *Tailoring a 67 attosecond pulse through advantageous phase-mismatch*. Optics Letters, 2012. **37**(18): p. 3891-3893.

198. Corkum, P.B., *Plasma perspective on strong field multiphoton ionization*. Physical Review Letters, 1993. **71**(13): p. 1994-1997.
199. Walker, B., et al., *Precision Measurement of Strong Field Double Ionization of Helium*. Physical Review Letters, 1994. **73**(9): p. 1227-1230.
200. Seideman, T., M.Y. Ivanov, and P.B. Corkum, *Role of Electron Localization in Intense-Field Molecular Ionization*. Physical Review Letters, 1995. **75**(15): p. 2819-2822.
201. Guo, C., et al., *Single and double ionization of diatomic molecules in strong laser fields*. Physical Review A, 1998. **58**(6): p. R4271-R4274.
202. Moulton, P.F., *Spectroscopic and laser characteristics of Ti:Al<sub>2</sub>O<sub>3</sub>*. Journal of the Optical Society of America B, 1986. **3**(1): p. 125-133.
203. Spence, D.E., P.N. Kean, and W. Sibbett, *60-fsec pulse generation from a self-mode-locked Ti:sapphire laser*. Optics Letters, 1991. **16**(1): p. 42-44.
204. Strickland, D. and G. Mourou, *Compression of amplified chirped optical pulses*. Optics communications, 1985. **56**(3): p. 219-221.
205. Mourou, G.A., C. Barty, and M.D. Perry, *Ultrahigh-intensity laser: physics of the extreme on a tabletop*. 1997, Lawrence Livermore National Lab., CA (United States).
206. Key, M., *Physics at the frontiers of extremely high laser intensity*. Physikalische Blätter, 1995. **51**(7-8): p. 671-675.
207. Timmers, H., et al., *Generating high-contrast, near single-cycle waveforms with third-order dispersion compensation*. Optics Letters, 2017. **42**(4): p. 811-814.
208. Wang, P., et al., *2.6mJ/100Hz CEP-stable near-single-cycle 4μm laser based on OPCPA and hollow-core fiber compression*. Optics Letters, 2018. **43**(9): p. 2197-2200.
209. Jeong, Y.-G., et al., *Direct compression of 170-fs 50-cycle pulses down to 1.5 cycles with 70% transmission*. Scientific reports, 2018. **8**(1): p. 11794.
210. Hädrich, S., et al., *Exploring new avenues in high repetition rate table-top coherent extreme ultraviolet sources*. Light: Science & Applications, 2015. **4**: p. e320.
211. Carstens, H., et al., *High-harmonic generation at 250MHz with photon energies exceeding 100eV*. Optica, 2016. **3**(4): p. 366-369.
212. Hädrich, S., et al., *High photon flux table-top coherent extreme-ultraviolet source*. Nature Photonics, 2014. **8**: p. 779.
213. Beetar, J.E., S. Gholam-Mirzaei, and M. Chini, *Spectral broadening and pulse compression of a 400 μJ, 20 W Yb:KGW laser using a multi-plate medium*. Applied Physics Letters, 2018. **112**(5): p. 051102.
214. Zhavoronkov, N., et al., *Chirped-pulse stimulated Raman scattering in barium nitrate with subsequent recompression*. Optics letters, 2001. **26**(1): p. 47-49.
215. Stapelfeldt, H. and T. Seideman, *Colloquium: Aligning molecules with strong laser pulses*. Reviews of Modern Physics, 2003. **75**(2): p. 543.
216. Seideman, T., *Revival structure of aligned rotational wave packets*. Physical Review Letters, 1999. **83**(24): p. 4971.
217. Bartels, R., et al., *Nonresonant control of multimode molecular wave packets at room temperature*. Physical Review Letters, 2002. **88**(3): p. 033001.
218. Bartels, R., et al., *Phase modulation of ultrashort light pulses using molecular rotational wave packets*. Physical review letters, 2001. **88**(1): p. 013903.
219. Jeong, Y.-G., et al., *Direct compression of 170-fs 50-cycle pulses down to 1.5 cycles with 70% transmission*. Scientific reports, 2018. **8**(1): p. 1-6.
220. Brabec, T. and F. Krausz, *Intense few-cycle laser fields: Frontiers of nonlinear optics*. Reviews of Modern Physics, 2000. **72**(2): p. 545.
221. Krausz, F. and M. Ivanov, *Attosecond physics*. Reviews of Modern Physics, 2009. **81**(1): p. 163.
222. Vicario, C., et al., *High-power femtosecond Raman frequency shifter*. Optics letters, 2016. **41**(20): p. 4719-4722.
223. Spanner, M. and M.Y. Ivanov, *Optimal generation of single-dispersion precompensated 1-fs pulses by molecular phase modulation*. Optics letters, 2003. **28**(7): p. 576-578.

224. IBRAHIM, A., *High energy red-shifted and enhanced spectral broadening by molecular alignment*. 2019.
225. Wahlstrand, J., et al., *Optical nonlinearity in Ar and N<sub>2</sub> near the ionization threshold*. Physical review letters, 2011. **107**(10): p. 103901.
226. Mitschke, F.M. and L.F. Mollenauer, *Discovery of the soliton self-frequency shift*. Optics letters, 1986. **11**(10): p. 659-661.
227. Klas, R., et al., *Generation of coherent broadband high photon flux continua in the XUV with a sub-two-cycle fiber laser*. Optics Express, 2020. **28**(5): p. 6188-6196.
228. Corkum, P.B., *Plasma perspective on strong field multiphoton ionization*. Physical review letters, 1993. **71**(13): p. 1994.